



Universiteit
Leiden
The Netherlands

Quantum computation with Majorana zero modes in superconducting circuits

Heck, B. van

Citation

Heck, B. van. (2015, May 6). *Quantum computation with Majorana zero modes in superconducting circuits. Casimir PhD Series*. Retrieved from <https://hdl.handle.net/1887/32939>

Version: Not Applicable (or Unknown)

License: [Leiden University Non-exclusive license](#)

Downloaded from: <https://hdl.handle.net/1887/32939>

Note: To cite this publication please use the final published version (if applicable).

Cover Page



Universiteit Leiden



The handle <http://hdl.handle.net/1887/32939> holds various files of this Leiden University dissertation.

Author: Heck, Bernard van

Title: Quantum computation with Majorana modes in superconducting circuits

Issue Date: 2015-05-06

Quantum computation with Majorana modes in superconducting circuits

PROEFSCHRIFT

TER VERKRIJGING VAN DE GRAAD
VAN DOCTOR AAN DE UNIVERSITEIT LEIDEN,
OP GEZAG VAN DE RECTOR MAGNIFICUS
PROF. MR. C.J.J.M. STOLKER,
VOLGENS BESLUIT VAN HET COLLEGE VOOR PROMOTIES
TE VERDEDIGEN OP WOENSDAG 6 MEI 2015
KLOKKE 15.00 UUR

DOOR

Bernard van Heck

GEBOREN TE ROME, ITALIË IN 1986

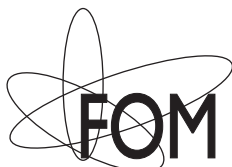
Promotiecommissie:

Promotor: Prof. dr. C. W. J. Beenakker
Co-promotor: Dr. A. R. Akhmerov (Technische Universiteit Delft)
Overige leden: Dr. L. DiCarlo (Technische Universiteit Delft)
Prof. dr. E. R. Eliel
Prof. dr. F. Hassler (Rheinisch-Westfälische Technische Hochschule Aachen)
Prof. dr. J. Zaanen

Casimir PhD Series, Delft-Leiden 2015-10
ISBN 978-90-8593-218-5

Dit werk maakt deel uit van het onderzoekprogramma van de Stichting voor Fundamenteel Onderzoek der Materie (FOM), die deel uit maakt van de Nederlandse Organisatie voor Wetenschappelijk Onderzoek (NWO).

This work is part of the research programme of the Foundation for Fundamental Research on Matter (FOM), which is part of the Netherlands Organisation for Scientific Research (NWO).



On the cover: schematic illustration of a superconducting circuit where Majorana modes can be braided (front) and where the braiding result can be measured (back), see chapter 4.

Alla mia famiglia

Contents

1	Introduction	1
1.1	Identical particles and Berry's phase	2
1.2	Non-Abelian statistics of Majorana modes	4
1.3	Topological quantum computation	7
1.4	Superconducting circuits with Majorana modes	8
1.4.1	Cooper pair box in the transmon limit	8
1.4.2	Flux-controlled Coulomb interaction of Majorana modes	9
1.5	This thesis	11
2	Coulomb stability of the 4π-periodic Josephson effect of Majorana modes	17
2.1	Hamiltonian of a DC SQUID with Majorana modes	18
2.2	DC SQUID with two Majorana junctions	20
2.3	DC SQUID with a single Majorana junction	21
3	Coulomb-assisted braiding of Majorana modes in a Josephson junction array	25
3.1	Majorana-Coulomb Hamiltonian	26
3.1.1	Single island	26
3.1.2	Multiple islands	28
3.1.3	T-junction	29
3.2	Majorana braiding	31
3.3	Discussion	33
3.A	Derivation of the Majorana-Coulomb Hamiltonian	34
3.A.1	Single island	34
3.A.2	Multiple islands	35
3.B	Calculation of the Berry phase of the braiding operation	36
4	Flux-controlled quantum computation with Majorana modes	39
4.1	Minimal circuit for the demonstration of non-Abelian statistics	41
4.1.1	Flux-controlled braiding	43
4.1.2	Initialization and readout	44
4.2	Random Access Majorana Memory	45

4.3	Multi-qubit measurements as a source of computational power	47
4.3.1	Quantum gates	47
4.3.2	Preparation of 2D cluster states	47
4.3.3	Efficient quantum error correction	50
4.4	Discussion	50
4.A	Theoretical description of the π -shaped circuit	51
4.A.1	Braiding	53
4.A.2	Readout	55
4.B	Measurement through photon transmission	56
4.C	Low energy Hamiltonian for a Random Access Majorana Memory architecture	57
4.C.1	Low-energy Hamiltonian in braiding configuration	59
4.C.2	Low-energy Hamiltonian in the readout configuration	60
4.D	Universal gates for quantum computation	61
4.D.1	Notation	62
4.D.2	Single-qubit operations	63
4.D.3	CNOT gate	64
4.D.4	$\pi/8$ Phase Gate	65
4.E	Computation of the error thresholds	66
4.E.1	Realization of the Steane code with the RAMM	69
4.E.2	Steane's code without multi-qubit measurements	69
4.E.3	Comparison of the error thresholds for the quantum memory .	70
4.E.4	Comparison of the error threshold in quantum computation .	70
4.F	Characteristic energy scales of the problem	72
5	Effects of disorder on Coulomb-assisted braiding of Majorana modes	75
5.1	Braiding protocol in the presence of disorder	77
5.2	Analysis of the braiding protocol errors.	79
5.2.1	Effects of disorder on the braiding cycle	79
5.2.2	Effect of disorder on initialization and readout	81
5.3	Summary	82
5.A	Symmetry relations for the braiding errors	82
5.B	Analytical solutions for the braiding errors	84
6	Minimal circuit for a flux-controlled Majorana qubit in a quantum spin-Hall insulator	87
6.1	Top-transmon	88
6.2	Minimal circuit	90
6.3	Characteristic energy scales	92
6.4	Discussion	94
6.A	Energy spectrum of the top-transmon	95
6.A.1	Full Hamiltonian of the circuit	96
6.A.2	Hamiltonian in the measurement configuration	97
6.A.3	Energy spectrum in the measurement configuration	98

7 Realization of microwave quantum circuits using hybrid superconducting-semiconducting nanowire Josephson elements	101
7.1 Description of the experimental setup	102
7.2 Spectroscopy of single-junction devices	103
7.3 Spectroscopy of a double-junction device	104
7.A Materials and Methods	108
7.B Additional data for Device 2	110
7.C Data extraction from flux-bias spectroscopy	111
7.D Theoretical model and fits for Device 3	111
7.E Estimation of Device 3 parameters from model	115
8 Topological blockade and measurement of topological charge	117
8.1 The model	119
8.2 Readout	121
8.3 Extensions	123
8.3.1 Detection of non-Abelian statistics	123
8.3.2 Coupling with conventional qubits	124
8.4 Conclusions	124
9 Braiding of non-Abelian anyons using pairwise interactions	127
9.1 The T-junction	129
9.1.1 Ground state degeneracy	130
9.1.2 Projectors	131
9.2 The adiabatic cycle	133
9.3 Discussion and conclusions	136
9.3.1 Restoring scalability and topological protection	136
9.3.2 Summary	138
10 Topological phases in 2D arrays of parafermionic modes	141
10.1 Effective Hamiltonian for 2D parafermionic architectures	144
10.1.1 Josephson energy	147
10.1.2 Charging energy	148
10.1.3 Effective Hamiltonian	149
10.1.4 Conserved quantities and charge constraints	150
10.2 Mapping to 2D quantum clock models	151
10.3 Topological phases and orders	154
10.3.1 A physical realization of \mathbb{Z}_{2m} toric code anyons: the tile model	156
10.3.2 The stripe model and the \mathbb{Z}_{2m} gauge theory	161
10.4 Conclusions and Outlook	168
10.A Description of the system through bosonization	169
10.B Collective modes of the stripe model and the Z_{2m} gauge theory	171

11 Thermal conductance as a probe of the non-local order parameter for a topological superconductor with gauge fluctuations	173
11.1 Quantum phase slips in a Majorana chain	175
11.2 Connection with a Higgs lattice field theory	176
11.3 Numerical study of the linear response of the chain	177
11.4 Conclusions	180
12 Outlook	183
References	185
Samenvatting	201
Summary	203
Curriculum Vitæ	205
List of Publications	207

Chapter 1

Introduction

When we solve the Schrödinger equation to study the evolution of a quantum system, the solution takes the form of a vector $|\Psi(t)\rangle$ in the Hilbert space. Unlike the more familiar Euclidean space of classical mechanics, it is hard to gain intuition about the Hilbert space using our everyday experience of the physical world. Indeed, $|\Psi(t)\rangle$ is usually a very large vector with complex entries, making it difficult to visualize its trajectory. The vastness of the Hilbert space makes the solution of the Schrödinger equation computationally very expensive, to the point that a full solution for $|\Psi(t)\rangle$ is often out of reach. Rather than being discouraged, we may change point of view and take this fact as a great opportunity. That is, we can look at the quantum state as a computational resource, where information can be stored and manipulated by exploiting features of quantum mechanics such as superposition, entanglement and interference [1, 2]. Surprisingly, the computational power of quantum mechanics seems to supersede that of classical physics, making quantum information a promising field for technological innovation.

However, preparing and controlling at will a quantum state is not an easy task. First, we need to be able to reliably store a quantum state, protecting it from the decoherence due to interaction with the environment. Second, we need a quantum state to follow precisely the trajectory in the Hilbert space corresponding to a desired algorithm. In principle, both goals can be achieved using quantum error correction [3, 4], at the cost of an overhead in memory and time requirements. An alternative approach, *topological quantum computation* [5, 6], shows that it is possible to imagine quantum systems which are naturally endowed with a resilience to decoherence and the possibility to execute algorithms with great accuracy. The topological approach uses the fact that some two-dimensional condensed matter systems can host a class of identical particles – called *non-Abelian anyons* – whose exchange causes a measurable change in the quantum state of the system. An entire algorithm can then be realized as a longer sequence of exchanges involving many particles. The algorithm does not rely on the details of how the exchanges are performed – similar trajectories will yield identical results – and is thus topological in nature. The quantum information

is encoded in the quantum state of the identical particles, and in the presence of an energy gap it stays protected as long as the particles stay far away from each other, or do not accidentally exchange their positions.

The theory of non-Abelian anyons is rooted in the abstract domains of mathematical physics and conformal field theory [7–10]. In condensed matter, non-Abelian anyons appeared first in the theory of the fractional quantum Hall effect [11–13] and later in that of superconductivity [14]. At present, there has been no clear experimental detection of non-Abelian statistics. The central theme of this thesis is to translate this set of beautiful ideas rooted in mathematical physics into a set of concrete devices where non-Abelian statistics can be demonstrated and used for quantum information purposes. The focus will be on the simplest type of particle which is known to obey non-Abelian statistics: Majorana modes occurring as zero-energy excitations in superconducting systems. We will see how the necessary manipulations of Majorana modes can be achieved using simple circuit elements such as capacitors and Josephson junctions, and thus arrive at a new concrete design for the experimental implementation of a fault-tolerant quantum computer. The two design principles behind this proposal are the use of Coulomb interaction as the fundamental physical mechanism permitting control of Majorana modes, and the use of magnetic fluxes as experimental knobs to tune these interactions.

In this introductory chapter, we introduce the main concepts necessary to follow the rest of the thesis. We first review the concept of identical particles in quantum mechanics by making use of the notion of the Berry phase. Then, we derive the non-Abelian statistics of Majorana modes and use them as a concrete example to understand how topological quantum computation works. Finally, we move on to describe how Majorana modes affect the behavior of superconducting circuits, and illustrate the fundamental design principles of our proposal for a *Coulomb-assisted, flux controlled* topological quantum computation with Majorana modes.

1.1 Identical particles and Berry’s phase

The symmetrization postulate is one of the cornerstones of quantum mechanics [15]. It divides particles into bosons and fermions according to their spin, integer or half-integer respectively, and states that quantum states of bosons or fermions have to be symmetric or antisymmetric with respect to the permutation of the positions of any two particles in the system. The symmetrization postulate is supported by a large amount of experimental evidence: the periodic table of chemical elements, the electron Fermi sea in solids and the phenomenon of Bose-Einstein condensation are among its most direct consequences. Furthermore, it follows directly from the union of quantum mechanics with special relativity, which yields a connection between spin and statistics (in fact, the necessary ingredient for such a connection is the existence of anti-particles [16]).

Nevertheless, and most interestingly, the symmetrization postulate is not the end of the story [17]. In two spatial dimensions, quantum mechanics is compatible with

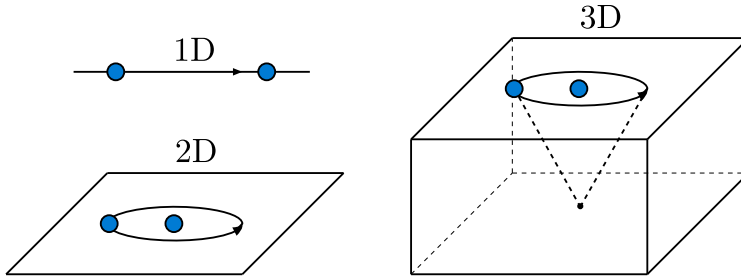


Figure 1.1: Exchanging identical particles in different dimensions. *Top left.* In one dimension, an attempt at exchanging two particles leads unavoidably to a collision. Hence, quantum statistics of identical particles can not be unambiguously defined. *Right.* In three dimensions (or more), the trajectory of a particle enclosing a second one can always be contracted to a single point. This fact implies that the exchange phase of the particles is constrained to two possible values only, corresponding to bosonic and fermionic statistics. *Bottom left.* In two dimensions, a loop around a particle cannot be contracted to a single point. Identical particles can therefore exhibit exotic quantum statistics.

the existence of particles, known as *anyons*, which do not obey bosonic or fermionic statistics. In order to see why two dimensions are special, we can consider the closed trajectory C of a particle around a second, identical particle (Fig. 1.1). This trajectory is equivalent to a sequence of two position exchanges between the particles, hence it gives direct insight into their exchange statistics.

The evolution of the system along the loop C is described by a unitary operator \mathcal{U} connecting the initial and final quantum states,

$$|\Psi(T)\rangle = \mathcal{U}(C, T)|\Psi(0)\rangle. \quad (1.1)$$

Here, T is time it takes the first particle to complete its trajectory. We consider a situation in which no “quantum jumps” occur: at all times $0 \leq t \leq T$, the quantum state $|\Psi(t)\rangle$ is an instantaneous eigenstate of the Hamiltonian with energy $E(t)$. Under these conditions, the quantum adiabatic theorem [15] states that as $T \rightarrow \infty$,

$$\mathcal{U}(C, T) = \exp \left[-i \int_0^T E(t) dt \right] \exp [i\gamma(C)]. \quad (1.2)$$

The first phase factor is the usual dynamical phase factor found in the solution of the Schrödinger equation. We are more interested in the second phase factor $\gamma(C)$, which is known as the Berry phase [18, 19],

$$\gamma(C) = \int_0^T \left\langle \Psi(t) \left| \frac{d\Psi(t)}{dt} \right. \right\rangle dt. \quad (1.3)$$

Since dt appears both on numerator and denominator in the expression above, the Berry phase does not depend on T nor on the kinematics of the trajectory, but only

on the loop C . In general, the Berry phase is the sum of two components. The first component depends on the *geometrical properties* of C – for instance, if an external magnetic field is present, this geometric contribution is the Aharonov-Bohm phase, which is proportional to the magnetic flux enclosed by the loop, and hence to the area of the loop. The second component only depends on the *topological properties* of C , i.e. on the winding number n , the number of times that the first particle encircles the second ($n = 1$ for the paths in Fig. 1.1). Different trajectories which can be continuously deformed into each other have the same winding number, and hence are characterized by the same topological contribution to the Berry phase. Its value is given by $2n\theta$, where θ specifies the quantum statistics of the two particles and the factor of two is due to the fact that every loop is equivalent to two exchanges.

As shown in Fig. 1.1, in three dimensions a closed loop C can always be deformed to a single point, that is to a trajectory where the first particle does not move at all. Therefore, the topological contribution to the Berry phase vanishes for all loops. We must in other words require that $2\theta = 0 \pmod{2\pi}$, which yields two possible exchange phases $\theta = 0$ or $\theta = \pi$, corresponding to bosonic and fermionic quantum statistics respectively. In two dimensions, however, the winding number of a loop can not be changed via a continuous deformation of the loop. Hence, in principle there is no restriction on the value of θ . Particles which have a value of θ different from 0 or π are called *Abelian anyons*.

So far we have implicitly assumed the state $|\Psi(t)\rangle$ to be non-degenerate. Let us now consider the case of a degeneracy D . In this case, the quantum state is specified by D components $|\Psi_n(t)\rangle$, and the Berry phase factor $\exp[i\gamma(C)]$ appearing in Eq. (1.2) has to be substituted by a $D \times D$ matrix [20],

$$U(C) = P \exp \left[\int_0^T A(t) dt \right]. \quad (1.4)$$

Here, P is the path-ordering operator and A is a skew-Hermitian matrix ($A^T = -A^*$) known as the Berry connection, with matrix elements $A_{nm}(t) = \langle \Psi_m(t) | d\Psi_n(t) / dt \rangle$. Like its one-dimensional counterpart, the Berry matrix $U(C)$ will have a geometric component and a topological one. It is therefore possible that the exchange of two particles results in a non-trivial unitary rotation in the degenerate ground state manifold. Crucially, Berry matrices corresponding to the exchange of two different pairs of particles need not commute. *Non-Abelian anyons* are precisely the class of identical particles having this property. In the following section, we will clarify this concept with a concrete and simple example which is central to the whole thesis: Majorana modes.

1.2 Non-Abelian statistics of Majorana modes

Majorana modes are mid-gap (zero energy) quasiparticles which can appear in superconducting systems with broken time-reversal and spin-rotation symmetry [22–24]. Since a clean superconductor does not allow for bulk excitations with energy smaller

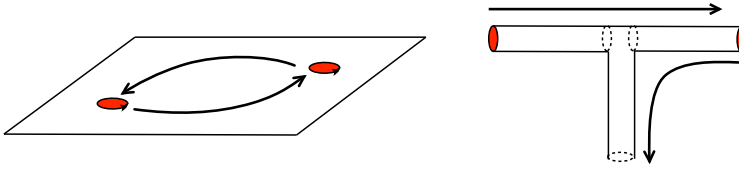


Figure 1.2: Majorana modes (red dots) can appear bound to vortices in superconducting thin films (left, [14]), or equivalently at domain walls in networks of quantum wires (right, [21]). In both cases, their positions can be exchanged in space, as depicted by the arrows. Because of the non-Abelian statistics of the Majorana modes, the procedure results in a non-trivial rotation on the quantum state of the superconductor.

than the pairing gap, a Majorana mode can be found either bound to a vortex in a superconducting film [14, 25] or localized at the end of a superconducting nanowire [26]. In virtue of particle-hole symmetry of the superconductor and in the absence of degeneracies, the creation and annihilation operators of a zero energy mode coincide: $\gamma = \gamma^\dagger$. Operators corresponding to different modes anti-commute, as normal fermionic operators, leading to the unusual set of relations

$$\gamma_n \gamma_m + \gamma_m \gamma_n = 2\delta_{nm}. \quad (1.5)$$

Note in particular that $\gamma_n^2 = 1$, so that we cannot speak of the Majorana mode being ‘empty’ or ‘occupied’. Out of two Majorana modes, say γ_1 and γ_2 , we can however construct an ordinary fermionic annihilation operator $c = \frac{1}{2}(\gamma_1 + i\gamma_2)$ satisfying $cc^\dagger + c^\dagger c = 1$. Hence, the two Majorana modes can be thought as the real and imaginary part of a conventional fermion mode. Their peculiarity is that they are well separated in space. This argument reveals that Majorana modes can only occur in pairs: if the number of vortices is odd, an additional mode must lie somewhere along the boundary of the superconductor. It also reveals that the two Majorana modes form a two-level system, with the two states differing by the presence or absence of a fermion. As long as the Majorana modes are kept at a distance much longer than the coherence length, the two levels are degenerate in energy, so that it is not costly to remove or add a fermion to the system.

Let us now consider a two-dimensional superconductor with $2N$ vortices hosting Majorana modes $\gamma_1, \dots, \gamma_{2N}$. We can group the Majorana modes in pairs to form N fermionic creation operators c_1, \dots, c_N . These operators span a degenerate manifold with 2^N states $|p_1 \dots p_N\rangle$ labeled by the occupation numbers $p_n = 0, 1$ of the N fermionic modes. In an isolated superconductor fermion parity is a conserved quantity, so the manifold is divided in two subspaces containing all the states of even and odd parity. They are distinguished by the eigenvalue ± 1 of the fermion parity operator

$$\mathcal{P} = i^N \gamma_1 \dots \gamma_{2N}, \quad \mathcal{P}^2 = 1. \quad (1.6)$$

Within the even or odd subspace, which have dimension 2^{N-1} , superpositions of states are allowed.

Let us see what happens when two vortices are adiabatically exchanged in space [27]. We might of course do so by computing the Berry matrix using Eq. (1.4). However, there is a more direct way which allows to arrive at the result without much effort. It is convenient to adopt the Heisenberg picture, where the Majorana operators depend explicitly on time. In particular, the two Majorana modes bound to the vortices being moved are related to the Berry matrix by the equation

$$\gamma_{n,m}(T) = U_{nm} \gamma_{n,m}(0) U_{nm}^\dagger, \quad (1.7)$$

up to a phase factor. We have denoted the Berry matrix as U_{nm} since it is natural to assume that it will only depend on the Majorana modes γ_n, γ_m involved in the exchange. Furthermore, U_{nm} has to preserve fermion parity, $[U_{nm}, \mathcal{P}] = 0$. This means that it can only depend on the product $\gamma_n \gamma_m$. Finally, unitarity imposes that the Berry matrix is of the form $U_{nm} = \exp(\alpha \gamma_n \gamma_m)$, with α a real coefficient to be determined. Direct calculation yields

$$\gamma_n(T) = \cos(2\alpha) \gamma_n(0) - \sin(2\alpha) \gamma_m(0), \quad (1.8a)$$

$$\gamma_m(T) = \cos(2\alpha) \gamma_m(0) + \sin(2\alpha) \gamma_n(0). \quad (1.8b)$$

We want the two operators to be interchanged by U , leading to the choice $\alpha = \pm\pi/4$. The sign of α distinguishes clockwise and counterclockwise exchanges of the vortices, the precise assignment being arbitrary. The final result is therefore

$$U_{nm} = \exp\left(\frac{\pi}{4} \gamma_n \gamma_m\right). \quad (1.9)$$

We see that the Berry matrix resulting from the exchange is not simply an overall phase, but a non-trivial rotation in the ground state manifold. Also, we see that Berry matrices corresponding to exchanges of different pairs do not commute if the two pairs share one Majorana, and commute otherwise.

To understand the multiplication properties of these matrices better, let us imagine that initially all Majoranas are ordered on a line according to their index n . The exchange between any pair of Majoranas can be generated via a succession of exchanges between neighboring Majoranas, hence we may focus on the matrices $U_{n,n+1}$. To keep track of all the exchanges, we may imagine that a strand is attached to each vortex, such that a succession of exchanges forms a braid out of the $2n$ strands. We see that to each different braid, we may associate a corresponding unitary operator via a multiplication of an appropriate sequence of matrices $U_{n,n+1}$. It can be checked that these matrices obey the following relations,

$$U_{n,n+1} U_{n+1,n+2} U_{n,n+1} = U_{n+1,n+2} U_{n,n+1} U_{n+1,n+2}. \quad (1.10)$$

Mathematically, these are precisely the relations obeyed by the generators of the *braid group*, which is a generalization of the permutation group to a situation where the order of the exchanges matter. For this reason, the exchange of two Majorana modes (or of non-Abelian anyons in general) is usually referred to as *braiding*.

1.3 Topological quantum computation

The discussion of the previous section is a good starting point to understand topological quantum computation more in detail, using Majorana modes as a practical example of non-Abelian anyons. The main ideas are the following:

1. The ground state manifold of $2N$ Majorana modes is taken as the computational space. At a fixed total fermion parity, it forms a register of $N - 1$ qubits. The physical degree of freedom which is used to encode the qubits is the fermion parity of pairs of Majorana modes, sometimes also referred to as their *topological charge*.
2. Operations on the register are performed by braiding Majorana modes in space.
3. Initialization and measurement of the register entries are carried out by bringing two Majorana modes very close to each other, an operation sometimes called *fusion*. When this happens, the ground state degeneracy splits, allowing for a readout of the fermion parity of the two joint Majorana modes.

It is essential that the ground state manifold is protected by an energy gap from the excited states. This ensures that the adiabatic limit can be reached when operating on the register, and protects the register from dissipation.

The advantages of this approach are:

1. The quantum gates which can be executed via braiding are extremely accurate and do not depend on the exact trajectory followed during the exchange. In this sense, they are extremely resilient to implementation inaccuracies.
2. The quantum state of the register is encoded in the fermion parity degrees of freedom, which are shared non-locally by the Majorana modes. This means that no local perturbation can change the state of the register and cause decoherence. An experimentally relevant exception is a change in fermion parity due to the tunneling of a stray quasiparticle into the system (quasiparticle poisoning).

A crucial question in topological quantum computation is whether braiding operations are universal, in the sense that any unitary operation on the register can be approximated with arbitrary accuracy by a finite sequence of braiding operations. Unfortunately, this is not the case for Majorana modes. In this case, braiding operation have to be supplemented by non-topological ones.

So far our discussion has not addressed the problem of how to initialize, braid and measure Majorana modes in practice. As already mentioned and as discussed in more detail in the next section, our proposal is to use microwave superconducting circuits for all these purposes.

1.4 Superconducting circuits with Majorana modes

In superconducting circuits, macroscopic physical observables such as currents and voltages exhibit quantum behavior. In fact, superconducting circuits are one of the most prominent platforms for quantum information processing [28–31]. In this section we will describe in simple terms how Majorana modes affect the physics of superconducting circuits. In order to do so, we start by describing the “hydrogen atom” of superconducting circuits - the Cooper pair box.

1.4.1 Cooper pair box in the transmon limit

A Cooper pair box consists of two superconductors connected by a capacitor and a Josephson junction, possibly split in two arms, see Fig. 1.3. Cooper pairs can flow between the two island by quantum tunneling across the Josephson junction. This motion results in fluctuations in the voltage $v(t)$ and current $i(t)$ between the two nodes of the circuit. The dynamics of the system can be described in terms of the integrals of current and voltages, which are the phase and charge difference across the junction,

$$\phi = \frac{2\pi}{\Phi_0} \int_{-\infty}^t v(t') dt', \quad N = \frac{1}{e} \int_{-\infty}^t i(t') dt'. \quad (1.11)$$

Here, $\Phi_0 = h/2e$ is the superconducting flux quantum. These two quantities are canonically conjugate variables, similarly to position and momentum of a particle,

$$[\phi, N] = 2i. \quad (1.12)$$

The factor of two in the commutation relations is due to the fact that electrons form Cooper pairs in the superconducting condensate, and hence charge is transferred in units of $2e$ across the junction. The Hamiltonian describing the Cooper pair box is

$$H = E_C N^2 + E_J (1 - \cos \phi), \quad (1.13)$$

with $E_C = e^2/2C$ the charging energy and E_J the Josephson energy. In the split-junction geometry, the Josephson energy can be varied by threading a magnetic flux Φ in the loop formed by the two arms of the junction. Neglecting any asymmetry between the strengths of the two arms, one has $E_J = E_{J,0} \cos(\pi\Phi/\Phi_0)$.

The circuit exhibits quantized energy levels, which are observable provided that temperature and damping-induced broadening of the levels are both much smaller than the level spacing. We will be particularly interested in the limit $E_J \gg E_C$, where the level spacing is approximately constant,

$$E_n \simeq \hbar\Omega(n + 1/2), \quad (1.14)$$

where $\hbar\Omega = \sqrt{8E_J E_C}$ is the plasma frequency, which characterizes current oscillations across the Josephson junction. Typical values of Ω are in the range 5 to 30 GHz,

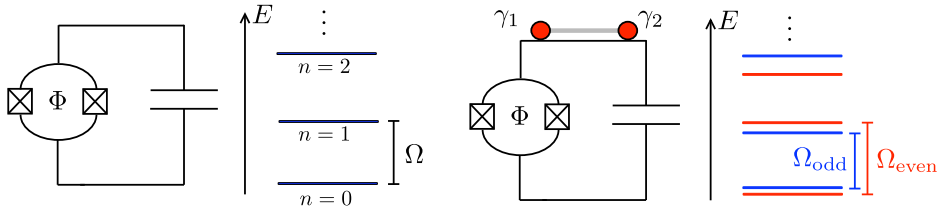


Figure 1.3: *Left:* A Cooper pair box with a split Josephson junction. When the Josephson energy is much larger than the charging energy, and at very low temperatures, the energy spectrum consists of almost equally spaced levels separated by the plasma frequency $\Omega \simeq \sqrt{8E_J E_C}$. *Right:* If one of the two islands hosts Majorana modes (red circles), for instance appearing at the ends of a nanowire (grey), every level splits into a doublet of levels with different fermion parity [35].

allowing the system to be controlled with microwave radiation, using all the technology of RF electronic engineering. A Cooper pair box in this regime and coupled to a transmission line resonator constitutes a *transmon*, one of the most common and successful superconducting qubits.

Importantly, the Cooper pair box Hamiltonian only describes the quantum dynamics of the superconducting condensate, neglecting the contribution of unpaired quasiparticles. In principle, this description is accurate when $k_B T \ll \Delta$, the superconducting gap. Only states of even fermion parity are then relevant to the dynamics of the circuit, as states with odd parity have all energies greater than Δ . In practice, however, non-equilibrium quasiparticles are often observed in superconducting circuits even at very low temperatures, and cause random switches in the fermion parity of a superconducting island. For the sake of conceptual simplicity, and also motivated by recent progress in the enhancement of the parity lifetime of superconducting circuits [32–34], in what follows we disregard this complication.

1.4.2 Flux-controlled Coulomb interaction of Majorana modes

If one of the two superconducting islands forming the Cooper pair box hosts two Majorana modes γ_1 and γ_2 , one quasiparticle can be accommodated with no energy cost. The situation changes drastically, because now there are now two distinct superconducting condensates, one with even and one with odd parity. In the limit $E_C \rightarrow 0$, when the phase ϕ becomes a good quantum number, the even and odd states are to a good approximation given by a coherent superposition of all the charge states with the appropriate parity,

$$|\phi, e\rangle = \sum_n e^{i\phi n} |2n\rangle, \quad (1.15a)$$

$$|\phi, o\rangle = \sum_n e^{i\phi(n+1/2)} |2n+1\rangle. \quad (1.15b)$$

Even and odd states behave differently with respect to a shift of the superconducting phase by 2π : $|\phi + 2\pi, e/o\rangle = \pm|\phi, e/o\rangle$. In other words, even and odd states are respectively periodic and anti-periodic under a shift of ϕ by 2π . This boundary condition imposes a constraint between the Majorana operators and the number operator [36],

$$i\gamma_1\gamma_2 = (-1)^N. \quad (1.16)$$

The expression above is the mathematical statement corresponding to the fact that the fermion parity of a superconductor with Majorana modes is equal to the total charge contained in the superconductor, modulo $2e$. Eq. (1.16) is a gauge constraint on the Hilbert space of the Cooper pair box with Majorana modes. It has to be taken into account when solving the Cooper pair box Hamiltonian (1.13). A way to do so is to make a unitary transformation $|\Psi\rangle \mapsto R|\Psi\rangle$, with

$$R = \exp[i(1 - i\gamma_1\gamma_2)\phi/4]. \quad (1.17)$$

This transformation acts trivially on the even states, but makes the odd states periodic under a shift of ϕ by 2π . The Hamiltonian becomes (recall that $N = -2i\partial_\phi$)

$$RHR^\dagger = E_C[N + (1 - i\gamma_1\gamma_2)/2]^2 + E_J(1 - \cos\phi). \quad (1.18)$$

We see that the Majorana modes now appear explicitly in the charging energy term. At the same time, since the new Hamiltonian acts on a space of 2π -periodic functions, the eigenvalues of N are restricted to the even numbers,. Note that the argument would apply equally to the case of a superconductor having more than two Majorana modes - in this case, the product $i^N\gamma_1 \dots \gamma_{2N}$ would appear in the Hamiltonian instead of $i\gamma_1\gamma_2$.

One might at first be surprised that Majorana modes are related to the charge in the superconductor, since they are usually presented as neutral objects. The neutrality of the Majorana modes is due to the presence of a superconducting condensate, which “absorbs” the charge corresponding to the fermion parity encoded in a pair of Majorana modes. In a grounded superconductor it is possible to forget about the charge degrees of freedom by fixing the phase ϕ of the superconductor, so that the boundary condition becomes irrelevant. However, in a floating superconductor this is no longer possible, and the relation between fermion parity and electric charge has to be restored explicitly.

In the transmon limit, one finds that the energy spectrum of the Cooper pair box with Majorana modes is given by a sequence of closely spaced doublets corresponding to states with different parity. Subsequent doublets are still separated by the plasma frequency $\hbar\Omega$. The n -th doublet has a parity-dependent energy splitting given by

$$\Delta_n \simeq E_C \left(\frac{E_C}{2E_J} \right)^{n/2+3/4} \exp\left(-\sqrt{8E_J/E_C}\right). \quad (1.19)$$

The expert reader may recognize in the above expression the charge dispersion of a transmon [37]. In fact, the change in the energy spectrum due to the parity encoded in

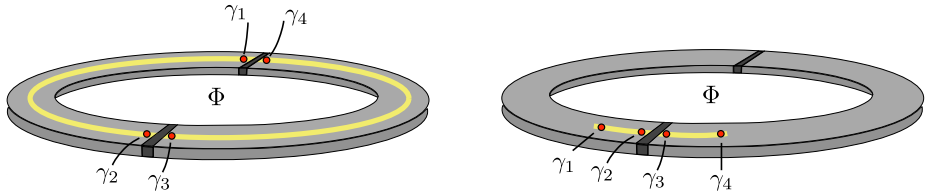


Figure 1.4: The two DC SQUID geometries studied in chapter 2, where we show that, in the presence of charging energy, the system shown in the left has a 4π -periodic Josephson energy, while the one on the right has a 2π Josephson-energy due to quantum phase slips through the Josephson junction without Majorana modes.

the Majorana mode is equivalent to the change determined by increasing or decreasing by e the induced charge on the capacitor plates.

Eq. (1.19) has two important consequences for our purposes. The first is that the frequencies of the circuit become parity-dependent, as also shown in the rightmost panel of Fig. 1.3. For the two lowest transmon states, the difference $\hbar(\Omega_{\text{even}} - \Omega_{\text{odd}})$ is typically in the range 1 to 100 MHz. Such a frequency shift in a transmon can be easily detected using microwaves, and the detection allows us to measure the fermion parity of the Majorana modes. The second consequence is that the parity splitting is very sensitive to the ratio E_J/E_C . This means that using a split junction and varying the flux Φ by half of a superconducting flux quantum, the energy splitting between different fermion parity states can be varied by a few orders of magnitude.

This exponential sensitivity gives us a very practical handle to operate on the quantum state of a collection of Majorana modes, while still keeping them at distances much larger than the coherence length. This is the main design principle behind our proposal for a superconducting implementation of topological computation.

1.5 This thesis

Before moving on, we give here an outline of the contents go this thesis. In chapters two to six, we will develop in detail the theory of Majorana modes in superconducting circuits and the blueprint for a topological quantum computer which is based on that theory. Chapter seven reports on the first experimental realization of hybrid superconducting microwave circuits with semiconducting nanowires¹. The remaining chapters extend the results of the first six chapters in different directions and physical systems. Chapter eight discusses how to measure and manipulate Majorana modes in fractional quantum Hall systems, while chapter nine generalizes the Majorana braiding scheme developed in chapter two to a generic model of non-Abelian anyons. Finally, chapter ten is a study of superconducting arrays in the presence of electron

¹The experiments described in chapter seven were performed in Dr. Leo DiCarlo's group in Delft. My contribution consisted in the theoretical analysis and interpretation of the experimental data.

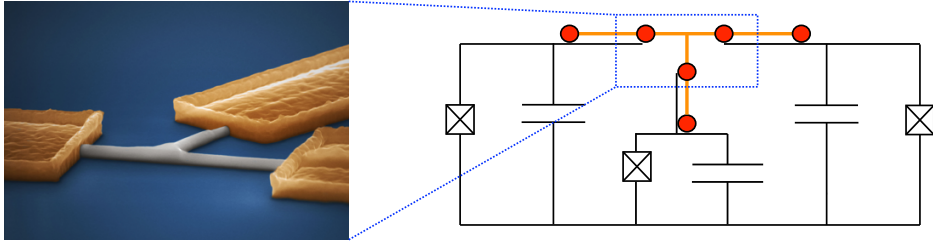


Figure 1.5: The superconducting circuit introduced in chapter three, able to perform flux-controlled braiding of Majorana modes. An essential element of the circuit is a T-junction, such as the InSb nanocross [38] shown in the image on the left (image courtesy of the Kouwenhoven group, TU Delft).

fractionalization, and chapter eleven a study of the transport properties of a linear array of superconducting islands with Majorana modes. We now give a brief description of the content of each chapter.

Chapter two. A peculiar signature of Majorana modes is the fact that the Josephson energy of two superconducting islands containing Majorana modes is a 4π -periodic function of the superconducting phase difference. If the islands have a small capacitance, their ground state energy is governed by the competition of Josephson and charging energies. In this chapter, we calculate this ground state energy in the ring geometries of Fig. 1.4. We show that the dependence on the Aharonov-Bohm phase $2e\Phi/\hbar$ remains 4π -periodic regardless of the ratio of charging and Josephson energies — provided that the entire ring is in a topologically nontrivial state. If part of the ring is topologically trivial, then the charging energy induces quantum phase slips that restore the usual 2π -periodicity. This chapter elucidates the consequences of the parity constraint, Eq. (1.16), on the properties of superconducting circuits, and it provides a preliminary understanding on how one can control the coupling of Majorana modes using Coulomb interactions.

Chapter three. We show how to braid Majorana modes in a network of superconducting nanowires by control over Coulomb interaction. The key idea behind flux-controlled braiding is to control independently the charging energy of the three arms of a T-junction using flux bias lines. Hence, the required circuit essentially consists of three copies of a Cooper pair box connected by a T-junction, see Fig. 1.5. T-junctions can be realized using InSb nanowires [38], making the proposed circuit experimentally feasible. Furthermore, as we see further in chapter 6, the flux-controlled braiding scheme can in fact be adapted to other systems which can support Majorana modes, such as quantum spin-Hall insulator/superconductor heterostructures. An advantage of this proposal is that the positions of the Majorana modes do not need to be changed, and local control gates do not need to be tuned during the braiding

operation.

Chapter four. Here we build on the results of the previous chapter, expanding the circuit of Fig. 1.5 to a larger one where the state of the Majoranas can be initialized and the result of a braiding operation can be measured. We identify the minimal circuit that can perform the initialization–braiding–measurement steps required to demonstrate non-Abelian statistics of Majorana modes. We then analyze the scalability of the circuit from a quantum information perspective. To this purpose, we introduce a quantum register, which we call a Random Access Majorana Memory, that can perform a joint parity measurement on Majoranas belonging to a selection of topological qubits. Such multi-qubit measurements allow for the efficient creation of highly entangled states and simplify quantum error correction protocols by avoiding the need for ancilla qubits.

Chapter five. A major obstacle towards the experimental demonstration of non-Abelian statistics in nanowire networks might be constituted by the presence of disorder in the nanowires. Strong disorder may indeed induce the presence of accidental Majorana modes at unwanted positions in the nanowire networks. In this chapter, we show that the Coulomb-assisted braiding protocol of the previous two chapters can be efficiently realized also in the presence of accidental modes. In particular, the errors occurring during the braiding cycle are small if the couplings of the computational Majorana modes to the accidental ones are much weaker than the maximum Coulomb coupling which is necessary during the braiding operation.

Chapter six. In this chapter, we construct a minimal circuit to rotate a qubit formed out of four Majorana modes at the edge of a two-dimensional quantum spin-Hall insulator. This circuit is smaller than the one required for a braiding operation, and might represent a good intermediate step towards braiding. Indeed, unlike braiding operations, generic rotations have no topological protection, but they do allow for a full characterization of the coherence times of the Majorana qubit. The rotation is controlled by variation of the flux through a pair of split Josephson junctions in a Cooper pair box, without any need to adjust gate voltages. The Rabi oscillations of the Majorana qubit can be monitored via oscillations in the resonance frequency of the microwave cavity that encloses the Cooper pair box.

Chapter seven. We present and analyze measurement on quantum microwave circuits with hybrid Josephson elements, comprised of semiconducting InAs nanowires contacted by the highly-disordered superconducting alloy NbTiN. Capacitively-shunted single elements behave as weakly anharmonic oscillators, or transmons, but with electrically tunable transition frequencies. Double-element circuits display similar transmon-like behavior at zero applied flux, while when biased at half the flux quantum they exhibit instead a strongly anharmonic spectrum, similar to that of a flux qubit. Theoretical analysis of the data explains this behavior via the formation of a double-well Josephson potential, due to the non-sinusoidal current-phase relation

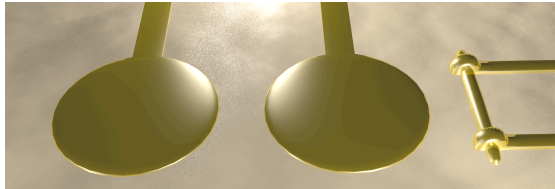


Figure 1.6: An illustration of the measurement device proposed in chapter 8 to measure the presence of the Majorana modes bound to charged quasiparticles in the $\nu = 5/2$ quantum Hall plateau. Two gates suspended on the quantum Hall liquid form two small dots, each binding a single quasiparticle. Double occupancy on one of the two dots comes with an extra energy cost associated with the fusion of two Majorana modes, and this energy can be detected by a charge sensor (right).

of the nanowire Josephson junctions. Close to half a flux quantum, we observe microwave-driven transitions between states with oppositely flowing persistent currents, manifesting macroscopic quantum coherence. The hybrid nanowire transmon devices presented in this chapter are magnetic-field compatible, hence they represent a first milestone on the road towards experiments combining superconducting circuits with Majorana modes.

Chapter eight. In this chapter, we shift our attention to the $\nu = 5/2$ quantum Hall plateau, whose fractionally charged quasiparticles are predicted to have an extra non-local degree of freedom, known as topological charge. This extra degree of freedom can in fact be understood as a Majorana mode bound to the quasiparticle. We show how this topological charge can block the tunneling of these quasiparticles, and how such *topological blockade* can be used to readout their topological charge (see Fig. 1.6), similarly to a charge readout of singlet-triplet qubits. We argue that the short time scale required for this measurement is favorable for the detection of the non-Abelian anyonic statistics of the quasiparticles. We also show how topological blockade can be used to measure braiding statistics, and to couple a topological qubit with a conventional one.

Chapter nine. The common approach to topological quantum computation is to implement quantum gates by adiabatically moving non-Abelian anyons around each other. However, chapters three and four of this thesis presented an alternative perspective based on the possibility of realizing the braiding of Majorana modes by adiabatically varying pairwise interactions between them, rather than their positions. In this chapter we show that this alternative approach is not specific to Majorana modes, but it works for generic non-Abelian anyons. We analyze a system composed by four anyons whose couplings define a T-junction and we show that the braiding operator of two of them can be obtained through a particular adiabatic cycle in the space of the coupling parameters. We also discuss how to couple this scheme with

anyonic chains in order to recover the topological protection.

Chapter ten. It is possible to generalize the notion of Majorana modes to system with electron fractionalization. So-called parafermionic modes with non-Abelian statistics may indeed exist at the interface between a superconductor and a ferromagnet along the edge of a fractional topological insulator. This chapter studies two-dimensional architectures of these non-Abelian anyons, whose interactions are generated by the charging and Josephson energies of the superconductors. We derive low-energy Hamiltonians for two different arrays of fractional topological insulators on the plane, revealing an interesting interplay between the real-space geometry of the system and its topological properties. On the one hand, in a geometry where the length of the FTI edges is independent on the system size, the array has a topologically ordered phase, giving rise to a qudit toric code Hamiltonian in perturbation theory. On the other hand, in a geometry where the length of the edges scales with system size, we find an exact duality to an Abelian lattice gauge theory and no topological order.

Chapter eleven. The last chapter is dedicated to the study of the transport properties of a linear array of superconducting islands with Majorana modes. In particular, we investigate the effect of quantum phase slips on the linear response of the array to an external voltage or temperature gradient. The effective low-energy description of the wire is that of a Majorana chain minimally coupled to a dynamical \mathbb{Z}_2 gauge field. Hence the wire emulates a matter-coupled gauge theory, with fermion parity playing the role of the gauged global symmetry. Quantum phase slips lift the ground state degeneracy associated with unpaired Majorana edge modes at the ends of the chain, a change that can be understood as a transition between the confined and the Higgs-mechanism regimes of the gauge theory. We identify the quantization of thermal conductance at the transition as a robust experimental feature separating the two regimes. We explain this result by establishing a relation between thermal conductance and the Fredenhagen-Marcu string order-parameter for confinement in gauge theories.

Chapter 2

Coulomb stability of the 4 π -periodic Josephson effect of Majorana modes

The energy H_J of a tunnel junction between two superconductors (a Josephson junction) depends on the difference ϕ of the phase of the order parameter on the two sides of the junction. The derivative $I_J = (2e/\hbar)dH_J/d\phi$ gives the supercurrent flowing through the junction in the absence of an applied voltage. In a ring geometry, the supercurrent depends periodically on the flux Φ enclosed by the ring, with periodicity $h/2e$. This familiar DC Josephson effect [39, 40] acquires a new twist if the junction contains Majorana modes [26, 41, 42].

Majorana modes are charge-neutral quasiparticles bound to mid-gap states, at zero excitation energy, which appear in a so-called topologically non-trivial superconductor [43, 44]. While in the conventional Josephson effect only Cooper pairs can tunnel (with probability $\tau \ll 1$), Majorana modes enable the tunneling of single electrons (with a larger probability $\sqrt{\tau}$). The switch from $2e$ to e as the unit of transferred charge amounts to a doubling of the fundamental periodicity of the Josephson energy, from $H_J \propto \cos \phi$ to $H_J \propto \cos(\phi/2)$. In a ring geometry, the period of the flux dependence of the supercurrent I_J doubles from 2π to 4π as a function of the Aharonov-Bohm phase¹ $\varphi_0 = 2e\Phi/\hbar$. This 4π -periodic Josephson effect has been extensively studied theoretically [42, 45–50], as a way to detect the (so far, elusive) Majorana modes [51].

Since the Majorana modes in a typical experiment will be confined to superconducting islands of small capacitance C , the Coulomb energy $H_C = Q^2/2C$ associated with a charge difference $2Q$ across the junction competes with the Josephson energy.

¹As a function of the enclosed flux, I_J has the same h/e periodicity as the persistent current I_N through a normal metal ring (radius R). One can distinguish the two currents by their size dependence: While I_N decays as $1/R$ or faster, I_J has the R -independence of a supercurrent.

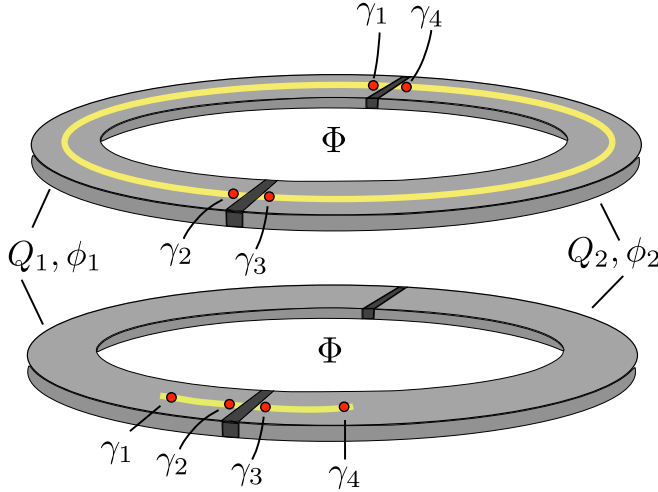


Figure 2.1: Geometry of a DC SQUID, consisting of a superconducting ring (grey) interrupted by two tunnel junctions (black) and threaded by a magnetic flux Φ . A semiconductor nanowire (yellow) contains Majorana modes at the end points (red dots). The two panels distinguish the cases that Majorana modes are present at both junctions (top), or only at a single junction (bottom). The 4π -periodic Josephson effect is stable against quantum phase slips in the first case, but not in the second case.

The commutator $[\phi, Q] = 2ei$ implies an uncertainty relation between charge and phase differences, so that a nonzero H_C introduces quantum fluctuations of ϕ in the ground state [40]. What is the fate of the 4π -periodic Josephson effect?

As we will show in this chapter, the supercurrent through the ring remains a 4π -periodic function of φ_0 , regardless of the relative magnitude of H_C and H_J . This Coulomb stability requires that all weak links in the ring contain Majorana modes. If the ring has a topologically trivial segment, then quantum phase slips restore the conventional 2π -periodicity of the Josephson effect on sufficiently long time scales. We calculate the limiting time scale for the destruction of the 4π -periodic Josephson effect by quantum phase slips and find that it can be much shorter than the competing time scale for the destruction of the 4π -periodicity by quasiparticle poisoning [42].

2.1 Hamiltonian of a DC SQUID with Majorana modes

We apply the general theory of Majorana-Josephson junction arrays of Xu and Fu [52] to the DC SQUID geometry of Fig. 2.1, consisting of two superconducting islands separated by tunnel junctions. The islands have a charge difference $2Q = Q_1 - Q_2$, with $Q_n = -2ei\partial/\partial\phi_n$ canonically conjugate to the superconducting phase ϕ_n . The

gauge invariant phase differences across the two junctions are given by $\phi = \phi_1 - \phi_2$ and $\varphi_0 - \phi$. Here we assume that the ring is sufficiently small that the flux generated by the supercurrent can be neglected, so the enclosed flux equals the externally applied flux².

Each island contains a segment of a semiconductor nanowire, driven into a topologically nontrivial superconducting state by the proximity effect [45, 46] (alternatively, the nanowire could be replaced by the conducting edge of a two-dimensional topological insulator [42]). The Majorana modes appearing at the end points of each segment are represented by anti-commuting Hermitian operators $\gamma_1, \gamma_2, \gamma_3, \gamma_4$ that square to unity,

$$\gamma_n = \gamma_n^\dagger, \quad \gamma_n \gamma_m + \gamma_m \gamma_n = 2\delta_{nm}. \quad (2.1)$$

The Majorana modes are coupled by the tunnel junction. We distinguish two cases. In the first case (top panel in Fig. 2.1) each of the two tunnel junctions couples a pair of Majorana modes. In the second case (bottom panel) one pair of Majorana modes is coupled by a Josephson junction, while the other pair remains isolated.

The Hamiltonian $H = H_C + H_{J,1} + H_{J,2}$ is the sum of charging and Josephson energies,

$$H_C = \frac{1}{2C}(Q + q_{\text{ind}})^2, \quad (2.2)$$

$$H_{J,1} = E_{M,1}\Gamma_1 \cos \frac{\phi}{2} - E_{J,1} \cos \phi, \quad (2.3)$$

$$H_{J,2} = E_{M,2}\Gamma_2 \cos \frac{\varphi_0 - \phi}{2} - E_{J,2} \cos(\varphi_0 - \phi), \quad (2.4)$$

$$\Gamma_1 = i\gamma_2\gamma_3, \quad \Gamma_2 = i\gamma_4\gamma_1. \quad (2.5)$$

The induced charge $q_{\text{ind}} = C_g V_g$ accounts for charges on nearby electrodes, controlled by a gate capacitance C_g and gate voltage V_g . The energy scales $E_{M,n}$ and $E_{J,n}$ quantify the Josephson coupling strength of, respectively, single electrons and electron pairs. With this Hamiltonian we can describe both cases considered, by putting $E_{M,2} = 0$ for the junction without Majorana modes.

The eigenstates $\Psi(\phi_1, \phi_2)$ of H should satisfy the fermion parity constraint [36]

$$\Psi(\phi_1 + 2\pi n, \phi_2 + 2\pi m) = (-1)^{nq_1}(-1)^{mq_2}\Psi(\phi_1, \phi_2), \quad (2.6)$$

$$q_n = \frac{1}{2}(1 - p_n), \quad p_1 = i\gamma_1\gamma_2, \quad p_2 = i\gamma_3\gamma_4. \quad (2.7)$$

The operators q_n and p_n have, respectively, eigenvalues 0, 1 and ± 1 , depending on whether island n contains an even or an odd number of electrons. The constraint (2.6) enforces that the eigenvalues of Q_n are even multiples of e for $q_n = 0, p_n = 1$ and odd multiples of e for $q_n = 1, p_n = -1$.

²The flux induced by the supercurrent I_J due to the nonzero inductance $L \simeq \mu_0 R$ of the ring may be neglected relative to the applied flux if $LI_J \ll \hbar/e$. The magnitude of the supercurrent can be estimated by $\hbar I_J/e \simeq \min(E_J, E_J^2/E_C) \equiv E_c$. For $E_c \simeq 1$ meV the induced flux can be neglected if $R \ll 1$ cm.

It is possible to solve the eigenvalue problem $H\Psi = E\Psi$ subject to the constraint (2.6), along the lines of Ref. [52], but alternatively one can work in an unrestricted Hilbert space. The restriction is removed by the unitary transformation

$$\Psi = U_1 U_2 \tilde{\Psi}, \quad U_n = \exp(iq_n \phi_n/2). \quad (2.8)$$

The function $\tilde{\Psi}(\phi_1, \phi_2)$ is 2π -periodic in each of its arguments, so the constraint (2.6) is automatically satisfied. Now the eigenvalues of Q_n are all even multiples of e . The transformed Hamiltonian $\tilde{H} = (U_1 U_2)^\dagger H U_1 U_2$ becomes

$$\begin{aligned} \tilde{H} = & \frac{1}{2C} \left(Q + \frac{eq_1 - eq_2}{2} + q_{\text{ind}} \right)^2 \\ & + \frac{1}{2} \left[e^{-iq_1 \phi_1} (E_{M,1} \Gamma_1 + E_{M,2} \Gamma_2 e^{i\varphi_0/2}) e^{iq_2 \phi_2} + \text{H.c.} \right] \\ & - E_{J,1} \cos \phi - E_{J,2} \cos(\varphi_0 - \phi), \end{aligned} \quad (2.9)$$

where we have used the identity

$$U_n^\dagger \Gamma_m e^{i\phi_n/2} = \Gamma_m U_n. \quad (2.10)$$

Notice that the Hamiltonian has become 2π -periodic in the superconducting phases ϕ_1, ϕ_2 , while remaining 4π -periodic in the flux φ_0 . Notice also that \tilde{H} may depend on the ϕ_n 's separately, not just on their difference. This does not violate charge conservation, because the conjugate variables Q_n now count only the number of Cooper pairs on each island — not the total number of electrons.

The four Majorana modes encode a qubit degree of freedom [6]. The states of the qubit are distinguished by the parity of the number of electrons on each island. If the total number of electrons in the system is even ($\mathcal{P} = 1$), the qubit states are $|11\rangle$ and $|00\rangle$, while for an odd total number of electrons ($\mathcal{P} = -1$) the states are $|10\rangle$ and $|01\rangle$. In this qubit basis, the products of Majorana operators appearing in the Hamiltonian (2.9) are represented by Pauli matrices,

$$q_1 = \frac{1}{2} + \frac{1}{2} \sigma_z, \quad q_2 = \frac{1}{2} + \frac{1}{2} \mathcal{P} \sigma_z, \quad \Gamma_1 = -\sigma_x, \quad \Gamma_2 = \mathcal{P} \sigma_x. \quad (2.11)$$

It is straightforward to calculate the eigenvalues of \tilde{H} , by evaluating its matrix elements in the basis of eigenstates of Q . The spectrum $E_n^\mathcal{P}(\varphi_0, q_{\text{ind}})$ as a function of the enclosed flux and the induced charge has two branches distinguished by the total fermion parity $\mathcal{P} = \pm 1$, with

$$E_n^+(\varphi_0, q_{\text{ind}}) = E_n^-(\varphi_0 + 2\pi, q_{\text{ind}} + e/2). \quad (2.12)$$

2.2 DC SQUID with two Majorana junctions

We first consider the case that both junctions contain Majorana modes (top panel in Fig. 2.1). A fully analytical calculation is possible in the limit that the charging energy dominates over the Josephson energy ($E_C \equiv e^2/2C \gg E_{M,n}, E_{J,n}$). Only the

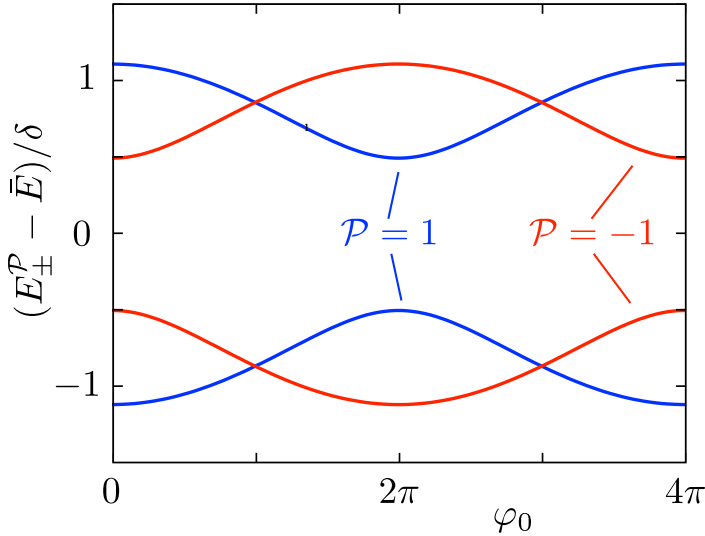


Figure 2.2: Spectrum of the DC SQUID in the top panel of Fig. 2.1, containing Majorana modes at both Josephson junctions. The curves are the result (2.13), in the limit that the charging energy dominates over the Josephson energy. The parameters chosen are $E_{M,1} = E_{M,2} = \delta$. The level crossing is between states of different fermion parity \mathcal{P} , and therefore there can be no tunnel splitting due to the Coulomb interaction (which conserves \mathcal{P}).

two eigenstates of Q with lowest charging energy $\bar{E} \pm \frac{1}{2}\delta$ are needed in this limit and $2e$ tunnel processes may be neglected relative to e tunnel processes (so we may set $E_{J,n} = 0$). We thus obtain the simple expression

$$E_{\pm}^{\mathcal{P}} = \bar{E} \pm \frac{1}{2} \left[\delta^2 + E_{M,1}^2 + E_{M,2}^2 + 2\mathcal{P}E_{M,1}E_{M,2} \cos \frac{\varphi_0}{2} \right]^{1/2}. \quad (2.13)$$

The resulting 4π -periodic spectrum is shown in Fig. 2.2.

The crossing of the two branches $E_+^{\mathcal{P}}$ and $E_-^{\mathcal{P}}$ at $\varphi_0 = \pi$ is protected, regardless of the value of E_C , because the charging energy cannot couple states of different \mathcal{P} . Quasiparticle poisoning (the injection of unpaired electrons) switches the fermion parity on a time scale T_p , which means that the 4π -periodicity of the energy of the ring can be observed if the enclosed flux is increased by a flux quantum in a time $T_{\Phi} \ll T_p$.

2.3 DC SQUID with a single Majorana junction

We now turn to the case that one of the two Josephson junctions does not contain Majorana modes (lower panel in Fig. 2.1). By putting $E_{M,2} = 0$ the Hamiltonian

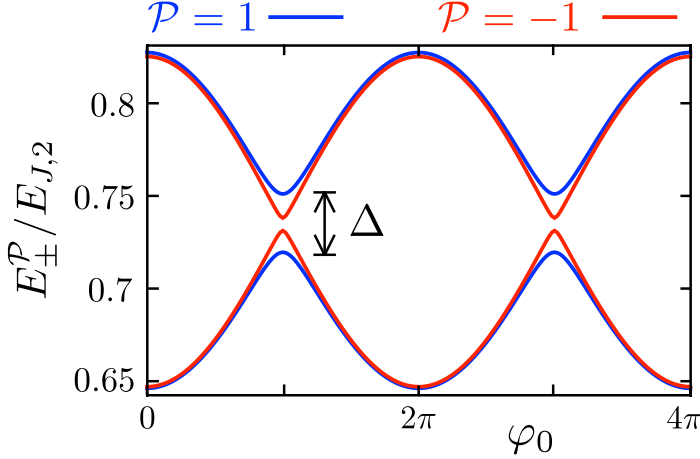


Figure 2.3: Spectrum of the DC SQUID in the bottom panel of Fig. 2.1, containing Majorana modes at only one of the two Josephson junctions. The curves are a numerical calculation for the full Hamiltonian, in the regime that the Josephson energy of the trivial junction is the largest energy scale. The parameters chosen are $E_{J,2} = 4E_C = 10E_{M,1}$, $E_{M,2} = 0 = E_{J,1}$, and $q_{\text{ind}} = 0$. In contrast to Fig. 2.2, a tunnel splitting Δ appears because the level crossing is between states of *the same* fermion parity.

becomes 2π -periodic in φ_0 . In Fig. 2.3 we show the spectrum for a relatively large Josephson energy of the trivial junction. The phase ϕ is then a nearly classical variable, which in the ground state is close to $\varphi_0 \pmod{2\pi}$. The charging energy opens a gap in the spectrum near $\varphi_0 = \pi \pmod{2\pi}$, by inducing tunnel processes from $\phi = \varphi_0$ to $\phi = \varphi_0 \pm 2\pi$ (quantum phase slips). A tunnel splitting by the \mathcal{P} -conserving charging energy is now allowed because the level crossing is between states of the same \mathcal{P} .

A semiclassical calculation of the tunnel splitting due to quantum phase slips at the trivial Josephson junction, along the lines of Ref. [37], gives for $E_J \equiv E_{J,2} \gg E_C \gg E_{M,1} \equiv E_M$ the spectrum

$$E_{\pm}^{\mathcal{P}} = -E_J + \sqrt{2E_C E_J} \pm \sqrt{E_M^2 \cos^2(\varphi_0/2) + \Delta^2}, \quad (2.14)$$

$$\begin{aligned} \Delta = 16(E_C E_J^3 / 2\pi^2)^{1/4} \exp(-\sqrt{8E_J/E_C}) \times \\ \times \sqrt{\cos^2(\pi q'_{\text{ind}}/e) + \frac{\pi^2 E_M^2}{8E_C E_J} \sin^2(\pi q'_{\text{ind}}/e)}, \end{aligned} \quad (2.15)$$

where we have abbreviated $q'_{\text{ind}} = q_{\text{ind}} + (e/4)(1 - \mathcal{P})$. The second term on the right-hand-side of Eq. (2.14) describes the effect of zero-point fluctuations of ϕ around the values φ_0 and $\varphi_0 \pm 2\pi$. Tunnel processes $\phi = \varphi_0 \mapsto \varphi_0 + 2\pi$ and $\phi = \varphi_0 \mapsto \varphi_0 - 2\pi$ produce the third term. The sine and cosine factors in Eq. (2.15) accounts for

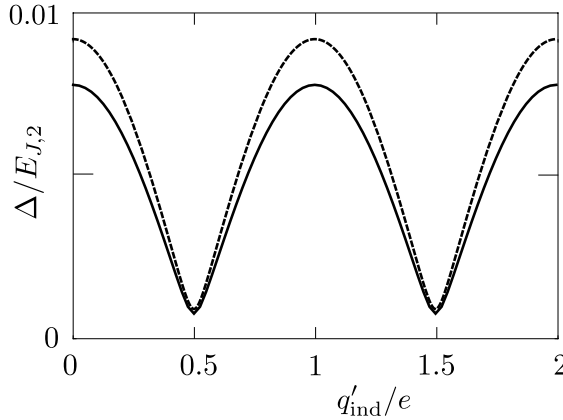


Figure 2.4: Tunnel splitting at $\varphi_0 = \pi$ as a function of the induced charge. The dashed curve correspond to Eq. (2.15), the solid curve to numerical calculations for the full Hamiltonian, for $E_{J,2} = 5 E_C = 25 E_{M,1}$ (with $E_{M,2} = 0 = E_{J,1}$).

interference between these two quantum phase slip processes (Aharonov-Casher effect) [35, 53–56]. The numerical calculation in Fig. 2.4 agrees quite well with the semiclassical approximation (2.15).

The tunnel splitting Δ ensures that the energy of the ring evolves 2π -periodically if the flux Φ is increased by a flux quantum $h/2e$ in a time T_Φ which is long compared to $T_\Delta = \hbar E_{M,1}/\Delta^2$. For $T_\Phi \lesssim T_\Delta$ there is a significant probability $\exp(-T_\Phi/T_\Delta)$ for a Landau-Zener transition through the gap, resulting in a 4π -periodic evolution of the energy.

This limiting time scale T_Δ originating from quantum phase slips can be compared with the time scale T_p for quasiparticle poisoning. We require T_Φ small compared to both T_Δ and T_p to observe the 4π -periodic Josephson effect. For $\Delta > (\hbar E_{M,1}/T_p)^{1/2}$ one has $T_\Delta < T_p$, so quantum phase slips govern. A recent experiment finds $T_p \simeq 2$ ms in Al for temperatures below 160 mK [57]. Since $E_{M,1}$ will be well below 1 meV, one has $T_\Delta < T_p$ if quantum phase slips occur with a rate Δ/\hbar higher than 30 MHz. While quantum phase slip rates can vary over many orders of magnitude due to the exponent in Eq. (2.15), typical values for a DC SQUID are in the GHz range.

In conclusion, we have shown that Coulomb charging effects do not spoil the 4π -periodic Josephson effect in a superconducting ring, provided that all weak links contain Majorana modes. Quantum phase slips at a weak link without Majorana modes restore the 2π -periodicity on time scales long compared to a time T_Δ , which may well be shorter than the time scale for quasiparticle poisoning.

The origin of the protection of the 4π periodicity if the entire ring is topologically nontrivial is conservation of fermion parity [42] (See Ref. [58] for a more general perspective.) This protection breaks down if part of the ring is a trivial superconductor, because then the level crossing involves states of the same fermion parity and tunnel

splitting by the charging energy is allowed (see Fig. 2.3).

We note in closing that the different stability of the 4π -periodic Josephson effect in the two geometries of Fig. 2.1, examined here with respect to Coulomb charging, extends to other parity-preserving perturbations of the Hamiltonian. For example, overlap of the wave functions of two Majorana bound states on the same island introduces a term $H_{\text{overlap}} = i\epsilon\gamma_1\gamma_2$. For the lower panel of Fig. 2.1, this term leads to a tunnel splitting $\Delta = 2\epsilon$ which spoils the 4π -periodicity [26]. For the upper panel of Fig. 2.1, $\Delta \equiv 0$ because H_{overlap} preserves fermion parity.

Chapter 3

Coulomb-assisted braiding of Majorana modes in a Josephson junction array

Non-Abelian anyons have a topological charge that provides a nonlocal encoding of quantum information [6]. In superconducting implementations [45, 46] the topological charge equals the electrical charge modulo $2e$, shared non-locally by a pair of mid-gap states called Majorana modes [26]. This mundane identification of topological and electrical charge by no means diminishes the relevance for quantum computation. To the contrary, it provides a powerful way to manipulate the topological charge through the well-established sub- e charge sensitivity of superconducting electronics [28, 59].

Following this line of thought, a hybrid device called a *top-transmon* was recently proposed, which combines the adjustable charge sensitivity of a superconducting charge qubit (the *transmon* [37, 60]) to read out and rotate a topological (*top*) qubit [61]. A universal quantum computer with highly favorable error threshold can be constructed [62] if these operations are supplemented by the braiding of Majorana modes, which is a non-Abelian operation on the degenerate ground state [14, 27].

Here we show how Majorana modes can be braided by means of charge-sensitive superconducting electronics. (Braiding was not implemented in Ref. [61] nor in other studies of hybrid topological/non-topological superconducting qubits [35, 63–66].) We exploit the fact that the charge-sensitivity can be switched on and off *with exponential accuracy* by varying the magnetic flux through a split Josephson junction [60]. This provides a macroscopic handle on the Coulomb interaction of pairs of Majorana modes, which makes it possible to transport and exchange them in a Josephson junction array.

We compare and contrast our approach with that of Sau, Clarke, and Tewari, who showed (building on the work of Alicea et al. [21]) how non-Abelian braiding statistics

could be generated by switching on and off the tunnel coupling of adjacent pairs of Majorana modes [67]. The tunnel coupling is controlled by a gate voltage, while we rely on Coulomb interaction controlled by a magnetic flux. This becomes an essential difference when electric fields are screened too strongly by the superconductor to be effective. (For an alternative non-electrical approach to braiding, see Ref. [68].)

The basic procedure can be explained quite simply, see Sec. 3.2, after the mechanism of the Coulomb coupling is presented in Sec. 3.1. We make use of two more involved pieces of theoretical analysis, one is the derivation of the low-energy Hamiltonian of the Coulomb coupled Majorana modes (using results from Refs. [36, 69]), and the other is the calculation of the non-Abelian Berry phase [20] of the exchange operation. To streamline the chapter the details of these two calculations are given in Appendices.

3.1 Majorana-Coulomb Hamiltonian

3.1.1 Single island

The basic building block of the Josephson junction array is the Cooper pair box [70], see Fig. 3.1, consisting of a superconducting island (capacitance C) connected to a bulk (grounded) superconductor by a split Josephson junction enclosing a magnetic flux Φ . The Josephson energy E_J is a periodic function of Φ with period $\Phi_0 = h/2e$. If the two arms of the split junction are balanced, each with the same coupling energy E_0 , the Josephson energy

$$E_J = 2E_0 \cos(\pi\Phi/\Phi_0) \quad (3.1)$$

varies between 0 and $2E_0 > 0$ as a function of $|\Phi| < \Phi_0/2$.

When the island contains no Majorana modes, its Hamiltonian has the usual form [40]

$$H = \frac{1}{2C} (Q + q_{\text{ind}})^2 - E_J \cos \phi, \quad (3.2)$$

in terms of the canonically conjugate phase ϕ and charge $Q = -2ei d/d\phi$ of the island. The offset q_{ind} accounts for charges on nearby gate electrodes. We have chosen a gauge such that the phase of the pair potential is zero on the bulk superconductor.

A segment of a semiconductor nanowire (typically InAs) on the superconducting island can have Majorana mid-gap states bound to the end points [45, 46]. For N segments there can be $2N$ Majorana modes on the island. They have identical creation and annihilation operators $\gamma_n = \gamma_n^\dagger$ satisfying

$$\gamma_n \gamma_m + \gamma_m \gamma_n = 2\delta_{nm}. \quad (3.3)$$

The topological charge of the island equals the fermion parity

$$\mathcal{P} = i^N \prod_{n=1}^{2N} \gamma_n. \quad (3.4)$$

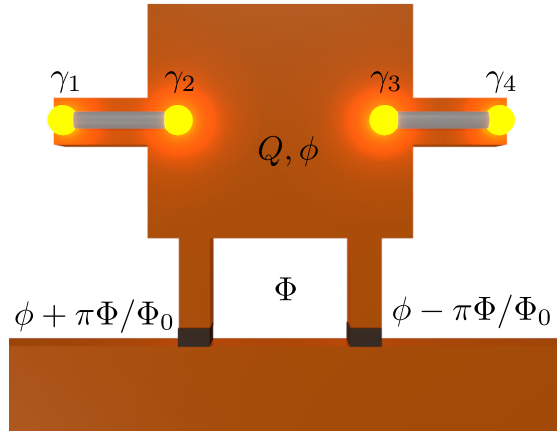


Figure 3.1: Cooper pair box, consisting of a superconducting island (brown) connected to a bulk superconductor by a split Josephson junction (black, with the gauge-variant phase differences indicated). The island contains Majorana modes (yellow) at the end points of a nanowire (grey). These are coupled by the Coulomb charging energy, tunable via the flux Φ through the Josephson junction.

The eigenvalues of \mathcal{P} are ± 1 , depending on whether there is an even or an odd number of electrons on the island.

The Majorana operators do not enter explicitly in H , but affect the spectrum through a constraint on the eigenstates [36],

$$\Psi(\phi + 2\pi) = (-1)^{(1-\mathcal{P})/2} \Psi(\phi). \quad (3.5)$$

This ensures that the eigenvalues of Q are even multiples of e for $\mathcal{P} = 1$ and odd multiples for $\mathcal{P} = -1$. Since \mathcal{P} contains the product of all the Majorana operators on the island, the constraint (3.5) effectively couples distant Majorana modes — without requiring any overlap of wave functions.

We operate the Cooper pair box in the regime that the Josephson energy E_J is large compared to the single-electron charging energy $E_C = e^2/2C$. The phase ϕ (modulo 2π) then has small zero-point fluctuations around the value $\phi_{\min} = 0$ which minimizes the energy of the Josephson junction, with occasional 2π quantum phase slips.

In Appendix 3.A we derive the effective low-energy Hamiltonian for $E_J \gg E_C$,

$$H_{\text{eff}} = -E_J + \sqrt{2E_C E_J} - U\mathcal{P}, \quad (3.6)$$

$$U = 16(E_C E_J^3/2\pi^2)^{1/4} e^{-\sqrt{8E_J/E_C}} \cos(\pi q_{\text{ind}}/e). \quad (3.7)$$

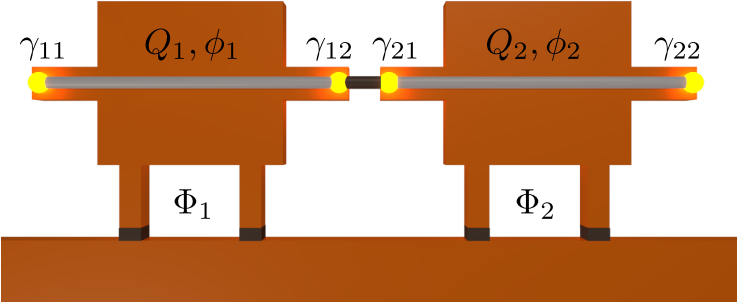


Figure 3.2: Two Cooper pair boxes, each containing a pair of Majorana modes. Single electrons can tunnel between the superconducting islands via the overlapping Majorana's γ_{12} and γ_{21} . This tunnel coupling has a slow (cosine) dependence on the enclosed fluxes, while the Coulomb coupling between the Majorana's on the same island varies rapidly (exponentially).

The energy minimum $-2E_0$ at ϕ_{\min} is increased by $\sqrt{2E_C E_J}$ due to zero-point fluctuations of the phase. This offset does not contain the Majorana operators, so it can be ignored. The term $-U\mathcal{P}$ due to quantum phase slips depends on the Majorana operators through the fermion parity. This term acquires a dynamics for multiple coupled islands, because then the fermion parity of each individual island is no longer conserved.

3.1.2 Multiple islands

We generalize the description to multiple superconducting islands, labeled $k = 1, 2, \dots$, each connected to a bulk superconductor by a split Josephson junction enclosing a flux Φ_k . (See Fig. 3.2.) The Josephson junctions contribute an energy

$$H_J = - \sum_k E_{J,k} \cos \phi_k, \quad E_{J,k} = 2E_0 \cos(\pi \Phi_k / \Phi_0). \quad (3.8)$$

We assume that the charging energy is dominated by the self-capacitance C of each island, so that it has the additive form

$$H_C = \sum_k \frac{1}{2C} (Q_k + q_{\text{ind},k})^2. \quad (3.9)$$

While both E_0 and C may be different for different islands, we omit a possible k -dependence for ease of notation. There may be additional fluxes enclosed by the regions between the islands, but we do not include them to simplify the expressions. None of these simplifications is essential for the operation of the device.

The set of Majorana's on the k -th island is indicated by γ_{kn} with $n = 1, 2, \dots, 2N_k$. The fermion parities $\mathcal{P}_k = i^{N_k} \prod_n \gamma_{kn}$ of neighboring islands k and k' are coupled with strength E_M by the overlapping Majorana's γ_{kn} and $\gamma_{k'm}$. We denote the gauge-invariant phase difference [40] by $\theta_{kk'} = \phi_k - \phi_{k'} + (2\pi/\Phi_0) \int_{k \rightarrow k'} \mathbf{A} \cdot d\mathbf{l}$. The corresponding tunnel Hamiltonian [26]

$$H_{kk'} = \Gamma_{kk'} \cos(\theta_{kk'}/2), \quad \Gamma_{kk'} = iE_M \gamma_{kn} \gamma_{k'm}, \quad (3.10)$$

is 4π -periodic in the gauge-invariant phase difference, as an expression of the fact that single electrons (rather than Cooper pairs) tunnel through the mid-gap state. For example, in the two-island geometry of Fig. 3.2 one has

$$H_{12} = iE_M \gamma_{12} \gamma_{21} \cos(\theta_{12}/2), \quad (3.11a)$$

$$\theta_{12} = \phi_1 - \phi_2 - \pi(\Phi_1 + \Phi_2)/\Phi_0. \quad (3.11b)$$

In Appendix 3.A we derive the effective low-energy Hamiltonian in the regime $E_J \gg E_C, E_M$,

$$H_{\text{eff}} = \text{const} - \sum_k U_k \mathcal{P}_k + \sum_{k,k'} \Gamma_{kk'} \cos \alpha_{kk'}, \quad (3.12)$$

$$\alpha_{kk'} = \lim_{\phi_k, \phi_{k'} \rightarrow 0} \frac{1}{2} \theta_{kk'}. \quad (3.13)$$

The single sum couples Majorana's within an island, through an effective Coulomb energy U_k . The double sum couples Majorana's in neighboring islands by tunneling. Both the Coulomb and tunnel couplings depend on the fluxes through the Josephson junctions, but in an entirely different way: the tunnel coupling varies slowly $\propto \cos(\pi\Phi/\Phi_0)$ with the flux, while the Coulomb coupling varies rapidly $\propto \exp[-4\sqrt{(E_0/E_C)\cos(\pi\Phi/\Phi_0)}]$.

3.1.3 T-junction

Since \mathcal{P}_k and $\Gamma_{kk'}$ in the Majorana-Coulomb Hamiltonian (3.12) do not commute, the evolution of the eigenstates upon variation of the fluxes is nontrivial. As we will demonstrate, it can provide the non-Abelian braiding statistic that we are seeking.

Similarly to earlier braiding proposals [21, 67], the minimal setup consists of three superconductors in a T-junction. (See Fig. 3.3.) Each superconductor contains a pair of Majorana modes γ_k, γ'_k , with a tunnel coupling between γ'_1, γ'_2 , and γ'_3 . The Majorana-Coulomb Hamiltonian (3.12) takes the form

$$H_{\text{eff}} = iE_M (\gamma'_1 \gamma'_2 \cos \alpha_{12} + \gamma'_2 \gamma'_3 \cos \alpha_{23} + \gamma'_3 \gamma'_1 \cos \alpha_{31}) - \sum_{k=1}^3 U_k i \gamma_k \gamma'_k, \quad (3.14)$$

with gauge-invariant phase differences

$$\alpha_{12} = -(\pi/2\Phi_0)(\Phi_1 + \Phi_2 + 2\Phi_3), \quad (3.15a)$$

$$\alpha_{23} = (\pi/2\Phi_0)(\Phi_2 + \Phi_3), \quad (3.15b)$$

$$\alpha_{31} = (\pi/2\Phi_0)(\Phi_1 + \Phi_3). \quad (3.15c)$$

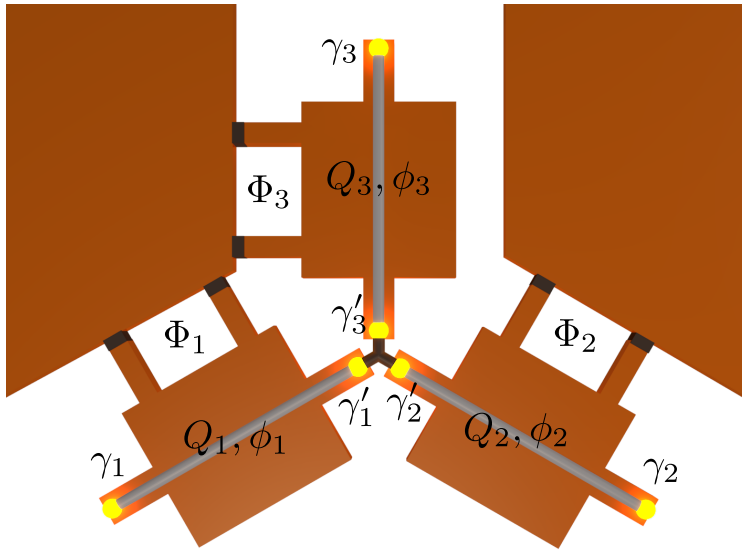


Figure 3.3: Three Cooper pair boxes connected at a T-junction via three overlapping Majorana modes (which effectively produce a single zero-mode γ_0 at the center). This is the minimal setup required for the braiding of a pair of Majorana's, controlled by the fluxes through the three Josephson junctions to a bulk superconductor.

As we vary $|\Phi_k|$ between 0 and $\Phi_{\max} < \Phi_0/2$, the Coulomb coupling U_k varies between two (possibly k -dependent) values U_{\min} and U_{\max} . We require $U_{\max} \gg U_{\min}$, which is readily achievable because of the exponential flux sensitivity of the Coulomb coupling expressed by Eqs. (3.1) and (3.7). We call the Coulomb couplings U_{\max} and U_{\min} *on* and *off*, respectively. We also take $U_{\max} \ll E_M$, meaning that the Coulomb coupling is weaker than the tunnel coupling. This is not an essential assumption, but it allows us to reduce the 6–Majorana problem to a 4–Majorana problem, as we will now show.

Consider first the case that $U_k = 0$ for all k . Then the Hamiltonian (3.14) has four eigenvalues equal to zero: three of these represent the Majorana's γ_k far away from the junction, while the fourth Majorana,

$$\gamma_0 = \frac{1}{\sqrt{3}}(\gamma'_1 + \gamma'_2 + \gamma'_3) \quad (3.16)$$

is situated at the T-junction. The T-junction contributes also two nonzero eigenvalues $\pm \frac{1}{2}E_{\text{gap}}$, separated by the gap

$$E_{\text{gap}} = E_M \sqrt{\cos^2 \alpha_{12} + \cos^2 \alpha_{23} + \cos^2 \alpha_{31}}. \quad (3.17)$$

For Φ_{\max} well below Φ_0 and $U_{\max} \ll E_M$ these two gapped modes can be ignored, and only the four Majorana's $\gamma_0, \gamma_1, \gamma_2, \gamma_3$ need to be retained.

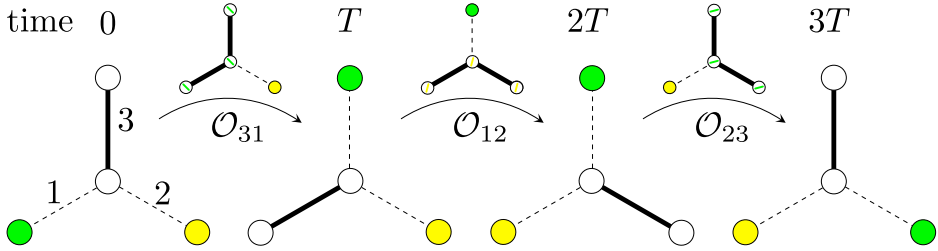


Figure 3.4: Schematic of the three steps of the braiding operation. The four Majorana's of the T-junction in Fig. 3.3 (the three outer Majorana's $\gamma_1, \gamma_2, \gamma_3$ and the effective central Majorana γ_0) are represented by circles and the Coulomb coupling is represented by lines (solid in the *on* state, dashed in the *off* state). White circles indicate Majorana's with a large Coulomb splitting, colored circles those with a vanishingly small Coulomb splitting. The small diagram above each arrow shows an intermediate stage, with one Majorana delocalized over three coupled sites. The three steps together exchange the Majorana's 1 and 2, which is a non-Abelian braiding operation.

The Hamiltonian H_{int} that describes the Coulomb interaction of these four Majorana's for nonzero U_k is given, to first order in U_k/E_M , by

$$H_{\text{int}} = \sum_{k=1}^3 \Delta_k i \gamma_0 \gamma_k, \quad \Delta_k = -(2E_M/E_{\text{gap}}) \beta_k U_k, \quad (3.18)$$

$$\beta_1 = \cos \alpha_{23}, \quad \beta_2 = \cos \alpha_{31}, \quad \beta_3 = \cos \alpha_{12}. \quad (3.19)$$

3.2 Majorana braiding

The Hamiltonian (3.18) describes four flux-tunable Coulomb-coupled Majorana modes. Although the coupling studied by Sau, Clarke, and Tewari [67] has an entirely different origin (gate-tunable tunnel coupling), their Hamiltonian has the same form. We can therefore directly adapt their braiding protocol to our control parameters.

We have three fluxes Φ_1, Φ_2, Φ_3 to control the couplings. The braiding operation consists of three steps, see Table 3.1 and Fig. 3.4. (Ref. [67] had more steps, involving 6 rather than 4 Majorana's.) At the beginning and at the end of each step two of the couplings are off ($\Phi_k = 0$) and one coupling is on ($|\Phi_k| = \Phi_{\text{max}}$). We denote by $\mathcal{O}_{kk'}$ the step of the operation that switches the coupling that is *on* from k to k' . This is done by first increasing $|\Phi_{k'}|$ from 0 to Φ_{max} and then decreasing $|\Phi_k|$ from Φ_{max} to 0, keeping the third flux fixed at 0.

During this entire process the degeneracy of the ground state remains unchanged (twofold degenerate), which is a necessary condition for an adiabatic operation. If,

time	Φ_1	Φ_2	Φ_3
0	0	0	$-\Phi_{\max}$
	Φ_{\max}	0	$-\Phi_{\max}$
T	Φ_{\max}	0	0
	Φ_{\max}	Φ_{\max}	0
$2T$	0	Φ_{\max}	0
	0	Φ_{\max}	$-\Phi_{\max}$
$3T$	0	0	$-\Phi_{\max}$

Table 3.1: Variation of the flux through the three Josephson junctions during the braiding operation, at time steps corresponding to the diagrams in Fig. 3.4. The flux Φ_3 is varied in the opposite direction as Φ_1, Φ_2 , to ensure that the coupling parameters $\Delta_k \propto \beta_k$ do not change sign during the operation.

instead, we would first have first decreased $|\Phi_k|$ and then increased $|\Phi_{k'}|$, the ground state degeneracy would have switched from two to four at some point during the process, precluding adiabaticity.

We start from coupling 3 *on* and couplings 1,2 *off*. The braiding operation then consists, in sequence, of the three steps \mathcal{O}_{31} , \mathcal{O}_{12} , and \mathcal{O}_{23} . Note that each coupling Δ_k appears twice in the *on* state during the entire operation, both times with the same sign s_k .

The step $\mathcal{O}_{kk'}$ transfers the uncoupled Majorana at site k' to site k in a time T . The transfer is described in the Heisenberg representation by $\gamma_k(T) = \mathcal{U}^\dagger(T)\gamma_{k'}\mathcal{U}(T)$. We calculate the unitary evolution operator $\mathcal{U}(T)$ in the adiabatic $T \rightarrow \infty$ limit in Appendix 3.B, by integrating over the Berry connection. In the limit $U_{\min} \rightarrow 0$ we recover the result of Ref. [67],

$$\gamma_k(T) = -s_k s_{k'} \gamma_{k'}(0). \quad (3.20)$$

The result after the three steps is that the Majorana's at sites 1 and 2 are switched, with a difference in sign,

$$\gamma_1(3T) = -s_1 s_2 \gamma_2(0), \quad \gamma_2(3T) = s_1 s_2 \gamma_1(0). \quad (3.21)$$

The corresponding unitary time evolution operator,

$$\mathcal{U}(3T) = \frac{1}{\sqrt{2}} (1 + s_1 s_2 \gamma_1 \gamma_2) = \exp\left(\frac{\pi}{4} s_1 s_2 \gamma_1 \gamma_2\right), \quad (3.22)$$

has the usual form of an adiabatic braiding operation [27]. For a nonzero U_{\min} the coefficient $\pi/4$ in the exponent acquires corrections of order U_{\min}/U_{\max} , see Appendix 3.B.

If one repeats the entire braiding operation, the Majorana's 1 and 2 have returned to their original positions but the final state differs from the initial state by a unitary

operator $\mathcal{U}(3T)^2 = s_1 s_2 \gamma_1 \gamma_2$ and not just by a phase factor. That is the hallmark of non-Abelian statistics [14].

3.3 Discussion

In summary, we have proposed a way to perform non-Abelian braiding operations on Majorana modes, by controlling their Coulomb coupling via the magnetic flux through a Josephson junction. Majorana modes are themselves charge-neutral particles (because they are their own antiparticle), so one may ask how there can be any Coulomb coupling at all. The answer is that the state of a pair of Majorana modes in a superconducting island depends on the parity of the number of electrons on that island, and it is this dependence on the electrical charge modulo $2e$ which provides an electromagnetic handle on the Majorana's.

The Coulomb coupling can be made exponentially small by passing Cooper pairs through a Josephson junction between the island and a bulk (grounded) superconductor. The control parameter is the flux Φ through the junction, so it is purely magnetic. This is a key difference with braiding by electrostatically controlled tunnel couplings of Majorana modes [67]. Gate voltages tend to be screened quite efficiently by the superconductor, so magnetic control is advantageous. Another advantage is that the dependence of the Coulomb coupling on the flux is governed by macroscopic electrical properties (capacitance of the island, resistance of the Josephson junction). Tunnel couplings, in contrast, require microscopic input (separation of the Majorana modes on the scale of the Fermi wave length), so they tend to be more difficult to control.

Both Ref. [67] and the present proposal share the feature that the gap of the topological superconductor is not closed during the braiding operation. (The measurement-based approach to braiding also falls in this category [71].) Two other proposals [21, 68] braid the Majorana's by inducing a topological phase transition (either by electrical or by magnetic means) in parts of the system. Since the excitation gap closes at the phase transition, this may be problematic for the required adiabaticity of the operation.

The braiding operation is called topologically protected, because it depends on the *off/on* sequence of the Coulomb couplings, and not on details of the timing of the sequence. As in any physical realization of a mathematical concept, there are sources of error. Non-adiabaticity of the operation is one source of error, studied in Ref. [72]. Low-lying sub-gap excitations in the superconducting island break the adiabatic evolution by transitions which change the fermion parity of the Majorana's.

Another source of error, studied in Appendix 3.B, is governed by the *off/on* ratio U_{\min}/U_{\max} of the Coulomb coupling. This ratio depends exponentially on the ratio of the charging energy E_C and the Josephson energy E_J of the junction to the bulk superconductor. A value $E_J/E_C \simeq 50$ is not unrealistic [60], corresponding to $U_{\min}/U_{\max} \simeq 10^{-5}$.

The sign of the Coulomb coupling in the *on* state can be arbitrary, as long as it does not change during the braiding operation. Since $U_{\max} \propto \cos(\pi q_{\text{ind}}/e)$, any

change in the induced charge by $\pm e$ will spoil the operation. The time scale for this quasiparticle poisoning can be milliseconds [57], so this does not seem to present a serious obstacle.

A universal quantum computation using Majorana modes requires, in addition to braiding, the capabilities for single-qubit rotation and read-out of up to four Majorana's [6]. The combination of Ref. [61] with the present proposal provides a scheme for all three operations, based on the interface of a topological qubit and a superconducting charge qubit. This is not a topological quantum computer, since single-qubit rotations of Majorana modes lack topological protection. But by including the topologically protected braiding operations one can improve the tolerance for errors of the entire computation by orders of magnitude (error rates as large as 10% are permitted [62]).

3.A Derivation of the Majorana-Coulomb Hamiltonian

3.A.1 Single island

Considering first a single island, we start from the Cooper pair box Hamiltonian (3.2) with the parity constraint (3.5) on the eigenstates. Following Ref. [69], it is convenient to remove the constraint by the unitary transformation

$$\tilde{H} = \Omega^\dagger H \Omega, \quad \Omega = \exp[i(1 - \mathcal{P})\phi/4]. \quad (3.23)$$

The transformed wave function $\tilde{\Psi}(\phi) = \Omega^\dagger \Psi(\phi)$ is then 2π -periodic, without any constraint. The parity operator \mathcal{P} appears in the transformed Hamiltonian,

$$\tilde{H} = \frac{1}{2C} \left(Q + \frac{1}{2}e(1 - \mathcal{P}) + q_{\text{ind}} \right)^2 - E_J \cos \phi. \quad (3.24)$$

For a single junction the parity is conserved, so eigenstates of H are also eigenstates of \mathcal{P} and we may treat the operator \mathcal{P} as a number. Eq. (3.24) is therefore the Hamiltonian of a Cooper pair box with effective induced charge $q_{\text{eff}} = q_{\text{ind}} + e(1 - \mathcal{P})/2$. The expression for the ground state energy in the Josephson regime $E_J \gg E_C$ is in the literature [37, 73],

$$E_{\text{ground}} = -E_J + \sqrt{2E_C E_J} - 16(E_C E_J^3 / 2\pi^2)^{1/4} e^{-\sqrt{8E_J/E_C}} \cos(\pi q_{\text{eff}}/e). \quad (3.25)$$

The first term $-E_J$ is the minimal Josephson energy at $\phi_{\text{min}} = 0$. Zero-point motion, with Josephson plasma frequency $\omega_p = \sqrt{8E_C E_J}/\hbar$, adds the second term $\sqrt{2E_C E_J} = \frac{1}{2}\hbar\omega_p$. The third term is due to quantum phase slips with transition amplitudes $\tau_{\pm} \simeq \exp(\pm i\pi q_{\text{eff}}/e) \sqrt{\hbar\omega_p E_J} \exp(-\hbar\omega_p/E_J)$ by which ϕ increments by $\pm 2\pi$.

Using $\mathcal{P}^2 = 1$, the ground state energy (3.25) may be written in the form

$$E_{\text{ground}} = -E_J + \sqrt{2E_C E_J} - U\mathcal{P}, \quad (3.26)$$

with U defined in Eq. (3.7). Higher levels are separated by an energy $\hbar\omega_p$, which is large compared to U for $E_J \gg E_C$. We may therefore identify $E_{\text{ground}} = H_{\text{eff}}$ with the effective low-energy Hamiltonian of a single island in the large- E_J limit.

3.A.2 Multiple islands

We now turn to the case of multiple islands with tunnel coupling. To be definite we take the geometry of two islands shown in Fig. 3.2. The full Hamiltonian is $H = H_1 + H_2 + H_{12}$, where H_1 and H_2 are two copies of the Cooper box Hamiltonian (3.2) and H_{12} is the tunnel coupling from Eq. (3.11).

To obtain 2π -periodicity in both phases ϕ_1 and ϕ_2 , we make the unitary transformation $\tilde{H} = \Omega^\dagger H \Omega$ with

$$\Omega = e^{i(1-\mathcal{P}_1)\phi_1/4} e^{i(1-\mathcal{P}_2)\phi_2/4}. \quad (3.27)$$

The Cooper pair box Hamiltonians are transformed into

$$\tilde{H}_k = \frac{1}{2C} (Q_k + eq_k + q_{\text{ind},k})^2 - E_{J,k} \cos \phi_k, \quad (3.28)$$

with $q_k = \frac{1}{2}(1 - \mathcal{P}_k)$. The tunnel coupling transforms into

$$\tilde{H}_{12} = \frac{1}{2} e^{-iq_1\phi_1} \Gamma_{12} e^{iq_2\phi_2} e^{i\pi(\Phi_1 + \Phi_2)/2\Phi_0} + \text{H.c.}, \quad (3.29)$$

where $\Gamma_{12} = iE_M \gamma_{12} \gamma_{21}$ and H.c. stands for Hermitian conjugate. Since $e^{iq\phi} = \cos \phi + iq \sin \phi$, the transformed tunnel coupling \tilde{H}_{12} is 2π -periodic in ϕ_1 and ϕ_2 .

For $E_J \gg E_C$ the phases remain close to the value which minimizes the sum of the Josephson energies to the bulk superconductor and between the islands. To leading order in $E_M/E_J \ll 1$ this minimal energy is given by

$$\begin{aligned} \mathcal{E}_{\text{min}} = & -E_{J,1} - E_{J,2} + \Gamma_{12} \cos[\pi(\Phi_1 + \Phi_2)/2\Phi_0] \\ & + \mathcal{O}(E_M^2/E_J). \end{aligned} \quad (3.30)$$

The Josephson coupling of the islands changes the plasma frequency $\omega_{p,k}$ for phase ϕ_k by a factor $1 + \mathcal{O}(E_M/E_J)$, so the zero-point motion energy is

$$\frac{1}{2}\hbar\omega_{p,k} = \sqrt{2E_C E_{J,k}} + E_M \times \mathcal{O}(E_C/E_J)^{1/2}. \quad (3.31)$$

The transition amplitudes τ_\pm for quantum phase slips of phase ϕ_k are similarly affected,

$$\tau_{\pm,k} = -U_k \mathcal{P}_k + E_M e^{-\hbar\omega_{p,k}/E_{J,k}} \times \mathcal{O}(E_C/E_J)^{1/4}. \quad (3.32)$$

These are the contributions to the effective Hamiltonian $H_{\text{eff}} = \mathcal{E}_{\text{min}} + \sum_k (\frac{1}{2}\hbar\omega_{p,k} + \tau_{+,k} + \tau_{-,k})$ for $E_J \gg E_C, E_M$,

$$\begin{aligned} H_{\text{eff}} = & \left(-U_1 \mathcal{P}_1 - U_2 \mathcal{P}_2 + \Gamma_{12} \cos[\pi(\Phi_1 + \Phi_2)/2\Phi_0] \right) \\ & \times [1 + \mathcal{O}(E_M/E_J)] + \text{const.} \end{aligned} \quad (3.33)$$

Eq. (3.12) in the main text generalizes this expression for two islands to an arbitrary number of coupled islands.

3.B Calculation of the Berry phase of the braiding operation

We evaluate the unitary evolution operator \mathcal{U} of the braiding operation in the adiabatic limit. This amounts to a calculation of the non-Abelian Berry phase (integral of Berry connection) of the cyclic variation of the interaction Hamiltonian $H_{\text{int}}(\Delta_1, \Delta_2, \Delta_3)$.

In the Fock basis $|00\rangle, |01\rangle, |10\rangle, |11\rangle$ the interaction Hamiltonian (3.18) of 4 Majorana modes is given by the occupation number of the two fermionic operators $c_1 = (\gamma_1 - i\gamma_2)/2$ and $c_2 = (\gamma_0 - i\gamma_3)/2$. It takes the form

$$H_{\text{int}} = \begin{pmatrix} -\Delta_3 & 0 & 0 & -i\Delta_1 - \Delta_2 \\ 0 & \Delta_3 & -i\Delta_1 - \Delta_2 & 0 \\ 0 & i\Delta_1 - \Delta_2 & -\Delta_3 & 0 \\ i\Delta_1 - \Delta_2 & 0 & 0 & \Delta_3 \end{pmatrix}. \quad (3.34)$$

The eigenvalues are doubly degenerate at energy $\pm\epsilon = \pm\sqrt{\Delta_1^2 + \Delta_2^2 + \Delta_3^2}$ (up to a flux-dependent offset, which only contributes an overall phase factor to the evolution operator). The two degenerate ground states at $-\epsilon$ are distinguished by an even (*e*) or odd (*o*) quasiparticle number,

$$|e\rangle = \sqrt{\frac{\epsilon - \Delta_3}{2\epsilon}} \begin{pmatrix} i \frac{\epsilon + \Delta_3}{\Delta_1 + i\Delta_2} \\ 0 \\ 0 \\ 1 \end{pmatrix}, \quad (3.35a)$$

$$|o\rangle = \sqrt{\frac{\epsilon + \Delta_3}{2\epsilon}} \begin{pmatrix} 0 \\ i \frac{\epsilon - \Delta_3}{\Delta_1 + i\Delta_2} \\ 1 \\ 0 \end{pmatrix}. \quad (3.35b)$$

This parameterization is smooth and continuous except along the line $\Delta_1 = \Delta_2 = 0$.

If we avoid this line the Berry connection can be readily evaluated. It consists of three anti-Hermitian 2×2 matrices \mathcal{A}_k ,

$$\mathcal{A}_k = \begin{pmatrix} \langle e | \frac{d}{d\Delta_k} | e \rangle & 0 \\ 0 & \langle o | \frac{d}{d\Delta_k} | o \rangle \end{pmatrix}. \quad (3.36)$$

Off-diagonal terms in \mathcal{A}_k are zero because of global parity conservation. Explicitly,

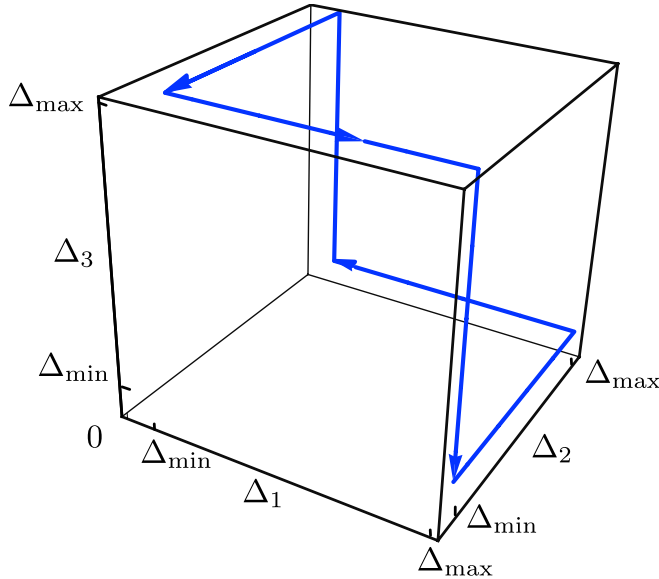


Figure 3.5: The braiding path in three-dimensional parameter space along which the Berry phase is evaluated. This path corresponds to the flux values in Table 3.1, with couplings $\Delta_k = \Delta_{\min}$ for $\Phi_k = 0$ and $\Delta_k = \Delta_{\max}$ for $|\Phi_k| = \Phi_{\max}$. The ratio $\Delta_{\min}/\Delta_{\max}$ in the figure is exaggerated for clarity.

we have

$$\mathcal{A}_1 = \frac{\Delta_2}{\Delta_1^2 + \Delta_2^2} \begin{pmatrix} i \frac{\varepsilon + \Delta_3}{2\varepsilon} & 0 \\ 0 & i \frac{\varepsilon - \Delta_3}{2\varepsilon} \end{pmatrix}, \quad (3.37)$$

$$\mathcal{A}_2 = \frac{-\Delta_1}{\Delta_1^2 + \Delta_2^2} \begin{pmatrix} i \frac{\varepsilon + \Delta_3}{2\varepsilon} & 0 \\ 0 & i \frac{\varepsilon - \Delta_3}{2\varepsilon} \end{pmatrix}, \quad (3.38)$$

$$\mathcal{A}_3 = 0. \quad (3.39)$$

A closed path \mathcal{C} in parameter space has Berry phase [20]

$$\mathcal{U} = \exp \left(- \oint_{\mathcal{C}} \sum_k A_k d\Delta_k \right). \quad (3.40)$$

The path \mathcal{C} corresponding to the braiding operation in Fig. 3.4 and Table 3.1 is shown in Fig. 3.5. We take all couplings Δ_k positive, varying between a minimal value Δ_{\min} and maximal value Δ_{\max} . The parametrization (3.35) is well-defined along the entire contour.

The contour integral evaluates to

$$\mathcal{U} = \exp \left[-i \left(\frac{\pi}{4} - \epsilon \right) \sigma_z \right], \quad \sigma_z = \begin{pmatrix} 1 & 0 \\ 0 & -1 \end{pmatrix}, \quad (3.41)$$

$$\epsilon = \frac{3}{\sqrt{2}} \frac{\Delta_{\min}}{\Delta_{\max}} + \mathcal{O} \left(\frac{\Delta_{\min}}{\Delta_{\max}} \right)^2. \quad (3.42)$$

The limit $\Delta_{\min}/\Delta_{\max} \rightarrow 0$ corresponds to the braiding operator (3.22) in the main text (with $s_1, s_2 > 0$ and $\sigma_z = 1 - 2c_1^\dagger c_1 = i\gamma_1 \gamma_2$).

Chapter 4

Flux-controlled quantum computation with Majorana modes

After the first signatures were reported [74–77] of Majorana bound states in superconducting nanowires [26, 45, 46], the quest for non-Abelian braiding statistics [11, 14, 21, 27] has intensified. Much interest towards Majorana modes arises from their technological potential in fault-tolerant quantum computation [6, 78–81]. Their non-Abelian exchange statistics would allow to perform quantum gates belonging to the Clifford group with extremely good accuracy. Moreover, topological qubits encoded non-locally in well-separated Majorana bound states would be resilient against many sources of decoherence. Even without the applications in quantum information processing, observing a new type of quantum statistics would be a milestone in the history of physics.

The two central issues for the application of Majorana modes are (i) how to unambiguously demonstrate their non-Abelian exchange statistics and (ii) how to exploit their full potential for quantum information processing. The first issue requires an elementary circuit that can perform three tasks: initialization of a qubit, braiding (exchange) of two Majoranas, and finally measurement (readout) of the qubit. In view of the second issue, this circuit should be scalable and serve as a first step towards universal fault-tolerant quantum computation.

Here we present such a circuit, using a superconducting charge qubit in a transmission line resonator (*transmon* [37, 60, 82, 83]) to initialize, control, and measure the topological qubit. In such a hybrid system, named *top-transmon* [61], the long-range Coulomb couplings of Majorana modes can be used to braid them and to read out their fermion parity [61, 84]. While there exist several proposals to control or measure Majorana modes in nanowires [21, 35, 61, 63–68, 84–87], combining braiding *and* measurement without local adjustment of microscopic parameters remains a chal-

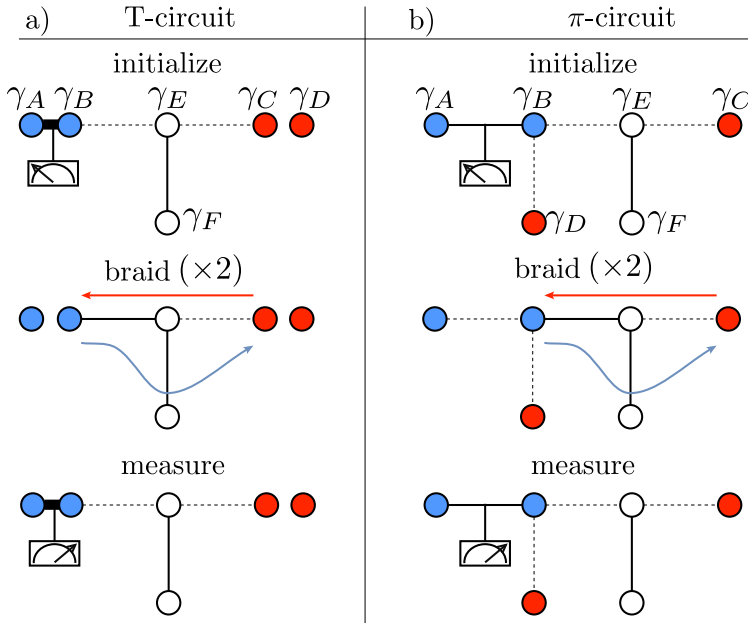


Figure 4.1: Two circuits that can demonstrate non-Abelian statistics, by the initialization, braiding, and measurement of pairs of Majorana bound states (circles). Braiding is performed twice to flip the fermion parity of γ_A and γ_B [79]. Majoranas that can be coupled by Coulomb charging energy are connected by a thin line; the line is solid if the Majoranas are strongly coupled, and dashed if they are uncoupled. A thick line indicates tunnel coupling of Majoranas. The T-shaped circuit of Ref. [21] (left column) requires control over tunnel couplings, while the π -shaped circuit considered here (right column) does not, because both readout *and* braiding involve a Majorana localized at a T-junction.

lence. We show that full macroscopic control is possible if during the measurement one of the Majorana modes is localized at a T-junction between three superconducting islands (see Fig. 4.1). All three steps of the braiding protocol, initialization–braiding–measurement, can then be performed by adjusting magnetic fluxes through split Josephson junctions. Because local control of microscopic parameters is not necessary, our scheme is less sensitive to problems arising from electrostatic disorder and screening of gate voltages by the superconductor.

This design principle of flux-controlled braiding and measurements can be scaled up from a minimal braiding experiment setup to a multi-qubit register that supports a universal set of quantum gates and allows measurement of any product of Pauli matrices belonging to a selection of topological qubits. Multi-qubit parity measurements are a powerful resource in quantum information processing, allowing for the efficient

creation of long-range entanglement and direct measurement of stabilizer operators (thus removing the overhead of ancilla qubits in quantum error correction schemes). Because the data stored in the register can be accessed in any random order, it truly represents a Random Access Majorana Memory.

The structure of this chapter is as follows. In Sec. 4.1 we present the circuit that can demonstrate the non-Abelian Majorana statistics. In Sec. 4.2 we take a longer-term perspective and describe the Random Access Majorana Memory, whose potential for quantum computation is discussed in Sec. 4.3. Finally, we conclude in Sec. 4.4. For the benefit of the reader, we include more detailed derivations and discussions in the Appendices.

4.1 Minimal circuit for the demonstration of non-Abelian statistics

To demonstrate non-Abelian Majorana statistics one needs to read out the parity of two Majoranas, γ_A and γ_B , and braid one of these Majoranas γ_B with another one, γ_C . We seek a transmon circuit that can combine these operations in a fully flux-controlled way, by acting on the Coulomb coupling of the Majoranas. Since γ_B must be coupled first to one Majorana (for the braiding) and then to another (for the readout), it must be able to contribute to two *different* charging energies. This is possible if γ_B is localized at a T-junction between three superconducting islands.

We thus arrive at the minimal circuit shown in Fig. 4.2a. It consists of five superconducting islands, each containing a nanowire supporting two Majorana bound states, enclosed in a transmission line resonator. The two bigger superconductors form a transmon qubit and the three smaller islands are embedded between the two transmon plates. The Josephson couplings between the islands can be controlled by magnetic fluxes Φ_k ($k = 0, 1, 2, 3$). The nanowires form a π -shaped circuit, with two T-junctions where three Majorana bound states belonging to adjacent superconductors are tunnel-coupled. At low energies the three overlapping Majorana bound states at a T-junction form a single zero mode, so that effectively the system hosts six Majorana bound states, $\gamma_A, \gamma_B, \dots, \gamma_F$.

The three relevant energy scales for the device are (i) the charging energy $E_{C,k} = e^2/2C_k$ determined by the total capacitance C_k of the four upper superconductors in Fig. 4.2a, (ii) the Josephson energies $E_{J,k}(\Phi_k) = E_{J,k}(0) \cos(e\Phi_k/\hbar)$, and (iii) the Majorana tunnel couplings E_M at both T-junctions. For strong Josephson coupling, $E_{J,k} \gg E_{C,k}, E_M$, the phases of the order parameter on superconducting islands (measured with respect to the lower superconductor) are pinned to the value $\phi_k \equiv 0$. We distinguish two different operating regimes of the device: one for the braiding procedure and one for initialization and readout.

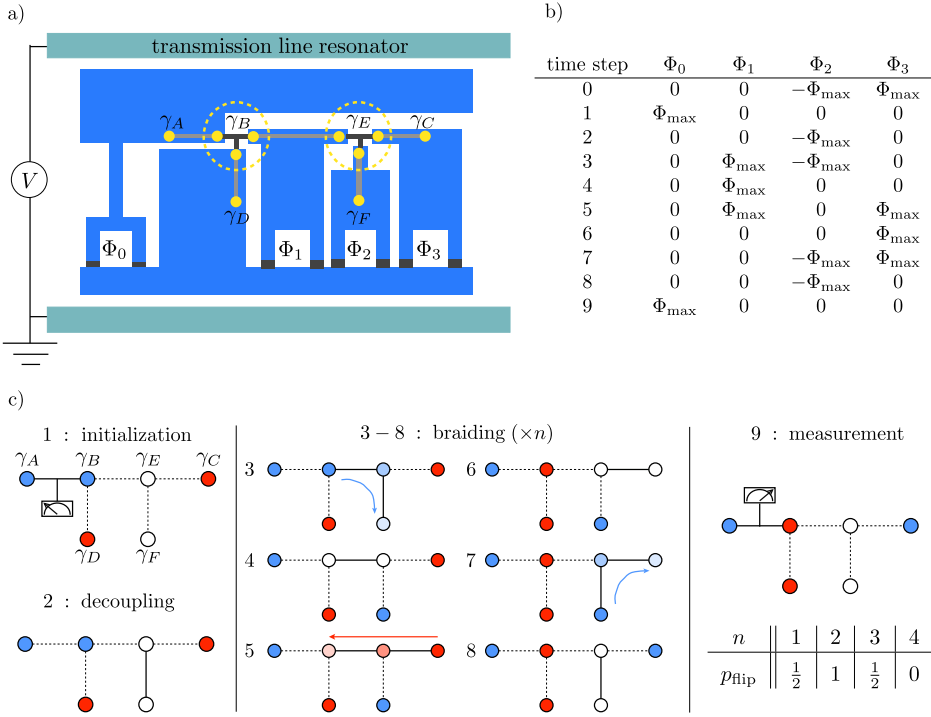


Figure 4.2: Panel a): Minimal circuit for flux-controlled demonstration of non-Abelian Majorana statistics. Two large superconducting plates form a Cooper pair box in a transmission line resonator, i.e. a transmon qubit. Three smaller superconducting islands are embedded between the two transmon plates. Each superconducting island contains a nanowire supporting two Majorana bound states. At low energies, the three overlapping Majorana bound states at a T-junction form a single zero mode so that effectively the system hosts six Majorana bound states, labeled γ_A , γ_B , γ_C , γ_D , γ_E , and γ_F . The Coulomb couplings between the Majorana modes can be controlled with magnetic fluxes Φ_k . This hybrid device can measure the result of the braiding operation as a shift in the microwave resonance frequency when the fermion parity $i\gamma_A\gamma_B$ switches between even and odd. Panel b): Sequence of variation of fluxes during the initialization (steps 0–2), braiding (steps 3–8) and measurement (step 9). Panel c): Illustration of the steps required for initialization, braiding and measurement. Fusion channels of pairs of Majorana modes colored red, blue and white are chosen to be the basis states in Eq. (4.4). To unambiguously demonstrate the non-Abelian nature of Majoranas, one needs to collect statistics of measurement outcomes when the adiabatic cycle describing the braiding operation (steps 3–8) is repeated n times between initialization and measurement. The probabilities of observing changes in the cavity's resonance frequency, p_{flip} , for different values of n should obey the predictions summarized in the table. The sequence of probabilities shown in the table repeats itself periodically for larger values of n .

4.1.1 Flux-controlled braiding

During the braiding procedure we set $\Phi_0 = 0$ so that the charging energy of the large island can be completely neglected. The charging energies of the small islands can be considered perturbatively [37], resulting in long-range Coulomb couplings,

$$U_k = 16 \left(\frac{E_{C,k} E_{J,k}^3}{2\pi^2} \right)^{\frac{1}{4}} e^{-\sqrt{8E_{J,k}/E_{C,k}}} \cos(q_k \pi/e), \quad (4.1)$$

between the Majorana bound states in the corresponding island [61]. The offset charge q_k accounts for the effect of nearby gate electrodes. In order to keep our analytic calculations more transparent, we assume that $U_k \ll E_M$. This condition is not required for braiding to stay accurate in view of the topological nature of the latter (see also App. 4.F). In this case, the low-energy sector of the system is described by the effective Hamiltonian (see Appendix 4.A)

$$H_{\text{braiding}} = -i\Delta_1 \gamma_B \gamma_E - i\Delta_2 \gamma_E \gamma_F - i\Delta_3 \gamma_E \gamma_C, \quad (4.2)$$

$$\begin{aligned} \Delta_1 &= \frac{U_1}{\sqrt{1 + 2\cos^2(e\Phi_1/2\hbar)}} \\ &\times \frac{\cos \alpha_{23}}{\sqrt{\cos^2 \alpha_{12} + \cos^2 \alpha_{23} + \cos^2 \alpha_{31}}}, \end{aligned} \quad (4.3a)$$

$$\Delta_2 = U_2 \frac{\cos \alpha_{31}}{\sqrt{\cos^2 \alpha_{12} + \cos^2 \alpha_{23} + \cos^2 \alpha_{31}}}, \quad (4.3b)$$

$$\Delta_3 = U_3 \frac{\cos \alpha_{12}}{\sqrt{\cos^2 \alpha_{12} + \cos^2 \alpha_{23} + \cos^2 \alpha_{31}}}, \quad (4.3c)$$

where $\alpha_{12} = (e/2\hbar)(\Phi_1 + \Phi_2)$, $\alpha_{23} = (e/2\hbar)(\Phi_2 + \Phi_3)$, and $\alpha_{31} = -\alpha_{12} - \alpha_{23}$ are gauge-invariant phase differences between the smaller islands. The three couplings Δ_i are all tunable with exponential sensitivity via the fluxes Φ_i , increasing from Δ_{\min} (the *off* state) to Δ_{\max} (the *on* state) when $|\Phi_i|$ increases from 0 to $\Phi_{\max} < h/4e$. On the other hand, the tunnel couplings at the T-junction vary slowly with the fluxes, so the three overlapping Majoranas remain strongly coupled throughout the operation.

Out of the six Majorana operators, we define three fermionic creation operators:

$$c_1^\dagger = \frac{1}{2}(\gamma_A + i\gamma_B) \quad (4.4a)$$

$$c_2^\dagger = \frac{1}{2}(\gamma_C + i\gamma_D) \quad (4.4b)$$

$$c_3^\dagger = \frac{1}{2}(\gamma_E + i\gamma_F). \quad (4.4c)$$

We will braid the Majoranas γ_B and γ_C by using γ_E and γ_F as ancillas, as specified in Fig. 4.2. At the beginning and at the end, the Majoranas γ_E and γ_F are strongly coupled ($|\Phi_2| = \Phi_{\max}$). If all other couplings are *off* we are left with two degenerate

states that define a topological qubit. In the odd-parity sector they are $\begin{pmatrix} 1 \\ 0 \end{pmatrix} = |10\rangle|0\rangle$ and $\begin{pmatrix} 0 \\ 1 \end{pmatrix} = |01\rangle|0\rangle$. During the exchange of Majoranas γ_B and γ_C the fluxes Φ_1, Φ_2, Φ_3 are varied between 0 and $\pm\Phi_{\max}$ according to the table shown in Fig. 4.2b. Computing the non-Abelian Berry phase for this adiabatic cycle as in Ref. [84] shows that braiding has the effect of multiplying the topological qubit state with the matrix

$$\mathcal{U} = \frac{1}{\sqrt{2}} \begin{pmatrix} 1 & -i \\ -i & 1 \end{pmatrix}, \quad (4.5)$$

up to corrections of order $\Delta_{\min}/\Delta_{\max}$, with $\Delta_{\min}/\Delta_{\max} \ll 1$ because of the exponential sensitivity of these quantities on magnetic fluxes. Repeating the cycle n times corresponds to applying the gate \mathcal{U}^n .

4.1.2 Initialization and readout

The ancillas need to be initialized in the state $|0\rangle$. This can be achieved by turning the couplings Δ_2 and Δ_3 on and allowing the system to relax to the ground state by adiabatically switching off Δ_3 before Δ_2 [step 0 in Fig. 4.2 (b)]. In addition to the initialization of the ancillas, the braiding needs to be preceded and followed by a readout of the topological qubit. For that purpose, before and after the braiding flux cycle we increase Φ_0 from 0 to Φ_{\max} , so that the spectrum of the transmon depends on the fermion parity $\mathcal{P} = i\gamma_A\gamma_B$ [61]. During the measurement we set $\Phi_1 = \Phi_2 = \Phi_3 = 0$, to decouple the four Majoranas $\gamma_C, \gamma_D, \gamma_E, \gamma_F$ from γ_A, γ_B and to minimize the effect of cross-capacitances [88].

In this configuration it is possible to execute a projective measurement on the fermion parity \mathcal{P} by irradiating the resonator with microwaves. The system composed by the transmon qubit and microwave resonator can be described by the Hamiltonian

$$H_{\text{readout}} = \sigma_z \left[\frac{1}{2} \hbar \Omega_0 + \mathcal{P} \Delta_+ \cos\left(\frac{\pi q_0}{e}\right) \right] + \mathcal{P} \Delta_- \cos\left(\frac{\pi q_0}{e}\right) + \hbar \omega_0 a^\dagger a + \hbar g (\sigma_+ a + \sigma_- a^\dagger). \quad (4.6)$$

Here, ω_0 is the bare resonance frequency of the cavity, g is the strength of the coupling between photons and the transmon qubit, and $\hbar \Omega_0 \simeq \sqrt{8E_{J,0}E_C}$ is the transmon plasma frequency, with E_C the charging energy of the transmon including the contributions of the small islands. We have defined $\sigma_{\pm} = (\sigma_x \pm i\sigma_y)/2$ and

$$\Delta_{\pm} = \frac{\delta\epsilon_1 \pm \delta\epsilon_0}{2} \frac{1}{\sqrt{1 + 2 \cos^2(e\Phi_0/2\hbar)}}, \quad (4.7)$$

where $\delta\epsilon_1, \delta\epsilon_0 \propto \exp(-\sqrt{8E_{J,0}/E_C})$ are determined by the energy levels $\epsilon_n = \bar{\epsilon}_n - (-1)^n \delta\epsilon_n \cos(\pi q_0/e)$ of the transmon [37]. We assume that the induced charge is fixed at $q_0 = 0$ for maximal sensitivity.

The transmission line resonator is typically operated far from resonance, in the so-called dispersive regime [37, 82, 83], when $(n+1)g^2 \ll \delta\omega^2$, with n the number

of photons in the cavity and $\delta\omega = \Omega_0 - \omega_0$. The Hamiltonian (4.6) then produces a parity-dependent resonance frequency (see Appendix 4.B)

$$\omega_{\text{eff}}(\mathcal{P}) = \omega_0 + \sigma_z g^2 (\delta\omega + 2\mathcal{P}\Delta_+/\hbar)^{-1}. \quad (4.8)$$

A flip of the topological qubit can thus be measured as a shift in the resonance frequency by the amount

$$\omega_{\text{shift}} = \frac{4\hbar g^2 \Delta_+}{\hbar^2 \delta\omega^2 - 4\Delta_+^2}. \quad (4.9)$$

The probability of observing a change in the resonance frequency of the cavity after n consecutive braidings, $p_{\text{flip}}(n)$, is dictated by the Majorana statistics: $p_{\text{flip}}(n) = |\langle 1 | \mathcal{U}^n | 0 \rangle|^2 = |\langle 0 | \mathcal{U}^n | 1 \rangle|^2$. The sequence of probabilities, $p_{\text{flip}} = \frac{1}{2}, 1, \frac{1}{2}, 0$ for $n = 1, 2, 3, 4$, repeats itself periodically. Therefore, the non-Abelian nature of Majoranas can be probed by collecting statistics for different values of n .

4.2 Random Access Majorana Memory

The π -circuit of Fig. 4.2 is the minimal circuit which can demonstrate non-Abelian Majorana statistics, but it does not allow for the application of two independent braidings. The full computational power of Majoranas can be achieved by increasing the number of T-junctions. We adopt the triangular loop geometry introduced by Sau, Clarke, and Tewari [67], which is the minimal circuit for a fully flux-controlled topological qubit (see Fig. 4.3a). It consists of five Majorana islands placed between the upper and lower superconducting plates of a transmon qubit, referred to as bus and (phase) ground respectively, and a transmission line resonator for the readout.

In this geometry the braiding and readout can be performed in a similar way as in the case of the π -circuit. In the braiding configuration, we set $\Phi_0 = 0$. Any pair of the Majoranas $\gamma_A, \gamma_B, \gamma_C$ can now be braided with the help of magnetic fluxes Φ_k ($k = 1, 2, \dots, 5$). The qubit manipulations and corresponding quantum gates are shown in Appendix 4.D. The fourth Majorana γ_D forming the topological qubit need not be moved and is situated on the ground island, while γ_E and γ_F serve as ancillas. Moreover, the parity of any pair of Majoranas $\gamma_A, \gamma_B, \gamma_C$ can be measured by moving them to the “measurement” island, the one coupled to the bus via the flux Φ_1 in Fig. 4.3a. During the measurement $\Phi_k = 0$ ($k = 1, 2, \dots, 5$) and $\Phi_0 = \Phi_{\text{max}}$, so that all the small islands are coupled via large Josephson energy either to the bus or to the ground. Therefore, the measurement configuration is described by the readout Hamiltonian (4.6), where \mathcal{P} is the parity of the two Majoranas in the measurement island.

Since the typical length of a transmon is hundreds of microns, it is in principle possible to scale up the design by considering a register of several topological qubits, shown in Fig. 4.3b. The measurement configuration is still described by the readout

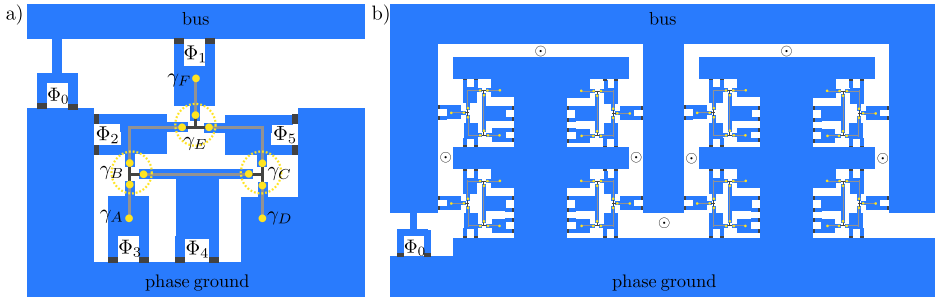


Figure 4.3: Panel a): Minimal transmon circuit for fully flux-controlled topological qubit. The nanowires are placed in a triangular loop formed out of three T-junctions [67]. In this geometry, all single-qubit Clifford gates can be implemented. Panel b): Schematic overview of a Random Access Majorana Memory consisting of eight topological qubits. Compensating fluxes (dotted circles) are included between the topological qubits to ensure that the gauge-invariant phase differences in the different topological qubits are independent of each other (see Appendix 4.C).

Hamiltonian (4.6) (see Appendix 4.C), where the parity operator is now

$$\mathcal{P} = i^N \prod_{n=1}^N \gamma_{nX} \gamma_{nY}. \quad (4.10)$$

Here γ_{nX} and γ_{nY} denote Majorana modes on the measurement island belonging to topological qubit n : $X, Y \in \{A, B, C\}$. Thus, a readout of the resonance frequency corresponds to a projective measurement of this multi-qubit operator. Although the product in Eq. (4.10) runs over all N qubits, we can still choose not to measure a qubit by moving the corresponding pair of coupled ancillas γ_{nE}, γ_{nF} to the measurement island. Because these ancillas are always in a state $|0\rangle$, they do not influence the measurement outcome. Since the Majorana modes can be selectively addressed, we call this architecture a Random Access Majorana Memory (RAMM).

The number of qubits in a RAMM register cannot be increased without limitations. Firstly, the frequency shift ω_{shift} decreases with the number of topological qubits. The main decrease is caused by the reduction of the coupling Δ_+ with the number of topological qubits, which occurs because the Majorana modes at the T-junctions are localized in three different islands (see Appendix 4.C). An additional decrease is caused by the renormalization of the total capacitance of the transmon due to the small islands. Furthermore, each topological qubit introduces an extra pathway for quasiparticles to be exchanged between the bus and the ground. Such quasiparticle poisoning rates at thermal equilibrium are negligibly small and the poisoning due to non-equilibrium quasiparticles can, at least in principle, be controlled by creating quasiparticle traps.

The limited number of qubits is not an obstacle for the scalability of quantum

computation. Beyond this limit, the computation can be scaled up by using several transmons in a single transmission line resonator, and the coupling between the topological qubits in different registers can be achieved by introducing tunable Josephson junctions between the transmons. Furthermore, the computation can be parallelized, because transmons can be coupled to several different transmission line resonators [89–91].

4.3 Multi-qubit measurements as a source of computational power

Multi-qubit measurements in the RAMM offer two significant benefits. Firstly, these measurements can be applied without any locality constraint, so that the quantum fan-out [90], the number of other qubits with which a given qubit can interact, can become large for the RAMM architecture. Secondly, the overhead in the computational resources can be reduced because the products of Pauli matrices involving several topological qubits can be measured directly. We demonstrate these advantages in the realization of a universal set of gates, fast creation of maximally entangled states, and implementation of error correction schemes.

4.3.1 Quantum gates

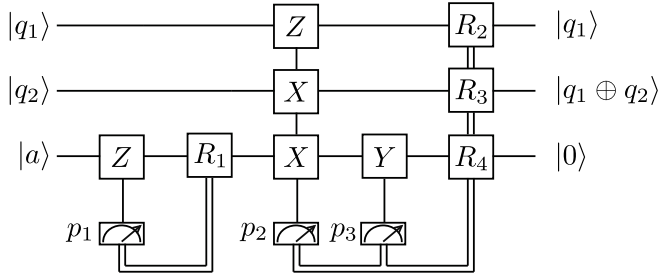
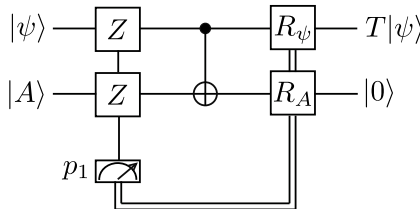
All single-qubit Clifford gates, the CNOT gate, and the $\pi/8$ phase gate required for universal quantum computation [1], can be realized in the RAMM with errors that are exponentially small in macroscopic control parameters (see Appendices 4.B and 4.D). Single-qubit Clifford gates can be realized with braiding operations only, and the quantum circuits for the two remaining gates are summarized in Fig. 4.4. The CNOT gate, shown in Fig. 4.4a, is a modified version of the Bravyi-Kitaev algorithm [92, 93] involving three topological qubits (target, control, and one ancilla). Efficient $\pi/8$ phase gate implementations are based on distillation protocols [62], requiring several noisy qubits to prepare one qubit in a particular state $|A\rangle = (|0\rangle + e^{i\pi/4}|1\rangle)/\sqrt{2}$. This state can then be used to perform the $\pi/8$ gate using the circuit shown in Fig. 4.4 b. Distillation may take place in dedicated RAMM registers (see Appendix 4.D) in parallel with other computation processes, and the distilled state can be teleported to the computational register (see Fig. 4.4c).

4.3.2 Preparation of 2D cluster states

The RAMM can be used to efficiently create maximally entangled multi-qubit states, such as 2D cluster states [94–96], which make it possible to realize any quantum circuit by means of single-qubit operations and measurements [97].

To generate a 2D cluster state in the RAMM architecture one has first to assign a label to each topological qubit in order to establish its position and neighbors on a

a) CNOT

b) $\pi/8$ phase gate

c) teleportation

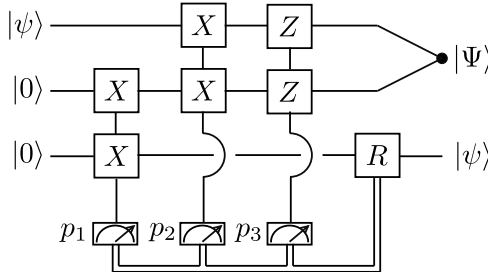


Figure 4.4: Quantum circuits for universal quantum computation in the RAMM. In this figure, $p_1, p_2, p_3 = \pm 1$ represent results of projective single- or multi-qubit measurements, whose outcomes, carried by classical channels (double lines), determine post-selected unitary operations. Panel a): CNOT gate. Here $R_1 = \exp[i\frac{\pi}{4}\sigma_x(1-p_1)]$, $R_2 = \exp[i\frac{\pi}{4}p_2p_3\sigma_z]$, $R_3 = \exp[i\frac{\pi}{4}p_2p_3\sigma_x]$, $R_4 = \exp[-i\frac{\pi}{4}p_3\sigma_x]$ are all gates obtainable by braidings. Panel b): $\pi/8$ phase-gate $T = \text{diag}(1, \exp i\frac{\pi}{4})$, relying on distillation of the state $|A\rangle = (|0\rangle + \exp i\frac{\pi}{4}|1\rangle)/\sqrt{2}$. The required unitary operations are in this case $R_\psi = \exp[-i\frac{\pi}{8}\sigma_z(1-p_1)]$ and $R_A = R_1$. Panel c): teleportation protocol. Here $R = \exp[i\frac{\pi}{4}\sigma_z(1-p_1p_2)]\exp[i\frac{\pi}{4}\sigma_x(1-p_3)]$. Apart from teleporting the unknown quantum state $|\psi\rangle$, the protocol leaves the remaining two qubits in an entangled Bell state $|\Psi\rangle$.

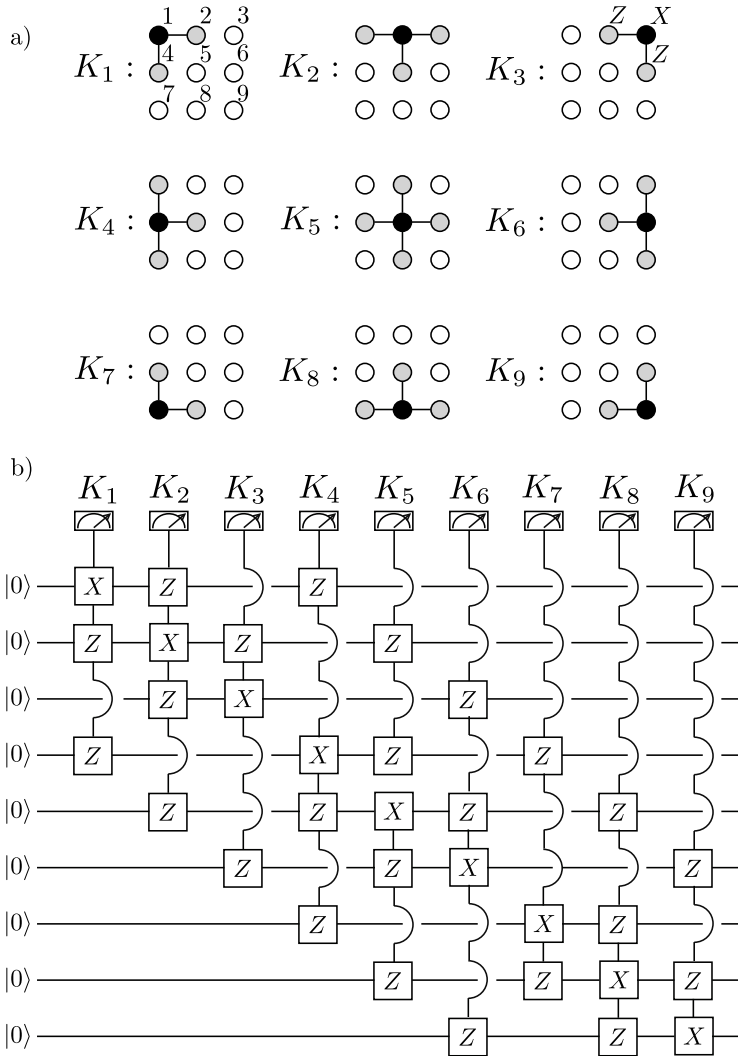


Figure 4.5: Preparation of a 9-qubit 2D cluster state with a RAMM. The nine qubits (represented by circles) are arranged in a 3×3 square logical lattice, and numbered from left to right and top to bottom. Panel a): The nine stabilizer operators K_1, \dots, K_9 necessary to prepare the 2D cluster state. They are products of Pauli matrices, involving all qubits connected by lines, with black and grey dots representing σ_x and σ_z operators, respectively. Panel b): The quantum circuit creating the 2D cluster state in a 9-qubit RAMM register, consisting in a sequence of projective multi-qubit measurement of the 9 stabilizers.

logical lattice (see Fig. 4.5a). Due to the non-locality of measurements in the RAMM, the logical lattice does not need to be related to the physical system. The cluster state may be prepared in several ways [94, 96]. An efficient procedure requires measuring the stabilizers

$$K_\alpha = \sigma_{x,\alpha} \prod_{\langle \beta, \alpha \rangle} \sigma_{z,\beta}, \quad (4.11)$$

where α goes through all sites of the logical lattice and β labels the nearest neighbors of α . The total number of measurements required is equal to the number of qubits in the cluster state. In Fig. 4.5b we draw a circuit to create the 9-qubit 2D cluster state in a RAMM register. To verify their entanglement properties, one possibility is provided by the teleportation protocol of Ref. [97].

4.3.3 Efficient quantum error correction

Although topological qubits have intrinsically low error rates, grouping them into a RAMM register allows to additionally implement efficient error correction. Error correction schemes [1, 3, 4] are based on measurements of stabilizer generators, which are products of Pauli matrices belonging to different qubits. The measurement outcomes give error syndromes, which uniquely characterize the errors and the qubits where they occurred. The RAMM allows for efficient error correction schemes, due to the possibility of measuring stabilizers of different length, as well as correcting errors using single-qubit Clifford gates. There are two advantages in comparison with architectures where only single- and two-qubit operations are available: higher error thresholds and reduced overhead in computational resources.

In order to quantitatively compare these advantages, we consider the 7-qubit Steane code [98] as a concrete example of quantum codes, and assume a realistic error model. We find that the error threshold of the RAMM can be an order of magnitude larger than the error threshold of a reference architecture that can only perform single- and two-qubit operations (see Appendix 4.E). Additionally, the RAMM implementation of the Steane code is much more compact. Already in the first level of concatenation, the fault-tolerant implementation of syndrome measurements in the reference architecture requires 24 ancillas for each logical qubit, while none are needed in the RAMM.

Although we have calculated the improvements only for the 7-qubit Steane code, the advantages are characteristic for all error correction schemes, including surface codes [99, 100].

4.4 Discussion

To control and manipulate quantum information contained in the Majorana zero-modes of superconducting nanowires it is necessary to braid them and measure their parity. We have designed a transmon circuit where both operations can be performed by controlling the magnetic fluxes through split Josephson junctions, without local

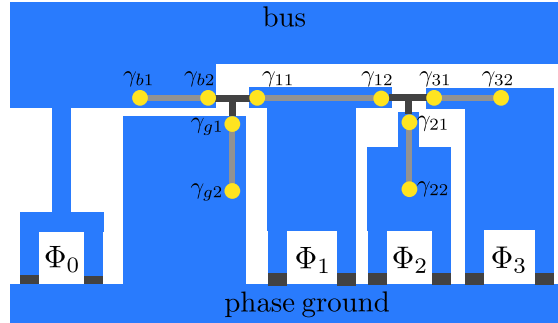


Figure 4.6: The π -shaped transmon circuit discussed in Sec. 4.1, reproduced here with labels of the ten Majorana bound states.

adjustment of microscopic parameters of the nanowires. The minimal circuit for the demonstration of non-Abelian Majorana statistics is a π -shaped circuit involving four independent flux variables. An extended circuit consisting of many topological qubits in parallel allows for non-local multi-qubit measurements in a Random Access Majorana Memory, providing the possibilities of efficient creation of highly entangled states and simplified (ancilla-free) quantum error correction.

Since all the requirements for the realization of the π -circuit and RAMM are satisfied with the typical energy scales of existing transmon circuits and transmission line resonators (see Appendix 4.F), flux-controlled circuits are a favorable architecture for the demonstration of non-Abelian Majorana statistics and the realization of fault-tolerant quantum computation.

4.A Theoretical description of the π -shaped circuit

The π -shaped circuit discussed in the main text is reproduced here in Fig. 4.6. We label the two superconducting plates forming the transmon ‘bus’ and ‘ground’, both hosting two Majorana bound states, labeled γ_{b1}, γ_{b2} and γ_{g1}, γ_{g2} respectively. The smaller superconducting islands are labeled with an integer $k = 1, 2, 3$. Each of them supports two Majorana bound states γ_{k1}, γ_{k2} . We will work in a gauge where all phases are measured with respect to the phase of the ground island. We denote with ϕ the phase of the bus and with ϕ_k that of the k -th island.

We start from the Lagrangian of the system,

$$\mathcal{L} = T - V_J - V_M. \quad (4.12)$$

The first term is the charging energy

$$T = \frac{\hbar^2}{8e^2} C_0 \dot{\phi}^2 + \frac{\hbar^2}{8e^2} \sum_{k=1}^3 \left[C_{G,k} \dot{\phi}_k^2 + C_{B,k} (\dot{\phi}_k - \dot{\phi})^2 \right] + \frac{\hbar}{2e} \left[q_0 \dot{\phi} + \sum_{k=1}^3 q_k \dot{\phi}_k \right]. \quad (4.13)$$

Here C_0 is the capacitance between bus and ground, while $C_{G,k}$ ($C_{B,k}$) is the capacitance between the k -th Majorana island and the ground (the bus). The last two terms include the induced charge q_0 on the bus and q_k on Majorana islands. The effect of cross-capacitances between Majorana islands is negligible assuming that they are small in comparison with the capacitances to the bus and the ground.

The second term is the Josephson potential

$$V_J = E_{J,0}(\Phi) (1 - \cos \phi) + \sum_{k=1}^3 E_{J,k}(\Phi_k) (1 - \cos \phi_k). \quad (4.14)$$

The Josephson energies $E_{J,0}(\Phi_0) = 2E_{J,0}(0) \cos(e\Phi_0/\hbar)$ and $E_{J,k}(\Phi_k) = 2E_{J,k}(0) \cos(e\Phi_k/\hbar)$ can be varied in magnitude by changing the fluxes between 0 and $|\Phi_{\max}| \lesssim h/4e$. We are assuming for simplicity that the split junctions are symmetrical, but this requirement can be removed without affecting our results.

The third term is the Majorana-Josephson potential

$$V_M = E_M \left[i\gamma_{b2}\gamma_{g1} \cos\left(\frac{1}{2}\phi + \alpha_{bg}\right) + i\gamma_{g1}\gamma_{11} \cos\left(\alpha_{g1} - \frac{1}{2}\phi_1\right) + i\gamma_{11}\gamma_{b2} \cos\left(\frac{1}{2}\phi_1 - \frac{1}{2}\phi + \alpha_{1b}\right) \right. \\ \left. + E_M \left[i\gamma_{12}\gamma_{21} \cos\left(\frac{1}{2}\phi_1 - \frac{1}{2}\phi_2 + \alpha_{12}\right) + i\gamma_{21}\gamma_{31} \cos\left(\frac{1}{2}\phi_2 - \frac{1}{2}\phi_3 + \alpha_{23}\right) + i\gamma_{31}\gamma_{12} \cos\left(\frac{1}{2}\phi_3 - \frac{1}{2}\phi_1 + \alpha_{31}\right) \right] \right]. \quad (4.15)$$

The two square brackets in this expression group the terms corresponding to the two T-junctions. All tunnel couplings are for simplicity assumed to be of equal strength E_M . The arguments of the cosines include single-electron Aharonov-Bohm phase shifts between different islands,

$$\alpha_{bg} = e\Phi_0/2\hbar \quad (4.16a)$$

$$\alpha_{g1} = e\Phi_1/2\hbar \quad (4.16b)$$

$$\alpha_{1b} = -(e\Phi_0 + e\Phi_1)/2\hbar \quad (4.16c)$$

$$\alpha_{12} = (e\Phi_1 + e\Phi_2)/2\hbar \quad (4.16d)$$

$$\alpha_{23} = (e\Phi_2 + e\Phi_3)/2\hbar \quad (4.16e)$$

$$\alpha_{31} = -(e\Phi_1 + 2e\Phi_2 + e\Phi_3)/2\hbar \quad (4.16f)$$

There is a constraint between the charge contained in each superconducting island and the parity of the Majorana modes belonging to that island [36]. The constraint can be eliminated via a gauge transformation [69]

$$\Omega = e^{in\phi/2} \prod_{k=1}^3 e^{in_k\phi_k/2} \quad (4.17)$$

$$n = \frac{1}{2} - \frac{1}{2}i\gamma_{b1}\gamma_{b2}, \quad n_k = \frac{1}{2} - \frac{1}{2}i\gamma_{k1}\gamma_{k2}, \quad (4.18)$$

where the products extends over all Majorana junctions. The transformation has two effects on the Lagrangian:

- it changes the induced charges appearing in Eq. (4.13),

$$q_0 \rightarrow q_0 + en, \quad q_k \rightarrow q_k + en_k \quad (4.19)$$

so that the Majorana operators enter explicitly in the charging energy, and

- it modifies the Majorana-Josephson potential $\Omega^\dagger V_M \Omega$ so that it becomes 2π -periodic in all its arguments ϕ, ϕ_k .

In the following, we will work in this new gauge where Eq. (4.19) holds. The explicit form of $\Omega^\dagger V_M \Omega$ is not necessary here, as we will only need the equality

$$\Omega^\dagger V_M \Omega \Big|_{\phi_k=\phi=0} = V_M \Big|_{\phi_k=\phi=0} \quad (4.20)$$

which is trivial since $\Omega|_{\phi_k=\phi=0} = 1$. Starting from the Lagrangian (4.12), we will now derive the low-energy Hamiltonians used in the main text for the braiding and the readout.

4.A.1 Braiding

When we want to braid or move the Majoranas, we maximize the energy $E_{J,0}(\Phi_0)$ by setting $\Phi_0 = 0$ and we require the condition

$$E_{J,0}(0), E_{J,k}(\Phi_k) \gg E_M, E_C, E_{C,k} \quad (4.21)$$

where $E_{C,0} = e^2/2C_0$ and $E_{C,k} = e^2/2(C_{B,k} + C_{G,k})$. Since the Josephson term V_J dominates over the kinetic and Majorana terms T and V_M , the action $S = \int \mathcal{L} dt$ is then minimized for $\phi = \phi_k = 0$ and $\dot{\phi} = \dot{\phi}_k = 0$. All the superconducting islands are in phase. Under the additional condition

$$\frac{E_{J,0}(0)}{E_{C,0}} > \frac{E_{J,k}(\Phi_k)}{E_{C,k}}, \quad (4.22)$$

we can neglect quantum phase slips around the minimum $\phi = 0$, but not around the other minima $\phi_k = 0$. The low-energy Hamiltonian H_M then contains only the Majorana operators:

$$H_{\text{eff}} = - \sum_{k=1}^3 i U_k \gamma_{k1} \gamma_{k2} + \Omega^\dagger V_M \Omega \Big|_{\phi_k = \phi = 0} \quad (4.23)$$

where

$$U_k = 16 \left(\frac{E_{C,k} E_{J,k}^3}{2\pi^2} \right)^{\frac{1}{4}} e^{-\sqrt{8E_{J,k}/E_{C,k}}} \cos(q_k \pi/e), \quad (4.24)$$

is the tunneling amplitude of a phase slip process from $\phi_k = 0$ to $\phi_k = \pm 2\pi$ [37], also reported in Eq. (1) of the main text.

There are still ten Majorana operators in the Hamiltonian (4.23), but we can eliminate four of them by assuming that the tunnel couplings are stronger than the Coulomb couplings: $E_M \gg U_k$. To first order in perturbation theory in the ratio U_k/E_M , we then obtain the Hamiltonian used in the main text

$$H = -i\Delta_1 \gamma_B \gamma_E - i\Delta_2 \gamma_E \gamma_F - i\Delta_3 \gamma_E \gamma_C \quad (4.25)$$

In this passage we have introduced the six Majorana operators $\gamma_A, \gamma_B, \gamma_C, \gamma_D, \gamma_E, \gamma_F$, given by

$$\gamma_A = \gamma_{b1}, \quad (4.26a)$$

$$\gamma_B = \frac{\cos \alpha_{g1} \gamma_{b2} + \cos \alpha_{1b} \gamma_{g1} + \cos \alpha_{bg} \gamma_{11}}{\sqrt{\cos^2 \alpha_{g1} + \cos^2 \alpha_{1b} + \cos^2 \alpha_{bg}}}, \quad (4.26b)$$

$$\gamma_C = \gamma_{32}, \quad (4.26c)$$

$$\gamma_D = \gamma_{g2}, \quad (4.26d)$$

$$\gamma_E = \frac{\cos \alpha_{23} \gamma_{12} + \cos \alpha_{31} \gamma_{21} + \cos \alpha_{12} \gamma_{31}}{\sqrt{\cos^2 \alpha_{23} + \cos^2 \alpha_{31} + \cos^2 \alpha_{12}}}, \quad (4.26e)$$

$$\gamma_F = \gamma_{22}. \quad (4.26f)$$

The coupling strengths are

$$\begin{aligned} \Delta_1 &= U_1 \frac{\cos \alpha_{bg}}{\sqrt{\cos^2 \alpha_{g1} + \cos^2 \alpha_{1b} + \cos^2 \alpha_{bg}}} \\ &\times \frac{\cos \alpha_{23}}{\sqrt{\cos^2 \alpha_{12} + \cos^2 \alpha_{23} + \cos^2 \alpha_{31}}}, \end{aligned} \quad (4.27a)$$

$$\Delta_2 = U_2 \frac{\cos \alpha_{31}}{\sqrt{\cos^2 \alpha_{12} + \cos^2 \alpha_{23} + \cos^2 \alpha_{31}}}, \quad (4.27b)$$

$$\Delta_3 = U_3 \frac{\cos \alpha_{12}}{\sqrt{\cos^2 \alpha_{12} + \cos^2 \alpha_{23} + \cos^2 \alpha_{31}}}. \quad (4.27c)$$

4.A.2 Readout

During the readout of the transmon qubit, we set $\Phi_0 = \Phi_{\max}$, so that the Josephson energy $E_{J,0}$ is minimized, and all $\Phi_k = 0$. We require then that

$$\frac{E_{J,k}(0)}{E_{C,k}} \gg \frac{E_{J,0}(\Phi_{\max})}{E_{C,0}}. \quad (4.28)$$

In physical terms, all Majorana islands are now in phase with the ground: $\phi_k = \dot{\phi}_k = 0$. Neglecting quantum fluctuations and phase slips around these minima, we may rewrite the Lagrangian in a form that depends only on ϕ

$$\mathcal{L} = \frac{\hbar^2}{8e^2} C \dot{\phi}^2 + \frac{\hbar}{2e} (q_0 + en) \dot{\phi} - E_{J,0} (1 - \cos \phi) - \Omega^\dagger V_M \Omega \Big|_{\phi_k=0}. \quad (4.29)$$

Apart from the contribution of the term V_M , the whole system can be treated as a single hybrid top-transmon [61], with Josephson energy $E_{J,0}$ and capacitance

$$C = C_0 + \sum_{k=1}^3 C_{B,k}. \quad (4.30)$$

In the regime $E_{J,0} \gg E_C = e^2/2C$, the energy levels of the transmon are given by [37]

$$\varepsilon_n = \bar{\varepsilon}_n - (-1)^n \delta \varepsilon_n i \gamma_{b1} \gamma_{b2} \cos(\pi q/e), \quad (4.31)$$

where

$$\bar{\varepsilon}_n \simeq -E_{J,0} + \left(n + \frac{1}{2}\right) \sqrt{8E_{J,0}E_C} - \frac{E_C}{12} (6n^2 + 6n + 3) \quad (4.32)$$

$$\delta \varepsilon_n = E_C \frac{2^{4n+4}}{n!} \sqrt{\frac{2}{\pi}} \left(\frac{E_{J,0}}{2E_C}\right)^{\frac{n}{2} + \frac{3}{4}} e^{-\sqrt{8E_{J,0}/E_C}}. \quad (4.33)$$

Taking into account the two lowest levels of the transmon ($n = 0, 1$), we arrive at a low-energy Hamiltonian

$$H_{\text{top-transmon}} = \sigma_z \left[\frac{1}{2} \hbar \Omega_0 + i \gamma_{b1} \gamma_{b2} \delta_+ \cos(\pi q_0/e) \right] + i \gamma_{b1} \gamma_{b2} \delta_- \cos(\pi q_0/e) + \Omega^\dagger V_M \Omega \Big|_{\phi_k=\phi=0} \quad (4.34)$$

with definitions $\hbar \Omega_0 = \bar{\varepsilon}_1 - \bar{\varepsilon}_0$, $\delta_\pm = (\delta \varepsilon_1 \pm \delta \varepsilon_0)/2$. The Pauli matrix σ_z acts on the qubit degree of freedom of the transmon. For $\delta_\pm \ll E_M$, the low energy sector of this Hamiltonian can be written in terms of $\gamma_A, \dots, \gamma_F$ as

$$\tilde{H}_{\text{top-transmon}} = \sigma_z \left[\frac{1}{2} \hbar \Omega_0 + i \gamma_A \gamma_B \Delta_+ \cos(\pi q_0/e) \right] + i \gamma_A \gamma_B \Delta_- \cos(\pi q_0/e) \quad (4.35)$$

where

$$\Delta_{\pm} = \frac{\delta_{\pm} \cos \alpha_{g1}}{\sqrt{\cos^2 \alpha_{bg} + \cos^2 \alpha_{g1} + \cos^2 \alpha_{1b}}}. \quad (4.36)$$

When combined with the Jaynes-Cummings Hamiltonian describing the coupling with the resonator, this Hamiltonian reproduces Eq. (5) of the main text. The interaction with the microwaves will be described in detail in the next Appendix 4.B.

4.B Measurement through photon transmission

The Hamiltonian H_{readout} of the main text describes the coupling between the top-transmon and the cavity modes in the system through a Jaynes-Cummings interaction of strength g . In particular the fermionic parity of the transmon \mathcal{P} is a conserved quantity in the Hamiltonian whose energy levels will directly depend on the value of \mathcal{P} .

We assume that the induced charge is fixed at $q_0 = 0$ to maximize the sensitivity of the read-out. The Jaynes-Cummings interaction couples the pairs of states ($|n, \uparrow, \mathcal{P}\rangle, |n+1, \downarrow, \mathcal{P}\rangle$) where n and $n+1$ label the number of photons in the cavity and $|\uparrow\rangle, |\downarrow\rangle$ denote the two lowest energy eigenstates of the transmon. Therefore, the eigenstates of H_{readout} are in general superpositions of the kind $\alpha|n, \uparrow, \mathcal{P}\rangle + \beta|n+1, \downarrow, \mathcal{P}\rangle$ with the exception of the uncoupled vacuum states $|0, \downarrow, \mathcal{P}\rangle$. Their eigenvalues are, respectively:

$$\varepsilon_{n,\pm,\mathcal{P}} = \left(n + \frac{1}{2} \right) \hbar \omega_0 + \mathcal{P} \Delta_- \pm \frac{1}{2} \sqrt{(\hbar \delta \omega + 2\mathcal{P} \Delta_+)^2 + 4\hbar^2 g^2 (n+1)}, \quad (4.37)$$

$$\varepsilon_{0,\mathcal{P}} = \mathcal{P} (\Delta_- - \Delta_+) - \frac{1}{2} \hbar \Omega_0. \quad (4.38)$$

In the dispersive regime, $\delta \omega^2 \gg g^2(n+1)$, the energies $\varepsilon_{n,\pm,\mathcal{P}}$ can be approximated at the first order in $g^2/\delta \omega^2$ as:

$$\varepsilon_{n,\uparrow,\mathcal{P}} = n \hbar \omega_0 + \mathcal{P} (\Delta_- + \Delta_+) + \frac{1}{2} \hbar \Omega_0 + \frac{\hbar^2 g^2 (n+1)}{\hbar \delta \omega + 2\mathcal{P} \Delta_+} \quad (4.39)$$

$$\begin{aligned} \varepsilon_{n+1,\downarrow,\mathcal{P}} = & (n+1) \hbar \omega_0 + \mathcal{P} (\Delta_- - \Delta_+) + \\ & - \frac{1}{2} \hbar \Omega_0 - \frac{\hbar^2 g^2 (n+1)}{\hbar \delta \omega + 2\mathcal{P} \Delta_+}. \end{aligned} \quad (4.40)$$

The respective eigenstates are approximately $|n, \uparrow, \mathcal{P}\rangle$ and $|n+1, \downarrow, \mathcal{P}\rangle$ up to corrections of the order $g^2/\delta \omega^2$. From the previous equations it is easy to obtain the effective resonance frequency $\omega_{\text{eff}}(\mathcal{P})$ and its shift ω_{shift} corresponding to the different states of the topological qubit. Since we are considering the dispersive regime with a positive detuning, $\Omega_0 > \omega_0$, we assume in the following that the state of the transmon remains in the ground state $|\downarrow\rangle$.

We also point out that in the Hamiltonian H_{readout} we are neglecting the excited states of the transmon, which result in a renormalization of the parameters, including ω_{shift} , through virtual transitions. The precise expressions for the renormalized parameters are known [37], but are not needed here.

To perform the measurement of the topological qubit we introduce in the cavity photons with a frequency which is approximately $\omega_{\text{eff}}(\mathcal{P} = +1)$. The photon transmission probability T_+ for the state $|P = 1\rangle$ is then larger than the probability T_- corresponding to $|P = -1\rangle$. We count the number of photons n_{ph} that passes through the cavity during a measurement time t_M . The probability distributions for n_{ph} in each state are Poissonian, and for sufficiently long measurement time can be approximated with normal distributions

$$\mathbb{P}(n_{\text{ph}}, |P = \pm 1\rangle) = \text{Pois}(n_{\text{ph}}, \lambda_{\pm}) \approx \mathcal{N}(n_{\text{ph}}, \lambda_{\pm}, \sqrt{\lambda_{\pm}}) \quad (4.41)$$

where $\lambda_{\pm} \propto T_{\pm} t_M \kappa$ and $\kappa \simeq 1 - 10 \text{ MHz}$ is the cavity decay rate. Since $T_+ > T_-$, also $\lambda_+ > \lambda_-$.

We decide that the measurement outcome is $\mathcal{P} = +1$ if $n_{\text{ph}} > x = \sqrt{\lambda_+ \lambda_-}$ and the outcome is $\mathcal{P} = -1$ if $n_{\text{ph}} < x$. Therefore the error of the measurement outcome is given by the following:

$$\begin{aligned} \epsilon_{\text{om}} = \frac{1}{2} \int_{-\infty}^x \frac{dn}{\sqrt{2\pi\lambda_+}} \exp\left(\frac{-(n-\lambda_+)^2}{2\lambda_+}\right) + \\ + \frac{1}{2} \int_x^{\infty} \frac{dn}{\sqrt{2\pi\lambda_-}} \exp\left(\frac{-(n-\lambda_-)^2}{2\lambda_-}\right). \end{aligned} \quad (4.42)$$

Since $\lambda_+, \lambda_- \gg 1$

$$\epsilon_{\text{om}} \simeq \frac{e^{-\bar{x}^2}}{2\bar{x}\sqrt{\pi}}, \quad (4.43)$$

where

$$\bar{x} = \frac{\sqrt{\lambda_+} - \sqrt{\lambda_-}}{\sqrt{2}}. \quad (4.44)$$

We notice that the probability of a measurement error decreases exponentially with κt_M . On the other hand, the probability of *storage* error, namely the chance that the topological qubit will decay during a time interval t_M , increases as $\Delta_{\text{min}} t_M / \hbar$. Because $\Delta_{\text{min}} / \kappa$ can be made exponentially small in macroscopic control parameters, exponentially small measurement errors can be achieved.

4.C Low energy Hamiltonian for a Random Access Majorana Memory architecture

We will now describe an effective Hamiltonian for RAMM architecture hosting N topological qubits, such as the one shown in Fig. 3 of the main text. Fig. 4.7a shows

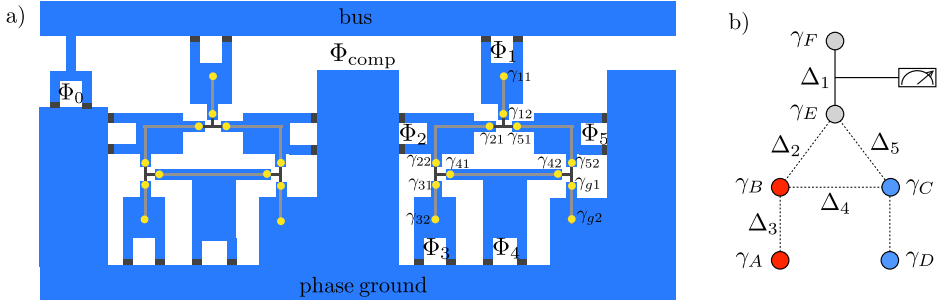


Figure 4.7: Panel (a): Part of the RAMM circuit showing two fully-controllable topological qubits. Compensating fluxes are included between the topological qubits in order that the gauge-invariant phase differences in the different topological qubits are independent of each other. Panel (b): Topological qubit formed by the six Majorana modes. The five couplings $\Delta_1, \dots, \Delta_5$, see Eq. (4.49e), can all be individually controlled by the fluxes Φ_1, \dots, Φ_5 . The parity of the two Majoranas coupled by Δ_1 can be measured, as explained in Appendix 4.C.2.

an equivalent setup, including only two topological qubits. By including compensating fluxes

$$\Phi_{comp,n} = - \sum_{k=1}^5 \Phi_{n,k} \quad (4.45)$$

after each topological qubit, the gauge invariant phases in each topological qubit are independent of each other. The single-electron Aharonov-Bohm phase-shifts $\alpha_{n,kk'}$ at the tunnel junction between islands k and k' of the n -th qubit are then given by

$$\begin{aligned} \alpha_{n,12} &= e(\Phi_0 + \Phi_{n,1} + \Phi_{n,2})/2\hbar \\ \alpha_{n,25} &= e(\Phi_{n,2} + 2\Phi_{n,3} + 2\Phi_{n,4} + \Phi_{n,5})/2\hbar \\ \alpha_{n,51} &= -e(\Phi_0 + \Phi_{n,1} + 2\Phi_{n,2} + 2\Phi_{n,3} \\ &\quad + 2\Phi_{n,4} + \Phi_{n,5})/2\hbar \\ \alpha_{n,23} &= e(\Phi_{n,2} + \Phi_{n,3})/2\hbar \\ \alpha_{n,34} &= e(\Phi_{n,3} + \Phi_{n,4})/2\hbar \\ \alpha_{n,42} &= -e(\Phi_{n,2} + 2\Phi_{n,3} + \Phi_{n,4})/2\hbar \\ \alpha_{n,4g} &= e\Phi_{n,4}/2\hbar \\ \alpha_{n,g5} &= e\Phi_{n,5}/2\hbar \\ \alpha_{n,54} &= -e(\Phi_{n,4} + \Phi_{n,5})/2\hbar. \end{aligned} \quad (4.46)$$

Here, the subscript g denotes the tunnel junctions to the ground island. By starting from a Lagrangian and following a similar approach to that of Appendix 4.A, we find

that the low-energy Hamiltonian is described by six Majorana modes

$$\begin{aligned}
 \gamma_{n,A} &= \gamma_{n,32}, \\
 \gamma_{n,B} &= \frac{\cos \alpha_{n,34} \gamma_{n,22} + \cos \alpha_{n,42} \gamma_{n,31} + \cos \alpha_{n,23} \gamma_{n,41}}{\sqrt{\cos^2 \alpha_{n,23} + \cos^2 \alpha_{n,34} + \cos^2 \alpha_{n,42}}}, \\
 \gamma_{n,C} &= \frac{\cos \alpha_{n,g5} \gamma_{n,42} + \cos \alpha_{n,54} \gamma_{n,g1} + \cos \alpha_{n,4g} \gamma_{n,52}}{\sqrt{\cos^2 \alpha_{n,4g} + \cos^2 \alpha_{n,g5} + \cos^2 \alpha_{n,54}}}, \\
 \gamma_{n,D} &= \gamma_{n,g2}, \\
 \gamma_{n,E} &= \frac{\cos \alpha_{n,25} \gamma_{n,12} + \cos \alpha_{n,51} \gamma_{n,21} + \cos \alpha_{n,12} \gamma_{n,51}}{\sqrt{\cos^2 \alpha_{n,12} + \cos^2 \alpha_{n,25} + \cos^2 \alpha_{n,51}}}, \\
 \gamma_{n,F} &= \gamma_{n,11}.
 \end{aligned} \tag{4.47}$$

that form the triangular loop network of Fig. 4.7b.

4.C.1 Low-energy Hamiltonian in braiding configuration

In the braiding configuration $\Phi_0 = 0$, and the low-energy Hamiltonian is, for each qubit n ,

$$\begin{aligned}
 H_{\text{qubit}}^{(n)} = & -i\Delta_{n,1}\gamma_F\gamma_E - i\Delta_{n,2}\gamma_E\gamma_B - i\Delta_{n,3}\gamma_B\gamma_A \\
 & - i\Delta_{n,4}\gamma_B\gamma_C - i\Delta_{n,5}\gamma_E\gamma_C,
 \end{aligned} \tag{4.48}$$

The Majorana γ_D is situated on the ground island and stays decoupled from the rest of the system. The long-range Coulomb couplings $\Delta_{n,k}$ are

$$\Delta_{n,1} = U_{n,1} \frac{\cos \alpha_{n,25}}{\sqrt{\cos^2 \alpha_{n,12} + \cos^2 \alpha_{n,25} + \cos^2 \alpha_{n,51}}}, \tag{4.49a}$$

$$\begin{aligned}
 \Delta_{n,2} = U_{n,2} & \frac{\cos \alpha_{n,34}}{\sqrt{\cos^2 \alpha_{n,23} + \cos^2 \alpha_{n,34} + \cos^2 \alpha_{n,42}}} \\
 & \times \frac{\cos \alpha_{n,51}}{\sqrt{\cos^2 \alpha_{n,12} + \cos^2 \alpha_{n,25} + \cos^2 \alpha_{n,51}}},
 \end{aligned} \tag{4.49b}$$

$$\Delta_{n,3} = U_{n,3} \frac{\cos \alpha_{n,42}}{\sqrt{\cos^2 \alpha_{n,23} + \cos^2 \alpha_{n,34} + \cos^2 \alpha_{n,42}}}, \tag{4.49c}$$

$$\begin{aligned} \Delta_{n,4} &= U_{n,4} \frac{\cos \alpha_{n,23}}{\sqrt{\cos^2 \alpha_{n,23} + \cos^2 \alpha_{n,34} + \cos^2 \alpha_{n,42}}} \\ &\quad \times \frac{\cos \alpha_{n,g5}}{\sqrt{\cos^2 \alpha_{n,4g} + \cos^2 \alpha_{n,g5} + \cos^2 \alpha_{n,54}}}, \end{aligned} \quad (4.49d)$$

$$\begin{aligned} \Delta_{n,5} &= U_{n,5} \frac{\cos \alpha_{n,12}}{\sqrt{\cos^2 \alpha_{n,12} + \cos^2 \alpha_{n,25} + \cos^2 \alpha_{n,51}}} \\ &\quad \times \frac{\cos \alpha_{n,4g}}{\sqrt{\cos^2 \alpha_{n,4g} + \cos^2 \alpha_{n,g5} + \cos^2 \alpha_{n,54}}}. \end{aligned} \quad (4.49e)$$

For computational purposes, one should be careful that the $\Delta_{n,k}$ do not change signs during the variation of the magnetic fluxes that takes place during a computational process. This may happen if some of the $\alpha_{n,kk'}$ in Eq. (4.46) cross the value $\pi/2$. However, during any computation, maximally two of the fluxes are simultaneously turned on. Therefore, it is always possible to adapt the signs of the magnetic fluxes in such a way that the fluxes can be tuned in a range $|\Phi_{n,k}| = [0, \Phi_{\max}]$, where $\Phi_{\max} < h/4e$. We also notice that the signs of the couplings $\Delta_{n,k}$ in Eq. (4.48) depend on the signs of the microscopic tunnel couplings E_M . These signs will determine the chirality of the braiding of the Majorana modes in each T-junction.

4.C.2 Low-energy Hamiltonian in the readout configuration

During the readout, we set $\Phi_0 = \Phi_{\max}$ and all other fluxes $\Phi_{n,k} = 0$. Following the same reasoning of Appendix 4.A.2, we set $\phi_{n,1} = \phi$ and $\phi_{n,k \neq 1} = 0$ for each topological qubit. The Lagrangian for the RAMM becomes

$$\begin{aligned} \mathcal{L} &= \frac{\hbar}{8e^2} C \dot{\phi}^2 + \frac{\hbar}{2e} \left(q_{\text{tot}} + \sum_{n=1}^N e \left(\frac{1}{2} - \frac{1}{2} i \gamma_{n,11} \gamma_{n,12} \right) \right) \dot{\phi} \\ &\quad - E_{J,0} (1 - \cos \phi) - \sum_{n=1}^N \Omega_n^\dagger V_M^{(n)} \Omega_n \Big|_{\phi_{n,k}=0} \end{aligned} \quad (4.50)$$

where $V_M^{(n)}$ describes the Majorana-Josephson potential for the three T-junctions in each topological qubit n ,

$$\Omega_n = \prod_{k=1}^5 e^{i(1-i\gamma_{n,k1}\gamma_{n,k2})\phi_k/4}, \quad (4.51)$$

$$C = C_0 + \sum_{n=1}^N \sum_{k=2}^5 C_{B,k} + \sum_{n=1}^N C_{G,1} \quad (4.52)$$

and

$$q_{\text{tot}} = q_0 + \sum_{n=1}^N q_{n,1}. \quad (4.53)$$

The low-energy Hamiltonian of the system can now be derived analogously as in Appendix 4.A.2. By using the equality

$$\cos\left(\pi q_{\text{tot}}/e + \pi \sum_{n=1}^N \left(\frac{1}{2} - \frac{1}{2} i\gamma_{n,11}\gamma_{n,12}\right)\right) = \prod_{n=1}^N i\gamma_{n,11}\gamma_{n,12} \cos(\pi q_{\text{tot}}/e), \quad (4.54)$$

we find

$$\begin{aligned} \tilde{H}_{\text{RAMM}} = & \sigma_z \left[\frac{1}{2} \hbar \Omega_0 + \mathcal{P} \Delta_+ \cos(\pi q_{\text{tot}}/e) \right] \\ & + \mathcal{P} \Delta_- \cos(\pi q_{\text{tot}}/e) \end{aligned} \quad (4.55)$$

where \mathcal{P} is now the joint parity operator of the Majorana modes at the measurement islands

$$\mathcal{P} = \prod_{n=1}^N i\gamma_{n,F}\gamma_{n,E}. \quad (4.56)$$

The couplings Δ_{\pm} decrease exponentially with the number of topological qubits involved in a single RAMM register

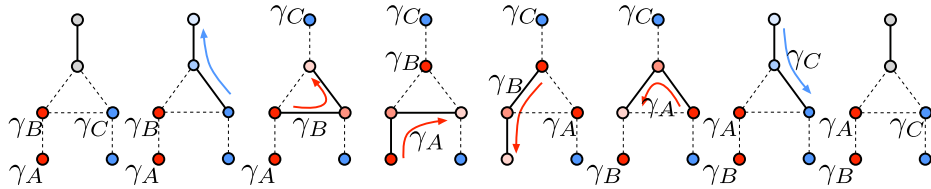
$$\Delta_{\pm} = \delta_{\pm} \prod_{n=1}^N \frac{\cos \alpha_{n,25}}{\sqrt{\cos^2 \alpha_{n,12} + \cos^2 \alpha_{n,25} + \cos^2 \alpha_{n,51}}}. \quad (4.57)$$

In the design of a RAMM register, shown in Fig. 3b in the main text, the frequency shift ω_{shift} is decreased by all topological qubits, including the ones which are not involved in a given multi-qubit measurement. This limitation of RAMM can be relaxed in a more optimal design, where additional tunable Josephson junctions are introduced from the measurement island to the ground. In this case only the topological qubits involved in the given measurement contribute to the decrease of frequency shift. The expense one needs to pay for introducing new Josephson junctions is that the gauge invariant fluxes have more complicated magnetic flux dependence and several Josephson couplings need be simultaneously controlled when the Coulomb couplings are turned on. We point out that although we have explicitly considered the control of the Coulomb couplings with the help of magnetic fluxes, at least some of the macroscopic control parameters $E_{J,k}/E_{C,k}$ of the superconducting islands can alternatively be controlled with gates.

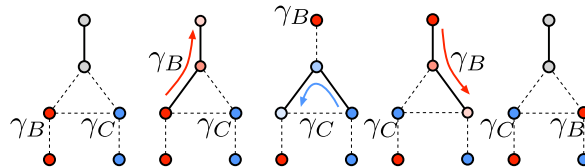
4.D Universal gates for quantum computation

The RAMM setup allows us to perform universal quantum computation in a fault-tolerant way. To show this, it is necessary to implement a universal basis of quantum gates using only braiding operators and multi-qubit measurements as building blocks, thus ensuring the possibility of obtaining arbitrary multi-qubit gates with errors that are exponentially small in the macroscopically tunable parameters. One possible set of gates allowing for universal quantum computation are the single-qubit Clifford gates, the CNOT gate and the $\pi/8$ phase gate. In the following we explain how to realize these gates in a RAMM architecture.

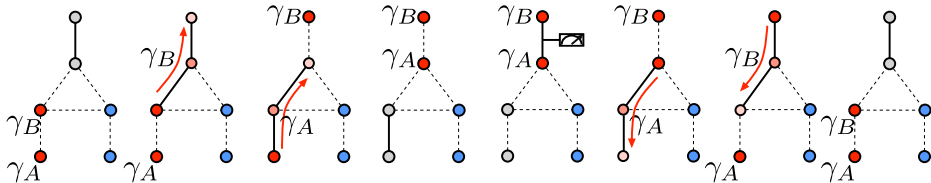
a) $\mathcal{U}_z = \exp(-i\frac{\pi}{4}\sigma_z)$



b) $\mathcal{U}_x = \exp(-i\frac{\pi}{4}\sigma_x)$



c) Projective measurement of σ_z



d) Projective measurement of σ_x

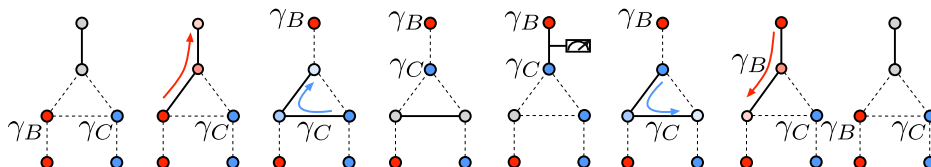


Figure 4.8: Flux-controlled sequences of operations that realize single-qubit Clifford gates and projective measurement on the Pauli basis.

4.D.1 Notation

Each topological qubit n has four computational Majoranas $\gamma_{n,A}, \gamma_{n,B}, \gamma_{n,C}, \gamma_{n,D}$ and two ancillary Majoranas $\gamma_{n,E}, \gamma_{n,F}$, which are needed to move or braid the computa-

tional ones. The Pauli matrices for each qubit can be chosen as

$$\sigma_{n,z} = i\gamma_{n,A}\gamma_{n,B} \quad (4.58a)$$

$$\sigma_{n,x} = i\gamma_{n,B}\gamma_{n,C} \quad (4.58b)$$

$$\sigma_{n,y} = i\gamma_{n,A}\gamma_{n,C}. \quad (4.58c)$$

4.D.2 Single-qubit operations

Projective measurements on the Pauli basis and a set of Clifford gates can be obtained by manipulating the positions of the four computational Majorana modes in the triangular loop geometry. The positions of the computational Majoranas $\gamma_{n,A}, \gamma_{n,B}, \gamma_{n,C}$ can be changed using the ancillary Majorana $\gamma_{n,E}, \gamma_{n,F}$, which remain strongly coupled throughout the process. The corresponding qubit transformation can be derived either by a direct computation of the non-Abelian Berry phase acquired by the ground state wave function of the Hamiltonian (4.48), or by following the evolution of the Majorana operators in the Heisenberg picture, as explained in detail in Ref. [86, 101].

Exchanging the positions of $\gamma_{n,A}, \gamma_{n,B}$ (as represented in Fig. 4.8a) or $\gamma_{n,B}$ and $\gamma_{n,C}$ (Fig. 4.8b) respectively yields the braiding gates

$$\mathcal{U}_z = e^{-i\frac{\pi}{4}\sigma_z}, \quad (4.59)$$

$$\mathcal{U}_x = e^{-i\frac{\pi}{4}\sigma_x}. \quad (4.60)$$

The chirality of the braiding operations (i.e., the sign of the exponent in $\mathcal{U}_z, \mathcal{U}_x$) is determined by the signs of the couplings of the qubit Hamiltonian, Eq. (4.48). Physically, the sign depends on the induced charges on the Majorana islands, the values of the fluxes and the signs of the microscopic tunnel couplings $\pm E_M$ at the T-junctions. Here, we have made a specific choice of chirality. Another possibility of chirality would not be harmful as long as they remain constant during the computation processes.

A combination of these two operations yields the quantum gate corresponding to the braiding of γ_A and γ_C ,

$$\mathcal{U}_y = \mathcal{U}_x^\dagger \mathcal{U}_z \mathcal{U}_x = e^{-i\frac{\pi}{4}\sigma_y}. \quad (4.61)$$

When combined with the $\pi/8$ phase gate described in Appendix 4.D.4, these quantum gates are sufficient to realize any single-qubit rotation.

To realize projective measurements on $\sigma_{n,z}$ (or $\sigma_{n,x}$), we first need to bring the two Majorana modes $\gamma_{n,A}, \gamma_{n,B}$ (or $\gamma_{n,B}, \gamma_{n,C}$) on the island connected to the bus, the one occupied by $\gamma_{n,E}, \gamma_{n,F}$ in Fig. 4.7a. Then we measure the fermion parity operator (4.56), where now the two Majoranas $\gamma_{n,E}, \gamma_{n,F}$ are replaced by the computational ones. For instance, in the case of a measurement of $\sigma_{n,z}$, we would measure the operator

$$\mathcal{P} = i\gamma_{n,A}\gamma_{n,B} \prod_{k \neq n} i\gamma_{k,E}\gamma_{k,F} \equiv \sigma_{n,z}, \quad (4.62)$$

since the parity of the ancillary Majorana of each topological qubit is preserved, $\mathcal{P}_{k,EF} = i\gamma_{k,E}\gamma_{k,F} = +1$. In the end, we bring the two computational Majoranas back to their original place. The whole operation, represented in Fig. 4.8c and Fig. 4.8d for $\sigma_{n,z}$ and $\sigma_{n,x}$ respectively, corresponds to the application of the projectors

$$\Pi_{z,n}(p) = \frac{1}{2} (1 + p\sigma_{n,z}), \quad (4.63a)$$

$$\Pi_{x,n}(p) = \frac{1}{2} (1 + p\sigma_{n,x}) \quad (4.63b)$$

to the wave function of the N topological qubits. Here, $p = \pm 1$ is the outcome of the measurement. Finally, a projective measurement on $\sigma_{n,y}$ is obtained as

$$\Pi_{y,n}(p) = \frac{1}{2} (1 + p\sigma_{n,y}) = \mathcal{U}_x^\dagger \Pi_{z,n}(p) \mathcal{U}_x. \quad (4.64)$$

Multi-qubit measurements on the Pauli basis are a straightforward extension of these projective measurements where Majorana modes on different topological qubits are moved according to Fig. 4.8 to achieve the required basis.

4.D.3 CNOT gate

Bravyi and Kitaev have demonstrated how to realize the CNOT gate with an algorithm that is based on the following expansion [92, 93]:

$$\begin{aligned} \exp\left(i\frac{\pi}{4}\gamma_0\gamma_1\gamma_2\gamma_3\right)|\psi\rangle &= 2e^{i\theta} \exp\left(\frac{\pi}{4}(1-p_1p_2)\gamma_0\gamma_1\right) \exp\left(\frac{\pi}{4}(1-p_1p_2)\gamma_2\gamma_3\right) \times \\ &\times \exp\left(-\frac{\pi}{4}p_2\gamma_2\gamma_5\right) \frac{1}{2}(1+p_2i\gamma_2\gamma_4) \frac{1}{2}(1-p_1\gamma_0\gamma_1\gamma_3\gamma_4)|\psi\rangle, \end{aligned} \quad (4.65)$$

where θ is an unimportant overall phase, γ_i ($i = 0, \dots, 5$) are Majorana operators and $p_i = \pm 1$ are measurements outcomes. The Majoranas γ_4 and γ_5 are used as ancillas and the wave function is initialized in state $(\gamma_4 + i\gamma_5)|\psi\rangle = 0$. Importantly, the Bravyi-Kitaev CNOT algorithm is based only on measurements and braidings of Majorana modes. However, as one can see from Eq. (4.65), its implementation requires a pair of ancillary Majoranas that must be coupled to two computational Majoranas in the target qubit, but must initially be completely independent on them. Due to the parity constraint in each topological qubit, this is impossible in the RAMM setup unless we extend the qubit layout shown in Fig. 3a in the main text. Rather than modifying the RAMM setup to account for these new ancillas, we propose an alternative version of the CNOT gate, which involves three topological qubits. This alternative version of the CNOT gate can be implemented with the quantum circuit shown in Fig. 4a in the main text.

In this circuit the role of the first measurement, with result p_1 , and of the gate R_1 is to initialize the third ancillary qubit in the state $|0\rangle_a$. After that, a CNOT gate with q_1 as a control and q_2 as a target gate is obtained as:

$$\begin{aligned} \frac{1}{2} e^{i\frac{\pi}{4}p_2p_3(\sigma_{1,z}+\sigma_{2,x})} e^{-i\frac{\pi}{4}p_3\sigma_{a,x}} (1 + p_3\sigma_{a,y}) \times \\ \times (1 + p_2\sigma_{1,z}\sigma_{2,x}\sigma_{a,x}) |q_1, q_2, 0\rangle = e^{i\theta} |q_1, q_1 \oplus q_2, 0\rangle. \end{aligned} \quad (4.66)$$

In terms of Majorana operators, this way of representing the CNOT relies on the following equality

$$\begin{aligned} & \exp\left(\frac{\pi}{4}\gamma_{1A}\gamma_{1B}\gamma_{2B}\gamma_{2C}\gamma_{3A}\gamma_{3B}\right)|\psi\rangle_{12}|0\rangle_a = \\ & 2e^{i\theta}\exp\left(-\frac{\pi}{4}(1+p_2p_3)\gamma_{1A}\gamma_{1B}\right)\exp\left(-\frac{\pi}{4}(1+p_2p_3)\gamma_{2B}\gamma_{2C}\right)\exp\left(\frac{\pi}{4}p_3\gamma_{3B}\gamma_{3C}\right)\times \\ & \times \frac{1}{2}(1+ip_3\gamma_{3A}\gamma_{3C})\frac{1}{2}(1-ip_2\gamma_{1A}\gamma_{1B}\gamma_{2B}\gamma_{2C}\gamma_{3B}\gamma_{3C})|\psi\rangle_{12}|0\rangle_a, \end{aligned} \quad (4.67)$$

which can be considered an extension of Kitaev and Bravyi result. In this case the applied projections are all on products of parity operators from different qubits, which can be reduced to the form (4.56) as explained above (see Fig. 4.8); all the other operators are braiding operators within single topological qubits.

4.D.4 $\pi/8$ Phase Gate

To complete the set of universal single-qubit gates we must implement the $\pi/8$ phase gate

$$T = \begin{pmatrix} 1 & 0 \\ 0 & e^{i\frac{\pi}{4}} \end{pmatrix}, \quad (4.68)$$

with an accuracy comparable to the other gates.

For this purpose the best techniques are based on distillation protocols [62]. The basic idea of the distillation procedure is the use of several noisy qubits to prepare one qubit in a particular state, $|A\rangle = (|0\rangle + e^{i\pi/4}|1\rangle)/\sqrt{2}$. A single ancilla qubit prepared in the state $|A\rangle$ is enough to implement the $\pi/8$ gate using the circuit shown in Fig. 4b in the main text.

The distillation protocol of Ref. [62] for the state $|A\rangle$ assumes that it is possible to prepare several noisy copies of $|A\rangle$ with an average initial error $\epsilon_i < 0.14$. In the RAMM setup this can be achieved by coupling the Majorana modes to break the ground state degeneracy [61]. A single distillation step is performed starting from 15 noisy qubits. Neglecting the errors in all the Clifford gates and measurements of the distillation process, the error of the final state after one iteration is approximately

$$\epsilon_{\text{dist}} \approx 35\epsilon_i^3 \quad (4.69)$$

in the limit of small ϵ_i .

Since 14 stabilizer multi-qubit measurements and 15 CNOT gates are involved in the distillation-decoding procedure, the error in the $\pi/8$ gate is approximately an order of magnitude larger than the errors occurring in braiding or in a single multi-qubit measurement. Moreover, assuming an achievable initial error $\epsilon_i = 0.01$ [61] only a single distillation step involving 15 noisy ancillas is needed to achieve a final error of the same order of measurement and gate errors, estimated as $\Delta_{\text{min}}/\Delta_{\text{max}} \sim 10^{-5}$. If the initial errors are larger or the gate errors are smaller, more distillation steps and a larger number of ancillas are preferable. Given the amount of qubits required, it is

realistic to imagine that the distillation procedure will take place in one (or several) dedicated RAMM registers, so that it can happen in parallel with all other computation processes. In this way, whenever a $\pi/8$ phase gate is needed in the computation, it will only be necessary to teleport the distilled state $|A\rangle$ from the distillation register to the computational one.

We also note that alternatively to the $\pi/8$ gate, the universality can also be obtained with the help of $\pi/12$ gate. This gate can be distilled with fewer noisy copies of the relevant state and a single distillation step also requires less multi-qubit measurements [62]. Moreover, the distillation can be improved by exploiting more efficient error correction codes: for example in Ref. [102] a different procedure is proposed that enables to obtain two distilled states $|A\rangle$ out of 10 noisy ancillas, providing a better scaling and threshold for the initial errors. Finally we must mention that the distillation techniques in Ref. [62] require not only multi-qubit measurements and braiding gates, but also a non-unitary dephasing process. However, it was shown in Ref. [103] that the dephasing process is not necessarily needed for the convergence of the noisy states to a high-fidelity final state.

4.E Computation of the error thresholds

Multi-qubit measurements give significant advantages in quantum error correction, as compared to the usual schemes where only single- and two-qubit operations are available. The advantages obtained are twofold. Firstly, multi-qubit measurements allow to significantly increase error thresholds. Secondly, the overhead in computational resources can be substantially decreased.

Quantum error correction schemes are generally based on measurements of multi-qubit operators, usually referred to as stabilizer generators g_i [1]. Their outcomes give error syndromes, β_i , which uniquely characterize the errors and the qubits where they have occurred. Depending on the error correction scheme, a different number of errors can be corrected.

For simplicity, we consider the Steane 7-qubit quantum code [98], which encodes a logical qubit into seven physical qubits and can recover an arbitrary error occurring in any of the physical qubits. Its stabilizer generators are $g_1 = X_1X_5X_6X_7$, $g_2 = X_2X_4X_6X_7$, $g_3 = X_3X_4X_5X_6$, $g_4 = Z_1Z_3Z_4Z_7$, $g_5 = Z_2Z_3Z_5Z_7$, and $g_6 = Z_1Z_2Z_3Z_6$. An error detected on the i -th qubit can be corrected by implementing a X_i , Z_i or X_iZ_j gate, depending on the type of the error.

In order to quantitatively compare the advantages obtained with the help of multi-qubit measurements to conventional schemes, we calculate the error threshold for a quantum memory. The error correction circuit consists of periodic syndrome measurements and recoveries, interrupted by a time-interval of N time steps. Time steps are defined so that a single gate (or measurement) can be performed within one time step. Our error model consists of storage errors, gate errors, data errors during the measurement and errors in the measurement outcomes. The corresponding error probabilities are ϵ_{st} , ϵ_g , ϵ_{dm} , and ϵ_{om} , respectively. All the errors are considered inde-

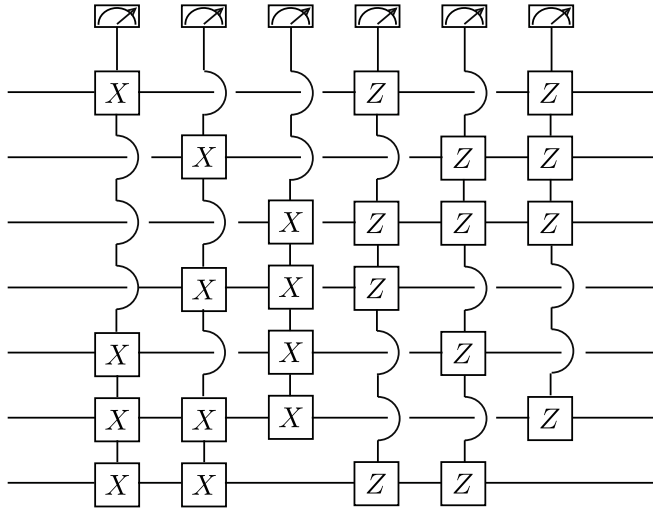


Figure 4.9: Measurement of the six generators of the Steane code. This circuit can be realized directly in a RAMM architecture.

pendent. In order to obtain the error threshold, we need to calculate the probability of failure happening during a single period of the error correction circuit, assuming that no failure has happened before that point. To keep the calculation tractable, we assume that two errors in different qubits always result in failure (independently on the type of errors), and that this happens also when one of the errors occurs during the syndrome-recovery part of the circuit and the other error has happened earlier in the circuit. Moreover, we assume that the errors occurring during the syndrome-recovery part of the circuit never get corrected by the same syndrome-recovery part of the circuit. This way we obtain that the probability of failure during a single period of the circuit is:

$$\begin{aligned} \mathbb{P}(\text{failure}, N) \approx & \mathbb{P}_{\text{om}}(2) + \mathbb{P}_{\text{om}}(1) \sum_i (2\mathbb{P}_{i,\text{sr}} + \mathbb{P}_{i,N}) + \\ & + \sum_{i < j} \left[(2\mathbb{P}_{i,\text{sr}} + \mathbb{P}_{i,N})(2\mathbb{P}_{j,\text{sr}} + \mathbb{P}_{j,N}) - \mathbb{P}_{i,\text{sr}} \mathbb{P}_{j,\text{sr}} \right]. \end{aligned} \quad (4.70)$$

Here $\mathbb{P}_{\text{om}}(m)$ is the probability of having m errors in the measurement outcomes, $\mathbb{P}_{i,\text{sr}}$ is the probability of obtaining single error in qubit i during syndrome measurement and recovery, and $\mathbb{P}_{i,N} = N\epsilon_{\text{st}}$ is the probability of obtaining single error in qubit i during the N time steps between the successive error detections and recoveries.

To estimate the error threshold we minimize the probability of failure per time step,

$$p_f = \min_{N>0} \{\mathbb{P}(\text{failure}, N)/(N + N_0)\}, \quad (4.71)$$

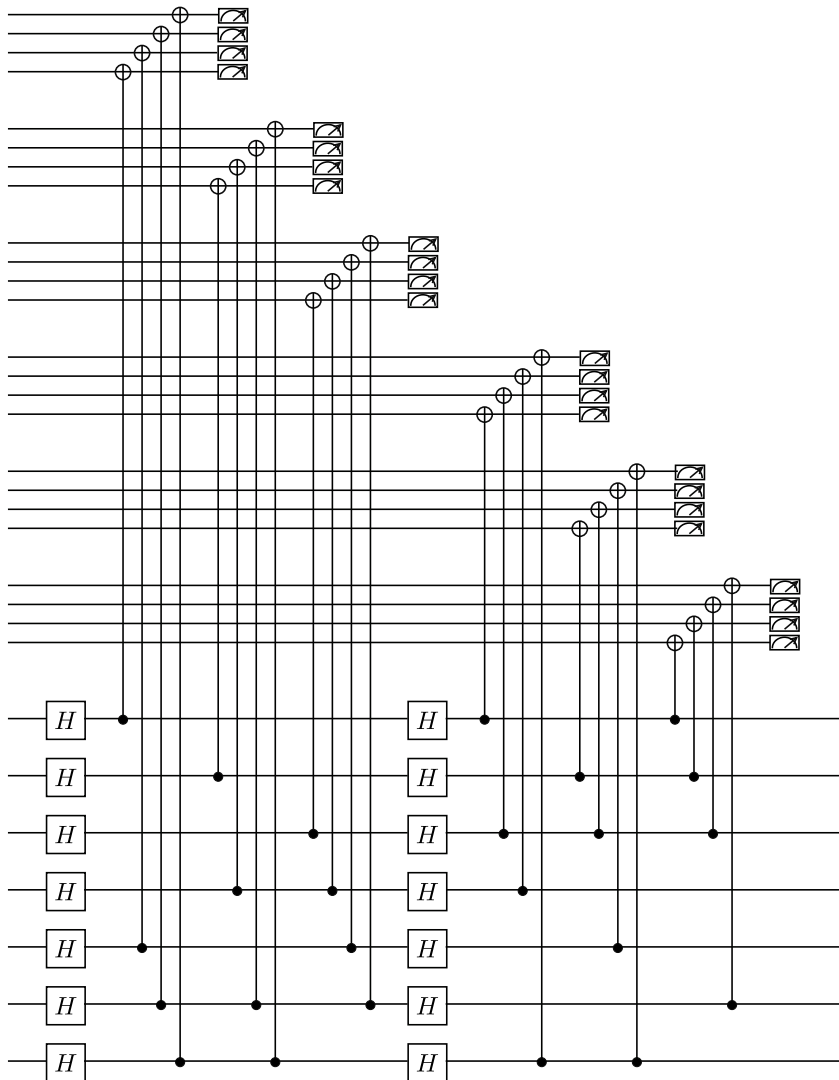


Figure 4.10: Quantum circuit to measure the generators of the Steane code in a traditional architecture that allows only for single- and two-qubit gates, and single-qubit measurements. Each of the six generator measurements is realized using four CNOT gates with an ancilla, which is in turn encoded using four physical qubits to avoid error propagation. This is the circuit we used to compare the error threshold with and without multi-qubit measurements.

where N_0 is the number of time steps required to perform the syndrome measurements and the recovery. The quantum error correction threshold is obtained by demanding that $p_f = \epsilon_{st}$. Because $p_f \propto \epsilon_{st}^2$, this equation determines a threshold value $\epsilon_{st}^{\text{th}}$. If $\epsilon_{st} < \epsilon_{st}^{\text{th}}$, the errors can be corrected by successively applying the scheme described above. For this kind of concatenated codes, the failure probability scales with the number of levels of encoding k as

$$p_{f,k} = \epsilon_{st}^{\text{th}} (\epsilon_{st}/\epsilon_{st}^{\text{th}})^{2^k}, \quad (4.72)$$

whereas the number of physical qubits needed to construct the logical qubits scales as 7^k . In addition to the physical qubits needed for construction of the logical qubits, a large number of ancillas are typically needed to perform the syndrome measurements. These ancillas constitute the overhead in the required computational resources.

4.E.1 Realization of the Steane code with the RAMM

In the case of the RAMM, the syndromes can be directly measured. For simplicity, we assume that one single-qubit gate is always performed during the recovery part of the circuit. Considering that each qubit is on average involved in 24/7 measurements, the total number of time-steps required to perform the syndrome measurements is 6, and the circuit contains 6 measurements, we obtain

$$\mathbb{P}_{\text{om}}(1) = 6 \epsilon_{\text{om}}, \quad (4.73a)$$

$$\mathbb{P}_{\text{om}}(2) = \frac{1}{2} \cdot 6 \cdot 5 \epsilon_{\text{om}}^2 = 15 \epsilon_{\text{om}}^2, \quad (4.73b)$$

$$\mathbb{P}_{\text{sr}} = \frac{24}{7} \epsilon_{\text{dm}} + \frac{24}{7} \epsilon_{\text{st}} + \frac{1}{7} \epsilon_g. \quad (4.73c)$$

These values allow to compute explicitly $\mathbb{P}(\text{failure}, N)$ for the RAMM via Eq. (4.70).

4.E.2 Steane's code without multi-qubit measurements

We want to compare the error threshold in RAMM with a reference system, where multi-qubit measurements are not available. The syndrome measurements are then performed with the help of ancillas. In particular, the fault-tolerant realization of the six syndrome measurements requires a total of 24 ancillas, each quadruplet being used for measuring one of the syndromes [4] (see Fig. 4.10).

Each syndrome is measured by first initializing the ancilla quadruplet in a Shor state, which guarantees that measuring the four ancillas will not destroy the state encoded in the logical qubit. The second step consists of encoding the syndrome into the quadruplet, which requires performing a total of four CNOT gates between different ancillas and physical qubits. Since these involve independent qubit pairs, we assume that these four gates are performed simultaneously. Additionally, we assume that the syndrome is measured immediately after the CNOT gates and the initialization of the ancilla quadruplet takes place already before the syndrome measurements.

Because errors occurring in the ancillas essentially have the same effect as the errors in the measurement outcomes, we include all possible ancilla errors in $\mathbb{P}_{\text{om}}(m)$.

The initialization of the ancillas to a Shor state is explained in Ref. [4]. It involves 7 time steps with 5 CNOT and 5 Hadamard gates. Moreover, a measurement is required to confirm that the Shor state was successfully encoded, otherwise the initialization process is repeated. We only consider gate and storage errors occurring in the initialization of the four ancillas. Each of the ancillas is acted on with 13/4 gates on average.

The syndrome measurements involve 9 time steps and each of the 7 physical qubits is acted upon with 38/7 gates on average, while recovery part only involves one single-qubit gate. Finally, we need to take into account the errors occurring in any of the 24 ancillas during the syndrome block, which contribute to \mathbb{P}_{om} . This way we obtain

$$\mathbb{P}_{\text{om}}(1) = 24(P_{\text{init}} + P_{\text{syndrome}}), \quad (4.74a)$$

$$\mathbb{P}_{\text{om}}(2) = \frac{24 \times 23}{2} (P_{\text{init}} + P_{\text{syndrome}})^2, \quad (4.74b)$$

$$\mathbb{P}_{\text{sr}} = \frac{38}{7} \epsilon_g + \frac{25}{7} \epsilon_{\text{st}} + \frac{1}{7} \epsilon_g + \frac{6}{7} \epsilon_{\text{st}}, \quad (4.74c)$$

with

$$P_{\text{init}} = \epsilon_{\text{om}} + \epsilon_{\text{dm}}, \quad (4.75a)$$

$$P_{\text{syndrome}} = \frac{13}{4} \epsilon_g + \frac{15}{4} \epsilon_{\text{st}} + \epsilon_g + \epsilon_{\text{om}} + \frac{72}{24} \epsilon_{\text{st}}. \quad (4.75b)$$

These values allow to compute $\mathbb{P}(\text{failure}, N)$ in the absence of multi-qubit measurements.

4.E.3 Comparison of the error thresholds for the quantum memory

We minimize the probability of failure per time step with respect to N for both implementations of the error correction scheme. We characterize the relative probabilities of errors by fixing the ratios $\epsilon_g/\epsilon_{\text{st}}$, $\epsilon_{\text{dm}}/\epsilon_{\text{st}}$ and $\epsilon_{\text{om}}/\epsilon_{\text{st}}$, and calculate the error threshold for ϵ_{st} . Results are shown in Fig. 4.11. We find that for $\epsilon_g = \epsilon_{\text{dm}} = \epsilon_{\text{om}} = \epsilon_{\text{st}}$ the error threshold of the RAMM is approximately an order of magnitude larger than the error threshold of a reference architecture that can only perform single- and two-qubit operations. The ratio of the error thresholds for the different architectures becomes smaller with increasing measurement errors (larger ratios $\epsilon_{\text{dm}}/\epsilon_{\text{st}}$ and $\epsilon_{\text{om}}/\epsilon_{\text{st}}$), because it becomes favorable to increase the waiting time between the consequent error correction steps; but even for $\epsilon_g = \epsilon_{\text{dm}} = \epsilon_{\text{om}} = 10\epsilon_{\text{st}}$ we still find that the RAMM has an error threshold five times larger than the reference architecture.

4.E.4 Comparison of the error threshold in quantum computation

To estimate the error threshold in quantum computation, we consider an algorithm where each qubit participates in a two-qubit gate with a randomly chosen other qubit

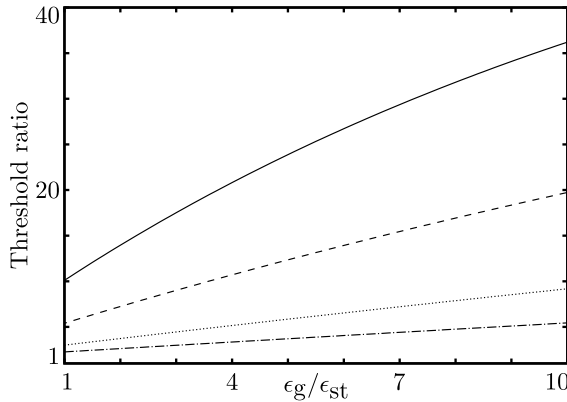


Figure 4.11: Ratio of the Steane code error thresholds with and without multi-qubit measurements as a function of the ratio between gate and storage errors, ϵ_g/ϵ_{st} . The solid, dashed, dotted, and dash-dotted curves correspond to ratios $\epsilon_{om}/\epsilon_{st} = \epsilon_{dm}/\epsilon_{st} = 1, 2, 5$, and 10 , respectively.

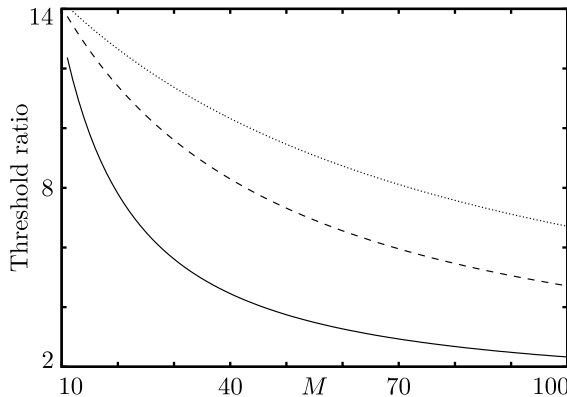


Figure 4.12: Ratio of the computational error thresholds with and without multi-qubit measurements as a function of M . Here $\epsilon = \epsilon_{om} = \epsilon_{dm} = \epsilon_g$, with $\epsilon/\epsilon_{st} = 1$ (solid), 5 (dashed), and 10 (dotted). The range of M starts from 11 , because of the condition $M - N_0 - 1 \geq 0$.

after every $M > N_0$ time steps. We assume that the syndrome and recovery steps are performed once after each two-qubit gate. To estimate the error threshold we calculate the probability of failure in any one of the logical qubits during the M -step period. To keep the calculation tractable, we consider that all the errors appearing in a logical qubit during the syndrome and recovery steps just before the two-qubit gate propagate to the other qubit. Notice that due to the special construction of the

Steane code, the error occurring in i th physical qubit in one of the logical qubits will affect only the i th physical qubit in the other logical qubit. As before, we assume that two errors in a single logical qubit always result in failure. This way, we find

$$\begin{aligned} \mathbb{P}(\text{failure}, M) \approx & \mathbb{P}_{\text{om}}(2) + \mathbb{P}_{\text{om}}(1) \sum_i (3\mathbb{P}_{i,\text{sr}} + \epsilon_g + \mathbb{P}_{i,M-N_0-1}) \\ & + \sum_{i < j} (3\mathbb{P}_{i,\text{sr}} + \epsilon_g + \mathbb{P}_{i,M-N_0-1})(3\mathbb{P}_{j,\text{sr}} + \epsilon_g + \mathbb{P}_{j,M-N_0-1}) \\ & - 2 \sum_{i < j} \mathbb{P}_{i,\text{sr}} \mathbb{P}_{j,\text{sr}}, \end{aligned} \quad (4.76)$$

which we compute for both architectures using Eqs. (4.73), (4.74). The probability of failure per time step is then

$$p_f = \mathbb{P}(\text{failure}, M)/M, \quad (4.77)$$

and the threshold for quantum error correction can be determined by comparing this probability to the probability of failure without error correction. Results are shown in Fig. 4.12. Similarly as in the case of quantum memory, we find that the error threshold for performing the quantum computation can be an order of magnitude larger for the RAMM.

4.F Characteristic energy scales of the problem

We need to satisfy the following inequalities

$$E_{J,k}, \hbar\Omega_k, \Delta_g > E_{J,0}, \hbar\Omega_0, \hbar\omega_0 \gg E_M, \Delta_{\max} \gg k_B T, \Delta_{\min}, \quad (4.78)$$

where $\hbar\Omega_k \approx \sqrt{8E_{J,k}E_{C,k}}$ is the plasma frequency of the small islands and $\Delta_g \sim 100$ GHz is the induced gap in the nanowire. The condition $E_M, \Delta_{\max} \gg k_B T$ is required to guarantee a relaxation to the ground state.

In the earlier sections we assumed that $E_M \gg U_k$ in order to turn our analytical calculations more transparent, but in view of the topological nature of the braiding our results must remain valid also when E_M and Δ_{\max} are comparable to each other. This is easy to understand, since independently on the ratio of U_k and E_M as long as the ground state manifold remains isolated from the excited states the adiabatic time-evolution operator for the braiding cycle takes the form of Eq. (4.5), because of the topological nature of the operation.

Additionally, during the measurement we need to satisfy the inequalities

$$E_M \gg \Delta_+, \quad (4.79)$$

and

$$\omega_{\text{shift}} > \kappa, \quad (4.80)$$

where $\kappa \sim 1 - 10$ MHz describes the characteristic cavity and qubit decay rates. The typical coupling between the microwaves and transmon is given by $g/2\pi \sim 100$ MHz.

The first set of inequalities can be satisfied taking $E_{J,0}, \hbar\Omega_0, \hbar\omega_0 \sim 100$ GHz, $E_M, \Delta_{\max} \sim 10$ GHz, and $k_B T \sim 1$ GHz. The condition $\Delta_{\max} \sim 10$ GHz can be satisfied by having very large plasma frequency Ω_k or alternatively by tuning the $E_{J,k}(\Phi_{\max})/E_{C,k}$ ratio smaller than 10, so that the superconducting islands do not stay in the transmon regime. Much larger Coulomb couplings can be achieved in this way, although the asymptotic expression given by Eq. (4.1) is not valid anymore.

Importantly, the insensitivity of the couplings Δ_k to noise is needed only when the couplings are turned off. Since the topological protection of the braiding result only allows errors of order $\Delta_{\min}/\Delta_{\max}$, the exponential smallness of Δ_{\min} guarantees that the result of the braiding cycle is not sensitive to low-frequency charge noise, which only affects the couplings which are turned on. Furthermore, by assuming that $E_{J,0}/E_{C,0} = 10$ during the measurement, we obtain $\Delta_+ \sim 10^{-2} E_{J,0}$ from Eq. (4.33), consistent with the chain of inequalities. The inequality (4.80) can be satisfied by tuning $\delta\omega$ and does not contradict with the requirement that we are working in the dispersive limit. Finally, as we have just remarked, the errors in the braiding are on the order $\Delta_{\min}/\Delta_{\max}$, which can be made exponentially small. The braiding and measurement should be performed fast in comparison to \hbar/Δ_{\min} and the characteristic quasiparticle tunneling time, which is on the order of milliseconds [104, 105]. In order that Δ_{\min} is limited by the charging energy, we need $\Delta_g \exp(-L/\xi) < \Delta_{\min}$, where L is the length of the wire and ξ is the Majorana decay length in the wire. Assuming that $\Delta_g \sim E_{J,k}$, this means that $L \approx 20\xi$, so that L should be at least several microns.

Chapter 5

Effects of disorder on Coulomb-assisted braiding of Majorana modes

Majorana zero-modes appear at domain walls between the topologically distinct phases that characterize one-dimensional superconductors [26]. The search for these quasiparticles is motivated by their non-Abelian statistics [11, 14, 21, 27, 106] and the perspective they offer in quantum computation [6, 107]. The topologically nontrivial phase can be realized with the help of an effective p -wave pairing in a spin-orbit coupled nanowire, proximity coupled to a superconductor [45, 46], and first signatures of Majorana modes have been reported in these setups[74, 77]. Other systems supporting Majorana modes include the edge of quantum spin Hall insulators [42, 108] and chains of magnetic atoms [109–114], with recent experimental progress in both directions [115–117]. After the first proposals for braiding protocols in nanowire networks [21, 63, 67, 84, 86, 107], there is a need for a detailed analysis of the limitations which might hinder the braiding operation [72, 118–120] or cause decoherence of Majorana qubits [121–127].

According to Anderson’s theorem, electrostatic disorder has little influence in s -wave superconductors [128], but in unconventional superconductors it can induce sub-gap states at arbitrarily low energies [129]. Indeed, electrostatic disorder is an unavoidable feature in experimental setups, and consequently much attention has been devoted to its impact on Majoranas [129–146]. Importantly, Majorana end modes are found to be surprisingly robust against strong disorder despite the presence of localized low-energy bound states [144].

It is therefore important to investigate what happens to their non-Abelian statistics in the presence of disorder. To understand the potential problem, let us consider a disorder potential inducing two weakly coupled accidental Majorana modes, pinned to

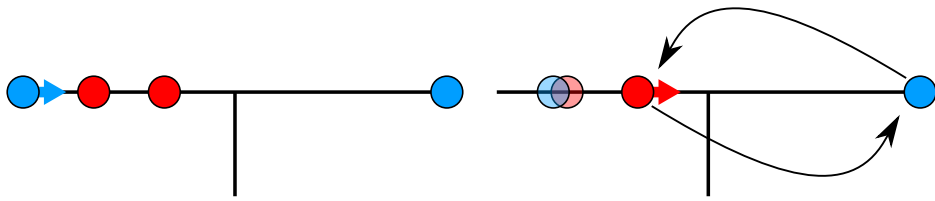


Figure 5.1: (Color online) Detrimental effect of accidental Majorana modes (red) on a braiding manipulation: when a domain wall binding a computational Majorana mode (blue) approaches an accidental one, these two Majoranas are fused. Quantum information is lost and the braiding protocol may proceed in a faulty manner, involving another accidental Majorana.

a particular location within the wire¹. When a domain wall binding a computational Majorana moves towards an accidental one, the two modes couple strongly and disappear into the continuum of states above the energy gap (see Fig. 5.1). This fusion event leads to a loss of the information stored in the computational Majoranas.

Non-Abelian Majorana statistics can also be demonstrated using superconducting circuits [61, 84, 107] implementing an interaction-based braiding protocol [147, 148]. In these hybrid Majorana-transmon qubit devices, the braiding and readout protocols are realized by controlling Coulomb couplings between the Majoranas. In this Letter, we show that these protocols are efficiently realized even in the presence of disorder. We identify the dangerous physical processes and show that the braiding errors are small if the couplings of the computational Majoranas to the accidental modes are much weaker than the maximum Coulomb coupling, leaving a large parameter space available for a braiding experiment.

The structure of this chapter is as follows. We start in Section 5.1 by shortly reviewing the transmon circuit for the Coulomb-assisted braiding protocol, which was introduced in Ref. [107], and by presenting an effective model for the setup which captures the presence of disorder in the nanowires. In Sec. 5.2 we study numerically the time-evolution of the system during the flux-controlled protocol, and evaluate the effects of disorder on the braiding as well as on the initialization and measurement. To better streamline the presentation of results, we include some of the material as Appendices. We conclude with a few remarks in Sec. 5.3.

¹If we consider for example a sufficiently strong long-range correlated disorder, there will be accidental domain walls within the wire, giving rise to spatially well-separated Majorana modes with an exponentially weak coupling. Alternatively, we may consider a strong impurity within the wire, which pins a pair of zero energy Majoranas as shown in Ref. [140].

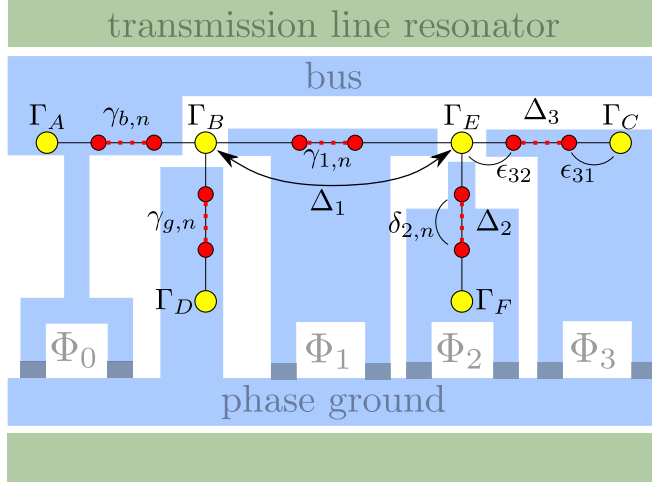


Figure 5.2: Transmon circuit for demonstration of non-Abelian statistics [107]. Two large superconducting islands (bus and ground) are used in the readout of the topological qubit and three smaller superconducting islands are needed for braiding. The nanowires form a π -shaped circuit hosting six computational Majoranas, $\Gamma_A, \Gamma_B, \dots, \Gamma_F$. A strong disorder can induce accidental Majorana modes $\gamma_{k,n}$, where k labels the island and n the accidental Majorana mode within the island. These accidental modes are coupled to each other with couplings $\delta_{k,n}$, and the accidental Majoranas closest to the end of the wires are coupled to the corresponding end states with ϵ_{k1} and ϵ_{k2} .

5.1 Braiding protocol in the presence of disorder

To demonstrate non-Abelian statistics it is necessary to read out a topological qubit, described by the parity of two Majoranas Γ_A and Γ_B , and to braid one of them, Γ_B , with another one, Γ_C . This task can be performed in a minimal fashion using a π -shaped nanowire network in a transmon circuit, following a flux-controlled braiding protocol [107]. Although we consider Majoranas at the ends of nanowires, our results are applicable also to quantum spin Hall systems, where circuits can be constructed by using constrictions [108].

The circuit for braiding and readout is shown in Fig. 5.2, and involves nanowires forming a π -shaped network hosting six computational Majoranas, $\Gamma_A, \Gamma_B, \dots, \Gamma_F$. The couplings between them can be controlled via the flux-dependence of the Josephson energy, $E_{J,k}(\Phi_k) = E_{J,k}(0) \cos(e\Phi_k/\hbar)$, of each superconducting island, k . The charging energies $E_{C,k}$ of the islands result in Coulomb couplings $\Delta_k(\Phi_k)$ between the Majoranas, which, for $E_{J,k}(\Phi_k) \gg E_{C,k}$, have an exponential dependence $\Delta_k(\Phi_k) \propto \exp(-\sqrt{8E_{J,k}(\Phi_k)/E_{C,k}})$ [61, 84], that allows to turn them on ($\Delta_k = \Delta_{\max}$) and off ($\Delta_k = \Delta_{\min}$) with fluxes. A non-demolition readout of the topological qubit is possible, because the plasma frequency of the transmon formed by the bus and ground islands

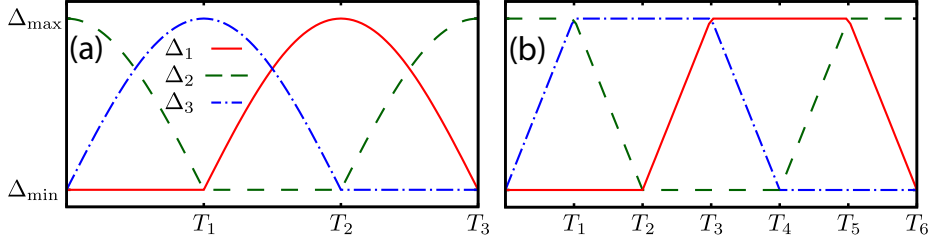


Figure 5.3: Two possible paths of variations of Coulomb couplings resulting in braiding of Majorana zero-modes Γ_B and Γ_C . The braiding errors caused by the accidental modes depend on the braiding path (see Fig. 5.4).

(see Fig. 5.2) can be tuned close to the resonance frequency of the transmission line resonator. Once the magnetic flux Φ_0 is turned on, the coupling between photons and the transmon qubit renormalizes the resonance frequency of the cavity, so that it is conditioned on the fermion parity of Γ_A and Γ_B [61, 107]. On the other hand, the Majorana modes Γ_B and Γ_C can be braided with the help of ancillas Γ_E and Γ_F , by varying the Coulomb couplings Δ_k along a specific type of closed path [84] (see Fig. 5.3). The corresponding operation on the topological qubit is $\mathcal{U} = \exp(is\pi\sigma_x/4)$ [27], where s describes the braiding chirality.

As we already pointed out, strong disorder induces accidental low-energy bound states in unconventional superconductors. These states can be described using Majorana operators $\gamma_{k,n}$, where k labels the island and n the accidental Majorana modes within it. We assume that neighboring Majoranas interact with random couplings. In particular, the accidental Majoranas closest to the end of each wire are coupled to the corresponding Γ end modes with couplings ϵ_{k1} and ϵ_{k2} (see Fig. 5.2). Unlike in the clean case, the Coulomb interaction involves the total fermion parity of each island, so braiding should be performed by controlling many-body interactions between Majoranas, instead of the simple pairwise ones considered in Refs. [84, 107]. Similarly, the measurement is now sensitive to the total fermion parity of the bus island.

During the braiding procedure we set $\Phi_0 = 0$ so that the charging energy of the bus island can be neglected. The low-energy Hamiltonian is

$$H_{\text{br}} = H_C + H_\delta + H_\epsilon \quad (5.1a)$$

$$H_C = i\Delta_1\Gamma_B\Gamma_1\Gamma_E + i\Delta_2\Gamma_E\Gamma_2\Gamma_F + i\Delta_3\Gamma_E\Gamma_3\Gamma_C, \quad (5.1b)$$

$$H_\delta = i \sum_{k,n} \delta_{k,n} \gamma_{k,n} \gamma_{k,n+1}, \quad (5.1c)$$

$$\begin{aligned} H_\epsilon = & i\epsilon_{b1}\Gamma_A\gamma_{b,1} + i\epsilon_{g1}\Gamma_B\gamma_{g,1} + i\epsilon_{11}\Gamma_B\gamma_{1,1} + i\epsilon_{21}\Gamma_E\gamma_{2,1} \\ & + i\epsilon_{31}\Gamma_E\gamma_{3,1} + i\epsilon_{b2}\gamma_{b,N_b}\Gamma_B + i\epsilon_{g2}\gamma_{g,N_g}\Gamma_D \\ & + i\epsilon_{12}\gamma_{1,N_1}\Gamma_E + i\epsilon_{22}\gamma_{2,N_2}\Gamma_F + i\epsilon_{32}\gamma_{3,N_3}\Gamma_C, \end{aligned} \quad (5.1d)$$

where H_C describes the Coulomb couplings between the Majoranas, and H_δ , H_ϵ describe the tunnel couplings of the accidental Majoranas to each other, and to the computational ones, respectively. We have denoted the total parity of the accidental Majoranas in island k with $\Pi_k = e^{-i\pi N_k/4} \prod_{n=1}^{N_k} \gamma_{k,n}$.

If $H_\epsilon = 0$, then $[H_{\text{br}}, \Pi_k] = 0$, which means that the computational and accidental Majoranas form two decoupled quantum systems. In a sector of the eigenstates of Π_k with eigenvalues p_k , $H_C(\{p_k\}) = ip_1\Delta_1\Gamma_B\Gamma_E + ip_2\Delta_2\Gamma_E\Gamma_F + ip_3\Delta_3\Gamma_E\Gamma_C$, which was considered in Refs. [84, 107]. The Hilbert space is divided into ground and excited state manifolds, separated by an energy $2E_0$, where $E_0 = \sqrt{\Delta_1^2 + \Delta_2^2 + \Delta_3^2} \geq \Delta_{\text{max}}$. Because the braiding is performed adiabatically with respect to Δ_{max} , the transitions between these manifolds can be neglected and the time-evolution operator within each parity sector is

$$\mathcal{U}_0(\{p_k\}, p_{\text{anc}}) = e^{is(\{p_k\}, p_{\text{anc}})\pi\sigma_x/4} \prod_i \mathcal{U}_{\text{int},i}(\{p_k\}, p_{\text{anc}}), \quad (5.2)$$

where $\mathcal{U}_{\text{int},i}(\{p_k\}, p_{\text{anc}})$ describes the internal time-evolution of the accidental Majoranas in island i , $s(\{p_k\}, p_{\text{anc}})$ denote the chirality of the braiding in different sectors of the Hilbert space, and p_{anc} is the parity of the ancillas Γ_E and Γ_F .

We now assume that the measurement projects the system to an eigenstate of total parity on the bus island $\mathcal{P} = -i\Gamma_A\Gamma_B$. (The requirements for a successful measurement are analyzed below.) The protocol for demonstrating non-Abelian Majorana statistics consists of a measurement \mathcal{P} followed by n braiding cycles, after which the parity is measured again. The probability of observing a parity flip after n consecutive braidings, $p_{\text{flip}}(n)$, is dictated by the Majorana statistics. For clean wires the sequence of probabilities is $p_{\text{flip}} = 1/2, 1, 1/2, 0$ for $n = 1, 2, 3, 4$, and it repeats itself periodically for larger values of n [107]. Given Eq. (5.2), the sequence is independent on the accidental Majoranas and the initial state of the ancillas as long as $H_\epsilon = 0$. Thus, the only limitations in this case are quasiparticle poisoning and inelastic relaxation processes².

5.2 Analysis of the braiding protocol errors.

5.2.1 Effects of disorder on the braiding cycle

The interaction H_ϵ between computational and accidental Majoranas may lead to fermion parity exchanges, giving rise to braiding errors. We assume that these coupling constants satisfy $\epsilon_{k1}, \epsilon_{k2} \ll \Delta_{\text{max}}$, which allows to choose the braiding speed so that $\epsilon_{k1}, \epsilon_{k2} \ll \Delta_0 \ll \Delta_{\text{max}}$, where the energy scale $\Delta_0 = \hbar/T_0$ is determined by the duration T_0 of one segment of the braiding cycle in Fig. 5.3. Thus, we can calculate the unperturbed time-evolution operator $U_0(t)$ in each parity sector using

²We note that while the accidental Majoranas do not influence the sequence of probabilities p_{flip} , they affect the chirality of the braiding, which can be important in more advanced quantum manipulations.

the adiabatic approximation and consider the effect of H_ϵ perturbatively. The total time-evolution operator for one braiding cycle can be written as

$$\mathcal{U} = \mathcal{U}_0 + \sum_k \left[\frac{\epsilon_{k1}}{\Delta_0} \delta \mathcal{U}_{k1} + \frac{\epsilon_{k2}}{\Delta_0} \delta \mathcal{U}_{k2} \right], \quad (5.3)$$

where \mathcal{U}_0 is the unperturbed time-evolution, which in different parity sectors is described by Eq. (5.2), and $\delta \mathcal{U}_{k1,2}$ are corrections which can in principle be computed for an arbitrary disordered wire. These corrections couple the different parity sectors and can result in braiding errors.

Next, we analyze in detail the case where each nanowire contains a single pair of accidental Majorana modes, which are coupled to each other by δ . This allows to identify the fundamental mechanisms of errors, which are present also in nanowires with many accidental Majorana modes.

We first note that the couplings ϵ_{b1} and ϵ_{g2} have no effect on the braiding protocol within the lowest order perturbation theory. We characterize the errors caused by other couplings by calculating the matrix norms $\|\delta \mathcal{U}_{ki}\|_2$ ³, which depend on δ and act as effective pre-factors of ϵ_{ki}/Δ_0 in Eq. (5.3). Based on symmetry arguments, we find that $\|\delta \mathcal{U}_{b2}\|_2 = \|\delta \mathcal{U}_{g1}\|_2$, $\|\delta \mathcal{U}_{11}\|_2 = \|\delta \mathcal{U}_{22}\|_2 = \|\delta \mathcal{U}_{33}\|_2$ and $\|\delta \mathcal{U}_{12}\|_2 = \|\delta \mathcal{U}_{31}\|_2$ (see Appendix 5.A). This leaves four different cases, which are plotted in Fig. 5.4 (a)-(d) and (e)-(h) for the two paths of Fig. 5.3(a),(b), respectively. The errors show peaks when accidental Majorana modes are either uncoupled ($\delta \approx 0$) or the energy of their bound state is in resonance with the energy gap between the ground and excited state manifolds ($\delta \approx E_0$). The peak appearing close to $\delta = 0$ is extremely narrow for both paths, but the resonance at $\delta \approx \Delta_{\max}$ is strongly path dependent. For the circular path, shown in Fig. 5.3(a), E_0 is constant during the whole braiding cycle resulting in narrow resonance peak at $\delta \approx \Delta_{\max}$. On the other hand, for the path shown in Fig. 5.3(b), E_0 varies between $[\Delta_{\max}, \sqrt{2}\Delta_{\max}]$ during the braiding cycle so that the resonance peak spreads over a wide range of δ . In the case of circular path it is possible to obtain closed form analytic solutions for $\delta \mathcal{U}_{ki}$. Away from the peaks where $\|\delta \mathcal{U}_{ki}\|_2 \sim 1$, they vanish asymptotically as $\sim \text{Max}[\Delta_0/\delta, \Delta_0/|\Delta_{\max} \pm \delta|]$ or faster (see Appendix 5.B). We have verified the validity of the perturbation theory for $\epsilon_{ki}/\Delta_0 < 0.1$ by numerically calculating the full time-evolution operator. We also point out that the assumption that the couplings $\delta_{k,n}$ and ϵ_{ki} are time-independent is not essential. Our qualitative findings are valid also if these couplings are changing adiabatically in time due to the variations of the Coulomb couplings.

With increasing disorder, more low-energy sub-gap states will appear in the energy spectrum. For an increased number of accidental bound states, the braiding errors as a function of Δ_{\max} will contain several peaks, appearing whenever an energy of the accidental Majoranas is in resonance with E_0 . This means that it becomes more and more difficult to avoid errors by properly choosing Δ_{\max} . At the same time, the accidental modes will appear closer to the ends of the wires, increasing the couplings ϵ_{ki} , which control the heights of the peaks in the braiding errors. As this

³The matrix norm $\|\mathcal{U}\|_2$ is defined as the largest singular value of \mathcal{U} .

coupling becomes comparable to the maximum Coulomb coupling, $\epsilon_{ki} \sim \Delta_{\max}$, one can no longer choose a Δ_0 such that the braiding process is adiabatic with respect to the Coulomb coupling and non-adiabatic with respect to ϵ_{ki} . At this point, the non-Abelian statistics is not observable anymore. An interesting theoretical question is whether this breakdown of the non-Abelian statistics happens in conjunction with a disorder-induced topological transition to a trivial phase of the nanowire, or whether it precedes it. We note that, in our model, the braiding process can in principle be optimized by choosing the coupling Δ_{\max} in such a way that it is comparable to the topological gap, $\Delta_{\max} \sim E_{\text{gap}}$. In this case, non-Abelian statistics becomes unobservable when $\epsilon_{ki} \sim E_{\text{gap}}$, so that the critical disorder strength is comparable to the critical disorder strength inducing the topological phase transition. However, our model is strictly speaking a low-energy effective theory, which is only valid in the nontrivial phase, and therefore it cannot be used for a detailed quantitative description of the breakdown of the non-Abelian braiding statistics and the topological phase transition happening at large disorder.

5.2.2 Effect of disorder on initialization and readout

Errors can arise not only during the braiding cycle, but also during the readout, performed through a measurement of the fermion parity $\mathcal{P} = -i\Gamma_A \Pi_B \Gamma_B$ of the bus island. The Hamiltonian describing the interaction of the transmon qubit and the cavity is [107]:

$$\begin{aligned} H_{\text{ro}} = & \hbar\omega_0 a^\dagger a + \hbar g (\tau_+ a + \tau_- a^\dagger) + \tau_z \left(\frac{1}{2} \hbar\Omega_0 + \Delta_+ \mathcal{P} \right) \\ & + \Delta_- \mathcal{P} + H_b (\epsilon_{bn}, \delta_{b,n,m}) + i\epsilon_{11} \Gamma_B \gamma_{11} + i\delta \gamma_{11} \gamma_{12}. \end{aligned} \quad (5.4)$$

The first line describes the photons with bare resonance frequency ω_0 and the interaction with the transmon qubit with a coupling constant g . Here Ω_0 is the transmon plasma frequency, Pauli matrices $\tau_{x,y,z}$ act on the transmon qubit and $\tau_\pm = (\tau_x \pm i\tau_y)/2$. The term proportional to \mathcal{P} arises due to the Coulomb coupling [107], and the Hamiltonian H_b defines the tunnel couplings of the Majoranas inside the bus island. The last two terms describe the coupling of the computational Majorana Γ_B to an accidental pair of modes outside the bus island. We assume that the transmission line resonator is operated in the dispersive regime, where $(n+1)g^2 \ll \delta\omega^2$, with n the number of photons in the cavity and $\delta\omega = \Omega_0 - \omega_0$.

Without accidental Majoranas, the Hamiltonian (5.4) produces a parity-dependent resonance frequency of the cavity $\omega_{\text{eff}}(\mathcal{P}) = \omega_0 + \tau_z g^2 (\delta\omega + 2\mathcal{P}\Delta_+/\hbar)^{-1}$, which allows to measure the topological qubit [61, 107]. As before, we consider perturbative corrections caused by the couplings between computational and accidental Majoranas. The term H_b conserves the parity \mathcal{P} and therefore it does not modify ω_{eff} within the lowest order perturbation theory. The presence of the external coupling ϵ_{11} implies that the measurement eigenstates of the renormalized cavity frequency no longer have a definite parity \mathcal{P} , but can be written in a form $\psi = \sqrt{1-\varepsilon^2} |\mathcal{P}, \dots\rangle + \varepsilon |-\mathcal{P}, \dots\rangle$,

where away from resonances the measurement error vanishes as $\varepsilon \sim \epsilon_{11}/(\Delta_+ - \Delta_- - |\delta|)$. This scaling is in agreement with the expected parity flow to the accidental Majorana modes. Close to the resonances $\Delta_+ - \Delta_- \approx |\delta|$ the parity flow will be limited by the finite measurement time t_M so that the errors are $\sim \epsilon_{11} t_M / \hbar$. Therefore, the conditions for successful measurement coincide with the requirements for small braiding errors.

5.3 Summary

We have shown that the Coulomb-assisted braiding protocol is realizable also in the presence of disorder-induced accidental bound states, and that the braiding errors are small if the coupling of the computational Majoranas to the accidental states is much weaker than the maximum Coulomb coupling. A few remarks are in order concerning the experimental relevance of our results. First, the requirement of weak coupling between the computational and accidental Majorana modes coincides with the definition of the topological phase in disordered systems, and therefore based on the findings in Ref. [144], we expect that there is a large parameter space available for braiding the Majorana modes. Secondly, the low-energy states in the wires can in principle be characterized using spatially resolved scanning tunneling microscopy [117] or by coupling to microwaves [149–152]. Because braiding errors depend strongly on the energies of the accidental modes, they can be systematically decreased by controlling these energies with the help of Zeeman fields or gate voltages. Finally, we point out that our results are relevant also in the case of clean wires, because they allow to simplify the experimental setup by replacing the π shaped network of Ref. [107] with two spatially separated T-junctions. In this case, two additional Majorana quasiparticles are intentionally created, which influence the braiding the same way as the accidental Majoranas considered here. However, in clean wires the additional Majoranas are automatically weakly coupled to the computational ones if the wires are sufficiently long, leading to negligible braiding errors.

5.A Symmetry relations for the braiding errors

When the couplings between the accidental and the computational Majoranas is much smaller than the maximum Coulomb coupling, their effects can be treated independently. In the following we analyze each of the ten terms in H_e and show that there are only four independent terms which contribute to errors during the braiding cycle.

Since the Coulomb Hamiltonian H_C commutes with both $i\epsilon_{b1}\Gamma_A\gamma_{b,1}$, as well as $i\epsilon_{g2}\gamma_{g,N_g}\Gamma_D$, it is clear that these terms cannot cause errors during the braiding cycle. Their counterparts, $i\epsilon_{b2}\gamma_{b,N_b}\Gamma_B$ and $i\epsilon_{g1}\Gamma_B\gamma_{g,1}$ involve accidental Majoranas outside the braiding T-junction and do cause errors, as shown in Fig. 5.4. Furthermore,

these errors are identical, $\|\delta \mathcal{U}_{b2}\|_2 = \|\delta \mathcal{U}_{g1}\|_2$, because they are only related by a relabeling of the accidental Majorana indices.

Out of the six remaining terms, only three contribute in an independent fashion. To make this apparent, we will consider the case where there are only two accidental Majoranas in the braiding T-junction, which we label γ_1 and γ_2 for ease of notation. They may be placed in any of the three islands, and connected to any of the computational Majoranas. The six resulting Hamiltonians read:

$$H_{11} = \Delta_1 \Gamma_B \gamma_1 \gamma_2 \Gamma_E + i \Delta_2 \Gamma_E \Gamma_F + i \Delta_3 \Gamma_E \Gamma_C + i \delta \gamma_1 \gamma_2 + i \epsilon \Gamma_B \gamma_1 \quad (5.5)$$

$$H_{12} = \Delta_1 \Gamma_B \gamma_1 \gamma_2 \Gamma_E + i \Delta_2 \Gamma_E \Gamma_F + i \Delta_3 \Gamma_E \Gamma_C + i \delta \gamma_1 \gamma_2 + i \epsilon \gamma_2 \Gamma_E \quad (5.6)$$

$$H_{21} = i \Delta_1 \Gamma_B \Gamma_E + \Delta_2 \Gamma_E \gamma_1 \gamma_2 \Gamma_F + i \Delta_3 \Gamma_E \Gamma_C + i \delta \gamma_1 \gamma_2 + i \epsilon \Gamma_E \gamma_1 \quad (5.7)$$

$$H_{22} = i \Delta_1 \Gamma_B \Gamma_E + \Delta_2 \Gamma_E \gamma_1 \gamma_2 \Gamma_F + i \Delta_3 \Gamma_E \Gamma_C + i \delta \gamma_1 \gamma_2 + i \epsilon \gamma_2 \Gamma_F \quad (5.8)$$

$$H_{31} = i \Delta_1 \Gamma_B \Gamma_E + i \Delta_2 \Gamma_E \Gamma_F + \Delta_3 \Gamma_E \gamma_1 \gamma_2 \Gamma_C + i \delta \gamma_1 \gamma_2 + i \epsilon \Gamma_E \gamma_1 \quad (5.9)$$

$$H_{32} = i \Delta_1 \Gamma_B \Gamma_E + i \Delta_2 \Gamma_E \Gamma_F + \Delta_3 \Gamma_E \gamma_1 \gamma_2 \Gamma_C + i \delta \gamma_1 \gamma_2 + i \epsilon \gamma_2 \Gamma_C. \quad (5.10)$$

Following Bravyi and Kitaev [92], we write a representation of the six Majorana operators as:

$$\Gamma_B = \sigma_0 \otimes \sigma_0 \otimes \sigma_x \quad (5.11)$$

$$\Gamma_C = \sigma_0 \otimes \sigma_0 \otimes \sigma_y \quad (5.12)$$

$$\Gamma_E = \sigma_0 \otimes \sigma_x \otimes \sigma_z \quad (5.13)$$

$$\Gamma_F = \sigma_0 \otimes \sigma_y \otimes \sigma_z \quad (5.14)$$

$$\gamma_1 = \sigma_x \otimes \sigma_z \otimes \sigma_z \quad (5.15)$$

$$\gamma_2 = \sigma_y \otimes \sigma_z \otimes \sigma_z, \quad (5.16)$$

where σ_i are the Pauli matrices and \otimes denotes the Kronecker product.

The three Hamiltonians containing a coupling of an accidental Majorana to Γ_B , Γ_F , or Γ_C are identical up to unitary transformations, and therefore lead to identical errors $\|\delta \mathcal{U}_{11}\|_2 = \|\delta \mathcal{U}_{22}\|_2 = \|\delta \mathcal{U}_{32}\|_2$. The unitary transformations are

$$H_{11} = U_{12} H_{22} U_{12}^\dagger, \quad H_{11} = U_{13} H_{32} U_{13}^\dagger, \quad (5.17)$$

with

$$U_{12} = \begin{pmatrix} \sigma_z \otimes \sigma_z & 0 \\ 0 & \sigma_x \otimes \sigma_x \end{pmatrix}, \quad (5.18)$$

$$U_{13} = \begin{pmatrix} \sigma_z \otimes \sigma_z & 0 \\ 0 & \sigma_z \otimes \sigma_0 \end{pmatrix}. \quad (5.19)$$

The Hamiltonians H_{12} and H_{31} can also be related by a unitary transformation, provided that one interchanges Δ_1 and Δ_3 ,

$$H_{12} = \tilde{U}_{13} H_{31} (\Delta_1 \leftrightarrow \Delta_3) \tilde{U}_{13}^\dagger, \quad (5.20)$$

where

$$\tilde{U}_{13} = \frac{1}{\sqrt{2}} \begin{pmatrix} i\sigma_0 \otimes (\sigma_x + \sigma_y) & 0 \\ 0 & \sigma_0 \otimes (\sigma_x + \sigma_y) \end{pmatrix}. \quad (5.21)$$

Since replacing Δ_1 with Δ_3 and vice versa amounts to performing the braiding cycle in a time-reversed order (see Fig. 5.3), these two Hamiltonians produce identical errors $\|\delta \mathcal{U}_{12}\|_2 = \|\delta \mathcal{U}_{31}\|_2$.

Such a transformation also exists for H_{12} and H_{21} , but involves replacing $\Delta_1 \leftrightarrow \Delta_2$, which changes the braiding path, and therefore leads to different errors, as shown in Fig. 5.4.

5.B Analytical solutions for the braiding errors

In order to calculate the four independent corrections $\|\delta \mathcal{U}_{ki}\|_2$, we write the total time-evolution operator as $U(t) = U_0(t)\tilde{U}(t)$, where $U_0(t)$ is the time-evolution operator for $H_\epsilon = 0$ and \tilde{U} describes the lowest order correction caused by H_ϵ . We assume that $\Delta_0 \ll \Delta_{\max}$, so that the unperturbed time-evolution operator $U_0(t)$ for the computational Majoranas in each parity sector can be calculated using the adiabatic approximation. The lowest order correction \tilde{U} can be found using the equation:

$$\tilde{U}(t) = 1 - \frac{i}{\hbar} \int_0^t dt_1 U_0^\dagger(t_1) H_\epsilon U_0(t_1). \quad (5.22)$$

In this way we obtain that the total time-evolution operator for one braiding cycle is given by Eq. (5.3), where \mathcal{U}_0 is the unperturbed time-evolution, which in different parity sectors is described by Eq. (5.2), and $\delta \mathcal{U}_{k1}$ and $\delta \mathcal{U}_{k2}$ are corrections, which can be solved by calculating the integral in Eq. (5.22).

For the circular braiding path [Fig. 5.3(a)] with one pair of accidental Majoranas in each island, the integral in Eq. (5.22) can be computed exactly, resulting in closed form analytic solutions for $\delta \mathcal{U}_{ki}$. Although the full expressions are not very insightful, they allow us to determine how the braiding error estimates, $\epsilon_{ki} \|\delta \mathcal{U}_{ki}\|_2 / \Delta_0$, vanish asymptotically far away from the resonant peaks in Fig. 5.4. We obtain

$$\begin{aligned} \|\delta \mathcal{U}_{12}\|_2 = \text{Max} \left[\frac{\pi |\cos(2\delta/\Delta_0)|}{4\delta^2/\Delta_0^2}, \right. \\ \left. \frac{|\cos(3(\delta \pm \Delta_{\max})/\Delta_0) \pm \sin(3(\delta \pm \Delta_{\max})/\Delta_0)|}{\sqrt{2}|\delta \pm \Delta_{\max}|/\Delta_0} \right], \end{aligned} \quad (5.23a)$$

$$\|\delta \mathcal{U}_{11}\|_2 = \frac{|\sin(3\delta/\Delta_0)|}{|\delta/\Delta_0|} \quad (5.23b)$$

$$\|\delta \mathcal{U}_{21}\|_2 = \text{Max} \left[\frac{|\sin(3\delta/\Delta_0)|}{|\delta/\Delta_0|}, \frac{\pi |\cos(3(\delta \pm \Delta_{\max})/\Delta_0)|}{4(\delta \pm \Delta_{\max})^2/\Delta_0^2} \right], \quad (5.23c)$$

and

$$\|\delta \mathcal{U}_{b2}\|_2 = \text{Max} \left[\frac{\sqrt{1 \pm \sin(6\delta/\Delta_0)}}{\sqrt{2}|\delta/\Delta_0|}, \frac{\pi|\cos(2(\delta \pm \Delta_{\max})/\Delta_0)|}{4(\delta \pm \Delta_{\max})^2/\Delta_0^2} \right]. \quad (5.23d)$$

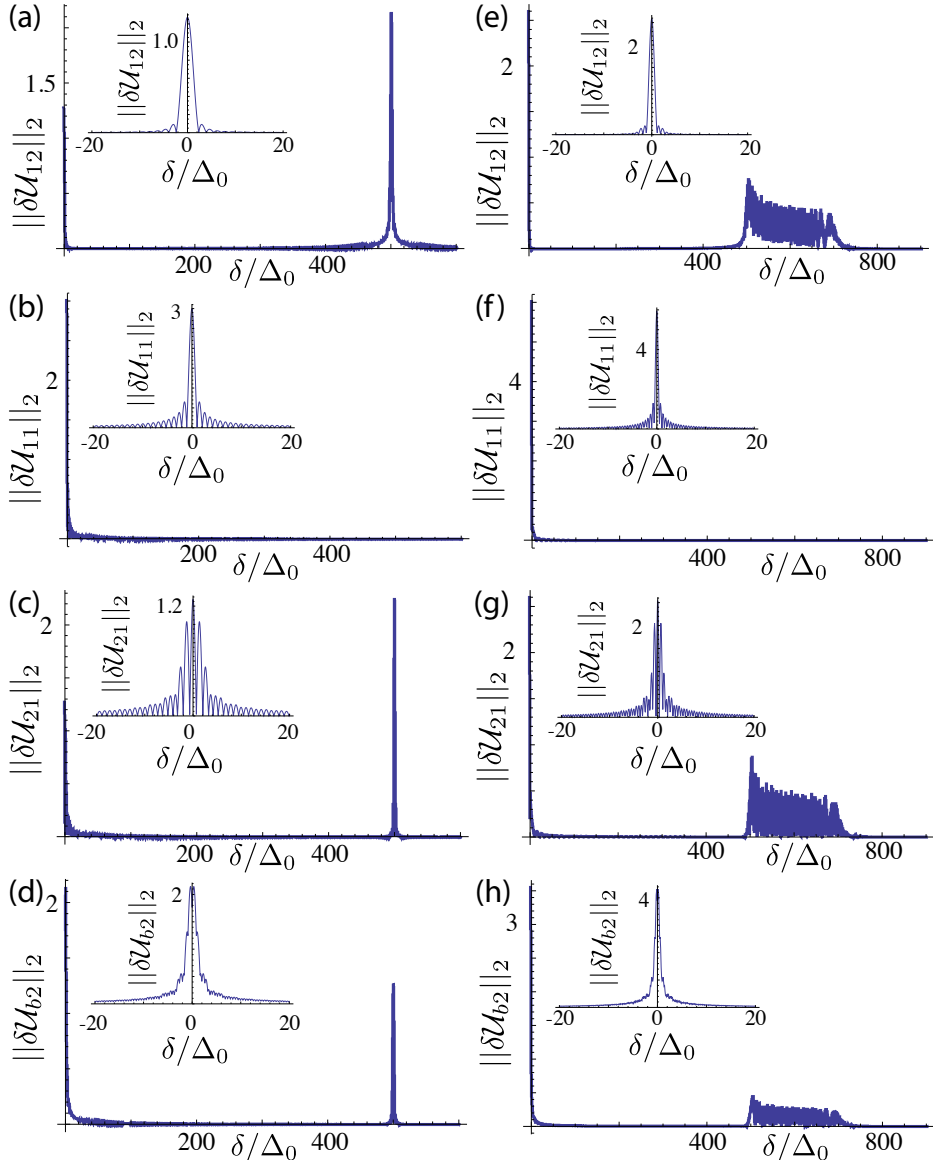


Figure 5.4: Errors occurring during the braiding cycle can be estimated by $\epsilon_{ki} \|\delta \mathcal{U}_{ki}\|_2 / \Delta_0$ [Eq. (5.3)], with four different types of corrections $\|\delta \mathcal{U}_{ki}\|_2$, which are plotted as a function of δ . These corrections, related to the two adiabatic cycles of Fig. 5.3(a),(b), are shown in figures (a)-(d) and (e)-(h), respectively. The insets show magnifications of the peaks around $\delta = 0$. Away from the peaks the errors are efficiently suppressed. In all figures $\Delta_{\max} = 500\Delta_0$.

Chapter 6

Minimal circuit for a flux-controlled Majorana qubit in a quantum spin-Hall insulator

Among the many exotic properties of topological insulators [43, 44], the prediction [153] that they can host Majorana zero-modes stands out both for its fundamental interest and for possible applications in topological quantum computing [6]. To braid Majoranas is the prize-winning experiment, since it would identify them as a fundamentally new type of quasiparticles with non-Abelian statistics [14]. The road towards this goal has several milestones, starting from the detection of the zero-mode itself [74].

One intermediate milestone is the construction of a qubit out of Majorana zero-modes and the measurement of its coherence times. This would be essential information for a subsequent braiding experiment to demonstrate its non-Abelian nature. Here we describe a minimal circuit that can initialize, rotate, and read-out the Majorana qubit by coupling it to a transmon (a superconducting charge qubit in a microwave transmission line resonator [37]). This is the hybrid topological-transmon qubit (*top-transmon*) introduced in Ref. [61].

The circuit we propose here for the characterization of the Majorana qubit is a reduced version of the full braiding circuit of Ref. [107]. By sacrificing the possibility to perform topologically protected operations, we now need only 4 and not 6 Majoranas. For an early generation of experiments this might well be a significant simplification. The reduced circuit shares with the full circuit the feature that all operations are performed by control over Coulomb interactions rather than tunneling [84]. This control is achieved by external variation of magnetic fluxes through macroscopic Josephson junctions, without requiring microscopic control over tunnel couplings.

We focus on Majorana zero-modes induced by the superconducting proximity effect at the edge of a quantum spin-Hall insulator [42], motivated by recent experimental

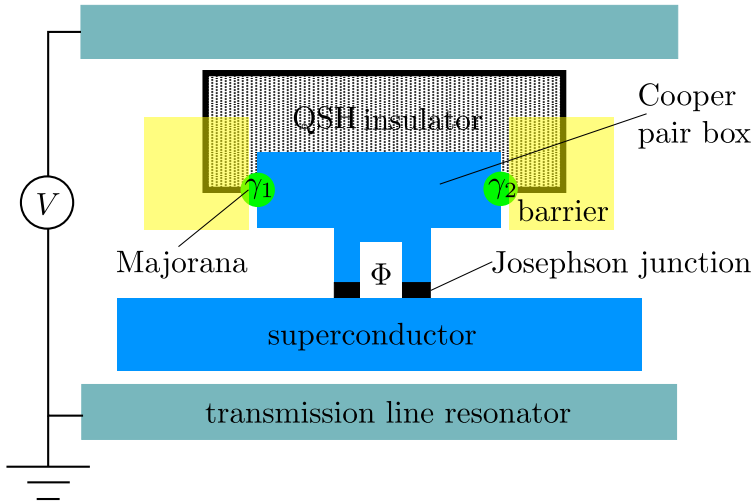


Figure 6.1: Schematic of a Cooper pair box in a transmission line resonator (*transmon*) containing a pair of Majorana zero-modes at the edge of a quantum spin-Hall insulator. This hybrid device (*top-transmon*) can couple charge qubit and topological qubit by variation of the flux Φ through a Josephson junction.

progress in this direction [115, 116, 154]. Relative to the nanowire realization [45, 46], this system has several favorable properties (single-mode conduction, insensitivity to disorder). It also brings along some challenges (how to confine the Majoranas, how to make a T-junction), that we propose to overcome along the lines suggested in Ref. [108].

6.1 Top-transmon

Before proceeding to a description in the next section of the minimal circuit that can operate on a Majorana qubit, we summarize the basic ingredients. The device is a hybrid structure [61], dubbed a *top-transmon*, combining a topological qubit formed out of Majorana zero-modes with a non-topological transmon qubit.

The basic building block of the transmon, shown in Fig. 6.1, is a Cooper pair box [70] (a superconducting island with charging energy $E_C \ll$ Josephson energy E_J) coupled to a microwave transmission line (coupling energy $\hbar g$). The plasma frequency $\hbar\Omega_0 \simeq \sqrt{8E_J E_C}$ is modulated by an amount $\Delta_+ \cos(\pi q_{\text{ind}}/e)$ upon variation of the charge q_{ind} induced on the island by a gate voltage V . Additionally, there is a q_{ind} -dependent contribution $\Delta_- \cos(\pi q_{\text{ind}}/e)$ to the ground state energy. The charge sensitivity $\Delta_{\pm} \propto \exp(-\sqrt{8E_J/E_C})$ can be adjusted by varying the flux Φ enclosed by the Josephson junction, which modulates the Josephson energy $E_J \propto \cos(2\pi e\Phi/\hbar)$. In a typical device [83], a variation of Φ between $\Phi_{\text{min}} \approx 0$ and $\Phi_{\text{max}} \lesssim h/4e$ changes

Δ_{\pm} by several orders of magnitude, so the charge sensitivity can effectively be switched on and off by increasing the flux by half a flux quantum.

Including also the coupling to the microwave photons (creation operator a^\dagger at resonant frequency ω_0), the Hamiltonian of the transmon has the form [37, 83]

$$H_{\text{transmon}} = \frac{1}{2}\hbar\Omega_0\sigma_z + (\Delta_+\sigma_z + \Delta_-)\cos(\pi q_{\text{ind}}/e) + \hbar\omega_0 a^\dagger a + \hbar g(\sigma_+ a + \sigma_- a^\dagger). \quad (6.1)$$

The charge qubit is represented by Pauli matrices $\sigma_x, \sigma_y, \sigma_z$, with $\sigma_{\pm} = (\sigma_x \pm i\sigma_y)/2$.

Majorana zero-modes are represented by identical creation and annihilation operators $\gamma_n = \gamma_n^\dagger$, with anti-commutation relation

$$\gamma_n \gamma_m + \gamma_m \gamma_n = 2\delta_{nm}. \quad (6.2)$$

The number of Majoranas on a superconducting island is necessarily even, say $2N$. They encode a topological quantum number, which is the ± 1 eigenvalue of the fermion parity operator [26]

$$\mathcal{P} = i^N \prod_{n=1}^{2N} \gamma_n. \quad (6.3)$$

The top-transmon Hamiltonian

$$H_{\text{top-transmon}} = \frac{1}{2}\hbar\Omega_0\sigma_z + (\Delta_+\sigma_z + \Delta_-)\mathcal{P} \cos(\pi q_{\text{ind}}/e) + \hbar\omega_0 a^\dagger a + \hbar g(\sigma_+ a + \sigma_- a^\dagger) \quad (6.4)$$

contains a term $\sigma_z \mathcal{P}$ that couples the charge qubit to the topological qubit, see Ref. [84] for a derivation.

Since Majorana modes are charge-neutral particles (being their own antiparticle), one may ask how there can be any coupling at all. The answer is that the state of the $2N$ zero-modes in a superconducting island depends on the parity of the number of electrons on that island, and it is this dependence on the electrical charge modulo $2e$ that provides for a flux-controlled Coulomb coupling between the Majoranas.

A measurement of the resonance frequency ω_{eff} of the transmission line now becomes a joint projective measurement of the charge qubit and topological qubit [61, 107],

$$\omega_{\text{eff}} = \omega_0 + \frac{\sigma_z g^2}{\Omega_0 - \omega_0 + 2\mathcal{P}\Delta_+/\hbar}. \quad (6.5)$$

This measurement is performed far off resonance ($g \ll |\Omega_0 - \omega_0|$, the so-called dispersive regime), so the charge qubit is not excited. If it is in the ground state we may just replace $\sigma_z \mapsto -1$ and ω_{eff} directly measures \mathcal{P} . In particular, a shift in the resonance frequency signals a bit-flip of the topological qubit.

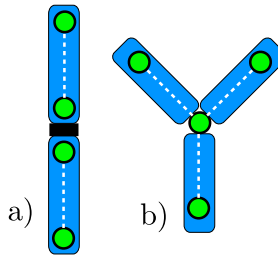


Figure 6.2: Topological qubit formed out of four Majorana zero-modes, on either two or three superconducting islands. Dashed lines indicate flux-controlled Coulomb couplings, as in the Cooper pair box of Fig. 6.1. In the linear layout (panel a) the coupling between Majoranas on different islands is via a tunnel barrier (thick horizontal line), requiring gate voltage control. By using a T-junction (panel b) all three couplings can be flux-controlled Coulomb couplings.

6.2 Minimal circuit

The conservation of fermion parity on a single superconducting island implies a minimum of two islands for a Majorana qubit, each containing a pair of Majorana zero-modes. The minimal circuit that can operate on a Majorana qubit would then have the linear layout of Fig. 6.2a. While the couplings between Majoranas on the same island are flux-controlled Coulomb couplings, the inter-island coupling is via a tunnel barrier, which would require microscopic control by a gate voltage.

An alternative layout that has only Coulomb couplings needs three rather than two islands, forming a T-junction as in Fig. 6.2b. A T-junction pins a Majorana zero-mode [21], which can be Coulomb-coupled to each of the other three Majoranas [107]. The T-junction also binds higher-lying fermionic modes, separated from the zero mode by an excitation energy E_M . This is the minimal design for a fully flux-controlled Majorana qubit. In Fig. 6.3 we have worked it out in some more detail for the quantum spin-Hall insulator.

Three superconducting islands allow for two independent charge differences, so they produce two charge qubits $\sigma_z^{(1)}$ and $\sigma_z^{(2)}$. These are coupled to four Majorana zero-modes γ_A , γ_B , γ_C , γ_D . The Hamiltonian is two copies of the top-transmon Hamiltonian (6.4),

$$\begin{aligned}
 H = & \hbar\omega_0 a^\dagger a + \sum_{n=1}^2 \left[\frac{1}{2} \hbar \Omega_0^{(n)} \sigma_z^{(n)} + \hbar g^{(n)} (\sigma_+^{(n)} a + \sigma_-^{(n)} a^\dagger) \right] \\
 & + i\gamma_A \gamma_B [\sigma_z^{(1)} \Delta_+^{(1)}(\Phi_0) + \Delta_-^{(1)}(\Phi_0)] \\
 & + i\gamma_B \gamma_C [\sigma_z^{(2)} \Delta_+^{(2)}(\Phi_1) + \Delta_-^{(2)}(\Phi_1)],
 \end{aligned} \tag{6.6}$$

where for simplicity we have set $q_{\text{ind}} = 0$ on each island. We have ignored the higher-lying fermionic modes at the T-junction, see the Appendix for a calculation

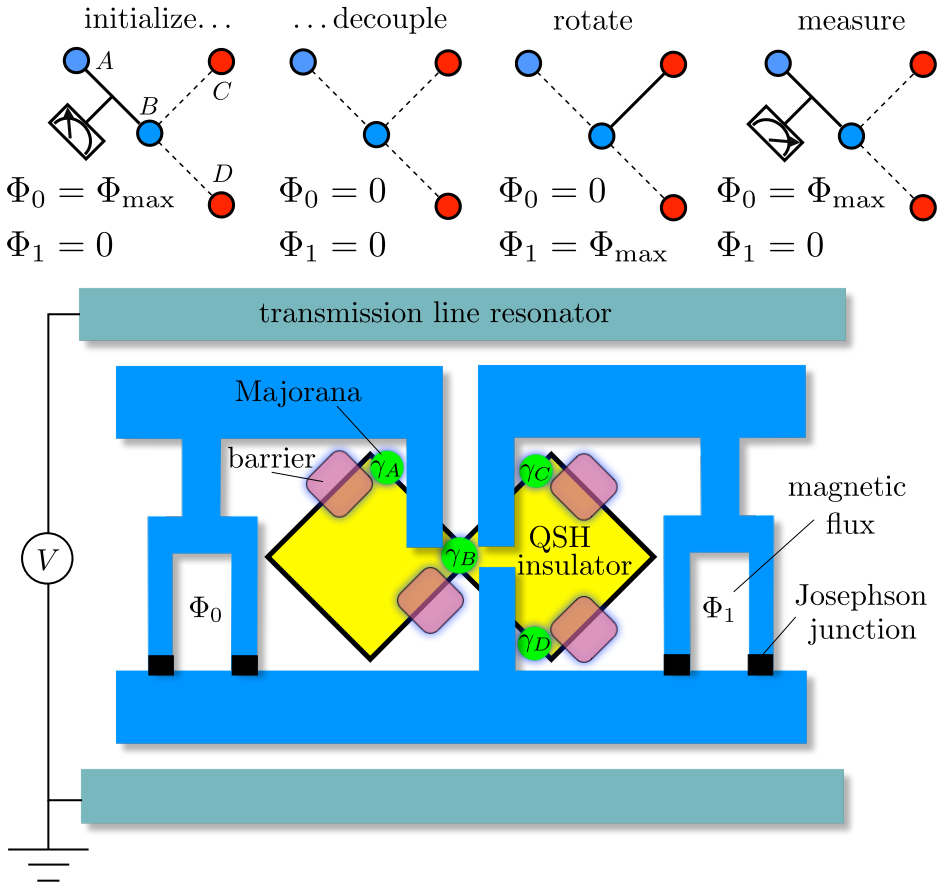


Figure 6.3: *Top-transmon* circuit to rotate the qubit formed out of four Majorana zero-modes at the edge of a quantum spin-Hall insulator. One of the Majoranas (γ_B) is shared by three superconductors at a constriction. The topological qubit is rotated by coupling it to a Cooper pair box in a transmission line resonator (*transmon*). The coupling strength is controlled by the magnetic flux Φ through a pair of split Josephson junctions. The diagrams at the top indicate how the Coulomb couplings of pairs of Majoranas are switched on and off: they are *off* (solid line) when $\Phi = 0$ and *on* (dashed line) when $\Phi = \Phi_{\max} \lesssim h/4e$. This single-qubit rotation does not have topological protection, it serves to characterize the coherence times of the Majorana qubit.

that includes these.

Without loss of generality, we will fix the overall parity to be even. The Majorana qubit then has the two states, $|00\rangle$ and $|11\rangle$, in terms of the occupation number of the fermionic modes $c_1^\dagger = \frac{1}{2}(\gamma_A + i\gamma_B)$ and $c_2^\dagger = \frac{1}{2}(\gamma_C + i\gamma_D)$. Pauli matrices that act on the states $\begin{pmatrix} 1 \\ 0 \end{pmatrix} = |00\rangle$ and $\begin{pmatrix} 0 \\ 1 \end{pmatrix} = |11\rangle$ are defined by

$$\tau_x = i\gamma_B\gamma_C, \quad \tau_y = i\gamma_A\gamma_C, \quad \tau_z = i\gamma_A\gamma_B. \quad (6.7)$$

With the resonator mode and the charge qubit in their ground state, the Majorana qubit has Hamiltonian

$$H_M = \Delta_z(\Phi_0)\tau_z + \Delta_x(\Phi_1)\tau_x, \quad (6.8)$$

with $\Delta_z = \Delta_-^{(1)} - \Delta_+^{(1)}$ and $\Delta_x = \Delta_-^{(2)} - \Delta_+^{(2)}$. Each of the two couplings $\Delta_x(\Phi)$ and $\Delta_z(\Phi)$ can be varied between Δ_{\min} and Δ_{\max} , by variation of the flux between $\Phi_{\min} \approx 0$ and $\Phi_{\max} \lesssim h/4e$. This circuit does not allow to implement braiding (not enough adjustable couplings). However, it does allow for a complete characterization of the Majorana qubit.

For starters, one can demonstrate that the four Majoranas constitute a quantum mechanical two-level system, by following these two steps. The first step is the initialization of the qubit in an eigenstate of τ_z , by setting $\Delta_z = \Delta_{\max}$, $\Delta_x = \Delta_{\min}$ and waiting for the system to relax to its ground state; or alternatively, one can perform a projective measurement onto a τ_z eigenstate via microwave irradiation of the transmon qubit [61]. Once the qubit is initialized, the second step is to set $\Delta_x = \Delta_{\max}$. The qubit will then start to rotate around the x -axis of the Bloch sphere at a frequency Δ_{\max}/\hbar . This Rabi oscillation can be detected via a shift in the resonant frequency of the microwave transmission line.

Since the Hamiltonian (6.8) is that of a fully controllable qubit, and since we are allowed to measure τ_z , all usual qubit tests can be performed. In particular, the coherence times T_1 and T_2 can be measured. The switching time T_1 will likely be dominated by quasiparticle poisoning when all Coulomb couplings are *off* ($\Delta_x = \Delta_z = \Delta_{\min}$). The intrinsic coherence time T_2 is usually measured via a Ramsey fringe experiment, applying two $\pi/2$ rotations around the x -axis separated by a time delay δt , while keeping Δ_z *on* so that the two qubit states are separated in energy. In the time interval between the $\pi/2$ pulses, the qubit rotates freely around the z -axis. A measurement of τ_z after the second pulse should result in decaying oscillations as a function of δt , allowing to determine T_2 . In principle, such measurements can also be used to determine Δ_{\min} and Δ_{\max} through the period of the Ramsey fringes.

6.3 Characteristic energy scales

The characteristic energy scales of the two charge qubits are the magnetic flux dependent Josephson energy $E_J(\Phi)$ and the charging energy E_C , which give a plasma

frequency $\hbar\Omega_0 \simeq (8E_J E_C)^{1/2}$. The Josephson and charging energies may or may not be the same on the two islands, that does not matter for the operation of the circuit.

For the sake of generality we allow for an asymmetry d in the arms of the split Josephson junction, leading to a flux-dependence [37]

$$E_J(\Phi) = E_J^{(0)} \cos(e\Phi/\hbar) \sqrt{1 + d^2 \tan^2(e\Phi/\hbar)}. \quad (6.9)$$

Typical values of d are in the 10% range. Hence, for $\Phi_{\max} \simeq h/4e$ one obtains $E_J(\Phi_{\max}) \simeq 0.1 E_J^{(0)}$. In the transmon regime one has

$$E_C \ll E_J(\Phi_{\max}) \ll E_J^{(0)}. \quad (6.10)$$

For a flux-controlled coupling of the Majorana zero-modes we require that the inter-island tunnel coupling E_M (across the constriction in Fig. 6.3) and the intra-island Coulomb coupling satisfy [84]

$$\Delta_{\max}, \Delta_+(\Phi_{\max}) \ll E_M \ll E_J(\Phi_{\max}) \ll E_J^{(0)}. \quad (6.11)$$

The inequalities involving E_M should not be interpreted too strictly, in particular since we do not require E_M to be under accurate experimental control. In the Appendix we show that E_M can vary in a large energy window without compromising the functionality of the device.

The inequalities can be satisfied for $E_J^{(0)} \simeq 300$ GHz, $E_C \simeq 5$ GHz, $E_M \simeq 5$ GHz and a split junction asymmetry of $d \simeq 0.1$, such that $E_J(\Phi_{\max}) \simeq 30$ GHz. Numerical calculation of the energy spectrum for this set of parameters, see Fig. 6.6, yields $\Delta_{\max} \simeq 120$ MHz, $\Delta_+(\Phi_{\max}) \simeq 0.85$ GHz, and $\Omega_0(\Phi_{\max}) \simeq 27.5$ GHz, for induced charges close to zero.

Let us now turn to the parameters of the microwave cavity. The dispersive regime requires $g \ll (\Omega_0 \pm 2\Delta_+ - \omega_0)$. Furthermore, g should be strong enough that the dispersive frequency shift from Eq. (6.5) is large compared to the resonance width κ ,

$$\kappa \ll \omega_{\text{shift}} = \frac{4g^2 \Delta_+(\Phi_{\max})}{|\Omega_0(\Phi_{\max}) - \omega_0|^2 - 4\Delta_+^2}. \quad (6.12)$$

Both conditions can be satisfied for $\omega_0 \simeq 25$ GHz, $g \simeq 100$ MHz, $\kappa \simeq 1$ MHz, yielding in particular $\omega_{\text{shift}} \simeq 10$ MHz. (We have set $\hbar \equiv 1$.)

The operating temperature should be low enough that excitation of the circuit can be avoided,

$$k_B T \ll E_M, \hbar\Omega_0, \Delta_{\text{gap}}, \quad (6.13)$$

where Δ_{gap} is the excitation gap induced at the quantum spin Hall edge by the superconducting proximity effect. At $T = 10$ mK the thermal energy $k_B T = 1.3$ GHz, so one would need $\Delta_{\text{gap}} \gtrsim 10$ GHz.

In the braiding circuit of Ref. [107] the initialization of the ancillas also requires that $k_B T \ll \Delta_{\max}$, so the Coulomb coupling Δ_{\max} cannot be much smaller than 10 GHz.

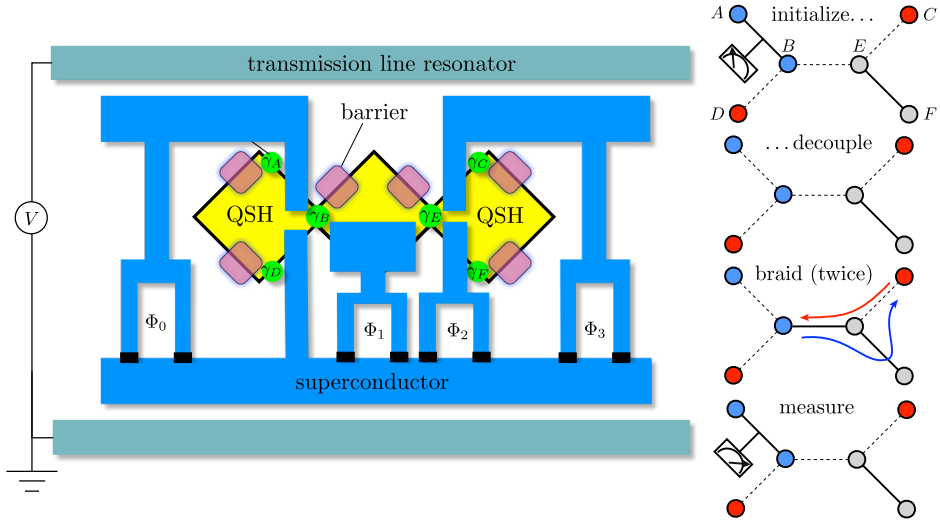


Figure 6.4: Implementation of the braiding circuit of Ref. [107] in a quantum spin-Hall insulator. The two T-junctions are formed by a pair of constrictions. The flux-controlled braiding protocol requires four independently adjustable magnetic fluxes. The Majorana qubit formed out of zero-modes $\gamma_A, \gamma_B, \gamma_C, \gamma_D$ is flipped at the end of the operation, as can be measured via a shift of the resonant microwave frequency. This braiding operation has topological protection.

There is no such requirement for the simpler circuit of Fig. 6.3, because no ancillas are needed for the non-topological rotation of a Majorana qubit. This is one reason, in addition to the smaller number of Majoranas, that we propose this circuit for the first generation of experiments on Majorana qubits.

6.4 Discussion

The key ingredients of the top-transmon [61] are: 1) a charge qubit to couple Majorana zero-modes; 2) a flux-controlled Josephson junction to switch the Coulomb coupling *on* and *off*; 3) a microwave resonator to read out the Majorana qubit. There exist many alternative proposals to operate on Majorana qubits [21, 64, 67, 68, 85, 86, 149, 151, 155–160], including an alternative hybrid design that uses a flux qubit instead of a charge qubit [35, 63, 65, 66, 150, 161, 162].

In addition, there is a great variety of candidate systems that could host the Majoranas. Three stand out as being closest to experimental realization: 1) semiconductor nanowires [45, 46, 74]; 2) chains of magnetic nanoparticles [109, 111]; 3) the quantum spin-Hall edge [42, 115, 116, 154]. All three systems can be integrated with a transmon device, see for example Fig. 6.4 for a circuit that can braid the Majoranas

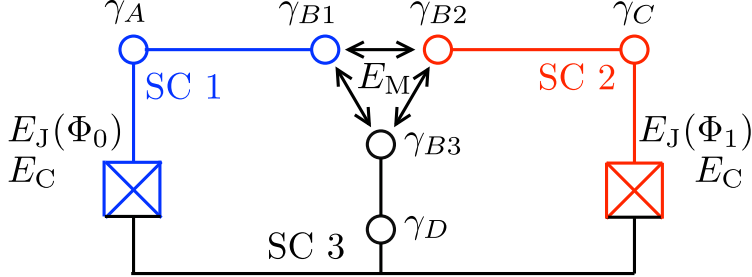


Figure 6.5: Schematic representation of the top-transmon circuit of Fig. 6.3. Colors distinguish different superconducting islands. The three Majoranas coupled by the constriction at the center together produce one zero-mode γ_B .

via a pair of constrictions in a quantum spin-Hall insulator.

The braiding operation is called “topologically protected” because ideally the error is of order $\Delta_{\min}/\Delta_{\max}$ and can be made exponentially small [84]. Larger errors are to be expected in the first generation of experiments, caused by quasiparticle poisoning [124], non-adiabatic effects [72, 119], non-equilibrium noise [121], and coupling of the Majoranas to localized low-energy states induced by disorder [163]. The quasiparticle poisoning time may well remain as the ultimate limiting factor — times $\gtrsim 100$ ms have been reported in Al-Cu devices [164], but the quantum spin-Hall insulator is likely to be less favorable.

In Figs. 6.3 and 6.4 we showed an implementation of the top-transmon circuits at the quantum spin-Hall edge, because of recent experimental developments that suggest this might be a favorable host of Majorana zero-modes [115, 116, 154]. The role of T-junctions [21, 107], which in nanowire networks can be fabricated by allowing nanowires to meet and merge during the growth process [38], is played by constrictions [108], but since a constriction has four legs rather than three, one of the edges has to be closed off by a barrier. This will require breaking of the time-reversal symmetry that prevents backscattering of the helical edge states [43, 44]. The weak-field barriers suggested in Ref. [108] will presumably not be sufficiently resistive to realize the braiding operation. The alternative is to open up a gap at the edge by a ferromagnetic insulator or by an in-plane magnetic field. Ref. [116] found no gap opening in their InAs/GaSb quantum wells for in-plane fields up to 10 T, but this might be strongly dependent on the detailed structure of the quantum wells.

6.A Energy spectrum of the top-transmon

In the main text we have described the top-transmon circuit of Fig. 6.3 via the Hamiltonian (6.6), which captures the essential features of the coupling of the topological Majorana qubit to the non-topological charge qubit. Two simplifying assumptions are

made in this Hamiltonian [84, 107]. Firstly, it is assumed that the superconducting phase on each island is pinned to zero by the large Josephson energy $E_J \gg E_C$, so it does not enter as a dynamical variable. Secondly, the fermionic excited states in the tunnel junction connecting the islands are neglected. In this Appendix we relax both assumptions and calculate the full energy spectrum numerically, following the general procedure of Ref. [107]. For simplicity we do not include the coupling to the microwave cavity.

6.A.1 Full Hamiltonian of the circuit

A schematic representation of the circuit of Fig. 6.3 is given in Fig. 6.5. The circuit is formed by three superconductors, numbered 1 to 3 in Fig. 6.5. Two split Josephson junctions connect the superconductors 1 and 2 to the third one. A further connection between all three superconductors is provided by the quantum spin Hall constriction. We will work in a gauge where all superconducting phases are measured with respect to that of the third superconductor.

The circuit is described by the Hamiltonian

$$H = H_1 + H_2 + H_M, \quad (6.14)$$

where H_1 and H_2 are two copies of a Cooper-pair box Hamiltonian describing superconductors 1 and 2,

$$H_n = E_C(N_n + q_{\text{ind}}^{(n)}/e)^2 - E_J(\Phi_n) \cos(\phi_n - \tilde{\phi}_n). \quad (6.15)$$

The phase and charge operators ϕ_n, N_n of the two superconductors are canonically conjugate variables, with commutator $[\phi_n, N_n] = 2i$. The charge induced capacitively is $q_{\text{ind}}^{(n)}$. The energy $E_C = e^2/2C$ is the charging energy due to the capacitance C to the third superconductor. We have taken the same charging energy for superconductors 1 and 2 and assumed that their mutual capacitance is negligible. The Josephson energies E_J of the two Josephson junctions depend on the flux via Eq. (6.9). The asymmetry d_n in the arms of each split junction introduces a phase offset $\tilde{\phi}_n$ for each island, determined by $\tan \tilde{\phi}_n = d_n \tan(e\Phi_n/\hbar)$.

The term H_M in Eq. (6.14) describes the constriction in the quantum spin Hall (QSH) insulator, where three superconducting islands meet. Each superconductor contributes one of the three Majorana modes γ_{B1} , γ_{B2} , and γ_{B3} . Their tunnel coupling is given by the Hamiltonian

$$H_M = iE_M [\gamma_{B2}\gamma_{B1} \cos(\frac{1}{2}\phi_1 - \frac{1}{2}\phi_2 + \alpha_{12}) + \gamma_{B1}\gamma_{B3} \cos(\frac{1}{2}\phi_1 - \alpha_{13}) + \gamma_{B3}\gamma_{B2} \cos(\frac{1}{2}\phi_2 + \alpha_{23})]. \quad (6.16)$$

We take the same strength E_M for all three couplings, but the flux-induced phase shifts differ: $\alpha_{12} = -e(\Phi_0 + \Phi_1)/2\hbar$, $\alpha_{23} = e\Phi_1/2\hbar$, and $\alpha_{13} = e\Phi_0/2\hbar$. The three eigenvalues of H_M are symmetrically arranged around zero energy, so there is one

flux-independent zero-mode. This is the Majorana mode γ_B of Fig. 6.3. Additionally, there is a fermionic mode at excitation energy $\simeq E_M$.

The other Majorana modes of Fig. 6.3 have no tunnel coupling, so they do not appear explicitly in the Hamiltonian (6.14). They influence the spectrum via a constraint on the number operators [36],

$$i\gamma_A\gamma_{B1} = (-1)^{N_1}, \quad i\gamma_{B2}\gamma_C = (-1)^{N_2}. \quad (6.17)$$

These constraints express the fact that for each island separately the fermion parity (represented on the left-hand-side) equals the number of electrons modulo 2 (represented on the right-hand-side). The product $\gamma_D\gamma_{B3}$ enters only via the global fermion parity of the three superconducting islands, but since this is conserved it does not provide for an independent constraint.

6.A.2 Hamiltonian in the measurement configuration

We wish to extract the parameters Ω_0 and Δ_\pm appearing in Eq. (6.6) from the full Hamiltonian (6.14). In order to do so, it is sufficient to consider the measurement configuration of the circuit, i.e. set $\Phi_1 = 0$ and $\Phi_0 = \Phi_{\max} \simeq h/4e$. The second superconductor then remains in its ground state, and the Hamiltonian reduces to

$$\begin{aligned} H = & E_C(N_1 + q_{\text{ind}}^{(1)}/e)^2 - E_J(\Phi_{\max}) \cos(\phi_1 - \tilde{\phi}_1) \\ & + iE_M [\gamma_{B1}(\gamma_{B3} - \gamma_{B2}) \cos(\frac{1}{2}\phi_1 - \frac{1}{4}\pi) + \gamma_{B3}\gamma_{B2}]. \end{aligned} \quad (6.18)$$

For concreteness, we take even global fermion parity,

$$(i\gamma_A\gamma_{B1})(i\gamma_{B2}i\gamma_{B3})(i\gamma_C\gamma_D) = +1. \quad (6.19)$$

The product $i\gamma_C\gamma_D = \pm 1 \equiv P$ is conserved in the measurement configuration, so it can be treated as a c-number. The other products of Majorana operators can be represented by Pauli matrices ρ_i ,

$$i\gamma_A\gamma_{B1} = P i\gamma_{B3}\gamma_{B2} = P\rho_z, \quad (6.20a)$$

$$i\gamma_{B1}\gamma_{B3} = P i\gamma_A\gamma_{B2} = P\rho_x, \quad (6.20b)$$

$$i\gamma_A\gamma_{B3} = -P i\gamma_{B1}\gamma_{B2} = P\rho_y. \quad (6.20c)$$

Following Ref. [69], we remove the parity constraint (6.17) by a unitary transformation,

$$\tilde{H} = U^\dagger H U, \quad U = \exp \left[\frac{i\phi}{4} (1 - P\rho_z) \right]. \quad (6.21)$$

The transformed Hamiltonian is

$$\begin{aligned} \tilde{H} = & E_C \left[N_1 + \frac{1}{2}(1 - P\rho_z) + q_{\text{ind}}^{(1)}/e \right]^2 \\ & - E_J(\Phi_{\max}) \cos(\phi_1 - \tilde{\phi}_1) + E_M\rho_z \\ & + \frac{1}{2} E_M P (\rho_x + \rho_y) [\cos(\phi_1 - \frac{1}{4}\pi) + \cos(\frac{1}{4}\pi)] \\ & + \frac{1}{2} E_M (\rho_x - \rho_y) [\sin(\phi_1 - \frac{1}{4}\pi) + \sin(\frac{1}{4}\pi)]. \end{aligned} \quad (6.22)$$

Notice that, while H from Eq. (6.18) is 4π -periodic in ϕ_1 , the transformed \tilde{H} has become 2π -periodic. This is why now we can forget about the parity constraint (6.17) and straightforwardly diagonalize the Hamiltonian.

6.A.3 Energy spectrum in the measurement configuration

We numerically diagonalize the Hamiltonian \tilde{H} in the basis of eigenstates of N_1 and ρ_z , truncating the Hilbert space until convergence is reached. To obtain the full spectrum for even global fermion parity, we diagonalize \tilde{H} for both values of $P = \pm 1$ and merge the results. The low-lying part of the spectrum is shown in Fig. 6.6 for the choice of parameters of Sec. 6.3.

From the effective Hamiltonian (6.6), we can identify two good quantum numbers for the low-lying part of the spectrum of \tilde{H} in the measurement configuration: the σ_z eigenvalues $\sigma = \pm 1$ of the charge qubit and the τ_z eigenvalues $\tau = \pm 1$ of the topological qubit. Additionally, there is the occupation number $f = 0, 1$ of the fermionic state in the constriction. These three quantum numbers can be used to label the eight lowest energy states $|\sigma, \tau\rangle |f\rangle$ and their energies $\epsilon_{\sigma, \tau}^f$. The top-transmon parameters Ω_0 , Δ_{\pm} , and Δ_{\max} follow from

$$\Omega_0 = \frac{1}{2}[(\epsilon_{+1,+1}^0 + \epsilon_{+1,-1}^0) - (\epsilon_{-1,-1}^0 + \epsilon_{-1,+1}^0)] \quad (6.23a)$$

$$\Delta_{\pm} = \frac{1}{4}[(\epsilon_{+1,+1}^0 - \epsilon_{+1,-1}^0) \pm (\epsilon_{-1,-1}^0 - \epsilon_{-1,+1}^0)] \quad (6.23b)$$

$$\Delta_{\max} = \Delta_+ - \Delta_- = \frac{1}{2}(\epsilon_{-1,-1}^0 - \epsilon_{-1,+1}^0). \quad (6.23c)$$

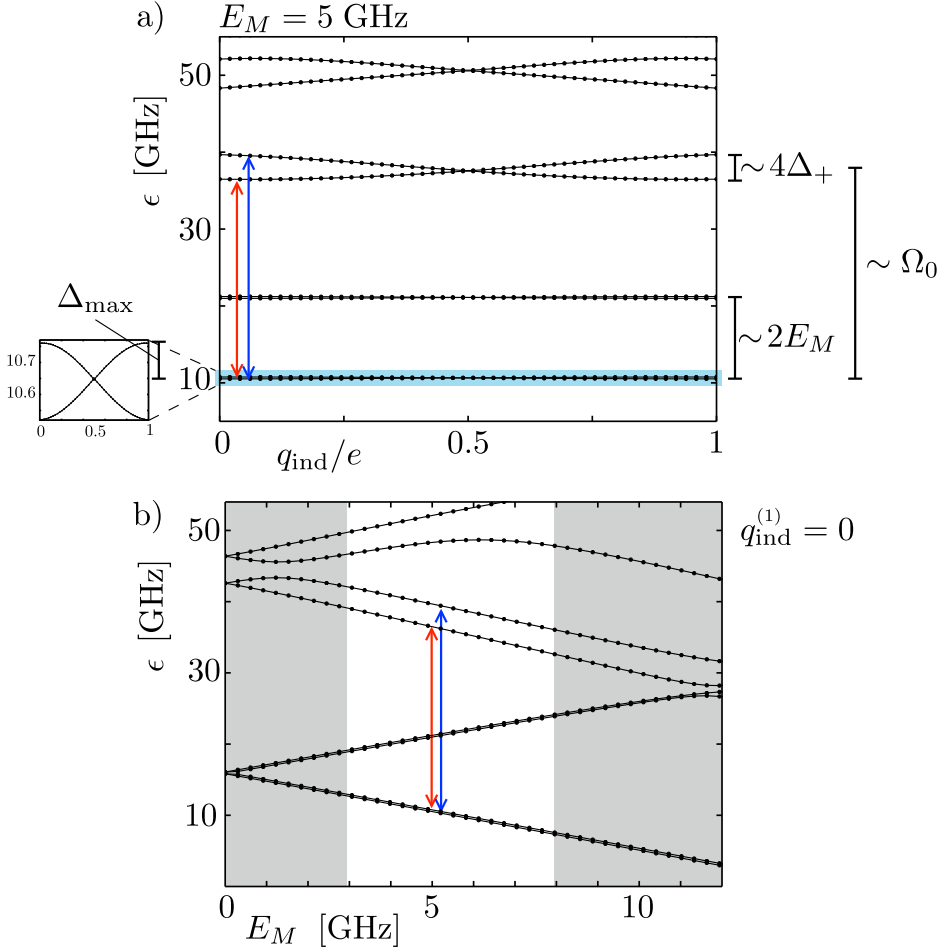


Figure 6.6: Energy spectrum of the top-transmon circuit of Fig. 6.3, obtained from numerical diagonalization of the Hamiltonian (6.22) for $E_J = 300$ GHz, $E_C = 5$ GHz, $\Phi_{\text{max}} = h/4e$. The junction asymmetry was $d = 0.1$, so that $E_J(\Phi_{\text{max}}) \simeq 30$ GHz. In panel (a), the lowest eight energy levels for $E_M = 5$ GHz are shown as a function of the induced charge $q_{\text{ind}}^{(1)}$. They correspond to the eight eigenstates $|\sigma, \tau\rangle |f\rangle$, where $\sigma = \pm 1$ labels the excited/ground state of the charge qubit, $\tau = \pm 1$ labels the even/odd parity state of the topological qubit, and $f = 0, 1$ the occupation number of the fermionic state in the constriction. As indicated by the colored arrows, the ground and excited state of the charge qubit are separated by an energy $\Omega_0 \pm 2\Delta_+ \simeq (27.5) \pm (1.7)$ GHz, depending on the state of the topological qubit. The inset shows the weak charge dispersion of the ground state doublet ($\Delta_{\text{max}} \simeq 120$ MHz). In panel (b), the same energy levels are shown as a function of the tunnel coupling E_M for a fixed value of $q_{\text{ind}}^{(1)} = 0$. For a proper operation of the circuit it is required that the states $f = 1$ with an excited fermionic mode are well separated from both ground and excited states of the charge qubit. We have highlighted between grey panels a large energy window 3 GHz $\lesssim E_M \lesssim 8$ GHz where this requirement is met.

Chapter 7

Realization of microwave quantum circuits using hybrid superconducting-semiconducting nanowire Josephson elements

In superconducting electronic circuits, macroscopic degrees of freedom like currents and voltages can exhibit quantum mechanical behavior. These circuits can be designed to behave as artificial atoms, having a discrete set of energy levels which can be driven coherently [30]. In the field of circuit quantum electrodynamics (cQED), these artificial atoms are coupled to resonators to perform microwave quantum optics in the solid state [165, 166]. Over the last decade, cQED has also grown into a promising platform for quantum information processing, wherein the ground and first-excited levels of each atom serve as an effective qubit [31]. To date, implementations of superconducting quantum circuits have relied almost exclusively on aluminum/aluminum-oxide/aluminum (Al/AlO_x/Al) tunnel junctions as the source of non-linearity without dissipation. However, many exciting applications require magnetic fields (~ 0.5 T) at which superconductivity in aluminum is destroyed, calling for an alternative approach to realizing microwave artificial atoms.

Recent advances in materials development and nanowire (NW) growth have enabled the development of superconductor-semiconductor (super-semi) structures supporting coherent charge transport without dissipation [167], and providing signatures of Majorana bound states citemourik2012. To date, super-semi-super Josephson elements (JEs) have been studied exclusively in quasi-DC transport [168–171]. Building microwave circuits operating in the quantum regime, in which transition energies between levels exceed the thermal energy, offers new ways to investigate the physics of hybrid super-semi structures using spectroscopy [150, 151, 155].

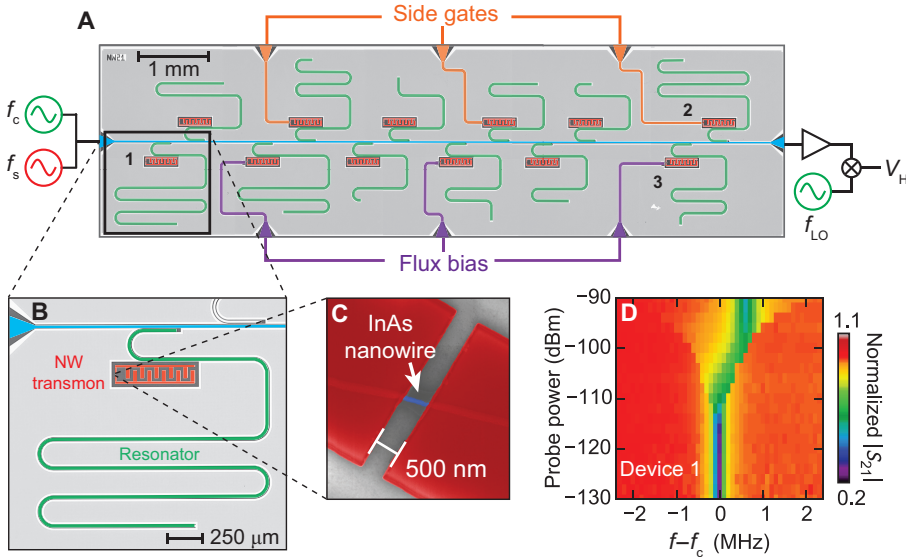


Figure 7.1: Hybrid Josephson elements in cQED. (A) Overview of cQED chip allowing control and readout of NW circuits using dedicated resonators (green) coupled to a common feedline (blue). For readout, a microwave tone with frequency f_c is applied near the fundamental of the resonator coupling to the NW circuit under study. The signal is amplified and down-converted to 1 MHz using a local oscillator at f_{LO} for subsequent digitization and processing. Additional controls on a subset of devices include side gates (orange) for electrostatic tuning of carrier density in the NW of single-junction devices, and short-circuited transmission lines (purple) for threading flux through the loops of split-junction devices. (B) Optical zoom-in of Device 1, containing a single-junction NW circuit (red). (C) Scanning electron microscope (SEM) image of an InAs NW (blue) contacted by NbTiN electrodes (red) separated by 500 nm. (D) Normalized feedline transmission as a function of readout power. The resonator shifts from $f_c = 3.9464$ GHz at single-photon level to $f_{bare} = 3.9470$ GHz above 10^5 photons. This shift confirms the coupling of the resonator to a non-linear circuit..

7.1 Description of the experimental setup

We report the realization of super-semi microwave circuits in cQED. Our chip (Fig. 7.1A) contains multiple capacitively shunted single and double NW JEs coupled to dedicated transmission-line resonators for control and readout using a common feedline (Fig. 7.1B). The chip contains side gates for electrostatic tuning of some single-junction devices and current-bias lines for threading flux through the loops of split-junction devices. We created each JE by deterministically placing an InAs NW between the leads

of a pre-patterned NbTiN interdigitated capacitor (IDC) and contacting the NW to each lead in a subsequent NbTiN deposition. The charging energy $E_C \approx h \times 300$ MHz of the devices is chosen much smaller than the estimated Josephson coupling energy E_J of the NW junction, as in conventional transmon devices [37], leading to a weakly anharmonic energy spectrum (energies E_i) of circuit plasma modes. We first verify the presence of the non-linear NW circuit by measuring the feedline transmission near the fundamental frequency of the coupled resonator (Fig. 7.1D). The Jaynes-Cummings interaction leads to different resonator frequencies f_c and f_{bare} at single- and many-photon probe levels, respectively [172, 173]. We then search for the qubit transition frequency f_{01} of the NW circuit by monitoring feedline transmission at f_c while sweeping a second tone [60] near the estimated frequency $f_{\text{bare}} + (f_{\text{bare}} - f_c)/g^2$, where g is the coupling strength between NW circuit and resonator.

7.2 Spectroscopy of single-junction devices

We first investigate the electric-field effect on the NW-circuit spectrum (Fig. 7.2A). Device 2 has one NW junction (measured length $L \approx 550$ nm) and a proximal side-gate electrode for tuning the carrier density in the NW. We observe fully reproducible fluctuations (see Appendix 7.B) in f_{01} as a function of the side-gate voltage V_g , indicating diffusive charge transport in the NW. Using the plasma-oscillation relation [37], $E_J \approx f_{01}^2/8E_C$, we determine the root-mean-square Josephson-energy fluctuation $\sqrt{\langle \delta^2 E_J \rangle}/h \approx 2$ GHz in the $V_g = 0 - 10$ V range. Matching this scale to the Thouless energy [174], $E_{\text{Th}} = \hbar D/L^2$, and assuming highly transparent contacts [170], we estimate the diffusion constant $D \approx 40$ cm²/s. This value is typical for InAs wires [168].

Side-gate tuning of the NW junction offers a new means to control the spectrum of transmons. Decreasing V_g brings f_{01} into resonance with the resonator, revealing multiple avoided crossings (Fig. 7.2B). The minimum splitting indicates $g/2\pi = 34 \pm 1$ MHz (Fig. 7.2C). We note that while we only perform quasistatic field-effect tuning of f_{01} throughout this experiment, nanosecond control should be possible by increasing the bandwidth of off-chip filtering.

We now discuss the impact of charge fluctuations on the observed linewidth of the f_{01} transition, which is of interest for qubit applications. Transmon qubits are by design insensitive to charge offset fluctuations on the superconducting islands [37], owing to the exponential suppression of charge dispersion when $E_J \gg E_C$. Field-effect control of the Josephson coupling can make f_{01} sensitive to nearby fluctuating charges. One may expect a region with $\partial f_{01}/\partial V_g = 0$ to constitute a charge sweet-spot [175] and thus to correlate with a linewidth reduction. However, we do not observe a correlation between the linewidth $\gamma/2\pi > 10$ MHz and $|\partial f_{01}/\partial V_g|$, suggesting a different dominant decoherence channel (see Appendix 7.B). We surmise a connection between this broad linewidth and the soft gap induced in NWs contacted by NbTiN using similar fabrication techniques [74]. Parallel experiments by the Copenhagen group achieve hard induced gaps in epitaxial Al-InAs NWs [176] and $\sim 1 \mu\text{s}$ coherence

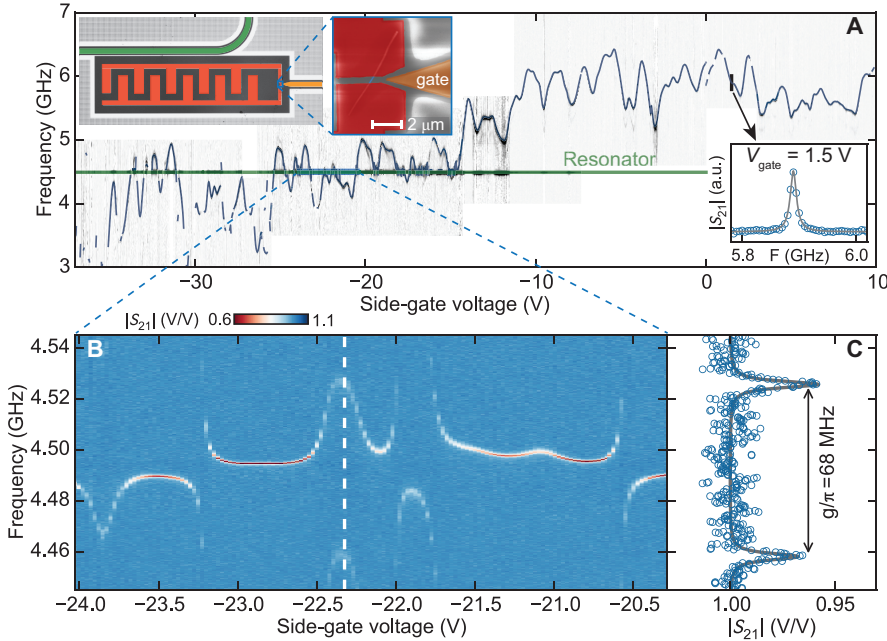


Figure 7.2: Side-gate tuning of a NW circuit and mesoscopic Josephson coupling fluctuations. (A) Left inset; false-colored optical image of Device 2. Right inset; SEM micrograph showing the single NW junction and the proximal side gate (orange) for voltage control. Sweeping this voltage induces reproducible fluctuations in the qubit transition frequency f_{01} . Lower inset; example spectroscopy of the qubit transition, showing an inhomogeneously broadened linewidth $\gamma/2\pi = 13.2 \pm 0.3$ MHz. A downward trend in f_{01} is observed as V_g decreases. At $V_g < -15$ V, f_{01} fluctuates around the resonator fundamental (green line). (B) A zoom-in around $V_g = -22$ V shows multiple avoided crossings. (C) At $V_g = -22.3$ V, the NW circuit fully hybridizes with the resonator. From the minimum splitting, we extract the NW circuit-resonator coupling strength $g/2\pi = 34 \pm 1$ MHz.

times in a single-JE hybrid transmon [177].

7.3 Spectroscopy of a double-junction device

Next, we consider a split-junction device where the two parallel JEs (each with $L = 150$ nm) are created from one 5 μm long NW (Fig. 7.3A). As in conventional transmons, f_{01} first decreases as flux Φ is threaded through the loop. However, near $\Phi \sim \Phi_0/2$ ($\Phi_0 = h/e$ is the flux quantum), a clear departure from transmon-like

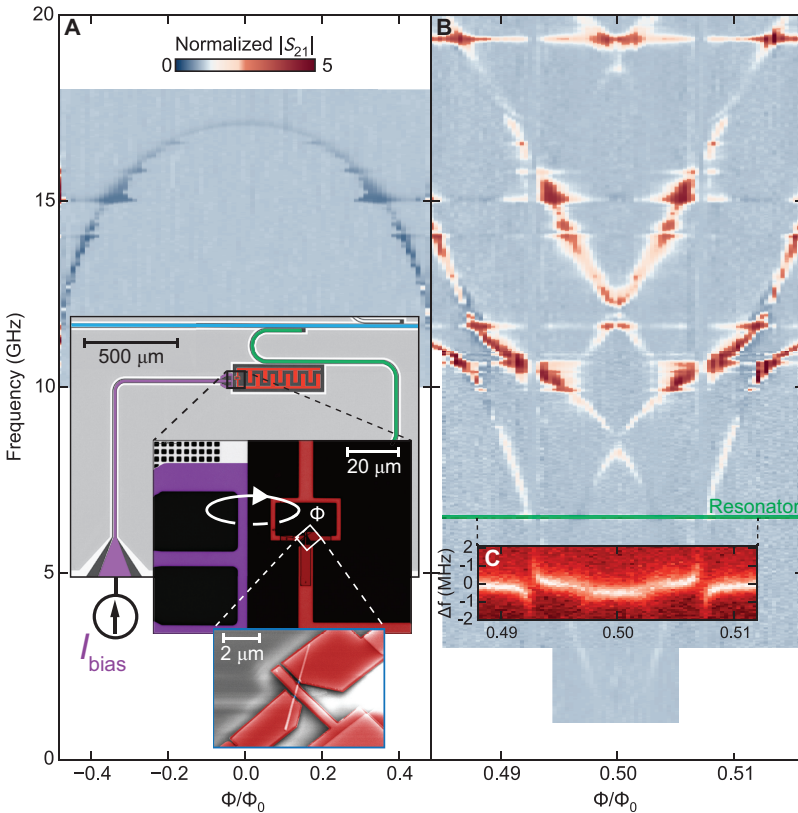


Figure 7.3: Flux bias spectroscopy of a split-junction NW circuit. (A) Inset: false-colored optical image showing Device 3 (red), its resonator (green), and flux-bias line (purple). Bottom inset: SEM micrograph of the two JEs made from one NW. Flux-bias spectroscopy shows the tuning of f_{01} with Φ . (B) A high-resolution sweep around $\Phi = \Phi_0/2$ shows a strong flux dependence of the NW circuit transitions. (C) Measurement of resonator transmission around f_c with same horizontal range as in (B). The avoided crossing of the lowest transition with the resonator reveals a much reduced coupling strength.

behavior is observed (Fig. 7.3B). Multiple strongly flux-dependent transitions and a new, strong avoided crossing appear symmetrically about $\Phi_0/2$. In addition, the avoided crossing between the lowest transition and the resonator is strongly reduced

(Fig. 7.3c) compared to that of Device 2 ¹.

The observed deviation from the conventional transmon energy spectrum provides a signature of non-sinusoidal current-phase relations (CPRs) in the NW junctions [178]. We now show that the observed spectrum can be fully explained by the Hamiltonian of a Cooper-pair box (CPB): $H = 4E_C\hat{N} + V_1(\hat{\delta}) + V_2(2\pi\Phi/\Phi_0 - \hat{\delta})$, provided its split junctions do not follow a cosine-shaped Josephson potential (Fig. 7.4A). Here, the operators \hat{N} and $\hat{\delta}$ represent the charge imbalance between islands and the phase difference across NW junction 1, respectively. The Josephson potential $V_i(\varphi_i)$ of junction i is linked to its CPR by $I_i(\varphi_i) = (2\pi/\Phi_0)\partial V_i/\partial \varphi_i$, where $\varphi_1 \equiv \hat{\delta}$ and $\varphi_2 \equiv 2\pi\Phi/\Phi_0 - \hat{\delta}$. Crucially, we require V_i to be 2π -periodic but not necessarily cosine shaped. Using a simple phenomenological model [174] of the form $V_i(\varphi_i) = -K_i\sqrt{1 - T_i \sin^2(\varphi_i/2)}$ and performing a non-linear least-squares fit with five free parameters, we obtain a quantitative match to all spectral data (best-fit values are $E_C/h = 279 \pm 1$ MHz, $K_1/h = 376 \pm 13$ GHz, $K_2/h = 233 \pm 2$ GHz, $T_1 = 0.86 \pm 0.02$, and $T_2 = 0.885 \pm 0.004$, see also Appendix 7.D). As shown in Fig. 7.4A, the corresponding CPRs are evidently skewed. A three-parameter fit using V_i corresponding to the CPR of a short, diffusive point contact in the many-channel limit [178, 179] showed only slightly worse agreement, as did a truncated Fourier series expansion of V_i . All approaches produce similar skewed CPRs (see Appendix 7.D).

Interestingly, this device can be operated in two distinct regimes by tuning Φ . Near $\Phi = 0$, it operates like a transmon, whose eigenstates are plasma modes with a weakly anharmonic spectrum. Around $\Phi \simeq \Phi_0/2$, it operates like a flux qubit [180] whose two lowest energy levels carry opposite persistent currents $I_{p,i} = \partial E_i / \partial \Phi$, which we estimate to be of order ± 100 nA (see Appendix 7.E). The possibility to drive transitions between these distinct persistent-current states using coherent microwaves constitutes a manifestation of macroscopic quantum coherence [181] in our NW circuits.

In conclusion, we have realized the first hybrid microwave circuits made from super-semi NW JEs and characterized them using spectroscopy. NW circuits offer several advantages over traditional aluminum circuits. First, tuning qubit transitions using the field effect in single NW JE devices offers an attractive alternative to flux biasing of split-junction Al devices. Second, these NW circuits are made exclusively from magnetic-field compatible materials. Magnetic-field compatible super-semi NW microwave circuits have the potential to open new avenues of research. In particular, very pure solid-state electron spin ensembles (e.g., nitrogen impurities in diamond or phosphorous donors in silicon) could be field-polarized to make coherent quantum memories [182, 183] for hybrid quantum processors. In addition, the microwave circuits realized here may be useful to control and readout Majorana bound states [21, 107] in proposed demonstrations of non-Abelian exchange statistics [6, 11, 14, 27]. Immediate next experiments will therefore focus on the study of these circuits in up

¹Moreover, several flux-independent lines appear. We can attribute many of these to the fundamentals and higher harmonics of other resonators on the chip (they are also observed when we studied other devices on this chip) and are not considered henceforth.

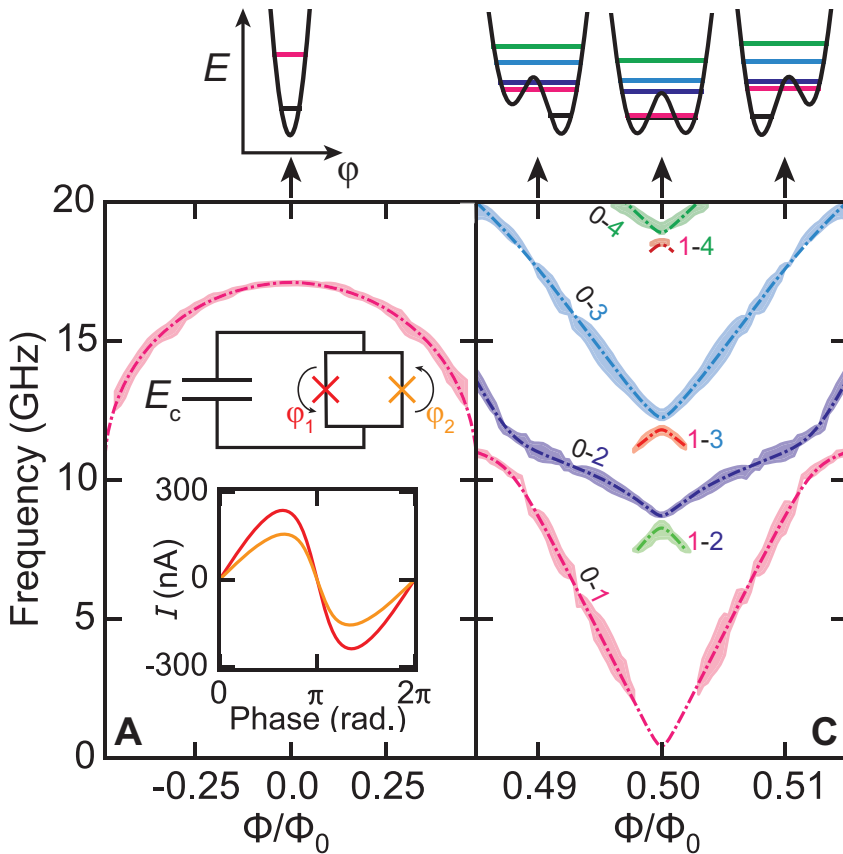


Figure 7.4: Fitting theory to the spectrum of the split-junction NW circuit. (A) Top inset; equivalent circuit of the device, a split Cooper-pair box containing a loop interrupted by two NW JEs (phase differences $\varphi_{1,2}$), threaded by an externally applied flux Φ , and shunted by a capacitance, giving total charging energy E_C . Around $\Phi = 0$, the Josephson potential has a single minimum, producing a weakly anharmonic spectrum. (B) The non-sinusoidal current-phase relation of the NW JEs determines the particular flux-dependence of the transition frequencies around $\Phi = \Phi_0/2$ as the Josephson potential develops a symmetric double-well profile that tilts as Φ is tuned away from $\Phi_0/2$. All curves are the result of a least-squares non-linear fit of the theoretical model described in the text. We identify four fundamental transitions from the ground state and three transitions from the first-excited state.

to ~ 0.5 T in-plane magnetic fields.

7.A Materials and Methods

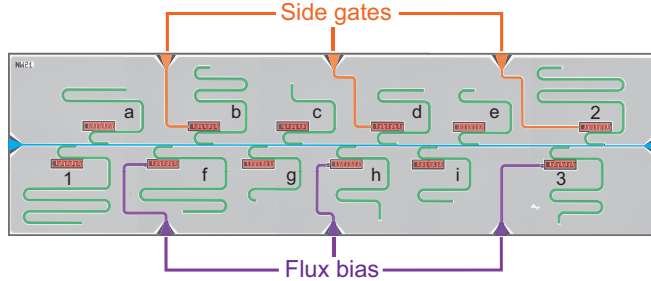


Figure 7.5: Overview of the chip.

Device	R_{RT} (k Ω)	L (nm)	f_c (GHz)	f_{01} (GHz)	Description
1	5.7	500	4	6.7	single
2	6.2	500	4.5	6.2 ($V_g = 0$ V)	single, with gate
3	2.2	200	6.5	17 (max)	split, with flux control
a	3.03	200	7	not < 20	single
b	3.07	200	6	13.6	single, with gate
c	short	50	11	-	single
d	open	100	8.5	-	single, with gate
e	short	50	10	-	single
f	3.5	500	5	9.1 (max)	split, with flux control
g	short	50	10.5	-	single
h	1.4	100	8	not < 20	split, with flux control
i	2.6	100	9	not < 20	single

Table 7.1: Overview of devices on the chip. R_{RT} is the two-terminal resistance probed close to the junction at room temperature. L indicates the design length.. The first three devices in the table are those discussed in the main text, in Figures 7.1, 7.2, and 7.3 respectively.

The chip was fabricated on a sapphire substrate (single-side polished, C-plane cut, 430 μm thickness). After cleaning the substrate in buffered HF, a NbTiN film (80 nm thickness) was sputtered. Ground planes, resonators and IDCs were defined by negative tone electron-beam lithography and reactive ion etching.

In the next step, InAs NWs of typical length 5 – 10 μm and radius 50 – 100 nm were controllably deposited using a micro-manipulator setup equipped with an optical

microscope. Detailed structural and DC transport characterization of the InAs NWs used in this experiment have been published in earlier reports [184].

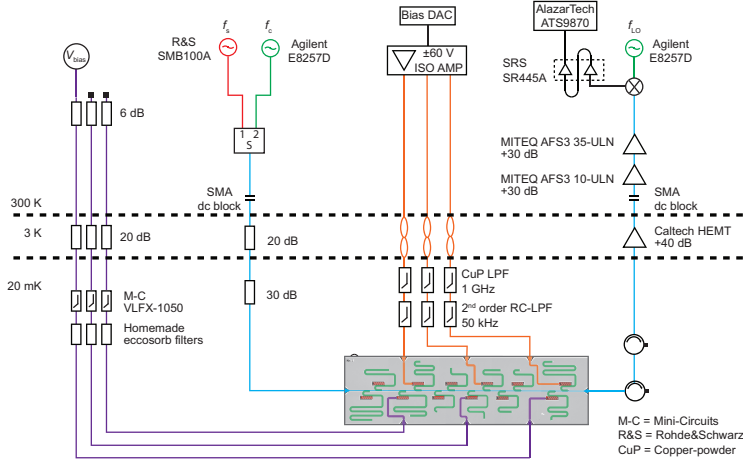


Figure 7.6: Wiring schematic of the experimental setup outside and inside the ^3He - ^4He dilution refrigerator (Leiden Cryogenics CF-650). Readout (green) and spectroscopic (red) microwave drives are combined in a single coax line (blue) at room temperature. The line is attenuated at the 3 K and 20 mK stages before connecting to the chip feedline. The feedline output is isolated from the higher temperature stages by two circulators. The signal is amplified at the 3 K stage by a HEMT amplifier (Caltech Cryo1-12, 0.06 dB noise figure) and at room temperature by two Miteq amplifiers. The signal is down-converted to 1 MHz, further amplified, digitized and saved for processing. The setup contains wiring for gate (orange) and flux (purple) control on a subset of devices. Both types of control line are low-pass filtered.

The fine patterns were designed based on optical alignment to the NWs. The semiconductor-superconductor interface area was maximized by covering the NW as much as possible. The overlap between the coarse and the fine superconducting structures in each IDC was designed to be several tens of μm^2 . After defining the fine pattern by positive tone electron-beam lithography, the semiconductor surface was cleaned in buffered HF for 20 s and then a 100 nm thick NbTiN film was sputtered in order to overlay the coarse structures as well.

In total, twelve devices were fabricated on the chip (Fig. 7.5), and each was coupled to a coplanar waveguide quarter-wave resonator with a distinct fundamental frequency in the range 4 to 11 GHz. Table 7.1 gives an overview of all the devices on the chip. Gate voltages in the range ± 40 V were applied through on-chip $50\ \Omega$ transmission lines with open ends proximal to the NW. Off-chip, the lines are filtered by a second-order RC filter and a copper-powder (CuP) filter mounted to the mixing chamber plate of the refrigerator (Fig. 7.1). The two filters have ~ 50 kHz and

~ 1 GHz cutoff frequencies, respectively. The JEs of split-junction devices were embedded in a superconducting loop of area $13 \times 24 \mu\text{m}^2$. Flux through the loop is controlled using on-chip 50Ω transmission lines, with short-circuited termination proximal to the loop. Off-chip, the lines are low-pass filtered with nominal 1 GHz cutoff frequency.

7.B Additional data for Device 2

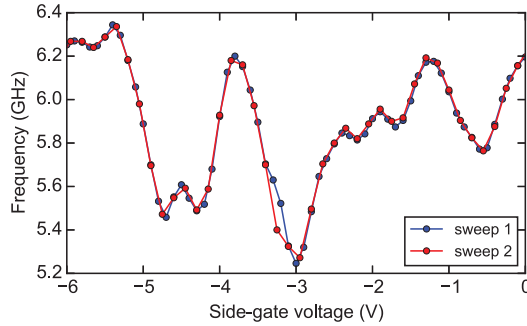


Figure 7.7: Reproducibility of the f_{01} fluctuations. Two sweeps of two-tone spectroscopy show the reproducibility of the f_{01} fluctuations. These sweeps were separated by two days.

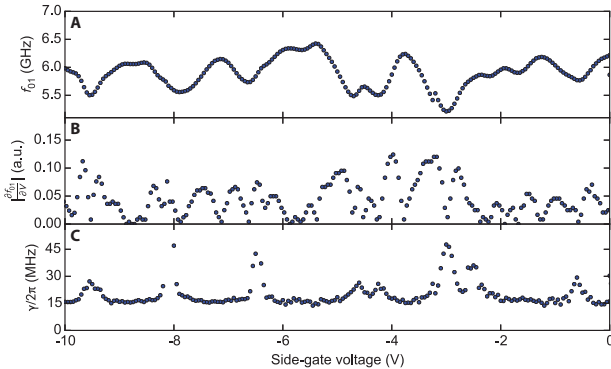


Figure 7.8: Absence of correlation between f_{01} field-effect sensitivity and linewidth γ . (A) Qubit transition frequency f_{01} as a function of V_g , extracted from Fig. 7.2. (B) Computed field-effect sensitivity $|\partial f_{01} / \partial V_g|$. (C) Extracted γ . Vanishing $|\partial f_{01} / \partial V_g|$ does not correlate with a reduction in γ .

7.C Data extraction from flux-bias spectroscopy

In order to perform fits to the observed spectroscopy lines, we have extracted a set of data points with error bars from the raw data, consisting of a 2D scan of feedline transmission measured as a function of frequency f and voltage V_{bias} applied to the 50Ω bias line. We used the following procedure to extract the points ².

1. We applied a Gaussian filter to suppress noise fluctuations, and subtracted the residual background signal.
2. We converted V_{bias} into flux Φ through the loop, assuming a linear relation $\Phi = AV_{\text{bias}} + B$.
3. We identified isolated features in the raw data by removing all points below a transmission threshold. Every isolated feature consisted of a connected set of data points surrounding peaks of high transmission in the f - Φ plane.
4. Within every feature, we extract a single data point for each voltage value. The frequency f and uncertainty Δf of every point was computed by taking the average frequency of all points in the same feature with the same V , weighted by their transmission amplitude. This procedure provided a collection of data points $(\Phi, f, \Delta f)$. The points were manually divided into groups forming continuous $f(\Phi)$ transition lines.

7.D Theoretical model and fits for Device 3

Many features of the observed transitions coincide with those expected for a double-well potential. The first is the linear vanishing of f_{01} at $\Phi = \Phi_0/2$, which is consistent with the small energy difference between the ground and first-excited states in a symmetric double-well potential. The second is the appearance of a strong avoided crossing between the two lowest transitions at $\Phi \simeq 0.49\Phi_0$. The avoided crossing naturally arises in a tilted double-well potential, when the lowest energy state in the shallower well becomes resonant with the first-excited state of the deeper well. The third is the visibility of transitions whose frequency decreases away from $\Phi = \Phi_0/2$, which is consistent with residual thermal population of the first-excited state close to $\Phi_0/2$.

The transition frequencies obtained from the energy levels of the split-junction CPB Hamiltonian,

$$H = 4E_C \hat{N} + V_1(\hat{\delta}) + V_2(2\pi\Phi/\Phi_0 - \hat{\delta}). \quad (7.1)$$

were fit to the extracted data points. The energy levels were computed numerically in the eigenbasis of the charge operator \hat{N} , truncating the Hilbert space to ~ 200 states

²A dynamic IPython Notebook containing the relevant code and illustrating the data extraction process is available online at the page <http://goo.gl/3xfGr8>.

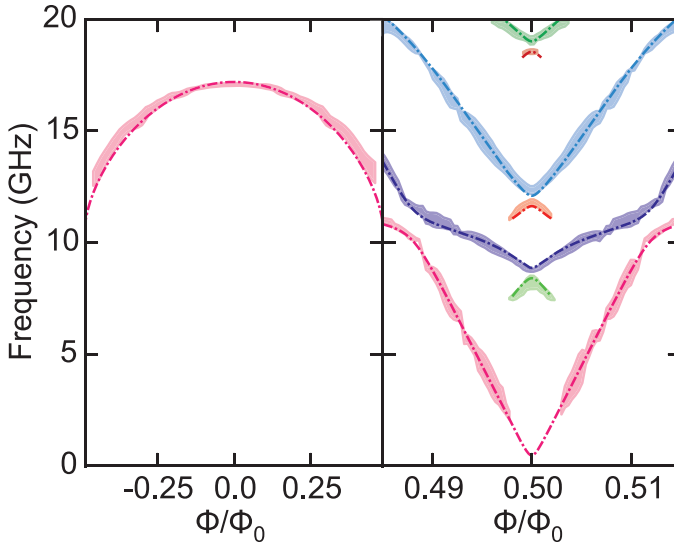


Figure 7.9: Fit to the K-O model. Best-fit values are $E_C/h = 266 \pm 2$ MHz, $K_1/h = 218 \pm 1$ GHz, and $K_2/h = 141 \pm 1$ GHz.

such that convergence was reached. Via a Fourier series expansion of the 2π -periodic functions

$$V_i(\varphi_i) = - \sum_n A_{i,n} \cos(n \varphi_i), \quad (7.2)$$

the Josephson terms in the Hamiltonian can be easily expressed in the same basis using the raising and lowering operators $\hat{N}_\pm = \exp(\pm i \hat{\delta})$,

$$\begin{aligned} V_1(\hat{\delta}) &= - \sum_n A_{1,n} (\hat{N}_+ + \text{h.c.}), \\ V_2(2\pi\Phi/\Phi_0 - \hat{\delta}) &= - \sum_n A_{2,n} (\hat{N}_+ e^{-i2\pi\Phi/\Phi_0} + \text{h.c.}). \end{aligned}$$

Hence, the Fourier series of V_i contains higher harmonics with period $2\pi/n$, with $n > 1$, allowing the total Josephson energy $V_1 + V_2$ to develop several local minima in a 2π interval, thereby forming a double-well potential. This situation is particularly relevant at $\Phi \simeq \Phi_0/2$, where the odd harmonics of V_1 and V_2 subtract. Time-reversal symmetry makes the minima degenerate at $\Phi = \Phi_0/2$ (Fig. 7.4).

Lacking exact knowledge of the CΦR of the junctions, we have tried different phenomenological models for the $V_i(\varphi_i)$:

1. The model presented in the text,

$$V_i(\varphi_i) = -K_i \sqrt{1 - T_i \sin^2(\varphi_i/2)}, \quad (7.3)$$

is strictly valid only for short junctions, with total amplitude $K_i \simeq n_i \Delta_0$, with Δ_0 the induced gap in the NW, resulting from n_i transport channels with a typical transparency T_i . This model leads to a Hamiltonian with five free parameters: E_C , K_1 , K_2 , T_1 , and T_2 . For the fit we took the Fourier series expansion of V_i and truncated to seven harmonics in the numerical diagonalization of the Hamiltonian.

2. The Kulik-Omelyanchuk (K-O) model for the zero-temperature current-phase relation of a diffusive and short point contact [178, 179] gives

$$V_i(\varphi_i) = -2K_i \int_0^{\pi/2} \sqrt{1 - \sin^2(\varphi_i/2) \sin^2 x} \, dx. \quad (7.4)$$

The above relation can be obtained from Eq. (3) by integrating over the probability distribution of transmission coefficients T in a diffusive point contact. This model leads to a Hamiltonian with three free parameters, E_C , K_1 , and K_2 . As before, the Fourier series was truncated to seven harmonics. The best-fit results are shown in Fig. 7.9.

3. We have also performed a direct fit of the Fourier coefficients $A_{i,n}$, increasing the number of coefficients until a good agreement with the data was observed. The fit is more sensitive to the Fourier coefficients of the weak junction, as the asymmetry in junction strength makes the phase difference across the strong junction stay close to zero at any Φ . The best-fit values of the seven-parameter fit are $E_C/h = 275 \pm 1$ MHz, $A_{1,1}/h = 95.5 \pm 0.4$ GHz, $A_{2,1}/h = 68.9 \pm 0.2$ GHz, $A_{2,2}/h = -11.78 \pm 0.06$ GHz, $A_{2,3}/h = 3.28 \pm 0.02$ GHz, $A_{2,4}/h = -0.98 \pm 0.03$ GHz, and $A_{2,5}/h = 0.21 \pm 0.03$ GHz. Including more Fourier coefficients did not improve the agreement with the data, and increased the variance of the best-fit values.

Due to the non-linearity of the fitting model and correlated errors in the extracted data points, it is not straightforward to extract a figure of merit for quantitative comparison of the models. All models require at least one non-sinusoidal CΦR to fully explain all the features of the data set.

Although the data are well fit by non-sinusoidal CΦRs, there are other mechanisms that can produce similar spectra in superconducting circuits. First, the presence of a super-inductance is known to produce a potential landscape with several minima, as for the fluxonium [185]. NbTiN is known for its high kinetic inductance L_k . Indeed, in our circuit we estimate $L_k \approx 0.2$ nH and loop geometric inductance $L_{geo} \approx 30$ pH. The associated total inductive energy $E_L = (\Phi_0/2\pi)^2/L_k \approx h \times 800$ GHz is, however, much larger than $E_J \approx (K_1 T_1 + K_2 T_2)/4 = h \times 132$ GHz and therefore cannot produce multiple minima (fluxonium requires $E_L < E_J$). Second, microwave-induced excitation of Andreev bound states (ABS) confined to the junction can also produce a qualitatively similar spectrum [186]. However, ABS transitions below 2 GHz require almost perfectly transparent transport channels, which has proven

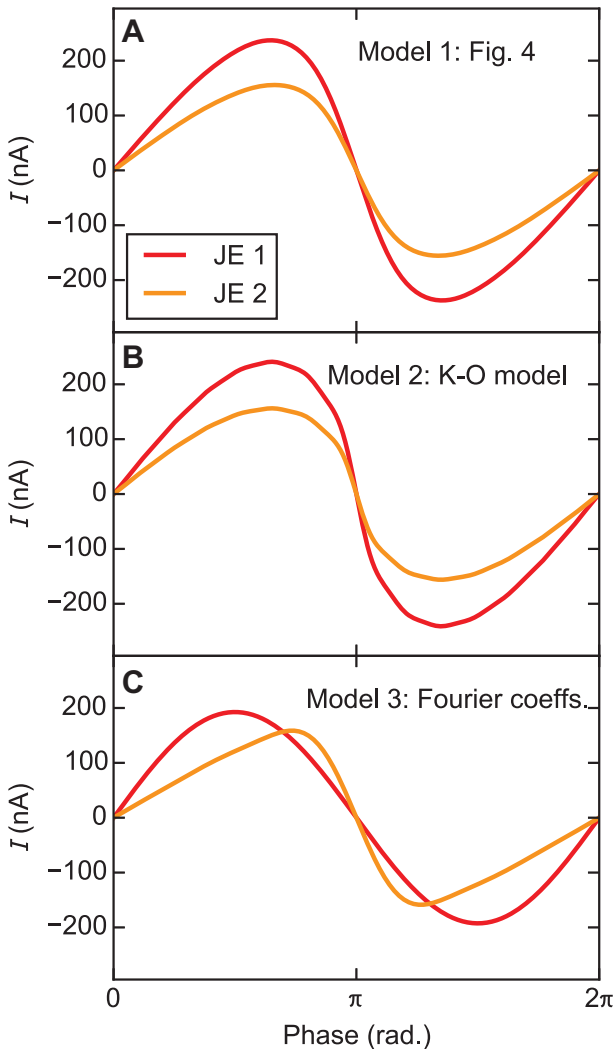


Figure 7.10: CPRs for the three models. (A) Phenomenological model used in the main text. (B) K-O model. (C) Fourier series using one harmonic for JE 1 and five harmonics for JE 2.

challenging in even the most ideal atomic point contacts [186]. We therefore surmise that the JEs remain in their ABS ground state and that the observed spectrum is fully due to plasma modes. The potential to observe ABS transitions provides an exciting prospect for future work.

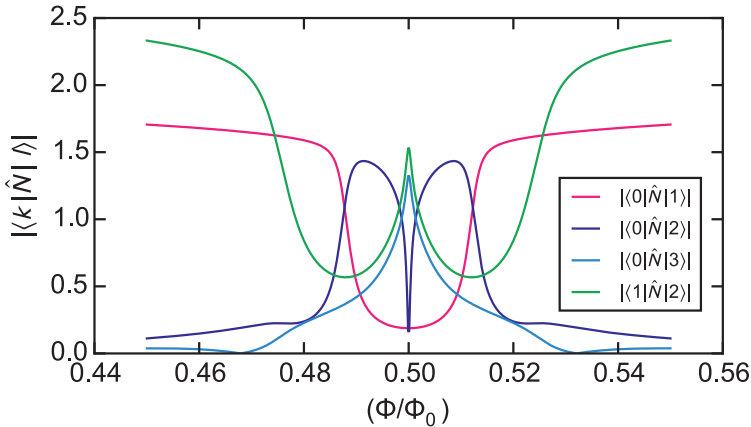


Figure 7.11: Flux-bias dependence of the NW-circuit-resonator coupling matrix elements for Device 3. The absolute matrix element $|\langle k|\hat{N}|l\rangle|$ determines the visibility of the transitions in Fig. 7.3 of the main text. As expected for transmons, only the matrix elements $|\langle k|\hat{N}|k+1\rangle|$ remain strong away from $\Phi = \Phi_0/2$.

7.E Estimation of Device 3 parameters from model

It is possible to estimate interesting properties of Device 3 using the best-fit model values presented in the main text. In particular, we can compute the dipolar couplings of the NW circuit to its resonator. The coupling strength of the dipole-induced transition between two eigenstates $|k\rangle$ and $|l\rangle$ of the split-junction CPB Hamiltonian is proportional to the corresponding matrix element of \hat{N} , $n_{kl} = \langle k|\hat{N}|l\rangle$.

Fig. 7.11 shows the calculated relative couplings $|n_{01}|$, $|n_{02}|$, $|n_{03}|$, and $|n_{12}|$ near $\Phi = \Phi_0/2$. Their flux dependence explains some interesting features of the data, in particular:

1. The vanishing visibility of the $0 \rightarrow 2$ transition at $\Phi = \Phi_0/2$.
2. The strong visibility of the $0 \rightarrow 3$ transition near $\Phi = \Phi_0/2$.
3. The reduction of $|n_{01}|$ near $\Phi_0/2$ (see Fig. 7.3) compared to that of Device 2.

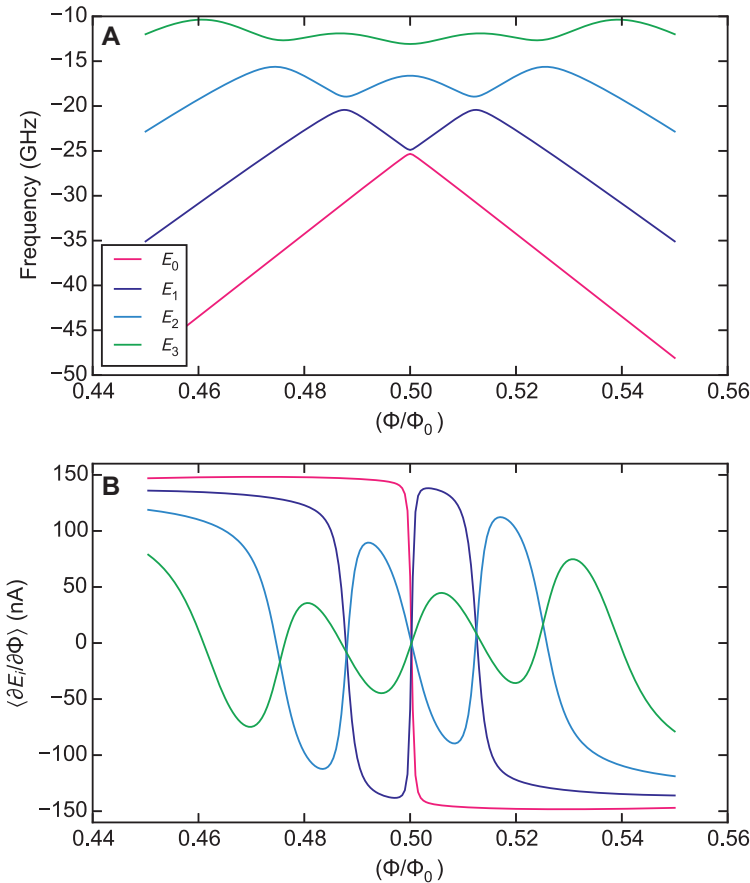


Figure 7.12: Energy levels of the split-junction NW circuit around $\Phi_0/2$. (A) Calculated energy levels for the parameters of Fig. 7.4 of the main text. (B) The states belonging to the lowest energy levels, E_0 and E_1 , carry opposite persistent currents $I_{p,i} = \partial E_i / \partial \Phi$. The two states hybridize at $\Phi = \Phi_0/2$. Driving f_{01} with microwaves induces transitions between these two macroscopically distinct current states.

Chapter 8

Topological blockade and measurement of topological charge

The $5/2$ fractional quantum Hall plateau is expected to be described by the Moore-Read wave function [11] or its particle-hole conjugate Anti-Pfaffian state [187, 188]. This means that every pair of $e/4$ quasiparticles appearing in this phase have an extra neutral degree of freedom, topological charge, which does not affect local measurements and does not influence the energy of the system as long as they are well separated.

Topological charge manifests itself in the peculiar braiding statistics of these quasiparticles [12, 189]: they are non-Abelian anyons and their topological degree of freedom can be manipulated through ordered exchanges of quasiparticles whose result is independent of the path used for braiding. Such stability under local perturbations allows to exploit non-Abelian anyons to store and process quantum information in a way that is highly protected from thermal noise and thus to potentially implement a topological quantum computer [5, 6].

However there is no definite experimental proof that topological charge indeed exists. Even when two quasiparticles are close to each other, there are no clear cut signatures of the topological charge: this extra degree of freedom is completely charge-neutral, and hence very hard to detect. The most actively developed tool predicted to readout the combined state of several non-Abelian anyons, and to prove they possess fractional statistics, is non-Abelian Fabry-Perot interferometry [6, 79–81, 190, 191]. However, the currently existing non-Abelian interference experiments [192–195] are not conclusive. The interferometers are relatively sensitive to dephasing, since the length of the trajectory has to be sufficiently large. Moreover they are described by a rather complicated theory [196] due to the presence of many types of edge excitations [197, 198]. In addition the interferometers are sensitive to all the anyons encircled

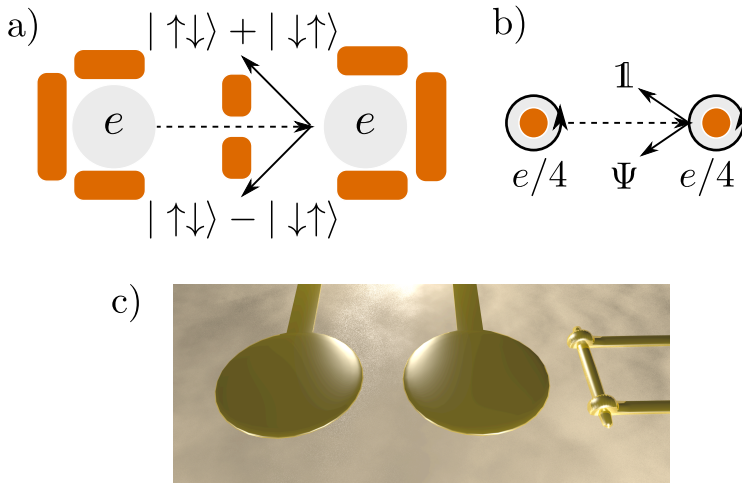


Figure 8.1: Panel (a): two electrons with charge e (grey circles) trapped by several gates (rectangles) form a singlet-triplet qubit. The singlet and triplet states of the qubit acquire different energies when one of the electrons tunnels. Panel (b): a topological qubit is formed by two quasiparticles of the Moore-Read quantum Hall state with charge $e/4$. They are trapped by gates (filled circles). When one of these quasiparticles tunnels to the other, two degenerate wave functions of the qubit corresponding to the vacuum and fermion fusion channels acquire different energies. Panel (c): A sketch of a possible implementation of the topological blockade measurement setup featuring two local gates to form the quantum dots with size ~ 100 nm, and a charge sensor. The voltage applied to each dot is just enough to attract a single quasiparticle.

by the interference loop, some of which may even be coupled to edge states, further obscuring the interpretation of the results [101, 199–202]. Other tools exist designed to probe macroscopic consequences of the existence of topological charge [203–206], however they do not allow to follow the behavior of a single anyonic excitation. Here we propose a setup for measuring the topological charge that does not suffer from these limitations. Our setup is local, so it is only sensitive to the topological charge of two anyons, and it does not rely on using edge states. Instead it is based on the phenomenon of topological blockade, explained below.

We begin our consideration from the simple observation that any inherent property of a particle that may impose an energy penalty, can also prevent its motion. The most commonly known examples are the electric charge, which causes Coulomb blockade, and spin, resulting in spin blockade [207–214]. Less common examples include the position of a particle, causing elastic blockade [215]. Topological charge makes no exception: if the energy cost required to move two anyons onto the same region in space (fusing) is too high due to their topological charge, then the anyons will not move. Since anyons have charge, detecting their position is not much harder than that

of usual electrons, and standard techniques such as QPC charge sensing [208, 216] or single electron transistor probes [217] can be used for this purpose [218]. Blockade measurements are a standard technique in quantum systems, and they are much simpler than the measurement of a force acting on a single quasiparticle, proposed as an alternative to interferometry in Ref. [219].

The particular setup for the detection of topological charge that we propose is very similar to that of a singlet-triplet spin qubit (see Fig. 8.1), where spin blockade is successfully used to distinguish a singlet state of two electrons from a triplet one [210, 213]. Two anyons are trapped to two dots formed by metallic gates¹. The energies of the anyons are controlled by gate voltages, and the charge position is measured by a nearby charge sensor.

In the following we analyze the performance of the proposed topological blockade readout of topological charge using a model calculation. We continue by discussing experimental challenges and important energy scales for measuring topological blockade. Finally, we propose several applications of topological blockade: a setup that should measure non-Abelian braiding statistics, and a setup allowing to entangle a topological qubit with a singlet-triplet qubit.

8.1 The model

A topological qubit, shown in Fig. 8.1b, consists out of two quantum dots trapping a pair of quasiparticles with charge $e/4$ (Ising anyons). The energy levels of the dots can be separately controlled by varying gate voltages. When the gate voltage difference is small, the occupation number of both dots is equal, so that the system is in the $(1, 1)$ configuration, where each index describes the occupation of each dot. When the voltage difference between the two dots is sufficiently large, a quasiparticle tunnels from the left dot to the neighboring one, and the ground state of the system becomes $(0, 2)$. Different states of the qubit are characterized by the fusion channel of two quasiparticles: vacuum ($\mathbb{1}$) or fermion (Ψ). We consider a limited gate voltage interval such that the excited orbital states and the charge $(2, 0)$ arrangement are higher in energy than the four states relevant for the readout: $\{|(0, 2)\mathbb{1}\rangle, |(1, 1)\mathbb{1}\rangle, |(0, 2)\Psi\rangle, |(1, 1)\Psi\rangle\}$.

Similar to the singlet-triplet qubit case [211], the Hamiltonian of the topological qubit is given by

$$H = \begin{pmatrix} H_{\mathbb{1}} & 0 \\ 0 & H_{\Psi} \end{pmatrix}, \quad \text{with} \quad H_a = \begin{pmatrix} \varepsilon_a & \delta \\ \delta & \varepsilon \end{pmatrix}. \quad (8.1)$$

Here ε is the energy of states $|(1, 1)\mathbb{1}\rangle$ and $|(1, 1)\Psi\rangle$, while $\varepsilon_{\mathbb{1}}$ and ε_{Ψ} are the energies of the states $|(0, 2)\mathbb{1}\rangle$ and $|(0, 2)\Psi\rangle$ respectively. For definiteness we assume that $\varepsilon_{\Psi} < \varepsilon_{\mathbb{1}}$ [219], however our conclusions are not limited to this assumption. The tunneling between different charge configurations has amplitude δ . As any local process, this tunneling preserves the topological charge.

¹The charge of the quasiparticle attracted to the gate voltage does not matter for our considerations: both dots, which trap $e/4$ quasiparticles, and anti-dots, which trap $e/4$ quasi-holes, work identically.

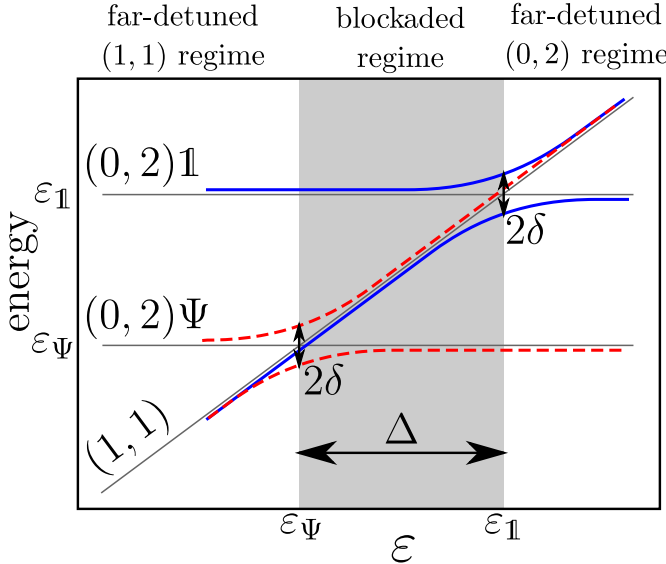


Figure 8.2: Main idea of topological blockade: spectrum of the Hamiltonian (8.1) as ε , which states the energy of the (1,1) charge configuration, is varied. Two avoided crossings occur when ε is degenerate with the fusion energies $\varepsilon_\Psi, \varepsilon_1$ of the anyons. Blue solid (red dashed) lines identify the eigenstates of the Hamiltonian with topological charge $\mathbb{1}$ (Ψ). In the energy window between ε_Ψ and ε_1 a blockaded regime occurs, with the (1,1) charge configuration favorable if the topological charge is $\mathbb{1}$ but not if it is Ψ . For $\varepsilon \ll \varepsilon_\Psi$ and $\varepsilon \gg \varepsilon_1$, the charge configurations (1,1) and (0,2) are respectively favored, independently on the topological charge shared by the anyons (far-detuned regimes).

The energy levels of the Hamiltonian (8.1) are shown in Fig. 8.2 as a function of ε , which is controlled by gate voltages. The two charge configurations (1,1), (0,2) become degenerate in the Ψ ($\mathbb{1}$) channel when $\varepsilon = \varepsilon_\Psi$ ($\varepsilon = \varepsilon_1$), and consequently δ leads to avoided crossings in the spectrum. Between the two crossings, there exists an energy window of width $\Delta = \varepsilon_1 - \varepsilon_\Psi$ where the (0,2) occupancy is favored with respect to the (1,1) occupancy if the topological charge is Ψ but not if it is $\mathbb{1}$. This identifies the blockaded regime, where charge tunneling is allowed or blocked depending on the fusion channel of the anyons. The energy Δ is similar to the singlet-triplet exchange splitting in spin blockade. This blocked region allows for efficient conversion from topological charge to real charge and hence allows readout of the topological state.

The topological charge of the double-dot system is subject to decoherence, due to

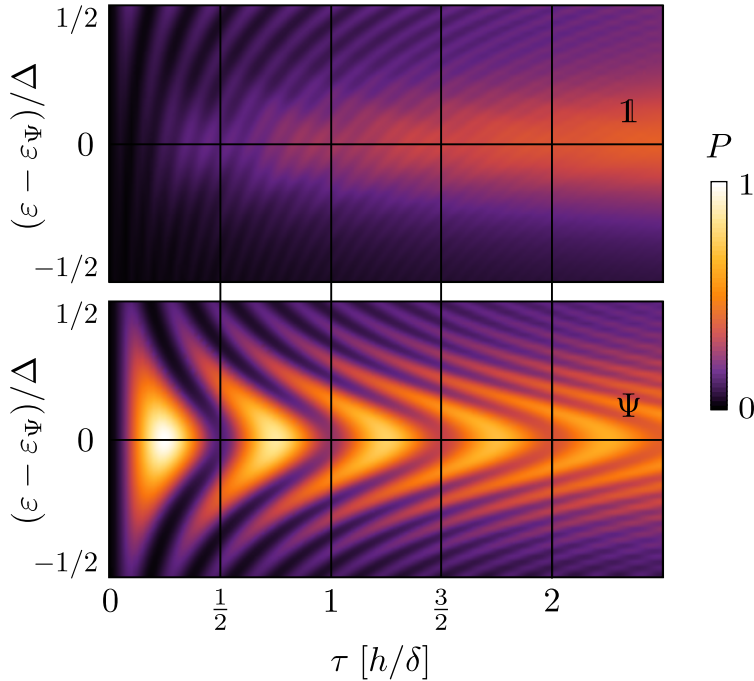


Figure 8.3: Probability P to measure the charge configuration $(0, 2)$ when the system starts in the configuration $(1, 1)$ with initial topological charge Ψ (bottom panel) or 1 (top panel), as a function of pulse duration τ and ε . Obtained from the numerical solution of the master equation (8.2), with parameters $\Delta = 10\delta$, $\gamma = 0.1\delta$.

coupling to the edges or other impurities in the quantum Hall liquid surrounding the system, which may cause transitions between the 1 and Ψ states in the same charge configuration. Assuming this process is independent of ε , we introduce a constant decay rate γ and model the time evolution of our system using a Lindblad master equation

$$\dot{\rho} = -i[H, \rho] + \frac{1}{2} \sum_j 2L_j \rho L_j^\dagger - \{L_j^\dagger L_j, \rho\} \quad (8.2)$$

with operators $L_1 = L_2^\dagger = \sqrt{\gamma}|(1, 1)\Psi\rangle\langle(1, 1)1|$ and $L_3 = L_4^\dagger = \sqrt{\gamma}|(0, 2)\Psi\rangle\langle(0, 2)1|$ describing the topological charge relaxation.

8.2 Readout

The topological charge in the $(1, 1)$ configuration at $\varepsilon \ll \epsilon_\Psi$, can be determined by bringing it adiabatically through the avoided crossing into the blocked region, and measuring the final charge configuration. This requires that the charge manipulation

is performed on a time scale $\tau \gg h/\delta$ (to avoid Landau-Zener transitions at the crossing).

If instead the topological charge relaxes too rapidly to perform the adiabatic passage, a faster readout procedure is needed. We describe here a method analogous to the rapid single-shot measurements of singlet-triplet qubits [213]. The system is initialized at $\epsilon \ll \epsilon_\Psi$ and the energy is then increased non-adiabatically to $\epsilon \sim \epsilon_\Psi$ for a short pulse of duration τ , after which ϵ is driven back to the initial value with a second fast pulse. The topological charge is again inferred by a charge measurement of the final occupancies of the dots.

During the pulse, two anyons in the Ψ channel oscillate between the $(1, 1)$ and $(0, 2)$ charge configurations with period $h/2\delta$. If τ equals half of this period, the transition probability from $|(1, 1)\Psi\rangle$ to $|(0, 2)\Psi\rangle$ is maximized. An analogous charge transition in the vacuum channel is strongly suppressed because the state $|(0, 2)\mathbb{1}\rangle$ lies at a higher energy $\epsilon_\mathbb{1}$. In the ideal case, the initial topological charge can be inferred by the final occupancies of the dot, with $(1, 1)$ and $(0, 2)$ corresponding to $\mathbb{1}$ and Ψ respectively. Unlike the adiabatic measurement, the time allowed for the charge measurement in this case is limited by the electric charge relaxation to the ground state, $(0, 2) \rightarrow (1, 1)$.

In a more realistic scenario, incoherent processes may alter the results and the position of the resonance cannot be known in advance with great accuracy. Fig. 8.3 shows the probability to measure the charge configuration $(0, 2)$ after a pulse of duration τ is performed at an energy ϵ , sweeping a range of width Δ centered around ϵ_Ψ , for the two different initial topological charges. Coherent oscillations dominate in the Ψ channel for $\tau \ll h/\gamma$, leading to fringes with peaks at $\tau_n^* = (n + 1/2)h/2\delta$. The brightest peak occurs at $\tau_0^* = h/4\delta$, making this the optimal duration of the pulse. If ϵ is varied for longer times and away from the resonance, the period of the fringes shortens and their intensity diminishes. Since this readout method works identically if $\epsilon \sim \epsilon_\mathbb{1}$ (only with the roles of $\mathbb{1}$ and Ψ states interchanged), either can be used to detect the topological charge of the prepared state.

The sum of the charge manipulation time τ and the charge readout time should be much shorter than the topological charge relaxation time, which is equal to h/γ . The adiabatic charge manipulation requires $\tau \gg h/\delta$, while the coherent manipulation requires a faster time scale $\tau \sim h/4\delta$, hence we arrive at the condition $\delta \gg \gamma$. If single shot readout is desired, the charge readout time should also be much shorter than the topological charge relaxation time h/γ . However, a quick low fidelity readout of the charge position is sufficient for the detection of the topological charge, since the measurements can be repeated many times. Additionally, in order for the two topological charges to be distinguishable, the blockaded region should be larger than the region where charge tunneling occurs $\delta \ll \Delta$.

The appropriate parameter conditions can be reached by a careful design of the setup. It has been estimated that an effective potential in the two-dimensional electron gas with a width of a few magnetic lengths (l_B) can trap single quasi-holes with a typical radius of $3l_B \approx 30$ nm [220–222]. Under this assumption, numerical works calculated $\Delta \approx 0.01e^2/\epsilon l_B$ with an upper bound of $1K$ [219, 221]. For larger dots Δ

is reduced since it is bounded from above by the level spacing. The speed of relaxation of the topological charge γ due to the coupling to disorder-induced anyons can be estimated as $\Delta e^{-l/\xi}$, with $\xi \approx 2.3l_B$ the characteristic length scale associated with the quantum Hall liquid excitation gap [219] and l the distance of the double-dot system from the nearest impurity. Requiring $\gamma \approx 0.01\Delta$ then yields a lower bound $l \approx 100$ nm. Finally δ is exponentially small in the distance between the dots, so the condition $\delta \ll \Delta$ requires the inter-dot distance to be larger than ξ .

These requirements are less stringent than the requirements for operation of a non-Abelian interferometer. There the readout time must still be shorter than h/γ , however it should also be much larger than the time of flight of a neutral excitation through the interferometer loop. This time of flight is given by $L/v \lesssim \hbar L/\Delta\xi$, with $L \gg \xi$ the length of the interferometer path. Additionally, γ is increased due to the coupling of the interferometer loop to bulk anyons [101, 201]. The non-Abelian interferometers however have the advantage that they are able to measure the Abelian part of the braiding statistics [6, 194, 202], to which topological blockade is completely insensitive. The interferometers can also measure topological charge of more than two anyons, unlike the topological blockade.

Quasiparticles in the Abelian 331 state [223], which is the most likely alternative to the Pfaffian state, have finite spin polarization, and hence may cause spin blockade. However due to the large Zeeman splitting, the equilibrium spin distribution is highly imbalanced, unlike the topological charge. This imbalance can be easily detected by performing a series of repeated blockade measurements.

Using existing technology, the smallest dots can be formed by local top gates with size ~ 100 nm. This is similar to the expected quasiparticle size. The effective confinement potential is expected to be still smoother than this scale because the 2DEG is located ~ 50 nm away from the gate. Nevertheless since the splitting is only suppressed linearly with the size of the un-gapped region, we expect that this will not result in big suppression of the Δ . As long as the gate potentials are sufficiently small, these local gates just attract excess quasiparticles without forming the edge states. A local charge sensor similar to the one used in Ref. [218] could be fabricated in proximity to one of the dots, as shown in Fig. 8.1c.

8.3 Extensions

8.3.1 Detection of non-Abelian statistics

In order to detect non-Abelian braiding statistics of the anyons, one needs to combine the topological blockade-based readout device with a minimal setup for exchanging two anyons [224]. This setup is shown in Fig. 8.4a, and it consists of a topological qubit with two extra dots hosting a single $e/4$ quasiparticle. The quasiparticles are moved by varying the potential of the dots. Both braiding and detection can then be performed in the four dot setup, using the same protocol proposed in Ref. [79] in the context of interferometric devices.

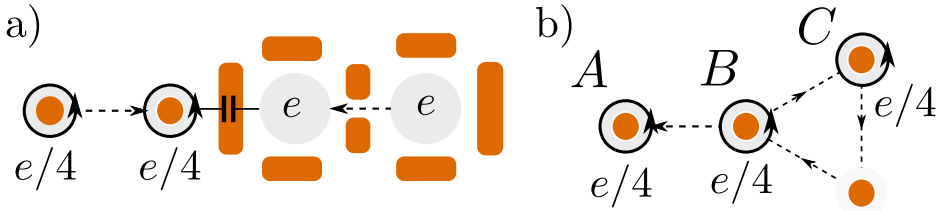


Figure 8.4: Applications of topological blockade. Panel (a): two-qubit system formed out of a topological and a spin qubit. For both qubits the computational degrees of freedom correspond to different charge configurations. Entanglement between the qubits can be induced by a capacitive coupling between the two double-dots. Panel (b): setup for the detection of non-Abelian statistics of the $\nu = 5/2$ fractional excitations. Three anyons (A, B, C) are hosted in four dots and can be moved by varying gate potentials. Two counterclockwise exchanges of B and C , implemented using the fourth empty dot, act as a NOT gate on the qubit formed by A and B [79].

8.3.2 Coupling with conventional qubits

Since topological blockade allows to translate the topological charge into the position of the electric charge, it becomes possible to couple a topological qubit with conventional quantum systems, similarly to what was done with Majorana qubits in superconducting systems [61, 65, 66]. Both topological and spin blockade translate the qubit degree of freedom into an electric charge configuration. In the case of singlet-triplet qubits, this effect has been used to couple two neighboring double dots in order to produce two-qubit entanglement [225]. The same method can be explored to couple capacitively a topological qubit to a singlet-triplet qubit hosted in a nearby double quantum dot (see Fig. 8.4b). Independent measurements on the two qubits can still be performed via two charge-sensing quantum point contacts. Additionally, the oscillatory motion of electric charge at the transition between $(1, 1)$ and $(0, 2)$ states can also be used to couple the topological charge to electromagnetic radiation, thus allowing coupling of a topological qubit with cavity qubits. Since the gate pattern needed to define the double-dot hosting the singlet-triplet qubit will likely introduce undesired edges in the quantum Hall liquid, it would be necessary to have the second qubit in a different layer of the nano-structure. Another difficulty to overcome is the presence of a strong magnetic field which increases the Zeeman splitting of the triplet states and makes it comparable with the exchange splitting in the singlet-triplet system, potentially ruining the operation of the spin qubit.

8.4 Conclusions

In conclusion, we have showed how to use topological blockade to measure topological charge. While we focused on the most experimentally relevant case of the $5/2$

fractional quantum Hall plateau, the same method applies to any non-Abelian phase as long as the anyons also have electric charge. We have shown that the topological blockade is more robust than the non-Abelian interferometry, in part due to being insensitive to the Aharonov-Bohm phase. The downside is that it cannot probe the Abelian part of the braiding statistics. Finally, we have also shown how to use topological blockade to measure braiding statistics and to couple topological qubits with a singlet-triplet spin qubit.

Chapter 9

Braiding of non-Abelian anyons using pairwise interactions

The purpose of topological quantum computation (TQC) is to realize a reliable quantum computer, exploiting the existence of non-Abelian anyons in certain condensed matter systems [5, 6]. The presence of several such particles gives rise to degenerate ground states which cannot be distinguished by local measurements. The ground state manifold is then adopted as the computational space, and quantum gates can be performed by braiding (exchanging the positions of the anyons), as shown in Fig. 9.1a). The resulting unitary transformation of the wave function depends only on the order of the exchanges and not on the details of their paths, thus these quantum gates are said to be topologically protected. In the standard scheme of TQC [6], there are two main ingredients needed to implement braiding. First, it must be possible to change the positions of anyons in such a way that the wave function of the system always belongs to the space of the degenerate ground states. Second, at all stages of the braiding the interactions between the anyons used for the computation must be negligible in order to preserve the degeneracy of the ground states and to avoid the presence of non-adiabatic time-dependent phases. This requires the anyons to be well separated in space.

The possibility to realize braiding operators without moving the anyons was then introduced by Bonderson, Freedman and Nayak in Refs. [71, 226]. In their scheme, the measurement-only TQC, the braid operators are obtained as a result of a probabilistically determined sequence of non-demolition measurements of the computational anyons as shown in Fig. 9.1b). This measurement would rely, for example, on the non-Abelian edge state interferometry [79–81, 190, 191, 227], which has been actively developed both experimentally and theoretically [101, 191–195, 199, 201, 202].

A different way to braid non-Abelian anyons without moving them around each other has been theoretically developed in the case of Majorana modes appearing

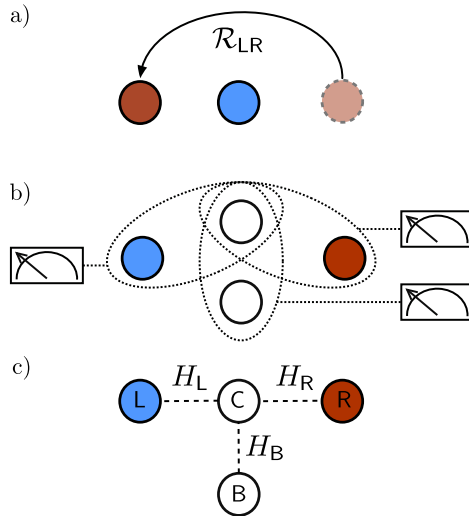


Figure 9.1: Different ways to braid quasiparticles in topological quantum computation. Panel (a): the original scheme for braiding, where quantum gates are obtained by moving the non-Abelian quasiparticles (red and blue dots) one around the other. Panel (b): measurement-only TQC, in which ancillary anyons are added to the system (white dot), and quantum gates are obtained as a sequence of non-demolition pairwise measurements (represented by the dashed ellipses) which induce teleportation of the computational anyons through the ancillary ones. Panel (c): the interaction-based braiding, which makes use of the interaction between computational and ancillary anyons in a T-junction geometry.

at the ends of one-dimensional topological superconductors [26, 45, 46]. Initially, it was shown in Ref. [21] how braids can be realized in wire networks by moving the Majorana modes through T-shaped junctions. In this case, the movement of the quasiparticles is restricted to a quasi one-dimensional system, thus relaxing the limitation of braiding to two dimensions. Subsequent proposals however have eliminated the need to physically move the topological defects altogether, showing how the same ground state transformations can be implemented using the mutual interactions between Majoranas, controlling either tunnel couplings via gate voltages [67] or capacitive couplings via magnetic fluxes [69]. Finally, in Ref. [86] a general theory of adiabatic manipulations of Majorana modes in nanowires was formulated. Unless we allow for physically bending and rotating the wires, the minimal setup required for the braid operation is a T-shaped configuration of nanowires where a central Majorana is coupled to at least three neighbors. The evolution over a path in parameter space results in the same non-Abelian Berry phase expected after an exchange of two quasiparticles in real space.

In this chapter, we aim to show that in a broad range of anyonic models braiding

is not only a property of the particle motion, but it is also encoded in the many-body Hamiltonian of coupled anyons. We will show how it is possible to engineer effective braidings by manipulating mutual couplings between neighboring anyons, rather than their coordinates in space. The motion of anyons is unnecessary also in measurement-only TQC, however our proposal is different because the braid operation is performed in a deterministic manner and does not rely on the procedure of anyon measurement.

The outline of this chapter is the following. In Section 9.1 we present the minimal braiding setup, formed by four anyons in a T-shaped junction, and we give an expression of the interaction Hamiltonian in terms of the \mathcal{F} -matrices of a generic anyon model. In Sec. 9.2 we present in detail the adiabatic cycle in parameter space used to braid the non-Abelian anyons, while in Sec. 9.3 we discuss how errors affecting the adiabatic evolution can be reduced by embedding the braiding junction in a bigger system of anyon chains and conclude.

9.1 The T-junction

We consider a system of four anyons with the same topological charge t in a T-junction geometry, with a central anyon (labeled t_C) coupled to other three (labeled t_L, t_R, t_B for left, right and bottom), as shown in Fig. 9.1c and Fig. 9.2. We assume that they have fusion rules

$$t \times t = \sum_{i=1}^n f_i \quad (9.1)$$

with $\{f_i\}$ the set of the n possible fusion channels (see Refs. [6, 78, 228] for introductions on non-Abelian anyons and their fusion rules).

We also assume that the anyons do not move, and we focus on the pairwise interactions between them. These interactions result in the fusion channels f_i having different energies, so that the Hamiltonian can be written as a sum of projectors onto different fusion outcomes. In the case of the T-junction and given the fusion rule (9.1), it takes the form

$$H = - \sum_K \sum_{i=1}^n \epsilon_{i,K} \Pi_i^K \quad (9.2)$$

where K runs over $\{L, B, R\}$ and Π_i^K is the projector onto the states in which the anyon t_K fuses with t_C into the i -th channel, with a relative coupling $\epsilon_{i,K}$. In order for braiding to work we require that the interaction of each anyon with the central one favors an Abelian channel $a_K \in \{f_i\}$, with a fusion energy $\epsilon_{a,K} \equiv \max\{\epsilon_{i,K}\}$. This means that the anyons C and K fusing in the a_K channel will be separated by an excitation gap from all the other mutual fusion channels. In the following we will assume that all the pairwise interactions favor the same fusion channel, i.e. $a_L = a_R = a_B = a$, even though this condition is not strictly necessary¹.

¹In the general case, the interactions between C and the other anyons may favor different Abelian fusion channels a_K if all the fusions $t \times a_K$ assume the same topological charge. The main example is the

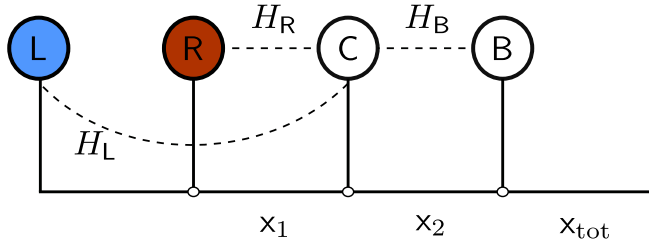


Figure 9.2: Graphical representation of the T-junction system as a fusion tree of the four anyons, corresponding to the basis choice made in the text, see Eq. (9.4). Different sequences of the fusion outcomes x_1, x_2, x_{tot} define the basis states of the Hilbert space. Three Hamiltonians H_L, H_R, H_B describe the interaction between different pairs of anyons. In particular, H_L couples the anyons L and C which, in this basis, are not nearest neighbors.

To the purpose of implementing a braiding operator between anyons t_L and t_R we require that all the pairwise interactions $H_K = \sum_{i=1}^n \epsilon_{i,K} \Pi_i^K$ in (9.2) can be adiabatically switched off. In reality a single interaction H_K can not be totally switched off (even though it can be likely made exponentially small), and we will relax this assumption in Sec. 9.3.1.

9.1.1 Ground state degeneracy

To prove that the Hamiltonian (9.2) is of any use for TQC, we must identify a degenerate manifold of its ground states, at least in some regions of the parameter space spanned by the energies $\epsilon_{i,K}$.

It has been shown that tunneling couplings between anyons lift completely the topological degeneracy of the ground state [229], and the Hamiltonian (9.2) makes no exception if all $\epsilon_{a,K}$ are non-zero. On the other hand, if all the couplings are zero, the ground state manifold coincides with the whole Hilbert space of the anyon system. We focus here on the intermediate domain between these two extreme cases, namely when only a subspace of the full Hilbert space has its degeneracy left intact.

The Hamiltonian (9.2) has an n -fold degenerate ground state when at least one of the H_K is zero and one is non-zero. Let us consider $H_L = H_R = 0, \epsilon_{a,B} > 0$. The two anyons L and R are completely decoupled and share an arbitrary topological

case of Ising anyons σ , which obey the fusion rules $\sigma \times \sigma = \mathbb{I} + \Psi, \sigma \times \mathbb{I} = \sigma \times \Psi = \sigma$, with both \mathbb{I} and Ψ Abelian; in this case changing the favored fusion channel of the pairwise interaction between L (or R) and C determines a change in the chirality of the braiding [67, 86]. This is due to an additional symmetry of the Ising anyon model:

$$\mathcal{R}_{LR}^{-1} \Pi_{\Psi}^L \mathcal{R}_{LR} = \mathcal{R}_{LR} \Pi_{\mathbb{I}}^L \mathcal{R}_{LR}^{-1} \quad (9.3)$$

where $\Pi_{\Psi} = 1 - \Pi_{\mathbb{I}}$ is the projector over the fermionic fusion channel Ψ . This relation implies that changing the favored fusion channel for one of the two anyons R or L, the role of \mathcal{R}_{LR} and \mathcal{R}_{LR}^{-1} are exchanged throughout the adiabatic cycle and effectively reverses the braiding direction.

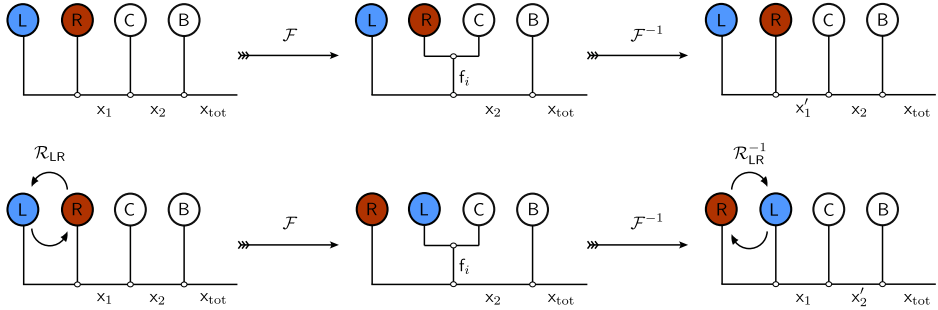


Figure 9.3: Top: graphical representation of Eq. (9.6). The fusion outcomes are explicitly written along the fusion tree. To write down the projectors Π_i^R in the basis of Fig. 9.4, we need two \mathcal{F} -moves. A similar transformation, not shown, is needed to write down Π_i^B , see Eq. (9.5). Bottom: in the case of Π_i^L , two braiding matrices \mathcal{R}_{LR} make their appearance in addition to the \mathcal{F} -moves. This introduces the braiding matrix \mathcal{R}_{LR} in the Hamiltonian of the T -junction.

charge x_1 which may assume one of the n different values $\{f_i\}$, while the anyons B and C fuse into the Abelian channel a. The total topological charge equals $x_{\text{tot}} = (t_R \times t_L) \times (t_B \times t_C) = x_1 \times a$. Since a is Abelian, the fusion $x_1 \times a$ can only have one possible outcome, and additionally there cannot be another charge x'_1 such that $x'_1 \times a$ has the same outcome. Therefore there exists a one-to-one mapping between the charges x_1 and x_{tot} , implying that the ground state wave function $|\Psi\rangle$ will generically be a superposition of n orthogonal ground states Ψ_i with total topological charge $f_i \times a$, $|\Psi\rangle = \sum_i a_i |f_i \times a\rangle$.

When a second coupling, say H_L , is also nonzero, the anyon L fuses with $t_C \times t_B = a$ and the three have a total charge $t \times a$. The overall degeneracy cannot change, since $t_R \times (t_L \times t_B \times t_C) = t \times (t \times a) = (\sum_i f_i) \times a$, which again gives n orthogonal states.

We conclude that if all the couplings H_K are neither *on* nor *off* at the same time, the ground state of the Hamiltonian (9.2) has an n -fold degeneracy.

9.1.2 Projectors

In order to describe the wave function evolution in the n -fold degenerate ground state subspace of (9.2), we need to write down the Hamiltonian (9.2) explicitly in a certain basis. To describe the evolution and the eigenstates of this system we closely follow the methods used for the study of anyon chains and lattices (see e.g. [230–234]).

The different quantum states of a system of anyons can be specified by the sequence of fusion outcomes along a certain fusion path. The choice of a fusion path is equivalent to the choice of a basis in the Hilbert space. Once a fusion path is chosen, the projector of two anyons on a given channel f_i is represented by a simple diagonal matrix if the two anyons fuse directly together along the path with outcome f_i . Otherwise a

projector must be written via appropriate transformations called \mathcal{F} -matrices (see e.g. [6, 228, 230]). We choose the following fusion path shown also in Fig. 9.2:

$$(((t_L \times t_R \rightarrow x_1) \times t_C \rightarrow x_2) \times t_B \rightarrow x_{\text{tot}}), \quad (9.4)$$

with x_1, x_2, x_{tot} belonging to the sets of possible fusion channels at each step of the fusion path. All states in the Hilbert space can be written as $|x_1, x_2, x_{\text{tot}}\rangle$. The basis (9.4) describes a path where t_L and t_R are first fused with outcome x_1 , then with t_C resulting in a second outcome x_2 , and finally with the fourth anyon t_B to give x_{tot} . The latter is the total topological charge of the system: subspaces of the Hilbert space corresponding to different x_{tot} are decoupled. Adopting this basis we can now write down explicitly all the terms appearing in the Hamiltonian (9.2). To this purpose we consider different bases in which each operator has a diagonal form, and then we move to the basis in Eq. (9.4) using appropriate basis transformations.

We start with Π_i^B . The anyons t_C and t_B are nearest neighbor, but they do not fuse directly together in our fusion path: to write Π_i^B we must use the appropriate \mathcal{F} -matrices,

$$\begin{aligned} [\Pi_i^B(x_1, x_{\text{tot}})]_{x'_2, x_2} &= \sum_y \left(\mathcal{F}_{x_{\text{tot}}}^{x_1 t_C t_B} \right)_{x'_2, f_i}^{-1} \delta_{f_i, y} \left(\mathcal{F}_{x_{\text{tot}}}^{x_1 t_C t_B} \right)_{y, x_2} = \\ &= \left(\mathcal{F}_{x_{\text{tot}}}^{x_1 t_C t_B} \right)_{x'_2, f_i}^{-1} \left(\mathcal{F}_{x_{\text{tot}}}^{x_1 t_C t_B} \right)_{f_i, x_2} \end{aligned} \quad (9.5)$$

with $y \in \{f_i\}$ and x_2, x'_2 belonging to the set of fusion channels of three t anyons. As indicated on the left hand side of Eq. (9.5), the matrix elements of the projector depend on indices x_1, x_{tot} . In a similar way we obtain for Π_i^R the following form:

$$[\Pi_i^R(x_2)]_{x'_1, x_1} = \left(\mathcal{F}_{x_2}^{t_L t_R t_C} \right)_{x'_1, f_i}^{-1} \left(\mathcal{F}_{x_2}^{t_L t_R t_C} \right)_{f_i, x_1} \quad (9.6)$$

with $x_1, x'_1 \in \{f_i\}$. The graphical representation of this equation is shown in the top panel of Fig. 9.3.

Unlike the two other cases, in the fusion tree of Fig. 9.2 the anyons L and C are not nearest neighbors in the chosen basis. Since they would be nearest neighbors if L and R were interchanged, the transformation to a basis when they fuse directly together includes a braiding matrix \mathcal{R}_{LR} , as shown in the bottom panel of Fig. 9.3. The particular braiding matrix (\mathcal{R}_{LR} or \mathcal{R}_{LR}^{-1}) that appears in this basis transformation depends on the real space positions of the anyons and on the microscopic details of the Hamiltonian. The two possible choices correspond to two mirror-symmetric anyon models [228]. It is this term that is responsible for the appearance of braiding during the adiabatic Hamiltonian evolution. In particular mirroring the T-junction layout inverts the chirality of \mathcal{R} . As shown in the bottom panel of Fig. 9.3, the projector Π_i^L can be obtained from Π_i^R via \mathcal{R}_{LR}

$$\mathcal{R}_{LR}^{-1} \Pi_i^R \mathcal{R}_{LR} = \Pi_i^L \quad (9.7)$$

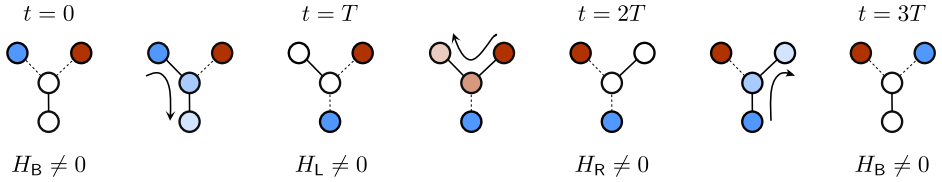


Figure 9.4: Illustration of the adiabatic cycle which reproduces the braiding operator \mathcal{R}_{LR} of two topological charges t (red and blue circles) in a four anyon system. The cycle is divided in three steps of duration T . At the end of each step only one interaction H_K is on. The arrows follow the transfer of an unpaired topological charge t at intermediate stages, represented as the spreading of the colored circles over different anyons.

In the fusion basis (9.4), \mathcal{R}_{LR} is a diagonal matrix and, explicitly, we have

$$\begin{aligned} [\Pi_i^L(x_2)]_{x'_1, x_1} &= (\mathcal{R}_{LR})_{x'_1} (\Pi_i^R)_{x'_1, x_1} (\mathcal{R}_{LR})_{x_1} = \\ &= (\mathcal{R}_{LR})_{x'_1} (\mathcal{F}_{x_2}^{t_L t_R t_C})_{x'_1, f_i}^{-1} (\mathcal{F}_{x_2}^{t_L t_R t_C})_{f_i, x_1} (\mathcal{R}_{LR})_{x_1}. \end{aligned} \quad (9.8)$$

Knowing the \mathcal{F} -matrices of a given anyon model, Eqs. (9.5,9.6,9.8) allow to write explicitly the four-anyon Hamiltonian (9.2). In particular, we note that the braiding operator \mathcal{R}_{LR} now appears explicitly in

$$H_L = \sum_i \epsilon_{i,L} \Pi_i^L = \sum_i \epsilon_{i,L} \mathcal{R}_{LR}^{-1} \Pi_i^R \mathcal{R}_{LR}. \quad (9.9)$$

Before concluding this section, we point out that because the interactions are local, the fusion product $t_B \times t_C$ cannot be affected by the braiding of R and L . The projectors Π_i^B and the braiding operator \mathcal{R}_{LR} must therefore commute:

$$\Pi_i^B \mathcal{R}_{LR} = \mathcal{R}_{LR} \Pi_i^B. \quad (9.10)$$

9.2 The adiabatic cycle

In this section we show that the braiding of the anyons R and L appears as a result of any closed path in parameter space starting from a point where only $H_B \neq 0$, and continuously passing through the points where first only $H_L \neq 0$, and finally only $H_R \neq 0$ in such a way that the degeneracy is always preserved. For the ease of presentation we divide the path into three separate steps of duration T such that during each step one of H_K is turned on and one off. The time evolution of the Hamiltonian along such a path is shown in Fig. 9.4.

Let us consider the evolution of the ground state wave function $|\Psi(t)\rangle$ of H along this adiabatic cycle. The wave function can at any moment be written as a

$$\begin{aligned}
 & \text{Diagram 1: } \text{R} \text{ (red circle)} \text{, L (blue circle)} \text{, C (green circle)} \text{, B (yellow circle)} \text{, total charge } x_{\text{tot}}. \\
 & = \sum_{x_2} \left(\mathcal{F}_{x_{\text{tot}}}^{t_R f_i t_B} \right)^{-1}_{t \times a, x_2} \text{Diagram 2: } \text{R} \text{ (red circle)} \text{, L (blue circle)} \text{, C (green circle)} \text{, B (yellow circle)} \text{, total charge } x_{\text{tot}}. \\
 & = \sum_{x_1, x_2} \left(\mathcal{F}_{x_2}^{t_R t_L t_C} \right)^{-1}_{f_i, x_1} \left(\mathcal{F}_{x_{\text{tot}}}^{t_R f_i t_B} \right)^{-1}_{t \times a, x_2} \text{Diagram 3: } \text{L (blue circle)} \text{, R (red circle)} \text{, C (green circle)} \text{, B (yellow circle)} \text{, total charge } x_{\text{tot}}. \\
 & = \sum_{x_1, x_2} (\mathcal{R}_{LR})^{-1}_{x_1} \left(\mathcal{F}_{x_2}^{t_R t_L t_C} \right)^{-1}_{f_i, x_1} \left(\mathcal{F}_{x_{\text{tot}}}^{t_R f_i t_B} \right)^{-1}_{t \times a, x_2} \text{Final state: } \text{L (blue circle)} \text{, R (red circle)} \text{, C (green circle)} \text{, B (yellow circle)} \text{, total charge } x_{\text{tot}}
 \end{aligned}$$

Figure 9.5: The derivation of Eq. (9.13). We transform the ground states $|\Psi_{x_{\text{tot}}}(t)\rangle$ from the basis $((t_L \times t_C \rightarrow f_i) \times t_B \rightarrow t \times a)$ to the basis (9.4). The phase factor $(\mathcal{F}_{x_{\text{tot}}}^{\text{tat}})_{t \times a, t \times a}$ from Eq. (9.13) is not explicitly shown here.

superposition over states with different total topological charge x_{tot} ,

$$|\Psi(t)\rangle = \sum_{x_{\text{tot}}} a_{x_{\text{tot}}} |\Psi_{x_{\text{tot}}}(t)\rangle. \quad (9.11)$$

The states $|\Psi_{x_{\text{tot}}}(t)\rangle$ define the n -fold ground state manifold. The absolute values of the superposition coefficients $a_{x_{\text{tot}}}$ are conserved because the total topological charge is a conserved quantity. This implies that the time evolution of the ground state manifold is a diagonal operator in the basis given by $|\Psi_{x_{\text{tot}}}(t)\rangle$. Therefore, each term in the superposition (9.11) can only acquire a phase, possibly dependent on x_{tot} , or in other words the Berry matrix is diagonal in this basis. This allows us to follow the evolution of each $|\Psi_{x_{\text{tot}}}(t)\rangle$ independently from all other states.

We should note that the superposition (9.11) is only possible if other anyons are present in the system other than L, R, C, B. We imagine that these anyons do not interact with the T-junction while the adiabatic cycle is performed, so that their presence can be ignored.

During the first step $0 \leq t \leq T$, the anyon R is left unpaired from the other three. The topological charge of the three anyons L, C, B is then conserved and equal to its initial value $t_L \times (t_C \times t_B) = t \times a$. The general form of a wave function satisfying this constraint is given by:

$$|\Psi_{x_{\text{tot}}}(t)\rangle = \sum_{x_1, x_2, f_i} U_{x_{\text{tot}}, x_1, x_2, f_i} \alpha_{f_i}(t) |x_1, x_2, x_{\text{tot}}\rangle, \quad (9.12)$$

where $\alpha_{f_i}(t)$ can always be chosen to not depend on x_{tot} , and the unitary matrix U is the transformation from the basis $((t_L \times t_C \rightarrow f_i) \times t_B \rightarrow t \times a)$, where the anyons L,

C and B fuse directly into $t \times a$ before adding the anyon R, to the basis (9.4):

$$U_{x_{\text{tot}}, x_1, x_2, f_i} = \left(\mathcal{F}_{x_{\text{tot}}}^{\text{tat}} \right)_{t \times a, t \times a} \left(\mathcal{R}_{LR}^{-1} \right)_{x_1} \left(\mathcal{F}_{x_2}^{t_R t_L t_C} \right)_{f_i, x_1}^{-1} \left(\mathcal{F}_{x_{\text{tot}}}^{t_R f_i t_B} \right)_{t \times a, x_2}^{-1}. \quad (9.13)$$

The \mathcal{F} - and \mathcal{R} -moves required for this transformation are shown in Fig. 9.5.

In particular, at $t = 0$, only $H_B \neq 0$ and each $|\Psi_{x_{\text{tot}}}(0)\rangle$ is an eigenstate of Π_a^B defined in Eq. (9.5):

$$|\Psi_{x_{\text{tot}}}(0)\rangle = \left(\mathcal{F}_{x_{\text{tot}}}^{\text{tat}} \right)_{t \times a, t \times a} \sum_{x_1, x_2} \left(\mathcal{R}_{LR}^{-1} \right)_{x_1} \times \left(\mathcal{F}_{x_{\text{tot}}}^{x_1 t_C t_B} \right)_{a, x_2}^{-1} \left(\mathcal{F}_{x_{\text{tot}}}^{t_R t_L a} \right)_{t \times a, x_1}^{-1} |x_1, x_2, x_{\text{tot}}\rangle, \quad (9.14)$$

These wave functions (9.14) can be obtained from the Eqs. (9.12) and (9.13) by substituting $\alpha_{f_i}(0) = \left(\mathcal{F}_{t \times a}^{t_L t_C t_B} \right)_{a, f_i}^{-1}$ and applying the pentagon equation [228]. The presence of the last \mathcal{F} symbol in Eq. (9.14) implies $x_1 = x_{\text{tot}} \times a$, which simplifies the sum over x_1 due to a being Abelian. The phase factor $(\mathcal{R}_{LR}^{-1})_{x_1}$ is needed in order to guarantee the independence of $\alpha_{f_i}(t)$ on x_{tot} .

As t evolves from 0 to T , these states acquire a Berry phase,

$$\theta_T = \int_0^T \langle \Psi_{x_{\text{tot}}}(t) | \partial_t | \Psi_{x_{\text{tot}}}(t) \rangle dt = \int_0^T \sum_{f_i} \alpha_{f_i}^* \partial_t \alpha_{f_i} dt. \quad (9.15)$$

The time-independent unitary matrix U naturally drops out of the expression for the Berry phase. We conclude that the Berry phase acquired in our basis during the first step is the same for every state, or in other words it is Abelian.

At $t = T$, only $H_L \neq 0$, and the ground state wave function must be in an eigenstate of Π_a^L ,

$$|\Psi_{x_{\text{tot}}}(T)\rangle = \sum_{x_1} \left(\mathcal{F}_{x_2}^{t_R t_L t_C} \right)_{a, x_1}^{-1} \left(\mathcal{R}_{LR}^{-1} \right)_{x_1} |x_1, x_2, x_{\text{tot}}\rangle, \quad (9.16)$$

now with $x_2 = t \times a$ since L and C fuse into a, and the phases once again fixed by the requirement that α_{f_i} do not depend on x_{tot} . Note that the wave functions (9.16) are of form given by Eq. (9.12). The net result of the evolution from $t = 0$ to $t = T$ is the transfer from L to B of an unpaired topological charge t.

During the second step $T \leq t \leq 2T$ the wave function coefficients can be chosen to be independent on x_{tot} in the basis of Eq. (9.4). The wave function evolves from the eigenstate (9.16) of Π_a^L into an eigenstate of Π_a^R . Due to the relation (9.7) and Eq. (9.16) we can write the ground state wave functions at $t = 2T$ as

$$|\Psi_{x_{\text{tot}}}(2T)\rangle = \sum_{x_1} \left(\mathcal{F}_{x_2}^{t_L t_R t_C} \right)_{a, x_1}^{-1} |x_1, x_2, x_{\text{tot}}\rangle. \quad (9.17)$$

The integral of the Berry connection $\langle \Psi_{x_{\text{tot}}}(t) | \partial_t | \Psi_{x_{\text{tot}}}(t) \rangle$ from T to $2T$ is common to all states and provides an Abelian Berry phase due to the independence of all the coefficients on x_{tot} .

In the last step, $2T \leq t \leq 3T$, we repeat the procedure of the first one. We write the wave function in a basis $((t_R \times t_C \rightarrow f_i) \times t_B \rightarrow t \times a)$, where t_R, t_C, t_B fuse into $t \times a$ before the anyon L is added. The corresponding transformation to the basis (9.4) is given by the Eq. (9.13), but without the matrix $(\mathcal{R}_{LR})^{-1}$. This ensures that the wave function $|\Psi_{x_{\text{tot}}}(t)\rangle$ stays continuous at $t = 2T$. In this last step, the wave function acquires another Abelian Berry phase and ends up again in an eigenstate of Π_a^B . We end up with:

$$|\Psi_{x_{\text{tot}}}(3T)\rangle = \left(\mathcal{F}_{x_{\text{tot}}}^{\text{tat}} \right)_{t \times a, t \times a} \sum_{x_1, x_2} \left(\mathcal{F}_{x_{\text{tot}}}^{x_1 t_C t_B} \right)_{a, x_2}^{-1} \left(\mathcal{F}_{x_{\text{tot}}}^{t_R t_L a} \right)_{t \times a, x_1}^{-1} |x_1, x_2, x_{\text{tot}}\rangle. \quad (9.18)$$

Having performed an adiabatic evolution over a closed path, the final wave function must be connected to the initial one via a unitary matrix \mathcal{U} , $|\Psi(3T)\rangle = \mathcal{U}|\Psi(0)\rangle$. Using Eq. (9.14) and (9.18) we find

$$\langle \Psi_{x_{\text{tot}}}(0) | \Psi_{x_{\text{tot}}}(3T) \rangle = (\mathcal{R}_{LR})_{x_1} \quad (9.19)$$

where we recall that $x_{\text{tot}} = x_1 \times a$. For the whole wave function we can write

$$|\Psi(3T)\rangle = \mathcal{R}_{LR} |\Psi(0)\rangle \quad (9.20)$$

up to an Abelian Berry phase. This means that the braiding of anyons L and R was performed in the adiabatic cycle. By performing the whole protocol in reverse, we obtain instead the inverse braiding.

9.3 Discussion and conclusions

9.3.1 Restoring scalability and topological protection

The braiding procedure of Sec. 9.2 relies on the ability to turn off the pairwise interactions H_K completely. This is only possible if the separation between the anyons becomes infinite, and hence one may argue that this procedure is only approximating topological quantum computation. In a finite system the non-Abelian Berry phase will in general have a correction, and additionally non-adiabatic errors will appear due to the presence of finite ground state splitting [72].

This imperfection can be removed and the topological nature of the braiding can be restored by bringing the anyons L, R, B further away from the central one C . If anyonic chains with controllable couplings are then introduced along the three arms of the T-junction (see Fig. 9.6), this still allows to perform the braiding in a similar fashion, but with a higher fidelity. Since we are interested in the low energy spectrum of the Hamiltonian we approximate the interactions between nearest-neighbor anyons K, K' with the projector $\Pi_a^{K, K'}$ over their lowest energy topological charge and we consider all the other fusion channels to have the same energy, so that the Hamiltonian of each junction becomes:

$$H_{K, K'} = -\epsilon \Pi_a^{K, K'}, \quad (9.21)$$

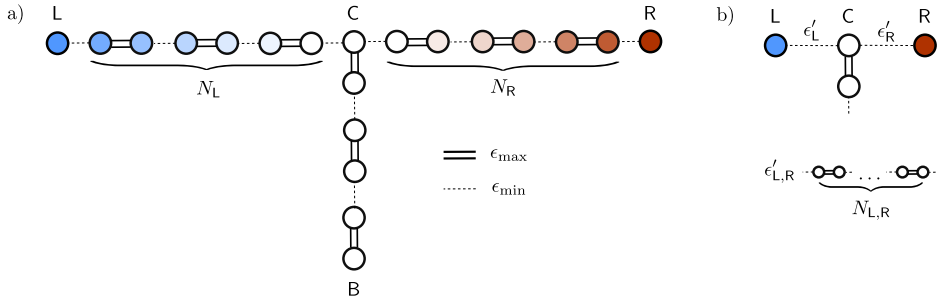


Figure 9.6: Panel (a): three staggered anyon chains forming a T-junction. Weak (ϵ_{\min} , dashed lines) and strong (ϵ_{\max} , double solid lines) couplings alternate. The bottom arm of the T-junction, connecting the original anyons C and B, is in a dimerized phase with no unpaired anyons and approximately contains no net topological charge. On the other hand, in the right and left arm the dimerization leaves two almost unpaired anyons L and R at the end (blue and red dot). Due to the residual coupling, the topological charge of L and R is spread over the neighboring anyon pairs, as represented by the color gradings. The left and right arm are therefore in the non-trivial phase. The two arms interact weakly via the centre of the T-junction, leading to renormalized couplings ϵ'_L and ϵ'_R between L, R and C, as in panel (b). The residual interaction splits the ground state degeneracy of an energy exponentially small in the length of the chains.

where a should again be Abelian. We require that ϵ can be varied in a range $(\epsilon_{\min}, \epsilon_{\max})$, so that the chains can be driven into a staggered phase with alternating weak and strong couplings, as in the Kitaev Majorana chain [26] and its parafermionic generalization [235].

The termination of the chain ending with a weak link differs from the termination by a strong link by the presence of an extra t anyon, and the chain ending with a strong link can be continuously connected to a chain of fully fused a -type anyons. This means that if the chain is gapped, whenever it ends in a weak link, its end has a topological charge of t , spread over several anyons, as shown in Fig. 9.6. While we are not aware of a proof that a general anyonic chain with staggered antiferromagnetic couplings is gapped, it is true for many relevant cases [232, 236, 237]. When $\epsilon_{\min} \ll \epsilon_{\max}$, the effective minimal coupling between an unpaired anyon at the edge of the T-junction and the central anyon C can be calculated perturbatively, and it is equal to $\epsilon' \simeq \epsilon_{\min} (\kappa \epsilon_{\min} / \epsilon_{\max})^N$, with N the number of anyon pairs in the chain, and κ a geometric factor which depends on the specific anyon model. For Ising anyons $\kappa = 1$, and for Fibonacci anyons $\kappa = 2/\phi^2$, with $\phi = (1 + \sqrt{5})/2$ the golden ratio [236, 237]. The maximal coupling is achieved in the staggered configuration which ends with a strong bond, and the maximal coupling ϵ_{\max} is only weakly modified.

To implement the braiding, each part of the adiabatic evolution can be decomposed into steps which require to change the pairwise couplings of three anyons, just as it

happens for the steps illustrated in Fig. 9.4. In this way, during the adiabatic cycle, we create and move domain walls which drive the transition between the two different staggered configurations of the chains (see Fig. 9.7). The two unpaired topological charges encoding the computational degree of freedom are localized in these domain walls which are moved along the three arms. Since the distance between the unpaired charges is always larger than the length N of a single arm of the T-junction, their residual interaction is exponentially suppressed, allowing to likewise exponentially suppress the error in the final result.

9.3.2 Summary

In summary, we have investigated an approach to topological quantum computation. In order to implement the necessary braiding operations of non-Abelian anyons, we couple the anyons instead of moving them or measuring their state. We have considered a simple system composed of four interacting non-Abelian anyons in a T-junction geometry and we have shown how adiabatic control over the interactions results in the Berry matrix expected when two anyons are moved around each other. If the coupling between the anyons cannot be completely turned off, errors are introduced in the braiding operations due to the residual splitting of the ground state degeneracy. We have discussed how these errors can be limited by means of enlarging the number of anyons involved in the adiabatic evolution. The protection is exponential in the number of anyons which are added to the system, so the whole procedure is similar to increasing the separation between anyons in the original approach.

Our approach, inspired by recent theoretical proposals for the braiding of Majorana modes in superconductors, is applicable to most anyon models. These include all the $SU(2)_k$ models (such as the Ising and Fibonacci anyons expected to appear in fractional quantum Hall systems), as well as the fractionalized Majorana modes very recently proposed in Refs. [235, 238–242].

A possible implementation of our scheme in the fractional quantum Hall systems, would require to engineer systems of dots hosting single anyonic quasiparticles and to tune their interactions via the voltages induced by gates or scanning tips, in a similar spirit to the blockade measurement of topological charge [243].

Alternative, but even more exotic, implementations of this scheme include for example the braiding procedure presented in Refs. [239, 244] for fractional Majorana modes in superconductor/quantum-Hall heterostructures. Additionally, the recent progress in the design of several systems thought to host non-Abelian excitations, ranging from physical realizations of the Kitaev honeycomb lattice model [78] (see, for example [245–247]) to ultra-cold atomic gases subjected to artificial gauge potentials [248, 249], could also fall into the category of systems where interactions between anyons are easier to control than their positions.

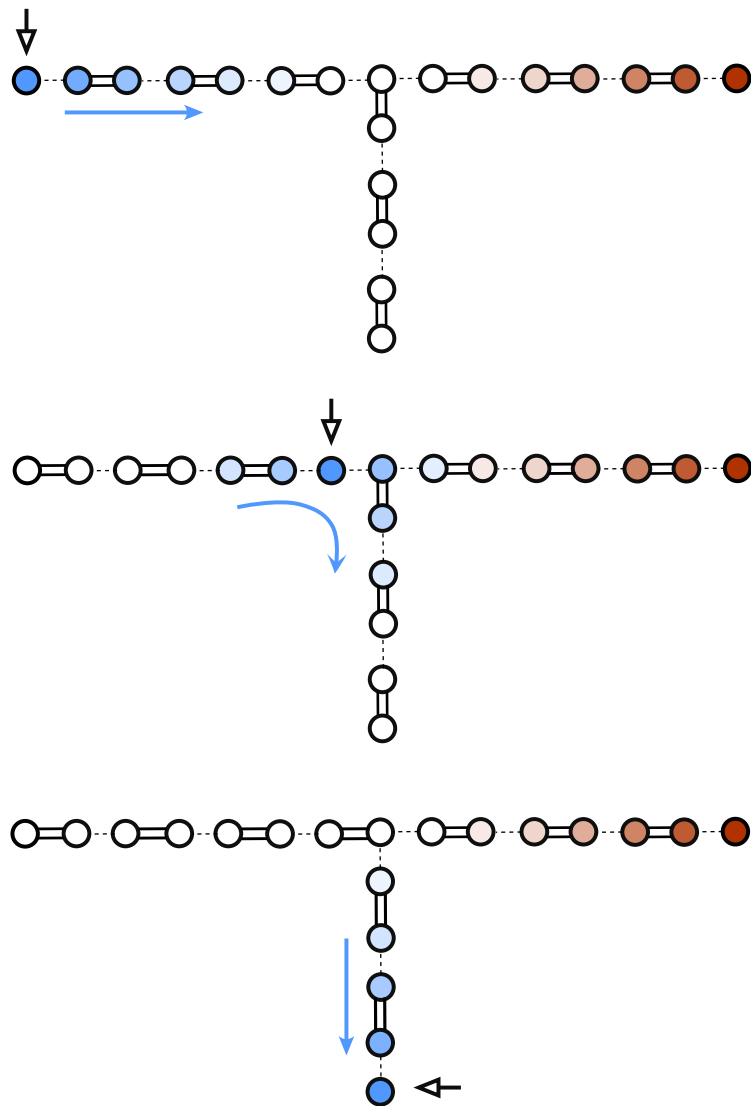


Figure 9.7: The first step of the adiabatic braiding sequence realized in a system of staggered anyonic chains. The topological charge t is moved from the left arm of the junction to the bottom arm. As in Fig. 9.6, blue and red colors represent a topological charge t spread over several anyons. The charges are localized at domain walls between the two possible phases of the staggered chain. Domain walls can be moved: each movement involves three different anyons of the chain. The domain wall that is moved is marked by a black arrow.

Chapter 10

Topological phases in 2D arrays of parafermionic modes

Systems that exhibit topological quantum order [250] have been a focus of attention in recent years. Part of the interest is due to the fact that they have been proposed as fault-tolerant quantum memories and platforms for quantum computation [6], the paradigmatic example being Kitaev's toric code [5]. The goal is to design architectures effectively governed by topologically-ordered Hamiltonians, where qubits may be stored and manipulated in a physically protected way. zero-modes Majorana zero-modes, realized as superconducting mid-gap excitations in either one [26] or two [14, 25] spatial dimensions, are promising building blocks for such architectures. Two unpaired Majorana modes at the ends of a one-dimensional (1D) superconducting wire encode non-locally a qubit [26] and, when allowed to move in a non-strictly 1D geometry, exhibit non-Abelian statistics [11, 21, 27], allowing to implement a non-universal set of quantum gates through ordered exchanges of their positions. Interest in Majorana modes has increased considerably in recent times, since there are now several experimentally accessible systems that may host these quasiparticles (see Refs. [22] and [23] for a review). A notable example is the edge of a two-dimensional (2D) topological insulator [43, 44], which hosts gapless helical (i.e., counter-propagating) modes, in proximity to an *s*-wave superconductor (SC) and a ferromagnet (FM). The competition between the proximity-induced SC and FM pairing along the edge results in the presence of a Majorana mode at each domain wall [42].

Recently, an interesting extension of this model was proposed in Refs. [238–241]. While the edge excitations of a 2D topological insulator are normal electrons, it is possible to consider instead edge quasiparticles with a fractional charge e/m , where m is an odd integer. Such gapless quasiparticles appear, for example, at the edge of the Laughlin fractional quantum Hall states, where they are described by a chiral Luttinger liquid theory [251, 252]. Due to the absence of time-reversal symmetry, these are chiral excitations. Helical e/m quasiparticles would arise at the interface

between two $\nu = 1/m$ quantum Hall liquids with Landé g -factors of opposite sign or, similarly, as a Kramers doublet at the edge of a fractional topological insulator [253] (FTI).

The simplest way to model FTIs is to consider them as fractional quantum spin Hall systems constituted by a two-dimensional gas of electrons subject to both a spin-dependent magnetic field (or a position-dependent spin-orbit coupling) and Coulomb interactions [254]. The first element creates two time-reversal symmetric Landau level structures, whereas the second gives rise to topologically ordered fractional states. These systems are gapped in the bulk (where Abelian anyonic excitations appear), but present fractional gapless edge modes. While such time-reversal invariant topological phases have been thoroughly studied theoretically [253, 255–258], no host material has emerged so far as an experimental candidate. We should also mention a recent proposal to realize a fractional helical liquid in quantum wires [259].

Along the FTI edges, the proximity effect with superconductors and ferromagnets results in the presence of zero-modes [238, 239]. Since the second-quantization operators associated with these zero-modes inherit a fractional exchange phase $(2\pi)/(2m)$ from the unperturbed edge fields, we shall refer to them as \mathbb{Z}_{2m} parafermionic (PF) zero-modes. They are projective non-Abelian anyons [244, 260], with fusion rules that generalize those of Majorana modes, affording extended computational power [238, 239, 242, 244, 261].

These superconducting zero-modes realize a 1D model with \mathbb{Z}_{2m} symmetry studied by Fendley [235], which is an extension of Kitaev's Majorana chain model [26] and hosts PF zero-modes localized at the edges of the system. While the Kitaev chain is dual to the quantum Ising chain via a Jordan-Wigner transformation, the \mathbb{Z}_{2m} chain model is dual to the 1D chiral Potts (p -clock) model, with $p = 2m$.

Indeed, PFs as collective degrees of freedom are indeed well-known in statistical mechanics (see for instance Ref. [262] and references therein). They appear naturally in the study of the 2D p -state clock models [263–265] and their quantum 1D counterparts [266]. In lattice systems, they arise as products of order and disorder operators defined for self-dual systems. Moreover, PFs admit a description in terms of a \mathbb{Z}_p invariant conformal field theory [267] (CFT) featuring the PFs as primary fields. PF zero-modes in superconducting systems are however related only to CFTs with unit central charge (see, for example, Ref. [268]), arising from a bosonization description of the FTIs edge modes.

In light of this body of research, it is interesting to extend the recent works on \mathbb{Z}_{2m} PFs to 2D networks of superconductors. For Majorana zero-modes, this question has already been addressed in literature [52, 269, 270]. Majorana lattice models can be mapped into Ising models, allowing for a description of their phase diagram. They can exhibit topologically ordered phases and realize the toric code in a perturbative regime [269]. The extension of these analyses to \mathbb{Z}_{2m} PFs may reveal new Hamiltonian realizations of fault-tolerant stabilizer codes [99, 271] for quantum bits with $2m$ states, and hence novel platforms for quantum memories generalizing the toric code [272]. However, for \mathbb{Z}_{2m} PFs the extension to 2D lattices is less immediate than in the Majorana case, partially because of the connection to clock models, which are less

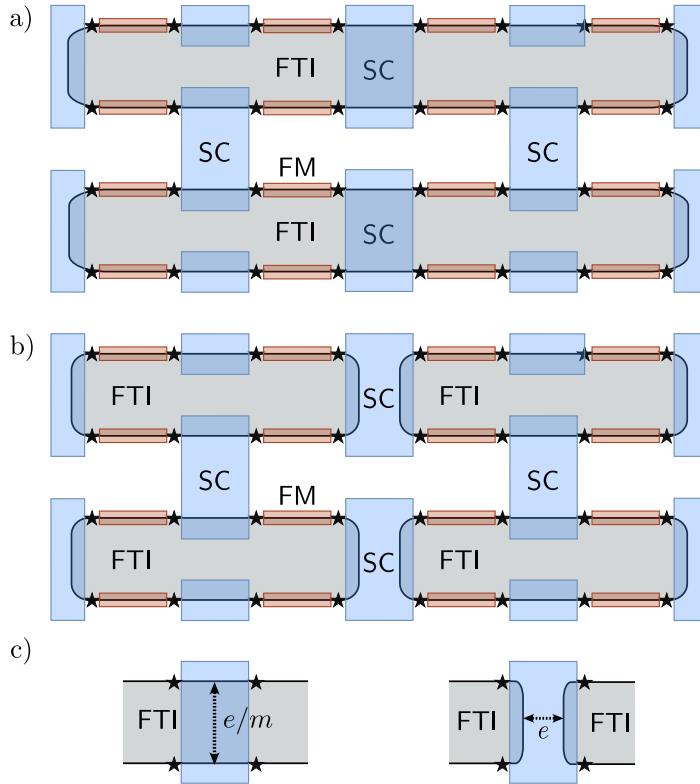


Figure 10.1: The two different 2D architectures considered in this chapter. They are composed of superconductors (SC, blue) and ferromagnets (FM, red) deposited on top of a 2D array of fractional topological insulators (FTI, grey). \mathbb{Z}_{2m} PF zero-modes, marked as black stars, arise at each SC/FM interface along the edge. We consider two possible geometries: in panel (a), the FTIs extend for the whole length of the system, while in panel (b) the FTIs have fixed size. If we enlarged on the horizontal direction the system in panel (a), the number of FTIs would stay constant and the edge length would increase, while the vice versa would happen in panel (b). In the main text, we refer to the two architectures as the *stripe* and *tile* models respectively. As shown schematically in panel (c), the two models can also be distinguished by different tunneling regimes between the two edge segments gapped out by the same superconducting island. If the SC covers a single FTI (left), tunneling of fractional charge e/m may take place between the two edges, while if the SC covers two different FTIs (right), only electron tunneling is allowed, since transport of a fractional charge cannot take place via a topologically trivial bulk. The tile model (b) only has SC islands of this second kind, while the stripe architecture (a) has both.

well understood than Ising models.

In order to fill this gap, in this chapter we consider two distinct 2D architectures of \mathbb{Z}_{2m} PFs, shown in Fig. 10.1. The architectures are obtained from a pattern of superconductors and ferromagnets layered on top of an array of 2D FTIs. The only difference between the two models is the geometry of the underlying FTI array. In Fig. 10.1(a) the array is formed by long stripes of FTIs extending for the whole length of the system, while in Fig. 10.1(b) the stripes are cut in smaller pieces (or tiles) of fixed dimension. For ease of discussion, we shall refer to these two architectures as the *stripe* and *tile* model respectively.

Similarly to Refs. [cite{xu2010}](#), [terhal2012](#), [nussinov2012](#), the effective Hamiltonian of the two models is dictated by two mesoscopic phenomena:

1. the fractional Josephson effect, mediated by the tunneling of e/m quasiparticle between two different superconductors, and
2. the charging energy of the superconductors.

The fractional Josephson effect arising with \mathbb{Z}_{2m} PF zero-modes has already been investigated in Refs. [238, 240], while to our knowledge the interplay between PF zero-modes and Coulomb energy was not considered in previous works.

While both the stripe and the tile architectures give rise to a square lattice of \mathbb{Z}_{2m} PF zero-modes, and despite the fact that the effective Hamiltonian contains the same set of local interactions in both models, we will show that the different geometry of the FTI edges is crucial to determine their properties, which turn out to be quite distinct. Indeed, since different edge geometries yield a different set of commutation rules for the \mathbb{Z}_{2m} PF operators and different physical constraints on the Hilbert space, they can determine different topological properties.

This chapter is organized as follows: in Sec. 10.1 we derive the effective Hamiltonian for the stripe and tile architectures, considering both Josephson and Coulomb energies, and explain the physical constraints and conservation laws specific to each array. In Sec. 10.2 we map the effective Hamiltonian into two different clock models, using two non-isomorphic sets of PF Jordan-Wigner transformations. We analyze the phase diagram of the two models in Sec. 10.3, where we show that the tile model realizes a qudit toric code Hamiltonian in perturbation theory while the stripe model is dual to a gauge theory. We conclude with an outlook in Sec. 10.4.

10.1 Effective Hamiltonian for 2D parafermionic architectures

In the two architectures in Fig. 10.1, each FM/SC interface along the edge of a FTI hosts a PF zero mode. Hence the stripe and tile architectures generate arrays of interacting \mathbb{Z}_{2m} PFs, which are protected by the superconducting and ferromagnetic gaps and thus determine the low-energy physics of the system. In this section we derive an effective Hamiltonian in terms of \mathbb{Z}_{2m} PF operators for a square lattice

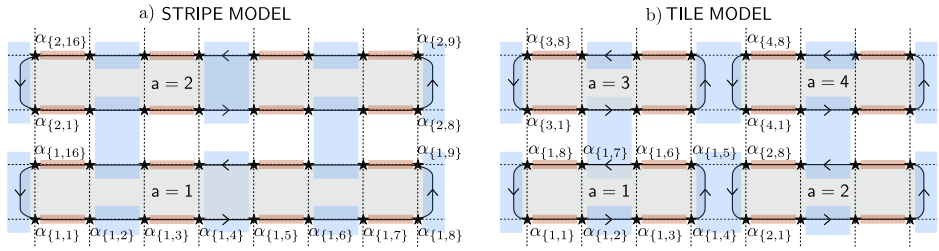


Figure 10.2: A square lattice of \mathbb{Z}_{2m} PF zero-modes of dimensions $L_x = 8$ and $L_y = 4$. To label the PFs, we follow the convention established in the main text: first we order the FTI edges with an index a , and then we order the PFs along each edge with an index j , starting from an arbitrary origin. Each PF zero mode is then denoted as $\alpha_{\{a,j\}}$, and all commutation rules between operators at different sites are fixed unambiguously.

of dimensions $L_x \times L_y$ with open boundaries¹. Generalizations to other boundary conditions can be easily implemented.

Each PF zero mode is described by a second-quantization operator α satisfying the relations:

$$\alpha^{2m} = 1, \quad (10.1)$$

$$\alpha^\dagger = \alpha^{2m-1}. \quad (10.2)$$

We can associate to α and α^\dagger respectively the annihilation and creation of a charge e/m on the adjacent superconductor, in such a way that a Cooper pair is split in $2m$ quasiparticles [239]. Eqs. (10.1-10.2) can be derived from the Luttinger liquid description of the FTI fractional edges, as done in detail in Refs. [238, 239] and as outlined in Appendix 10.A.

Furthermore, these PF operators obey unconventional commutation rules. Denoting two different PF operators with generic, ordered labels μ and ν , we have

$$\alpha_\mu \alpha_\nu = e^{-i\epsilon_{\mu\nu}\pi/m} \alpha_\nu \alpha_\mu, \quad (10.3)$$

$$\alpha_\mu^\dagger \alpha_\nu = e^{+i\epsilon_{\mu\nu}\pi/m} \alpha_\nu \alpha_\mu^\dagger, \quad (10.4)$$

where $\epsilon_{\mu\nu} = -\epsilon_{\nu\mu} = \pm 1$ is a sign that must be fixed by convention. As we outline in Appendix 10.A, Eqs. (10.1-10.4) can be derived from the underlying helical Luttinger liquid theory for the FTI edges. Note that for $m = 1$ the $\epsilon_{\mu\nu}$'s do not play any role and the equations (10.1-10.4) reproduce all the properties of Majorana modes.

In the 1D case, μ and ν are integers denoting the positions of the PFs on a line. All signs are fixed by assigning an orientation to the line, so that $\epsilon_{\mu\nu} = \text{sgn}(\mu - \nu)$. In two dimensions the ordering procedure is slightly more complicated and proceeds in the following way.

¹Note that the geometry of the array constrains L_y to be even and L_x to be a multiple of four.

1. We label each FTI edge of the system with an integer a , thus introducing an ordering of the edges. We also assign a counterclockwise orientation to each edge a .
2. Starting from an arbitrary origin and following the counterclockwise orientation, we label all ferromagnets along the edge with an integer $k = 1, \dots, M$ (similarly to what was done in Ref. [239]). The number M is the total number of FMs along each FTI edge: note that $M = 4$ for the tile model, while $M = L_x$ for the stripe model (see Fig. 10.2).
3. We identify the SC/FM interfaces at the left and the right of each FM with an integer $j = 2k - 1$ or $j = 2k$ respectively.

The PFs α_μ, α_ν are thus labelled by a composite index $\mu = \{a, j\}$, $\nu = \{a', j'\}$ and we fix all the conventional signs as

$$\epsilon_{\mu\nu} = \text{sgn}(a - a') + \delta_{aa'} \text{sgn}(j - j'). \quad (10.5)$$

In Fig. 10.2 we explicitly illustrate the procedure for labeling all the PFs of our square array, in both the tile and stripe architecture. Due to the different number and disposition of the FTIs, the PFs in the stripe model are actually distinct from (non-isomorphic to) the PFs in the tile model. The value of $\epsilon_{\mu\nu}$ may differ for pairs of PFs in the same site of the square lattice, and consequently the set of commutation relations Eqs. (10.3,10.4) is not the same for the two geometries. From the point of view of the physical components, this difference can be traced back to the following fact [see also Fig. 10.1(c)]. In the tile model, the array is fully constituted by SC islands connecting two different FTIs. Quasiparticle tunneling from one FTI edge to the other is forbidden since the two edges are separated by a topologically trivial region. The stripe model, instead, is composed also by a second type of SC island, connecting two edges of the same FTI. In this case, tunneling of a charge e/m from one edge segment to the other is possible, albeit suppressed by the bulk gap, akin to what happens in a fractional quantum Hall constriction [273].

In order to describe physical interactions between PFs, it is useful to introduce the operator

$$P_{\mu\nu} = e^{i\epsilon_{\mu\nu}\pi/2m} \alpha_\nu^\dagger \alpha_\mu, \quad (10.6)$$

defined for every given pair α_μ, α_ν . For $m = 1$, $P_{\mu\nu}$ represents the \mathbb{Z}_2 fermionic parity associated with two Majorana modes. Here we are extending this notion to the \mathbb{Z}_{2m} symmetry of the PFs, and we shall refer to $P_{\mu\nu}$ as \mathbb{Z}_{2m} charge. From its Hermitian conjugate,

$$P_{\mu\nu}^\dagger = e^{-i\epsilon_{\mu\nu}\pi/2m} \alpha_\mu^\dagger \alpha_\nu, \quad (10.7)$$

we see that it is a unitary operator,

$$P_{\mu\nu} P_{\mu\nu}^\dagger = P_{\mu\nu}^\dagger P_{\mu\nu} = 1. \quad (10.8)$$

Moreover $P_{\mu\nu}^{2m} = 1$. Thus its eigenvalues must be the $(2m)$ -th roots of unity,

$$\lambda_n = e^{in\pi/m}, \quad n = 0, 1, \dots, 2m-1. \quad (10.9)$$

A pair α_μ, α_ν can be irreducibly represented on a $2m$ -dimensional Hilbert space, with a basis given by the states $|n\rangle$ such that $P_{\mu\nu}|n\rangle = \lambda_n|n\rangle$. The Hilbert space dimension of a square lattice of PF zero-modes of size $L_x \times L_y$ is therefore $(2m)^{L_x \cdot L_y/2}$.

Now that we have set the basic algebraic rules, we can write down the physical ingredients of the model - Josephson and charging energy. These will form the basic local bonds used to write an effective 2D Hamiltonian for the PFs.

10.1.1 Josephson energy

Thanks to the presence of zero-modes, phase-coherent tunneling of e/m quasiparticles may take place across the ferromagnetic region between adjacent superconductors along a common edge. The resulting Josephson effect is characterized by an anomalous periodicity of $4\pi m$ (in units of the superconducting flux quantum $\Phi_0 = h/2e$), essentially because the tunneling quasiparticle's charge is reduced by a factor $2m$ with respect to the charge of a Cooper pair [42, 238–240]. In other words, the anomalous period reflects the fact that the junction can be in $2m$ different states associated to the \mathbb{Z}_{2m} charge of two PFs located at its ends. Physically, these states are distinguished by the fractional spin of the ferromagnet inside the junction [239], or equivalently by the number of the fractional quasiparticles trapped in it (modulo $2m$).

Using the notation introduced in Fig. 10.2, the \mathbb{Z}_{2m} charge of a junction situated on edge a can be written as

$$P_{\{a,2k-1\},\{a,2k\}} = e^{-i\pi/2m} \alpha_{\{a,2k\}}^\dagger \alpha_{\{a,2k-1\}}. \quad (10.10)$$

It acts as a transfer operator, destroying one e/m charge inside the superconductor on one side of the junction and creating it on the other side. Such tunneling processes can be modeled by an effective Hamiltonian of the form

$$H_J = -\frac{J}{2} \left(e^{i(\delta-\pi)/2m} \alpha_{\{a,2k\}}^\dagger \alpha_{\{a,2k-1\}} + \text{H.c.} \right). \quad (10.11)$$

Here J is the tunneling strength and δ is the phase difference between the two superconductors. The tunneling Hamiltonian splits the states of the junction in $2m$ energy branches given by

$$E_{J,n} = -J \cos \left(\frac{\delta}{2m} + \frac{n\pi}{m} \right) \quad (10.12)$$

with $n = 0, \dots, 2m-1$.

As in the case of Majorana zero-modes [42, 52], the fractional Josephson effect mediated by PF modes prevails over the ordinary Josephson effect mediated by Cooper pairs, which is a higher-order effect. Moreover, the addition of the ordinary Josephson term, with 2π periodicity in the phase difference, would not modify qualitatively our results, thus it is neglected here and in the following.

10.1.2 Charging energy

Let us now consider a single superconducting island of our array, and let us denote with ϕ and $N = -2i \frac{d}{d\phi}$ the phase and number operators of this island. The presence of the PF zero-modes becomes manifest through non-trivial (twisted) boundary conditions in the condensate ground state wave-function $\Psi(\phi)$ [36],

$$\Psi(\phi + 2\pi) = e^{i\pi q} \Psi(\phi). \quad (10.13)$$

Here q represents the charge in units of e inside the superconductor (modulo $2e$). The spectrum of the number operator depends on these twisted boundary conditions, since its twisted eigenfunctions $\chi_s(\phi) = e^{i(s+q/2)\phi} / \sqrt{2\pi}$ satisfy

$$N\chi_s = (2s + q)\chi_s, \quad s \in \mathbb{Z}. \quad (10.14)$$

In a conventional superconductor, $q = 0$, we have periodic boundary conditions, and N counts Cooper pairs. In the presence of Majoranas q may assume either value $\{0, 1\}$ giving periodic or anti-periodic boundary conditions depending on the fermion parity of the superconductor [36]. In the presence of \mathbb{Z}_{2m} PF zero-modes, the possible values of q are extended to fractional values:

$$q = \left\{ \frac{n}{m} \right\} = \left\{ 0, \frac{1}{m}, \frac{2}{m}, \dots, 1, \frac{m+1}{m}, \dots, \frac{2m-1}{m} \right\}. \quad (10.15)$$

The resulting boundary conditions are twisted with possible phases $e^{in\pi/m}$, and the spectrum of N is given by rational numbers with denominator m .

Ground states with different values of q are not anymore degenerate if the charging energy of the superconducting island,

$$H_{\text{ch}} = E_C (N - n_{\text{ind}})^2, \quad (10.16)$$

is taken into account. Here $E_C = e^2/2C$, C is the self-capacitance of the superconductor, and n_{ind} the charge (in units of e) induced on the island by nearby voltage gates.

For our purposes, it is useful to separate the contribution of the fractional charges to the charging energy from that of the Cooper pairs. We will therefore work in a regime which highlights the role of the former, as done in Ref. [84] for Majorana modes. If all superconducting islands are connected to a grounded superconductor via a conventional Josephson junction of energy $E_J \gg E_C$, the superconducting phases are pinned to their classical minima, freezing the bosonic degree of freedom associated with Cooper pairs. The charging energy splits the ground state degeneracy by inducing quantum phase slips. In this semiclassical regime, H_{ch} can be replaced by an effective Hamiltonian of the form [37]

$$H_{\Delta} = -\Delta \cos(\pi q + \pi n_{\text{ind}}). \quad (10.17)$$

The cosine dependence on the charge in this effective Hamiltonian is reminiscent of the Aharonov-Casher effect [274]. When a (Josephson) vortex encircles a superconducting island, it acquires a phase proportional to the charge contained in it. The energy Δ is exponentially small in the ratio E_J/E_C .

Let us now write explicitly the interaction (10.17) in terms of the PF operators. We denote as $q_{a,k}$ the fractional charge trapped inside the segment of an FTI edge a between the k -th and $(k+1)$ -th ferromagnet. As such, it can be expressed as

$$e^{i\pi q_{a,k}} \equiv P_{\{a,2k\}\{a,2k+1\}} = e^{-i\frac{\pi}{2m}} \alpha_{\{a,2k+1\}}^\dagger \alpha_{\{a,2k\}}. \quad (10.18)$$

In the special case $k = M$, Eq. (10.18) has to be supplemented with the boundary condition

$$\alpha_{\{a,2M+1\}} = e^{-i\pi q_a} \alpha_{\{a,1\}}, \quad (10.19)$$

where q_a is the total fractional charge along the edge a . Eq. (10.19) appears naturally in the bosonization description of the PFs as the boundary condition of a closed edge with total charge q_a surrounding no net magnetic flux [239], see also App. 10.A. This boundary condition constitutes a constraint that the physical states of the system must fulfill, as we will discuss more extensively in the final part of this section.

In our 2D architecture, each SC gaps out either one or two segments of an FTI edge, depending on whether it lies at the boundary of the system or in the bulk. In the second case, the total fractional charge q contained in it is the sum of two charges $q_{a,k}$, $q_{a',k'}$ and can be expressed as $e^{i\pi q} = e^{i\pi(q_{a,k}+q_{a',k'})} = P_{\{a,k\}\{a,k+1\}} P_{\{a',k'\}\{a',k'+1\}}$, since two \mathbb{Z}_{2m} charges operators always commute if they do not share a PF operator. The charging energy takes the form

$$H_\Delta = \begin{cases} -\frac{\Delta}{2} \left(e^{i\pi n_{\text{ind}}} e^{-i\pi/2m} \alpha_{\{a,2k+1\}}^\dagger \alpha_{\{a,2k\}} + \text{h.c.} \right) & \text{on the boundary} \\ -\frac{\Delta}{2} \left(e^{i\pi n_{\text{ind}}} e^{-i\pi/m} \alpha_{\{a,2k+1\}}^\dagger \alpha_{\{a,2k\}} \alpha_{\{a',2k'+1\}}^\dagger \alpha_{\{a',2k'\}} + \text{h.c.} \right) & \text{in the bulk} \end{cases} \quad (10.20)$$

The total charges q_a of the FTI edges may appear in the Hamiltonian (10.20) as additional phases, due to Eq. (10.19).

10.1.3 Effective Hamiltonian

Adding together the contributions from all islands and junctions, we arrive to an effective Hamiltonian

$$H = \sum_{\text{islands}} H_\Delta + \sum_{\text{junctions}} H_J. \quad (10.21)$$

Each PF of the array belongs to one superconducting island and one junction and therefore it appears twice in the effective Hamiltonian, once in H_Δ and once in H_J .

Note that the effective Hamiltonian is the same for the stripe and the tile architectures, which share the same lattice, the same number of parafermions and the same set of local interactions. Nevertheless, the presence of two different sets of commutation rules for the PF operators is enough to give the two systems markedly different properties.

10.1.4 Conserved quantities and charge constraints

The two different commutation rules between PFs in the stripe and tile architectures are due to the fact that the Hilbert spaces of the two system are constrained in physically different ways. To see this, notice that the total charge q_a at the edge of each FTI a must be conserved since no term in the Hamiltonian (10.21) introduces tunneling between different fractional topological insulators. That is,

$$[e^{i\pi q_a}, H] = 0 \quad (10.22)$$

for every a . Moreover, the total charge of each FTI (edge plus bulk) is not only conserved but also *constrained* to be an integer multiple of the electron charge e . Thus, if we make the simplifying assumption that there are no fractional excitations trapped in the bulk of the FTIs, we come to the conclusion that all q_a 's must be integer-valued. This requirement restricts the possible eigenvalues of $e^{i\pi q_a}$ to ± 1 , corresponding to the even or odd fermion parity sectors. Without loss of generality, we will assume that each FTI has an even number of electrons, $q_a = 0, \pm 2, \pm 4, \dots$, leading to the set of conditions

$$e^{i\pi q_a} = \prod_{k=1}^M P_{\{a,2k\},\{a,2k+1\}} = 1. \quad (10.23)$$

This choice amounts to restricting the twisted boundary conditions (10.19) to the periodic case.

The constraint (10.23) is violated if a quasiparticle or a quasi-hole is introduced in the bulk of the FTI. Due to the incompressibility of the FTI liquid, this process is related to the presence of an additional flux quantum $\Phi_0 = h/2e$ piercing the bulk FTI [253, 255]. Thus, we can translate the conservation of electric charge on the edge of the FTI into a conservation of the magnetic flux threaded through the bulk. The latter is measured by the Aharonov-Bohm phase of a quasiparticle performing a counter-clockwise loop along the edge of the FTI. Mathematically, the Aharonov-Bohm phase factor is given by the string product Σ_a of the tunneling operators along such loop,

$$\Sigma_a = \prod_{k=1}^M P_{\{a,2k-1\},\{a,2k\}} \quad (10.24)$$

which obeys $[\Sigma_a, e^{i\pi q_a}] = 0$, $[\Sigma_a, H] = 0$ and $(\Sigma_a)^{2m} = 1$ and has eigenvalues $\sigma_a = e^{i\pi n/m}$, $n = 0, \dots, 2m-1$. One can derive from Eqs. (10.3) and (10.4) the commutation rule

$$\Sigma_a \alpha_{\{a,j\}}^\dagger = e^{-i\pi/m} \alpha_{\{a,j\}}^\dagger \Sigma_a, \quad (10.25)$$

which confirms that the operator $\alpha_{\{a,j\}}^\dagger$, creating a charge e/m on the edge of the FTI, at the same time adds $-\pi/m$ to the Aharonov-Bohm phase.

Consistently with the constraint (10.23), we consider as physical only the sector of the full Hilbert space in which

$$\Sigma_a = 1, \quad (10.26)$$

so that the magnetic flux in each FTI must be a multiple of $4m\Phi_0$. Changing the fluxes that pierce each FTI, we choose a different set of eigenvalues σ_a and select a different physical sector.

The differences between the tile and stripe model originate from the fact that, for fixed system size, the number of FTIs is greater in the tile than in stripe model. This in turn determines the number of independent constraints on the Hilbert space, as reflected in the extent M of the product defining the string operator in Eq. (10.24) - we recall that $M = 4$ in the tile model and $M = L_x$ in the stripe model. The result is a different dimensionality of the physical sector of the Hilbert space of the two models.

10.2 Mapping to 2D quantum clock models

To highlight the differences between the two models, it helps to use a mapping onto quantum 2D $2m$ -clock models. These models are defined on a 2D lattice where each site r is a $2m$ -level quantum system and their Hamiltonians possess discrete \mathbb{Z}_{2m} local symmetries. Clock Hamiltonians are defined in terms of degrees of freedom σ_r and τ_r that satisfy

$$\sigma_r^{2m} = \tau_r^{2m} = 1 \quad (10.27)$$

$$\tau_r^\dagger = \tau_r^{-1}, \quad \sigma_r^\dagger = \sigma_r^{-1}. \quad (10.28)$$

Operators on any given site have commutation rules similar to those of PFs,

$$\sigma_r \tau_r = e^{i\pi/m} \tau_r \sigma_r \quad (10.29)$$

but operators on different sites commute. If $m = 1$ these relations are satisfied by Pauli matrices σ_r^z, σ_r^x . In the mathematical literature, the algebra describing PFs is known as a generalized Clifford algebra. Its representation theory has been worked out in detail in Refs. [275, 276], and from it, it is possible to infer a mapping relating the PF operators α and the clock operators σ, τ . This mapping can be achieved via a parafermionic Jordan-Wigner transformation [235, 275, 277].

To each couple of adjacent PFs $\alpha_{\{a,2k\}}, \alpha_{\{a,2k+1\}}$ on the same superconductor, we associate a couple of operators $\sigma_{a,k}, \tau_{a,k}$. These operators therefore live on (a subset of) the links of the square lattice defined by the PFs. The mapping between PFs and clock operators is given by

$$\alpha_{\{a,2k\}} = \kappa_a \sigma_{a,k+1} \prod_{1 \leq l \leq k} \tau_{a,l} \quad (10.30)$$

$$\alpha_{\{a,2k+1\}} = \kappa_a e^{i\frac{\pi}{2m}} \tau_{a,k+1} \sigma_{a,k+1} \prod_{1 \leq l \leq k} \tau_{a,l} \quad (10.31)$$

Here κ_a are fractional Klein factors taking care of the commutation rules between parafermions on different edges [278, 279],

$$\kappa_a^{-1} = \kappa_a^\dagger \quad (10.32)$$

$$\kappa_a \kappa_{a'} = e^{i \text{sgn}(a'-a)\pi/m} \kappa_{a'} \kappa_a. \quad (10.33)$$

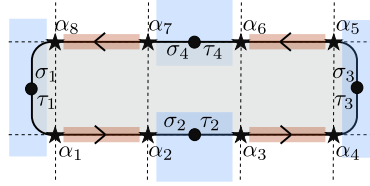


Figure 10.3: The transformation defined in Eqs. (10.30), (10.31) maps the PF operators living on the sites of a square lattice into a set of clock operators σ, τ defined on the links of the lattice occupied by a superconductor (marked in figure as black dots). Here, as an example, we show the positions of the clock operators in the case of a FTI in the tile model. The mapping between $\alpha_1 \dots, \alpha_8$ and $\sigma_1, \tau_1, \dots, \sigma_4, \tau_4$ shown in this figure is explicitly written down in Eq. (10.37).

These commutation rules must be compared with Eqs. (10.3,10.4,10.5). Apart from fixing the commutators, the Klein factors do not play a role and drop out from any quadratic operator considered in this chapter. The boundary conditions (10.19) and the constraints (10.23),(10.26) are taken into account by setting

$$\sigma_{a,M+1} = \sigma_{a,1} \quad (10.34)$$

$$\tau_{a,M+1} = \tau_{a,1} \quad (10.35)$$

$$\prod_{k=1}^M \tau_{a,k} = 1 \quad (10.36)$$

Let us write down an explicit example of the transformation for the case $M = 4$, relevant for the tile architecture. In this case the relations (10.30) and (10.31), dropping the index a and the Klein factors for clarity, read (see also Fig. 10.3)

$$\begin{aligned} \alpha_8 &= \sigma_1, & \alpha_1 &= e^{i\frac{\pi}{2m}} \tau_1 \sigma_1, \\ \alpha_2 &= \sigma_2 \tau_1, & \alpha_3 &= e^{i\frac{\pi}{2m}} \tau_2 \sigma_2 \tau_1, \\ \alpha_4 &= \sigma_3 \tau_2 \tau_1, & \alpha_5 &= e^{i\frac{\pi}{2m}} \tau_3 \sigma_3 \tau_2 \tau_1, \\ \alpha_6 &= \sigma_4 \tau_3 \tau_2 \tau_1, & \alpha_7 &= e^{i\frac{\pi}{2m}} \tau_4 \sigma_4 \tau_3 \tau_2 \tau_1. \end{aligned} \quad (10.37)$$

We now rewrite the Hamiltonian in terms of the clock operators. For the Josephson energy, Eq. (10.11), we obtain

$$H_J = -\frac{J}{2} \left(e^{i\delta/2m} \sigma_{a,k+1}^\dagger \sigma_{a,k} + \text{h.c.} \right), \quad (10.38)$$

while the charging energy, Eq. (10.20), becomes

$$H_\Delta = \begin{cases} -\frac{\Delta}{2} (e^{i\pi n_{\text{ind}}} \tau_{a,k} + \text{h.c.}) & \text{on the boundary} \\ -\frac{\Delta}{2} (e^{i\pi n_{\text{ind}}} \tau_{a,k} \tau_{a',k'} + \text{h.c.}) & \text{in the bulk} \end{cases} \quad (10.39)$$

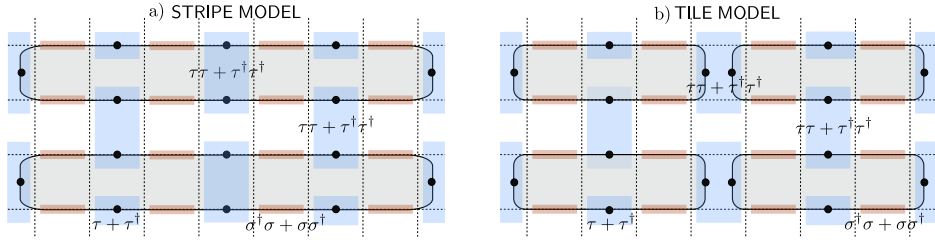


Figure 10.4: Layout of the stripe and tile architecture in terms of clock operators σ , τ (black dots), living on the links of the square lattice occupied by a superconductor. Since clock operators at different sites commute, it is not necessary to order the FTI nor to assign an orientation to the FTI edges. However, notice that the clock operators for the two models live on two inequivalent lattices.

Note that the locality of the interactions is preserved. At this point, it is useful to split the array Hamiltonian of Eq. (10.21) into bulk and boundary contributions,

$$H = H_{\text{bulk}} + H_{\text{boundary}}, \quad (10.40)$$

with

$$H_{\text{bulk}} = -\left[\frac{J}{2} \sum_{\text{junctions}} \sigma_{a,k+1}^\dagger \sigma_{a,k} + \frac{\Delta}{2} \sum_{\substack{\text{islands} \\ \in \text{bulk}}} \tau_{a,k} \tau_{a',k'}^\dagger\right] + \text{h.c.} \quad (10.41)$$

and

$$H_{\text{boundary}} = -\frac{\Delta}{2} \sum_{\substack{\text{islands} \\ \in \text{bdr}}} \left(\tau_{a,k} + \tau_{a,k}^\dagger \right), \quad (10.42)$$

see also Fig. 10.4. In writing Eqs. (10.41), (10.42) we have, for simplicity, set $n_{\text{ind}} = 0$ for all islands and, in agreement with our choice of the physical sector, $\delta = 0$ for all junctions. Then the couplings J, Δ become purely real and all equal.

Splitting the Hamiltonian into bulk and boundary contributions is useful for studying various boundary conditions. For simplicity, in the remainder of this chapter we will set $H_{\text{boundary}} = 0$ and focus on bulk properties of the array, assuming the system size is large enough to justify neglecting H_{boundary} . Also $H_{\text{boundary}} = 0$ corresponds (for any system size) to the exact boundary conditions in case every superconducting island at the boundary of the array is grounded (since in that case $\Delta = 0$ at the boundary).

The Hamiltonian H_{bulk} of Eq. (10.41) commutes with an extensive set of local operators

$$\xi_s = \sigma_{a,k} \sigma_{a',k'}^\dagger, \quad [\xi_s, H] = 0, \quad (10.43)$$

associated to every bulk superconducting island s for both the tile and stripe models. Notice however that only those operators ξ_s that commute with the constraints

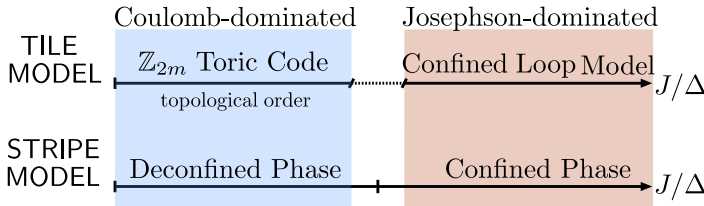


Figure 10.5: Sketch of the phase diagram of the two models, as outlined in the introduction to Sec. 10.3. We distinguish between two regimes, depending on whether Coulomb or Josephson energy dominates. The Coulomb regime shows, for both models, a non-local behavior, with degenerate ground states distinguished by the expectation values of string-operators. Only the tile model, however, presents a truly topological order characterized by anyonic excitations (see Sec. 10.3.1). The stripe model is instead dual to a \mathbb{Z}_{2m} lattice gauge theory (see Sec. 10.3.2) which undergoes a deconfinement/confinement phase transition with increasing J/Δ [280].

described in the previous section are actual physical symmetries: if $a \neq a'$, the operator (10.43) moves one fractional charge from one edge to the other, thus violating the charge constraint.

The difference between the tile and the stripe architectures can now be better appreciated, as shown in Fig. 10.4. The effective Hamiltonian (10.21) associated to either architecture is defined on the square lattice in terms of PFs. In contrast, H_{eff} is defined on inequivalent lattices when represented in terms of clock operators as in Eq. (10.41). The tile model Hamiltonian H_{tile} is obtained by specializing H_{bulk} to a decorated square lattice, while the stripe model Hamiltonian H_{stripe} is obtained by specializing H_{bulk} to a brick-wall lattice.

10.3 Topological phases and orders

The quantum phase diagram of the tile and stripe models at zero temperature is controlled by the single parameter J/Δ . In the following we will call *Coulomb-dominated* the regime $\Delta \gg J$ and *Josephson-dominated* the opposite regime $J \gg \Delta$. In this section we study the two regimes for both models, with a focus on the presence (or absence) of topological order. We dedicate Sec. 10.3.1 to the tile model and Sec. 10.3.2 to the stripe model. Let us summarize, here and in Fig. 10.5, the main findings.

The Josephson-dominated regime shows no topological features for either model. On one hand, the ground state of the tile model is singly degenerate in this limit due to the charge constraints. Moreover, exactly at $\Delta = 0$, the ground wave function reduces to a product state of wave functions for local four-body clusters, emphasizing the absence of long-range entanglement. On the other hand, at $\Delta = 0$ the stripe model reduces to a system of decoupled, one-dimensional vector Potts chains in zero

transverse field. Hence, in the thermodynamic limit, the stripe model has ferromagnetic order in the Josephson-dominated regime $J \gg \Delta$. The charge constraints do not suffice to select a unique ground state like for the tile model, but rather correlates the magnetization for pairs of chains.

In the opposite Coulomb-dominated regime, and specifically at $J = 0$, both the tile and stripe models show dramatically increased (relative to $\Delta = 0$) ground-manifold degeneracy. This suggests that at least one phase transition separates the two regimes in the thermodynamic limit for both models.

We will show that the tile model is topologically ordered in the Coulomb-dominated regime, since

1. the degeneracy of its ground manifold depends on the topology of the lattice, and
2. the model has anyonic excitations completely equivalent to those in the qudit toric code with \mathbb{Z}_{2m} discrete symmetry [272, 281].

The second point is especially noteworthy, since the tile model is akin but neither strictly equivalent to the \mathbb{Z}_{2m} toric code by Kitaev [5] nor to its generalizations [272, 281].

Unlike the tile model, which can be defined naturally on a surface of arbitrary genus due to the limited extension of its FTIs, the stripe model fits naturally only open, cylindrical, or periodic (toroidal) boundary conditions. We will see that in the Coulomb-dominated regime its ground state degeneracy is not protected against local operators. Hence we do not consider the stripe model topologically ordered. We will argue nevertheless that the $\Delta \gg J$ regime is characterized by a non-local order parameter, which we will define using a duality mapping the stripe model to the \mathbb{Z}_{2m} lattice gauge theory [280]. Thus, even in the absence of a topological order, the Coulomb-dominated phase of the stripe model can be addressed more generically as a topological phase.

The connection between topological order and lattice gauge theories in Josephson junction arrays has already been the subject of detailed studies, for both \mathbb{Z}_2 symmetric models [282–284] and more general Abelian and non-Abelian gauge symmetries [285]. These models are based on superconducting architectures of Josephson junctions, where the required degeneracies are obtained with fine tuned magnetic fluxes. Such architectures can present topological phases in the Josephson-dominated regime, as experimentally verified in Ref. [286]. The two models studied differ in two important aspects: the absence of fine-tuning to create and control the elementary components of the arrays, which is due to the topological origin of the PF modes, and the fact that the topological phases are obtained in the Coulomb-dominated regime, essentially exchanging the role of electric and magnetic excitations with respect to Ref. [282].

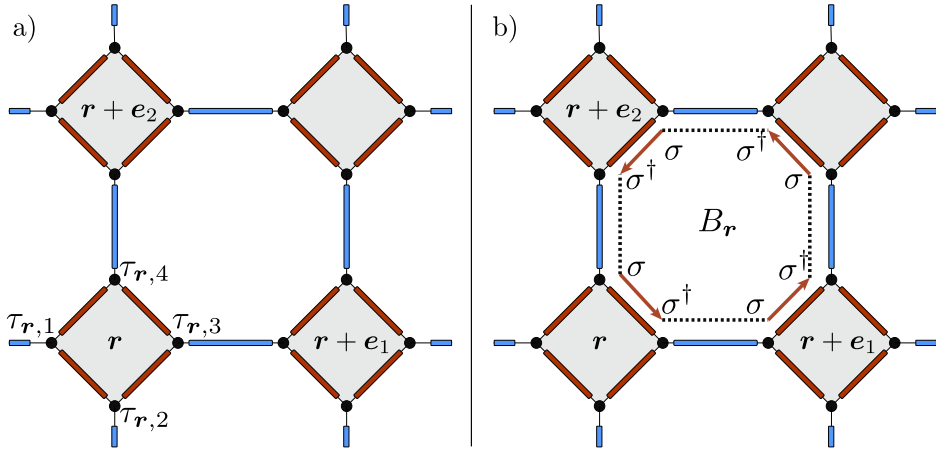


Figure 10.6: Panel (a): The notation adopted for the decorated square lattice on which the tile model can be conveniently rearranged. The grey diamonds, sitting on the sites r of a square lattice, are FTI. To each site r there correspond four clock operators $\sigma_{r,i}, \tau_{r,i}$, arranged counterclockwise. Blue links are SC, red links are FM. Panel (b): The operator B_r in Eq. (10.48) is the counterclockwise product of four $\sigma\sigma^\dagger$ operators around the same plaquette.

10.3.1 A physical realization of \mathbb{Z}_{2m} toric code anyons: the tile model

To analyze the effective Hamiltonian for the tile architecture, it is useful to adopt a decorated square lattice where each FTI sits on a site $r = ie_1 + je_2$, with (i, j) a pair of integers, see Fig. 10.6. In this lattice, the array Hamiltonian H_{bulk} of Eq. (10.41) is given by

$$H_{\text{tile}} = - \left[\frac{J}{2} \sum_r \sum_{i=1}^4 \sigma_{r,i}^\dagger \sigma_{r,i+1} + \frac{\Delta}{2} \sum_{\langle r, r' \rangle} Q_{\langle r, r' \rangle} \right] + \text{h.c.} \quad (10.44)$$

where $Q_{\langle r, r' \rangle}$ labels the charging energy terms of the superconducting islands, now sitting on the links of the square lattice between two neighboring diamonds,

$$Q_{\langle r, r+e_1 \rangle} = \tau_{r,3} \tau_{r+e_1,1}, \quad Q_{\langle r, r+e_2 \rangle} = \tau_{r,4} \tau_{r+e_2,2}. \quad (10.45)$$

Let us now consider the limit $J = 0$ deep in the Coulomb-dominated regime. The system is then in a limit state where tunneling between islands is forbidden. Each superconductor minimizes the charging energy in the space of physical states specified by the charge constraints:

$$Q_{\langle r, r+e_1 \rangle} = Q_{\langle r, r+e_2 \rangle} = 1. \quad (10.46)$$

These conditions allow for $(2m)$ -fold degeneracy for each superconducting link, corresponding to the presence of the local symmetries (10.43). However in the sector

of physical states we must impose the constraints

$$\prod_{i=1}^4 \tau_{r,i} = 1 \quad (10.47)$$

derived from Eq. (10.23). Nearly half of the previous states are then projected out, leaving a ground state manifold of dimension $(2m)^{\#SC/2}$. This number is exact asymptotically in the system size, but depends slightly on the boundary conditions. For example, for periodic boundary conditions the *exact* degeneracy of the ground manifold is $(2m)^{1+(\#SC/2)}$.

The degeneracy of the Coulomb-dominated limit at $J = 0$ is partially lifted when weak tunneling terms are reintroduced, that is, we allow $J \neq 0$. The Coulomb-dominated regime $J \ll \Delta$ can be treated perturbatively by introducing an effective low-energy Hamiltonian affecting only the ground state manifold at $J = 0$. We need to keep only those operators in the perturbative expansion that do not couple the ground state manifold to the excited states. This is a standard technique [287], and the computation is analogous to the perturbative derivation of the \mathbb{Z}_2 toric code Hamiltonian from Kitaev's honeycomb model [78], so we will only streamline the essential points.

At first order, the perturbation $\sigma_{r,i}^\dagger \sigma_{r,i+1}$ creates two charged $\pm e/m$ excitations on adjacent superconductors, increasing the energy of the system by an amount $G = 2\Delta(1 - \cos \pi/m)$. Similarly, at all odd orders we obtain terms that we neglect as they do not leave the $J = 0$ ground state manifold invariant. At second order, we obtain only terms describing the tunneling back and forth of a fractional charge e/m across a single Josephson link. These terms renormalize the ground energy level, that is, they provide an energy offset to the full Hamiltonian. At fourth order we obtain the first relevant contribution. It is a plaquette operator of the form (see Fig. 10.6)

$$B_r = (\sigma_{r,4} \sigma_{r,3}^\dagger) \times (\sigma_{r+e_1,1} \sigma_{r+e_1,4}^\dagger) \times \dots \times (\sigma_{r+e_1+e_2,2} \sigma_{r+e_1+e_2,1}^\dagger) \times (\sigma_{r+e_2,3} \sigma_{r+e_2,2}^\dagger), \quad (10.48)$$

describing the tunneling of an e/m excitation along a loop of four FTI edges and four superconducting islands. The resulting perturbative Hamiltonian reads

$$H_{\text{pert}}^{\text{tile}} = -\left[\frac{\Delta}{2} \sum_{\langle r, r' \rangle} Q_{\langle r, r' \rangle} + \frac{5J^4}{4G^3} \sum_r B_r \right] + \text{h.c.} \quad (10.49)$$

where we note that, in the case $m = 1$, the coefficient of B_r matches the one obtained in a similar perturbative expansion in Ref. [269], where equivalent plaquette operators are obtained.

Since the operators B_r commute with the charge constraints, the space of physical states for the perturbative Hamiltonian $H_{\text{pert}}^{\text{tile}}$ is left untouched. The bond operators $Q_{\langle r, r' \rangle}$ and B_r , together with their Hermitian conjugates, constitute a completely

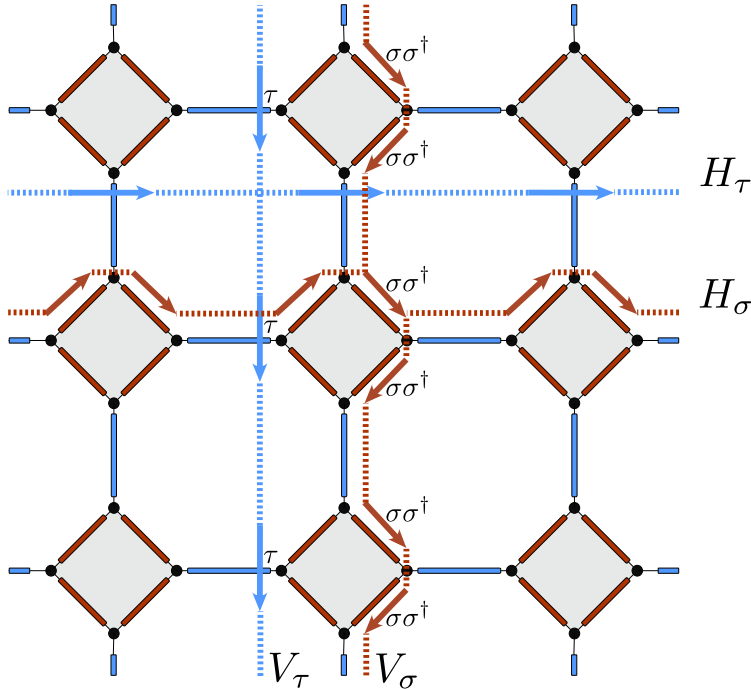


Figure 10.7: The four non trivial loop operators that define the ground state manifold of the tile model on a torus. The operators H_τ, V_τ are defined as the product of all τ along the path described by the two blue lines, in the order established by the arrows. Similarly, the operators H_σ, V_σ are defined as the product of all $\sigma\sigma^\dagger$ operators along the path given by the red lines. Loop operators corresponding to different paths only differ by a product of stabilizer operators $Q_{\langle r, r' \rangle}$ or B_r .

commuting set of stabilizers for a qudit surface code [272]. This surface code protects against every local error that excites a ground state of H_{pert} into a state of higher energy [272]. In particular, the $Q_{\langle r, r' \rangle}$ operators enforce the absence of charge excitations in the superconducting islands, while the B_r operators enforce the absence of flux excitations.

Let us note that the Hamiltonian $H_{\text{pert}}^{\text{tile}}$ is not exactly equivalent to the \mathbb{Z}_{2m} toric code originally discussed by Kitaev in Ref. [5], since the stabilizers $Q_{\langle r, r' \rangle}$ and B_r are not projectors. The construction of these operators is instead more closely related to the qudit surface codes introduced in Ref. [272] - although, strictly speaking, $H_{\text{pert}}^{\text{tile}}$ is not equivalent to those models as well, since it is not possible to canonically associate our stabilizers $Q_{\langle r, r' \rangle}$ and B_r to vertices and faces of a two-dimensional simplicial complex. Despite these minor differences, however, the topological properties of these models are the same.

The conditions

$$Q_{\langle r, r' \rangle} = 1, \quad B_r = 1, \quad \prod_i \tau_{r,i} = 1, \quad (10.50)$$

specify the ground manifold of the system. Its degeneracy can be determined from symmetry considerations. On the torus (periodic boundary conditions) there are four types of loop symmetries $H_\tau, H_\sigma, V_\tau, V_\sigma$, defined in Fig. 10.7, associated to non-contractible loops and compatible (commuting) with the charge constraints. It is interesting to notice (for comparison with other \mathbb{Z}_{2m} surface codes in the literature) that the loop symmetries $H_\tau, V_\tau, (H_\sigma, V_\sigma)$ are disjoint, that is, they do not have any clock degrees of freedom in common. As usual, any two loop symmetries of a given type, τ or σ , associated to equivalent but different non-contractible loops differ only by a product of the stabilizer operators in (10.50) (or their hermitian conjugate). Hence, in the ground manifold, all these loop symmetries collapse into just four inequivalent ones. These form two non-commuting pairs,

$$H_\tau V_\sigma = e^{-i\pi/m} V_\sigma H_\tau, \quad (10.51)$$

$$H_\sigma V_\tau = e^{-i\pi/m} V_\tau H_\sigma, \quad (10.52)$$

while $[H_\tau, H_\sigma] = [V_\tau, V_\sigma] = [V_\tau, H_\sigma] = [H_\tau, H_\sigma] = 0$. Since $V_\sigma^{2m} = 1 = H_\sigma^{2m}$, it follows that each pair identifies $2m$ different ground states, yielding a ground state degeneracy of $(2m)^2$. This is the dimension of the code space defined by $H_{\text{pert}}^{\text{tile}}$.

Our stabilizer code can be adapted to a planar geometry with open boundary conditions along the lines set in Ref. [99]. In this case there will be only two non-trivial string operators and thus $2m$ ground states. In planar geometries with g holes, the ground-state manifold degeneracy increases to $(2m)^g$.

The Hamiltonian $H_{\text{pert}}^{\text{tile}}$ has two different types of excitations illustrated in Fig. 10.8:

1. Two localized charge excitations $\pm e/m$ can be created on two different links by an open string of tunneling operator of the form $S = \prod (\sigma \sigma^\dagger)$. The operator S^\dagger switches the sign of the charges at the end of the open string.
2. Two $\pm h/2e$ vortices are created on neighboring plaquettes by one of the two operators τ on the link separating the plaquettes. (The other τ operator belonging to the same link creates the same vortices, but with opposite sign.) The vortices can be moved apart without further energy costs applying a string $T = \prod \tau$ of consecutive τ operators sharing one common plaquette.

Both charge and flux excitations are bosons when considered separately (since different S operators commute with themselves, as well as different T operators). However, when a charge excitation is moved in a loop around a flux excitation, the wave function will acquire a (Aharonov-Bohm) phase $e^{i\pi/m}$, implying that charges and flux excitation are mutually Abelian anyons with a fractional exchange phase $e^{i\pi/2m}$. This can be verified by computing the commutator of a pair of S and T strings intersecting each other. Additionally, the underlying \mathbb{Z}_{2m} symmetry allows the presence of multiple

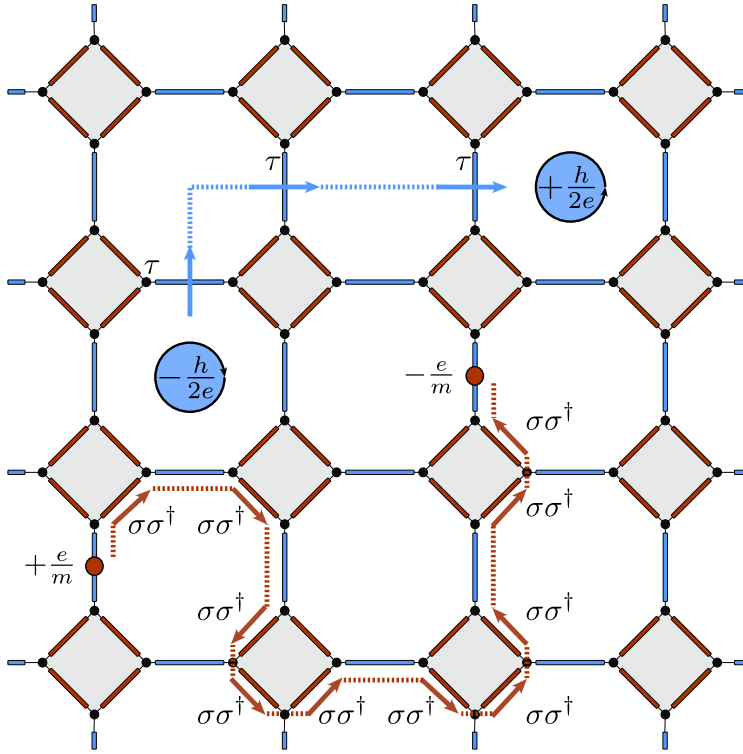


Figure 10.8: Vortex and charge excitations in the tile model, appearing at the ends of open string of τ and $\sigma\sigma^\dagger$ operators respectively. The vortices live on the plaquettes of the lattice, while the charges on the superconducting links. They are mutual Abelian anyons, with an exchange phase $e^{i\pi/2m}$.

excitations of charge ne/m and flux $nh/2e$, with $n = 0, \dots, 2m - 1$, created by the n -th power of S and T operators, as in the usual qudit surface codes [272].

Let us discuss possible terms that may destroy the topological order. Higher orders in perturbation theory yield larger loop operators, which can be decomposed in terms of products of B_r operators and their powers. These higher-order terms commute with $H_{\text{pert}}^{\text{tile}}$ and strengthen the absence of fluxes in the plaquettes, leaving the ground-state manifold intact. The description breaks down only when the perturbation order L is equal to the system size. At this point, the loop operators H_σ, V_σ are generated in the perturbative expansion, lifting the ground-state degeneracy by an energy $O(J^L/\Delta^{L-1})$.

However, we may worry about external perturbations of the form

$$h \sum_{r,i} (\tau_{r,i} + \tau_{r,i}^\dagger), \quad (10.53)$$

which would break the ground state degeneracy. This perturbation corresponds to

an external magnetic field in the vector Potts description and may drive a transition from the topologically ordered phase to a topologically trivial one constituted by a condensate of the vortex excitations. For the \mathbb{Z}_3 toric code, this transition was observed numerically in Ref. [281]. A general analysis [288, 289] of the phase diagram of \mathbb{Z}_p ($p = 2, 3, \dots$) Wen-Levin models [290] suggests that the transition, in the 2+1D transverse-field Potts universality class, is of the first order for any $p > 3$ ($m > 1$), thus easily detectable due to the discontinuity in the energy density. Our model however is of the vector Potts (rather than simple Potts) type and further investigations are required to assert the equivalence of the two cases for generic m .

Finally, let us briefly discuss the Josephson-dominated regime. The topological order in the Coulomb-dominated regime of the tile model disappears when the tunneling terms become comparable to the charging energy. In the opposite extreme limit, $\Delta = 0$, the FTIs decouple and the Hamiltonian is just the sum of the Josephson interactions along each diamond of the lattice in Fig 10.6. In particular, to minimize the energy, the four clock operators σ for each FTI must be aligned and, considering the charge constraint (10.36), one obtains that the ground state of each FTI is constituted by an equal superposition of all the polarizations:

$$|GS\rangle_r = \frac{1}{\sqrt{2m}} \sum_{k=0}^{2m-1} |\sigma_{r,1} = \sigma_{r,2} = \sigma_{r,3} = \sigma_{r,4} = e^{i\frac{k\pi}{m}}\rangle. \quad (10.54)$$

Thus the total ground state is simply the product of the states $|GS\rangle_r$ of all the FTIs. Due to the charge constraints, it is unique independently of the topology of the system.

For fixed system size, the ground state will remain non-degenerate also when we consider a small charging energy contribution, $\Delta \ll J$, in the Josephson-dominated regime. In particular the effect of applying all the charging operators $Q_{\langle r, r' \rangle}$ in a closed area \mathcal{S} is to rotate all the clock operators σ inside \mathcal{S} . The result is the formation of a domain wall constituted by all the links along the edge of \mathcal{S} , where the clock operators are not aligned anymore. The energy cost of the domain wall is proportional to $J\partial\mathcal{S}$, where $\partial\mathcal{S}$ is the number of broken Josephson links along the perimeter of \mathcal{S} . Therefore, the Hamiltonian in the Josephson dominated regime can be seen as the confined phase of a loop model [291], where the loops are the edges of domains with different spin alignment: J provides a tension to the loops whereas Δ constitutes their kinetic energy. Between the topologically ordered Coulomb-dominated regime and the topologically trivial Josephson-dominated regime other phases may appear and the full phase diagram of the tile model deserves further investigations.

10.3.2 The stripe model and the \mathbb{Z}_{2m} gauge theory

As anticipated at the end of the previous section, the stripe model is naturally supported on a brick-wall lattice. It is convenient to place the clock degrees of freedom $\sigma_{(i,j)}$ and $\tau_{(i,j)}$ on the sites

$$\{(i,j) \mid i = 0, \dots, L_x - 1, \quad j = 0, \dots, L_y - 1\}$$

of an $L_x \times L_y$ square lattice and distinguish between the two sub-lattices defined by the conditions $(i+j) = \text{even}$ and $(i+j) = \text{odd}$. In the bulk of this geometry the stripe model becomes the generalization of the XXZ honeycomb compass model [270] with \mathbb{Z}_{2m} symmetry:

$$H_{\text{stripe}} = -\left[\frac{\Delta}{2} \sum_{i+j=\text{even}} Q_{(i,j)} + \frac{J}{2} \sum_{j=0}^{L_y-1} \sum_{i=0}^{L_x-2} \sigma_{(i,j)} \sigma_{(i+1,j)}^\dagger\right] + h.c. \quad (10.55)$$

with

$$Q_{(i,j)} \equiv \tau_{(i,j)} \tau_{(i,j+1)}. \quad (10.56)$$

Depending on the chosen boundary condition, H_{stripe} must be supplemented with an additional boundary term that we will disregard for the sake of simplicity. The stripe unitary operators

$$S_j S_{j+1} = \prod_{i=0}^{L_x-1} Q_{(i,j)}, \quad j = 0, 2, \dots, L_y - 2 \quad (10.57)$$

represent the physical constraint on the electric charge of the FTIs, Eq. (10.36); therefore the physical states $|\Psi\rangle$ must satisfy:

$$S_j S_{j+1} |\Psi\rangle = |\Psi\rangle, \quad j = 0, 2, \dots, L_y - 2. \quad (10.58)$$

The next task is to specify the physical symmetries of the stripe model. The set of non-trivial unitary operators that commute with H_{stripe} is generated by

$$S_j = \prod_{i=0}^{L_x-1} \tau_{(i,j)}, \quad j = 0, 1, \dots, L_y - 1, \quad (10.59)$$

$$\xi_{(i,j)} = \sigma_{(i,j)} \sigma_{(i,j+1)}^\dagger, \quad i+j = \text{even}. \quad (10.60)$$

We need to specify those operators in this set that also commute with the charge constraints of Eq. (10.58). The symmetries S_j trivially satisfy this condition, but they are not all independent in the sector of physical states. We can keep

$$S_j, \quad j = 0, 2, \dots, L_y - 2, \quad (10.61)$$

as an independent set of one-dimensional symmetries for the stripe model. As explained in the introduction to this section, these symmetries are spontaneously broken in the Josephson-dominated regime (at zero temperature). The effective dimensional reduction displayed by the stripe model in this regime is intimately connected to the one-dimensional symmetries of Eq. (10.61) [270].

The local physical symmetries of the stripe model are given by the minimal combination of the operators $\xi_{(i,j)}$ that commute with the charge constraints and they assume the form

$$B_{(i,j)} = \xi_{(i,j)} \xi_{(i+2,j)}^\dagger, \quad i+j = \text{even}. \quad (10.62)$$

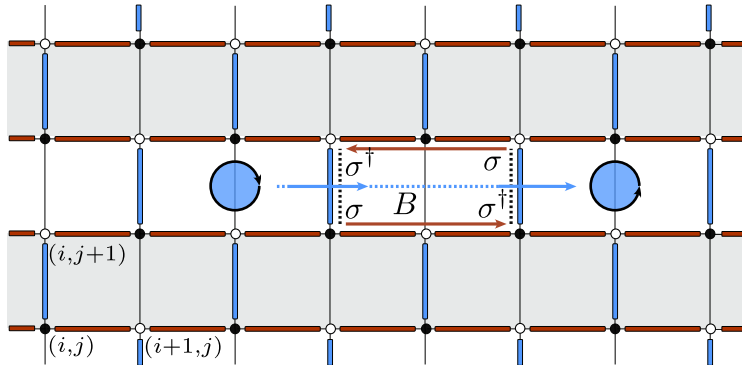


Figure 10.9: Notation adopted to study the stripe model. The black and white sites identify clock operators σ, τ , distinguished by a sub-lattice degree of freedom. Grey stripes are FTI, blue links are superconductors and red links ferromagnets. Notice that half of the vertical links are missing, thus the stripe model is effectively defined on a brick-wall lattice. The flux threaded through a single plaquette of the lattice is measured by the operator B in the figure (see Eq. (10.62)). As in the tile model, flux excitations (the oriented blue circles) can be created by an open string of τ operators: however, the geometry constrains their movement in the horizontal direction.

These local symmetries have an immediate interpretation: they describe the Aharonov-Bohm phase associated to the magnetic fluxes threading the plaquettes of the brick-wall lattice (see Fig. 10.9).

The stripe model has no global symmetries independent on the lower-dimensional symmetries already discussed. The global symmetry $S_1 S_3 \dots S_{L_y-1}$ is trivially spontaneously broken in the Josephson-dominated regime by the spontaneous breakdown of its one-dimensional constituents. Other global symmetries appear as products of the local symmetries discussed in the previous paragraph, and so cannot be spontaneously broken by Elitzur's theorem [292]. This suggests that any ordered phase of the stripe model (outside the Josephson-dominated limit) must be characterized in terms of a generalized, non-local order parameter [293]. However this is not enough to assert that the system shows topological order according to our previous definition based on the topological ground state degeneracy and the presence of anyonic excitation. Rather, in the absence of a Landau local order parameter, we speak more generically of topological phases.

To the purpose of comparing the tile and stripe models in the Coulomb-dominated regime it is useful to perform a perturbative analysis also of the stripe model in the limit $\Delta \gg J$. Just as for the tile model, the first non-trivial term appears at the fourth order in perturbation theory, where the perturbative Hamiltonian of the stripe model

becomes:

$$H_{\text{stripe}}^{\text{pert}} = - \sum_{i+j=\text{even}} \left[\frac{\Delta}{2} Q_{(i,j)} + \frac{5J^4}{4G^3} B_{(i,j)} \right] + \text{h.c.} \quad (10.63)$$

As in the case of the tile model, also for this Hamiltonian it is possible to define localized fractional charge excitations and vortex excitations as end of open strings of τ and $\sigma\sigma^\dagger$ operators. However, for this architecture the vortex excitations can propagate only in the horizontal direction, as can be realized noting that superconductors of different rows share no common plaquette.

Indeed, in the Hamiltonian $H_{\text{stripe}}^{\text{pert}}$ each row of superconducting islands is decoupled from the others, and is characterized by a ground state degeneracy of $2m$. However, the rows between different FTIs present a non-physical symmetry ξ which does not commute with the constraint (10.58). Thus, accounting for the charge constraints, the overall degeneracy of the ground states in the physical sector is $(2m)^{\#FTIs}$. Crucially, this degeneracy is not protected against the local symmetries $\xi_{(i,j)}$. Since these local operators may cause transitions between different ground states, the stripe model does not possess a proper topological order. Despite this fact, the model is characterized by a non-local order parameter, as we will discuss in the following.

To this purpose, and more in general to investigate the phase diagram, it is useful to exploit the bond-algebraic theory of dualities [266, 294] which allows us to study the bulk properties of the constrained stripe Hamiltonian for large system size. Our strategy will be to find a duality (consistent with the constraints), mapping H_{stripe} to a known model. As shown in Refs. [266, 294], quantum dualities can be obtained as isomorphisms of bond algebras of interactions preserving locality. In principle, we could study the minimal bond algebra of interactions generated by the bonds $Q_{(i,j)}$ ($i+j = \text{even}$) and $\sigma_{(i,j)}\sigma_{(i+1,j)}^\dagger$ in H_{stripe} . However, a duality derived from this bond algebra, that is, an alternative local representation of these interactions, may not preserve the charge constraints of Eq. (10.58), because these constraints are not contained in this minimal bond algebra. Hence we consider a larger set of generators

$$\begin{aligned} Q_{(i,j)}, & \quad i = 0, \dots, L_x - 1; \quad j = 0, \dots, L_y - 2; \\ \sigma_{(i,j)}\sigma_{(i+1,j)}^\dagger, & \quad i = 0, \dots, L_x - 2; \quad j = 0, \dots, L_y - 1 \end{aligned}$$

(and Hermitian conjugates) for the stripe model's bond algebra $\mathcal{A}_{\text{stripe}}$. That is, we are including also the bonds $Q_{(i,j)}$ ($i+j = \text{odd}$), which are absent from the Hamiltonian. Such extended bond algebra does contain the charge constraints in Eq. (10.58); hence a duality for $\mathcal{A}_{\text{stripe}}$ maps these constraints in a well defined fashion either to the identity operator (in which case the duality solves the constraints [266]) or to constraints of the dual model.

The characterization of $\mathcal{A}_{\text{stripe}}$ in terms of relations among its bond generators reveals the following dual representation of the bond algebra of interactions:

$$Q_{(i,j)} \xrightarrow{\Phi_d} B_{d(i,j)}, \quad (10.64)$$

$$\sigma_{(i,j)}\sigma_{(i+1,j)}^\dagger \xrightarrow{\Phi_d} \tau_{(i,j)}, \quad (10.65)$$

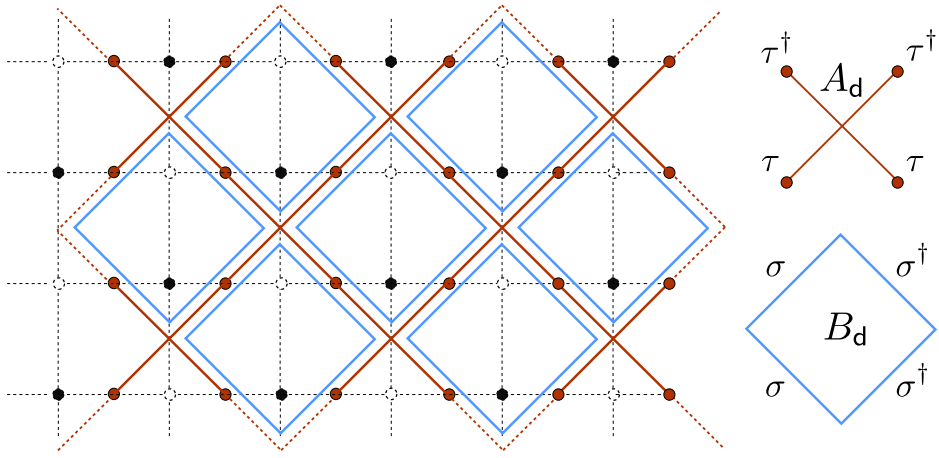


Figure 10.10: The dual lattice on which the Z_{2m} lattice gauge theory of Eq. (10.67) is defined. Clock operators now live on those links of the original square lattice which are marked by a blue dot. On this new lattice we find that in perturbation theory the physical interactions are given by the plaquette and star operators B_d and A_d defined in Eqs. (10.66), (10.69).

with

$$B_{d(i,j)} \equiv \begin{cases} \sigma_{(i,j)}^\dagger \sigma_{(i,j+1)}^\dagger & \text{if } i = 0, \\ \sigma_{(i,j)}^\dagger \sigma_{(i,j+1)}^\dagger \sigma_{(i-1,j)} \sigma_{(i-1,j+1)} & \text{otherwise.} \end{cases} \quad (10.66)$$

Then the dual Hamiltonian, $H_G = \Phi_d(H_{\text{stripe}})$, reads

$$H_G = -\left[\frac{\Delta}{2} \sum_{i+j=\text{even}} B_{d(i,j)} + \frac{J}{2} \sum_{j=0}^{L_y-1} \sum_{i=0}^{L_x-2} \tau_{(i,j)}\right] + \text{h.c.} \quad (10.67)$$

and it is unitarily equivalent [266] to the stripe model. In Appendix 10.B we write down explicitly the dual clock operators and show that it is possible to interpret the gauge theory Hamiltonian (10.67) as the Hamiltonian governing the collective modes of the stripe model.

Up to boundary terms, i.e. the incomplete plaquettes $B_{(0,j)}$ ($j = 0, 2, \dots, L_y - 2$), and a redefinition of the lattice that places the clock degrees of freedom on links rather than sites, we recognize H_G as the Hamiltonian of the \mathbb{Z}_{2m} lattice gauge theory studied in connection to the problem of confinement in QCD [280] (see Fig. 10.10). The local symmetries $B_{(i,j)}$ of the stripe model, Eq. (10.62), map under duality to

$$B_{(i,j)} \xrightarrow{\Phi_d} A_{d(i,j)}, \quad i + j = \text{even}, \quad (10.68)$$

with

$$A_{d(i,j)} \equiv \tau_{(i,j)} \tau_{(i+1,j)} \tau_{(i,j+1)}^\dagger \tau_{(i+1,j+1)}^\dagger. \quad (10.69)$$

As is guaranteed by the formalism, the unitary operators $A_{d(i,j)}$, ($i + j = \text{even}$), commute with the dual Hamiltonian H_G . They correspond to the gauge symmetries of the \mathbb{Z}_{2m} gauge theory and they have the interpretation of measuring the local density of external \mathbb{Z}_{2m} charge. Hence our duality maps the magnetic fluxes in the stripe model, as described by the Aharonov-Bohm operators $B_{(i,j)}$ in Eq. (10.62), to external \mathbb{Z}_{2m} electric charges in the gauge theory.

At this point we can exploit Eq. (10.68) to compute the dual representation $H_{\text{stripe}}^{\text{pert}D} = \Phi_d(H_{\text{stripe}}^{\text{pert}})$ of the perturbative Hamiltonian of Eq. (10.63),

$$H_G^{\text{pert}} = - \sum_{i+j=\text{even}} \left[\frac{\Delta}{2} B_{d(i,j)} + \frac{5J^4}{4G^3} A_{d(i,j)} \right] + \text{h.c.} . \quad (10.70)$$

Remarkably, this is the Hamiltonian for the qudit toric code model [272, 281]. To clarify the notation, notice that due to our definition of the plaquette operator Eq. (10.66), the two operators $A_{d(i,j)}, B_{d(i,j)}$ share one vertical link of the lattice, with $A_{d(i,j)}$ to the right and $B_{d(i,j)}$ to the left of that link (see Fig. 10.10). This duality, however, is a non-local transformation with respect to the clock operators σ and τ . Thus, even if the spectrum of $H_{\text{stripe}}^{\text{pert}}$ is equivalent to the \mathbb{Z}_{2m} toric code, the stripe model in the Coulomb-dominated regime does not present topological order.

To assert that the phase diagram of the gauge theory and the stripe model are connected by the duality Φ_d , we need to investigate the effect of the duality mapping on the charge constraints of Eq. (10.58). Remarkably, the charge constraints are *holographic* [293], since they map to boundary constraints for H_G ,

$$S_j S_{j+1} \xrightarrow{\Phi_d} \sigma_{(L_x-1,j)}^\dagger \sigma_{(L_x-1,j+1)}^\dagger, \quad (10.71)$$

for $j = 0, 2, \dots, L_y - 2$. Then the physical states $|\Psi\rangle_d = \Phi_d|\Psi\rangle$ for H_G , seen as a dual representation of the stripe model, are characterized by the condition

$$\sigma_{(L_x-1,j)}^\dagger \sigma_{(L_x-1,j+1)}^\dagger |\Psi\rangle_d = |\Psi\rangle_d \quad (10.72)$$

for $j = 0, 2, \dots, L_y - 2$, and not by the standard condition of gauge invariance [that is, invariance under the $A_{(i,j)}$, ($i + j = \text{even}$)]. [280] Despite this difference we will argue in the following that the stripe model and the \mathbb{Z}_{2m} lattice gauge theory share the same phase diagram.

The dual gauge theory H_G presents unusual open boundary conditions. Since the charge constraints are holographic, this is in perspective required to guarantee that the dual charge constraints supported on the boundary commute with the dual Hamiltonian H_G (just as the charge constraints commute with H_{stripe}).

However, the standard view that boundary conditions do not affect the phase diagram in the thermodynamic limit suggests in this case that the dual charge constraints do not affect the phase diagram of H_G , which must then coincide with the standard phase diagram of the \mathbb{Z}_{2m} gauge theory. This view is strengthened by the fact that the dual charge constraints commute with the gauge symmetries of H_G , and

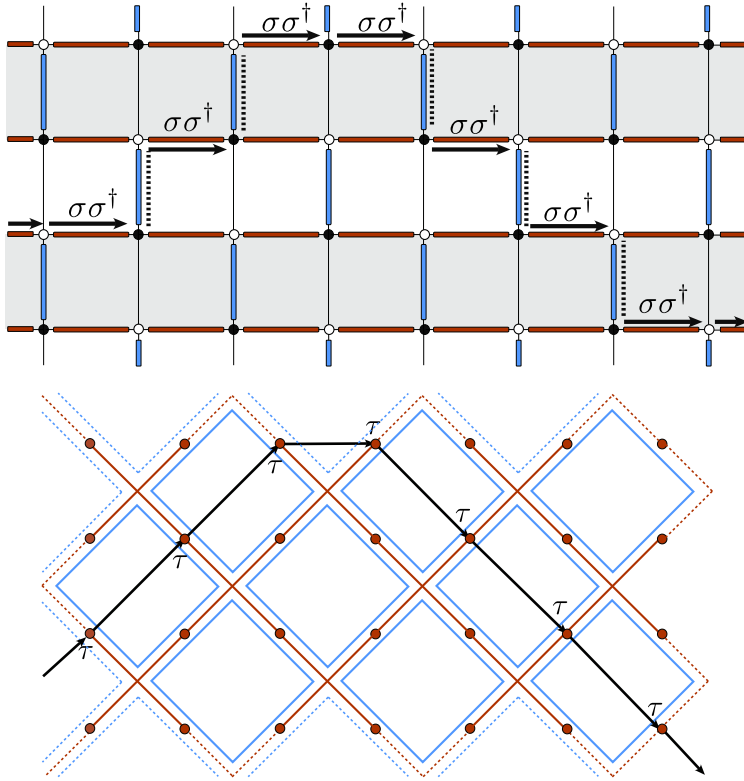


Figure 10.11: The generalized order parameter (string tension) in both the original and dual lattices.

so the ground state of H_G will belong to the gauge-invariant sector even after the condition Eq. (10.72) is imposed. Finally this implies that the stripe model presents the same phase diagram independently on the choice of the charge of each FTI edge in the constraint (10.23), thus in all the different physical sectors.

In view of these considerations, we can argue that the stripe model shares the phase diagram of the \mathbb{Z}_{2m} gauge theory as described in Ref. [280] (and references therein). It follows that there is indeed one second-order phase transition separating the Coulomb-dominated from the Josephson-dominated regime. In the gauge-theory language this transition is understood as a confinement-deconfinement transition. In particular, the Coulomb-dominated regime of the stripe model is dual to the deconfined phase of the gauge theory, while the Josephson-dominated regime corresponds to the confined phase.

The phases of a gauge theory cannot be distinguished by a Landau order parameter [292]. However, for the \mathbb{Z}_{2m} gauge theory dual to the stripe model, there exists a generalized order parameter, the so-called *string tension* [293], which is non-zero in

the confining phase and vanishes continuously, but non-analytically at the transition point. The string tension is the expectation value of a string of τ 's in the \mathbb{Z}_{2m} gauge theory, which corresponds to an open string of tunneling operators $\sigma\sigma^\dagger$ in the stripe model (see Fig. 10.11, analogously to the string operators creating charge excitations in the tile model. The ground-state expectation value of such string falls continuously, but non-analytically to zero at the second-order phase transition separating the Josephson-dominated regime (where it is different from zero) from the Coulomb-dominated regime. On the gauge theory side of the duality, the two phases can be distinguished also by a different scaling of the expectation value of the Wilson loops, which map to sets of τ operators in compact regions in the stripe model.

10.4 Conclusions and Outlook

In summary, we have studied two-dimensional arrays of interacting parafermionic zero-modes. Such exotic states form along the edge of fractional topological insulators, at the domain walls between proximity-induced superconducting and ferromagnetic pairing. The dynamic of these zero-modes is dictated by two competing effects: the charging energy of each superconducting island and the fractional Josephson tunneling of quasiparticles between different islands.

The underlying fractional edge modes, which are originally described by a helical Luttinger liquid theory, determine crucially the possible lattice geometries and the physical constraints of these parafermionic systems. We have analyzed two possible architectures, the tile and the stripe model. They differ mainly for the fact that in the former the length of the edges is constant, while in the latter it scales with the total size of the architecture. We have discussed how this feature gives rise to different physics, despite the fact that the models are characterized by the same lattice of parafermions and the same local interactions.

The difference is appreciated by exploiting a Jordan-Wigner transformation mapping the parafermionic operators into clock operators. Through this transformation the tile model is described by a Hamiltonian on a decorated square lattice whereas the stripe model becomes a compass model, with \mathbb{Z}_{2m} symmetry, on a brick-wall lattice.

The tile model presents, at least in perturbation theory, the same topological order of the surface codes characterized by a \mathbb{Z}_{2m} symmetry: it shows the same topological degeneracy of the ground state and the same anyonic excitations. Thus the system we described is a possible physical candidate to the realization of qudit surface code Hamiltonians. It is known that the ground state degeneracy of these systems suffers from thermal fragility [295, 296]. However, we note that the intrinsic noise due to the presence of induced charges on the superconducting islands could help localize the anyonic excitations of the system, and thus to protect the information which may be encoded in the ground states. [297, 298]

The stripe model provides instead a physical realization of the \mathbb{Z}_{2m} lattice gauge theory, a toy model often exploited to study confinement-related problems in lattice field theory. The duality mapping between the stripe model and the lattice gauge

theory is non-local in terms of the single clock degrees of freedom, but it is local in terms of the interactions. Unlike in the tile model, a toric code Hamiltonian can only be retrieved in the dual theory, where the operators are non-local. Interestingly enough the physical charge constraints of the FTI edges maps to an holographic constraint in the gauge theory which affects only boundary terms.

To conclude, our work addressed the problem of finding topologically ordered phases in the phase diagram of these two-dimensional collections of topological defects. Comparing the results obtained for the two architectures, we can see that that it is not only the nature of the interactions between the defects (in this case, the \mathbb{Z}_{2m} PF zero-modes) that determines the presence of topological order, but also the intrinsic geometry of the topological phases originally generating the defects (in this case, the edges of the fractional topological insulators). Understanding the interplay between this two aspects is crucial to design topologically-ordered architectures.

10.A Description of the system through bosonization

In this Appendix we summarize the main features of the bosonization description of our system and we provide an expression in terms of massless bosonic fields of the parafermion operators α and thus of the related interaction terms. We follow the approach in Refs. [239] and [238], where more details can be found.

In absence of the interactions provided by the superconducting islands and the ferromagnetic insulators, the edge of the FTIs defining our systems, or, equivalently, the double edges of juxtaposed fractional quantum Hall layers with opposite polarization, can be described in terms of the Luttinger liquid Hamiltonian proposed by Wen [251, 252]. In particular the massless edge modes are described by the following Hamiltonian:

$$H_0 = \frac{mv}{2\pi} \int dx [(\partial_x \varphi)^2 + (\partial_x \theta)^2], \quad (10.73)$$

where v is the speed of the two counter-propagating modes and φ, θ are dual massless bosonic fields obeying the commutation relation:

$$[\varphi(x_1, a, t), \theta(x_2, a', t)] = i \frac{\pi}{m} \delta_{a,a'} \Theta(x_2 - x_1), \quad (10.74)$$

where Θ is the Heaviside step function. In particular for each FTI edge a it is possible to define two chiral bosonic fields

$$\varphi_{L/R}(x \pm t, a) \equiv \varphi(x, t, a) \mp \theta(x, t, a), \quad (10.75)$$

in such a way that the left and right fermionic modes, with opposite spin polarization, are defined by the operators $\psi_{L/R}(x, t, a) = \eta_a e^{im\varphi_{L/R}(x \pm vt, a)}$ where η_a are fermionic Klein factors. The charge density associated with each edge is $\rho = \partial_x \theta / \pi$, thus, in a closed edge with length \mathcal{L} , the total charge of the edge is related to the boundary conditions of the θ field:

$$\pi q_{\text{tot}}(a) = \theta(x + \mathcal{L}, a) - \theta(x, a) \quad (10.76)$$

and analogous conditions relate the field φ with the spin density [239].

For each edge the interaction terms corresponding to the proximity induced superconducting coupling and the backscattering give rise to the interaction Hamiltonian:

$$H_I \propto \int dx [-g_S(x) \cos(2m\varphi) - g_F(x) \cos(2m\theta)] \quad (10.77)$$

where g_S and g_F describe respectively the position dependence of the induced superconducting and ferromagnetic couplings.

By selecting a position in the bulk of either a superconducting or a ferromagnetic segment of the edge, if the couplings g are strong enough, one can consider respectively the fields φ and θ as pinned to the semiclassical minima $\varphi_k, \theta_k = 0, \pi/m, 2\pi/m, \dots, (2m-1)\pi/m$. Adopting this approximation and considering the limit of sharp transitions between superconducting and ferromagnetic regions, the parafermion operators can be written as:

$$\alpha_{2k-1,a} = \kappa_a e^{i(\varphi_{k,a} - \theta_{k,a})} \quad (10.78)$$

$$\alpha_{2k,a} = \kappa_a e^{i(\varphi_{k+1,a} - \theta_{k,a})} \quad (10.79)$$

where $k = 1, \dots, M$ labels the ferromagnets and the superconductors along the edge a and the tile and stripe models are characterized respectively by $M = 4$ and $M = L_x$. The fractional Klein factors κ_a enforce the correct commutation rules (10.3) and (10.4). This definition of the parafermionic modes is not unique (see Refs. [239] and [238] for more detail) but it suffices to our purposes. Finally, for a complete description of the system, it is necessary to take into account the correct boundary conditions.

Through this definition of the parafermionic operators it is easy to derive Eqs. (10.1, 10.2, 10.3, 10.4) and verify that the tunneling operators assume the form

$$e^{-i(\varphi_{k+1,a} - \varphi_{k,a})} = P_{\{a,2k-1\}, \{a,2k\}}. \quad (10.80)$$

Thus we recover the usual form for the fractional Josephson interaction (10.11):

$$H_J = -J \cos\left(\varphi_{k+1,a} - \varphi_{k,a} - \frac{\delta}{2m}\right) \quad (10.81)$$

Moreover the tunneling string operator Σ_a defined in (10.24) for the two models becomes $\Sigma_a = \exp(-i(\varphi_{M+1,a} - \varphi_{1,a}))$, emphasizing the relation between the boundary conditions of the field φ and the magnetic flux enclosed by the FTI edges. The boundary condition (10.19) assumes a natural form in the bosonized description due to the boundary relation (10.76) since:

$$\alpha_{\{a,2M+1\}} = \kappa_a e^{i(\varphi_{M+1,a} - \theta_{M+1,a})} = e^{-i\pi q_a} \alpha_{\{a,1\}} \Sigma_a^\dagger. \quad (10.82)$$

Once we apply the parafermionic Jordan-Wigner transformation (10.30, 10.31) to map the system in a quantum clock model, the previous boundary conditions are

translated in the following relations:

$$e^{i\pi q_a} = e^{i(\theta_{M+1,a} - \theta_{1,a})} = \prod_{k=1}^M \tau_{k+1}^\dagger \quad (10.83)$$

$$\Sigma_a = e^{-i(\varphi_{M+1,a} - \varphi_{1,a})} = \sigma_{M+1}^\dagger \sigma_1 \quad (10.84)$$

which generalize the boundary conditions (10.34,10.35,10.36).

10.B Collective modes of the stripe model and the Z_{2m} gauge theory

It is interesting to reinterpret the duality for the stripe model in terms of collective modes. Let us define a new set of clock degrees of freedom as

$$\hat{\sigma}_{(i,j)} \equiv \Phi_d^{-1}(\sigma_{(i,j)}), \quad \hat{\tau}_{(i,j)} \equiv \Phi_d^{-1}(\tau_{(i,j)}). \quad (10.85)$$

Here Φ_d^{-1} is the duality mapping the Z_{2m} gauge theory to the stripe model, obtained from Eqs. (10.64) and (10.65) by reading all arrows in reverse. As we will show shortly, the dual variables $\hat{\sigma}_{(i,j)}, \hat{\tau}_{(i,j)}$ are non-local operators when written in terms of the clock degrees of freedom $\sigma_{(i,j)}, \tau_{(i,j)}$. The duality mapping Φ_d^{-1} shows that these collective modes of the stripe model are governed by the Z_{2m} gauge theory Hamiltonian, since

$$H_{\text{stripe}} = \Phi_d^{-1}(H_G) - \left[\frac{\Delta}{2} \sum_{i+j=\text{even}} \hat{B}_{d(i,j)} + \frac{J}{2} \sum_{j=0}^{L_y-1} \sum_{i=0}^{L_x-2} \hat{\tau}_{(i,j)} \right] + \text{h.c.}, \quad (10.86)$$

with $\hat{B}_{d(i,j)}$ defined just as in Eq. (10.66) up to the substitution $\sigma_{(i,j)} \rightarrow \hat{\sigma}_{(i,j)}$. It follows that the stripe model realizes the \mathbb{Z}_{2m} gauge theory in terms of its collective modes $\hat{\sigma}_{(i,j)}, \hat{\tau}_{(i,j)}$.

To compute the dual variables explicitly it is necessary to extend the bond algebra of the \mathbb{Z}_{2m} gauge theory by adding the boundary operators $\tau_{(L_x-1,j)}$ ($j = 0, \dots, L_y-1$), $\sigma_{(0,0)}^\dagger$, and $\sigma_{(i,0)}^\dagger \sigma_{(i-1,0)}$ ($i = 1, \dots, L_x-1$) to its list of bond generators. We also need to determine an algebraic extension of the duality mapping to these extra bonds,

$$\sigma_{(0,0)}^\dagger \xrightarrow{\Phi_d^{-1}} \tau_{(0,0)}, \quad (10.87)$$

$$\sigma_{(i,0)}^\dagger \sigma_{(i-1,0)} \xrightarrow{\Phi_d^{-1}} \tau_{(i,0)}, \quad (10.88)$$

$$\tau_{(L_x-1,j)} \xrightarrow{\Phi_d^{-1}} \sigma_{(L_x-1,j)}. \quad (10.89)$$

This completes the preliminaries. It follows that

$$\hat{\sigma}_{(i,j)} = \tau_{(0,j)}^\dagger \tau_{(1,j)}^\dagger \dots \tau_{(i,j)}^\dagger, \quad (10.90)$$

and

$$\hat{\tau}_{(i,j)} = \begin{cases} \sigma_{(L_x-1,j)} & \text{if } i = L_x - 1, \\ \sigma_{(i,j)} \sigma_{(i+1,j)}^\dagger & \text{otherwise.} \end{cases} \quad (10.91)$$

It is possible to check directly that the dual variables satisfy the correct algebra for clock degrees of freedom.

Chapter 11

Thermal conductance as a probe of the non-local order parameter for a topological superconductor with gauge fluctuations

Topological phases of matter cannot be characterized by any local order-parameter and, hence, signatures of these phases are not accessible by a local experimental probe. For free fermions, the complete classification of topological phases has recently been established [299–301] and a connection between the (experimentally accessible) linear response properties of a system and the value of its topological invariant has been obtained. A prominent and illustrative example are one-dimensional (1D) topological superconductors [26, 42, 45, 46], currently the subject of intense theoretical [22, 23] and experimental investigation [74–77, 115, 154]. In this case, the topological phase is characterized by unpaired Majorana zero-modes at the ends of the superconductor, whose presence allows to non-locally store one bit of quantum information encoded in the total fermion parity of the superconductor [26]. This topological phase can be recognized by striking transport properties [23]. Perfect Andreev reflection off a Majorana end mode leads to a quantized zero-bias conductance of $G_0 = 2e^2/h$. [302–305] The peak can only be removed if the system undergoes a phase transition into a phase without Majorana modes. Exactly at the transition, the two unpaired Majorana modes combine into a perfectly transmitting mode. As a consequence, the thermal conductance through the wire peaks at a value equal to its superconducting quantum $K_0 = \pi^2 k_B^2 T / 6h$ at temperature T [306]. The quantization of the peak is a way to identify the topological phase transition even in a wire of finite size [306]. In the topologically trivial phase, both zero-bias Andreev and thermal conductance are zero.

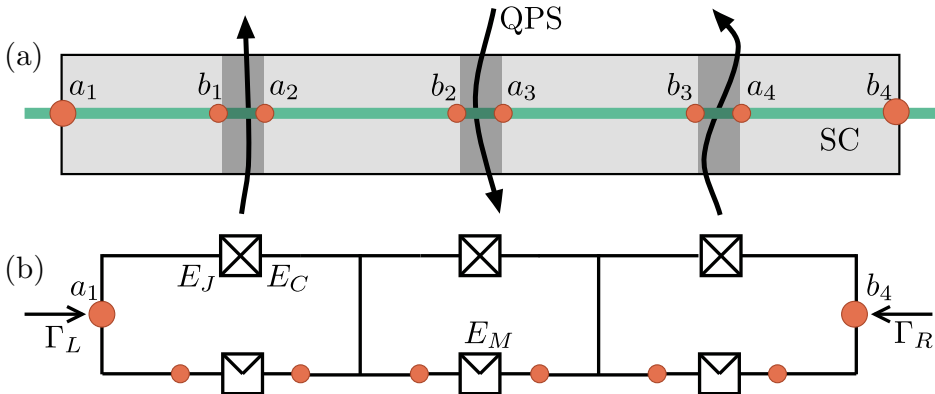


Figure 11.1: Panel (a): An s -wave superconductor (gray) is deposited on top of a helical quantum wire (green), which can be for example a semiconducting nanowire or the edge of a quantum spin Hall insulator. We consider the effect of quantum phase slips in the superconductor (black arrows). Once a moderate magnetic field is applied to break time reversal invariance, Majorana modes (orange dots) appear at the ends of the wire and at weak links when the phase slips happen. Panel (b): We show an equivalent circuit describing the system [see Eq. (11.1)]. Here, as usual, a box with a cross denotes a Josephson junction and its capacitance. On the other hand, a box with only half of a cross denotes the 4π -periodic Majorana junction. Arrows represent coupling to external leads to the Majorana modes at the end with strength Γ_L and Γ_R .

It is currently a challenge in condensed matter physics to extend the classification of topological phases to interacting fermionic systems (see Refs. [307–309]) and in particular to provide a similar connection with experimental probes. Often, insight into interacting topological phases is offered by non-local order parameters [310, 311]. However, such quantities lack an obvious thermodynamic meaning and do not enable natural mean-field approximations. If available, they are useful theoretical tools [293, 312], without direct experimental implications. Thus, not surprisingly, they are dubbed ‘hidden’.

In this chapter, we will show that non-local order parameters can be directly linked to transport properties in the linear response regime. We will show this for the case of a 1D topological superconductor subject to quantum phase slips, see Fig. 11.1. The system is described by an effective interacting Hamiltonian akin to a matter-coupled lattice gauge theory, the 1D \mathbb{Z}_2 Higgs model [313]. A non-local order parameter is in this case known: the Fredenhagen-Marcu string order parameter [314], originally proposed as a criterion for confinement [315] and recently revisited in the context of topological order [316]. We will show that the Fredenhagen-Marcu order parameter is connected in our system to a simple transport coefficient, the thermal conductance.

11.1 Quantum phase slips in a Majorana chain

Let us start by discussing the role of quantum phase slips (QPS) in topological superconductors. QPS are quantum tunneling events where the phase of the superconducting order parameter changes locally by 2π . In 1D, QPS destroy the superconducting phase at zero temperature [317–319] and thus remove the topological protection of a Majorana qubit [320], since the latter presupposes the superconducting ordering which breaks the electromagnetic U(1) symmetry down to \mathbb{Z}_2 . For d -dimensional superconductors with $d > 1$, QPS are suppressed as they generate a domain wall in the superconducting order parameter, leading to $\kappa \propto \exp[-(L/\xi)^{d-1}]$, with L the linear dimension of the system and ξ the coherence length. In this sense, Kitaev's model of topological protection is not purely one-dimensional, since a bulk (3D) superconductor is crucial for achieving the fault-tolerance of a Majorana qubit [67].

To study QPS in a concrete setting, we follow the approach of Ref. [321] and consider a chain of coupled superconducting islands, with superconducting phase ϕ_m , placed on top of a nanowire or of a quantum spin Hall edge, see Fig. 11.1. The junctions between the islands then naturally form weak links through which QPS happen. The Euclidean action describing a chain of N islands reads $\mathcal{S} = \int_0^{1/T} \mathcal{L} dt$, with [155, 322]

$$\mathcal{L} = \sum_{m=1}^{N-1} \left[\frac{\dot{\varphi}_m^2}{2E_C} + E_J(1 - \cos \varphi_m) - iE_M b_m a_{m+1} \cos(\varphi_m/2) \right] - \sum_{m=1}^N iha_m b_m, \quad (11.1)$$

with $\varphi_m = \phi_{m+1} - \phi_m$ the phase difference across each junction. The charging energy $E_C = e^2/2C$ and the Josephson energy $E_J = \hbar I_c/2e$ are respectively determined by the capacitance C and the critical current I_c of the junction. A topological superconducting wire hosts two Majorana zero-energy modes a_m, b_m on each island. They are responsible for the term proportional to E_M in (11.1), describing tunneling of individual electrons [42]. The Hermitian operators a_m, b_m obey the anti-commutation rules $\{a_m, b_n\} = 0$ and $\{a_m, a_n\} = \{b_m, b_n\} = 2\delta_{mn}$. Additionally, the finite size of the islands leads to an overlap between Majorana modes and an associated energy splitting denoted by h . The local fermion parity $p_m = \pm 1$ at each junction is defined via the occupation number of a fermionic mode $c_m = \frac{1}{2}(b_m - ia_{m+1})$ as $p_m = 1 - 2c_m^\dagger c_m = i b_m a_{m+1}$. The total fermion parity operator $(-1)^F = ia_1 \prod_{m=1}^{N-1} p_m b_N$ is a global symmetry of the system.

Different from previous studies [52, 88, 323], we are interested in the regime $E_J \gg E_M, E_C, h$, where the superconducting phase difference at any junction can only be a multiple of 2π , due to the large Josephson energy. The relevant quantum fluctuations in the chain are QPS connecting classical minima, whose amplitude $\kappa \simeq (E_C E_J^3)^{1/4} \exp(-8\sqrt{E_J/E_C})$ can be computed in the semiclassical approximation [321]. A shift of φ_m by 2π changes the sign of $E_M \cos(\varphi_m/2)$ and thus it also changes the energetically-favored value of the junction parity p_m [322]. In this regime, the value of $\cos(\varphi_m/2)$ is reduced to a \mathbb{Z}_2 quantum degree of freedom. The effective

Hamiltonian of the chain,

$$H = - \sum_{m=1}^N iha_m b_m - \sum_{m=1}^{N-1} \left[iE_M b_m a_{m+1} \tau_m^z + \kappa \tau_m^x \right], \quad (11.2)$$

describes Majorana modes coupled to $N - 1$ Pauli matrices $\tau_m^z = \cos(\varphi_m/2)$, one per junction [293]. The last term in the Hamiltonian describes QPS that change φ_m by 2π at a rate κ/\hbar .

In the absence of fluctuations of the superconducting order parameter, that is, at $\kappa = 0$, we recover the Kitaev model. In this case, the τ_m^z degrees of freedom are redundant. The Hamiltonian H can be block-diagonalized by freezing them in some classical configuration. All blocks in this decomposition have identical energy spectra. For any classical configuration of the spins τ_m^z , a quantum critical point at $h = E_M$ separates a topologically non-trivial phase at $h < E_M$ from the trivial phase at $h > E_M$. The non-trivial phase has a twofold ground state degeneracy if both even and odd total fermion parities $(-1)^F = \pm 1$ are considered, signaling the presence of unpaired Majorana modes at either ends of the chain.

The interaction of the fluctuating superconducting phase with the Majorana modes is such that, for each island, a local symmetry C_m of H emerges, given by

$$\begin{aligned} C_1 &= ia_1 b_1 \tau_1^x, & C_N &= \tau_{N-1}^x ia_N b_N, \\ C_m &= \tau_{m-1}^x ia_m b_m \tau_m^x \quad (m = 2, \dots, N-1). \end{aligned} \quad (11.3)$$

These local symmetries are gauge symmetries and appear because the phase difference and fermion parity of a junction are not independent degrees of freedom [36]: a change in the occupation number of the fermionic mode c_m is equivalent to advancing the phase φ_m by 2π . As a result, the global fermion parity $(-1)^F$ can be expressed as a product of the local gauge-symmetries $(-1)^F = \prod_{m=1}^N C_m$ [293]. It follows that the τ_m^z play the role of a \mathbb{Z}_2 gauge field, minimally coupled to the fermionic degrees of freedom and with dynamics generated by QPS.

11.2 Connection with a Higgs lattice field theory

The link to lattice field theories can be made more explicit. Our effective Hamiltonian H of Eq. (11.2) can be interpreted as an approximation to the lattice-regularized 1D Higgs model [313], given by

$$H_H = - \sum_{m=1}^N \frac{\lambda}{2} \partial_{\phi_m}^2 + \sum_{m=1}^{N-1} \left[-\frac{g^2}{2} \partial_{\theta_m}^2 + v^2 \cos(\varphi_m - \theta_m) \right]. \quad (11.4)$$

This Hamiltonian follows by standard techniques [324, 325] from the Euclidean action of the Higgs model of Ref. [313]. Here, the angular variables ϕ_m, θ_m represent the Higgs and electromagnetic gauge field respectively. The parameter v^2 is the vacuum

expectation value of the Higgs field in the broken-symmetry state. The parameters λ, g^2 control the strength of the fluctuations of the matter and gauge fields.

Our Hamiltonian H is obtained from that of the Higgs model H_H by using the approximation $-\pi^2 \partial_x^2/2 \approx \cos(\pi \partial_x) - 1$ for $x = \phi_m, \theta_m$ and truncating the angular variables to the values $\phi_m, \theta_m \in \{0, \pi\}$. Within the truncated Hilbert space, $\cos(\pi \partial_{\phi_m}) = \sigma_m^x$ and $\cos(\pi \partial_{\theta_m}) = \tau_m^x$. Hence, H_H reduces (up to an irrelevant additive constant) to the spin chain Hamiltonian

$$H_{\mathbb{Z}_2} = \sum_{m=1}^N \frac{\lambda}{\pi^2} \sigma_m^x + \sum_{m=1}^{N-1} \left[\frac{g^2}{\pi^2} \tau_m^x + v^2 \sigma_m^z \tau_m^z \sigma_{m+1}^z \right]. \quad (11.5)$$

The Hamiltonian $H_{\mathbb{Z}_2}$ is precisely that of the \mathbb{Z}_2 Higgs model [313]. Finally, the Jordan-Wigner transformation $a_m = \sigma_m^x \prod_{j=1}^{m-1} \sigma_j^z$, $b_m = \sigma_m^y \prod_{j=1}^{m-1} \sigma_j^z$ shows that the \mathbb{Z}_2 Higgs model is equivalent to our Hamiltonian H , provided we identify $h = -\lambda/\pi^2$, $\kappa = -g^2/\pi^2$, and $E_M = -v^2$. (Note that the phase diagram does not depend on the signs of λ, κ, E_M .)

As our effective Hamiltonian H is related to the Higgs model, we might expect the Higgs mechanism to be present. As a result, gapless excitations should become gapped for arbitrarily small values of κ , that is, for arbitrarily weak fluctuations of the superconducting order parameter. In other words, the small but finite charging energy E_C of each island breaks the ground state degeneracy and splits the otherwise unpaired Majorana modes. In this way, the Higgs-mechanism offers a way to locally break the topological degeneracy of the Majorana chain. It is known that this expectation is indeed correct in the thermodynamic limit, as at $\kappa \neq 0$ the Hamiltonian (11.5) has no phase transitions and describes a gapped phase with a single ground state [293, 313, 326]. However, in a finite chain signatures of the topologically non-trivial phase, which is present at $\kappa = 0$ and $h < E_M$, should survive up to a finite value of κ . If this is true, then the Hamiltonian of a finite chain should be gapless along a line in the (h, κ) plane.

11.3 Numerical study of the linear response of the chain

In the following, we will show that in the linear response regime, the topological transition reflects itself in the thermal conductance K through the system also at finite κ , whereas upon increasing κ , the local probe of Andreev conductance G quickly becomes blind to it. To this end, we couple the left and right end of the chain with Hamiltonian H to normal leads through tunneling Hamiltonians [36] $H_L = \gamma_L c_L^\dagger a_1 e^{-i\phi_1/2} + \text{H.c.}$, $H_R = \gamma_R c_R^\dagger b_N e^{-i\phi_N/2} + \text{H.c.}$; here, γ_L and γ_R denote the amplitudes for tunneling events into the left (L) and right (R) leads, and c_L^\dagger, c_R^\dagger are the creation operators for electrons in the non-interacting leads. We fix the gauge by choosing $\phi_1 = 0$, so that $\phi_N = \sum_{m=1}^{N-1} \varphi_m$. In the low-energy limit, $e^{-i\phi_N/2} = \prod_{m=1}^{N-1} \tau_m^z$,

so we get

$$H_L = \gamma_L(c_L^\dagger + c_L)a_1, \quad H_R = \gamma_R(c_R^\dagger + c_R)b_N \prod_{m=1}^{N-1} \tau_m^z. \quad (11.6)$$

The tunneling Hamiltonians must break one of the gauge symmetries, since a tunneling event changes the total fermion parity. Due to our gauge choice, we obtain $\{H_{L,R}, C_1\} = 0$ while $[H_{L,R}, C_m] = 0$ for $m = 2, \dots, N$.

The Andreev conductance G is determined by the charge transport across a normal metal-superconductor interface. To compute G , we set $\gamma_R = 0$, $\gamma_L = \gamma$, apply a bias voltage V to the left lead, and ground the rightmost superconducting island. In contrast, the thermal conductance K is determined by the heat transport between two normal leads. To compute K we set $\gamma_L = \gamma_R = \gamma$ and establish a small temperature difference between the right lead at temperature T and the left lead at temperature $T + \delta T$. In the limit $T, V \rightarrow 0$, we obtain G as $G = G_0 \Gamma \text{Im}[G_{11}(0)]$ [327], and K as $K = 4K_0 \Gamma^2 |G_{1N}(0)|^2$, in terms of the tunnel coupling $\Gamma = 2\pi|\gamma|^2\rho_0$ to a wide-band lead with density of states ρ_0 and the retarded Green's functions¹

$$G_{11}(\omega) = -i \int_0^\infty dt e^{i\omega t} \langle \{a_1(t), a_1(0)\} \rangle, \quad (11.7a)$$

$$G_{1N}(\omega) = -i \int_0^\infty dt e^{i\omega t} \langle \{b_N(t) \prod_{m=1}^{N-1} \tau_m^z(t), a_1(0)\} \rangle. \quad (11.7b)$$

The averages in Eqs. (11.7a) are taken over the ground state wave function $|0\rangle$ of our effective Hamiltonian H . For any $\kappa, h, E_M > 0$, the ground state of H is unique and belongs to the gauge-invariant sector with $C_m|0\rangle = |0\rangle$ for all m . Note that at $\kappa = 0$, the ground manifold is 2^{N-1} -times degenerate, but we continue to choose $|0\rangle$ to be the unique gauge-invariant state in the ground manifold. The time-evolution in Eqs. (11.7a) is determined by the total Hamiltonian $H_{\text{tot}} = H + H_R + H_L$. The retarded Green's function $G_{11}(t) = \int(d\omega/2\pi) e^{-i\omega t} G_{11}(\omega)$ is the amplitude for a reflection process whereby an electron enters the chain from the left lead at time $t_i = 0$ and exit again from the left lead after a time $t_f = t$. Similarly, $G_{1N}(t)$ is the amplitude for a transmission process whereby the electron enters at $t_i = 0$ from the left lead and exits from the right lead after a time $t_f = t$.

We highlight that the thermal transport probes *non-local* quasiparticle transfer processes through the chain characterized by the string correlator

$$G_{1N}(t) = -i \langle \{b_N(t) \prod_{m=1}^{N-1} \tau_m^z(t), a_1(0)\} \rangle, \quad (11.8)$$

which is a generalization of the conventional correlator $-i \langle \{b_N(t), a_1(0)\} \rangle$ studied in the context of the Majorana chain without the gauge degrees of freedom [303]. Due to the presence of the gauge string $\prod_{m=1}^{N-1} \tau_m^z$, the Green's function G_{1N} is similar to

¹In this formula for K we neglect inelastic processes mediated by phonons and assume that the occupation of single-particle states is that of independent particles in thermal equilibrium.

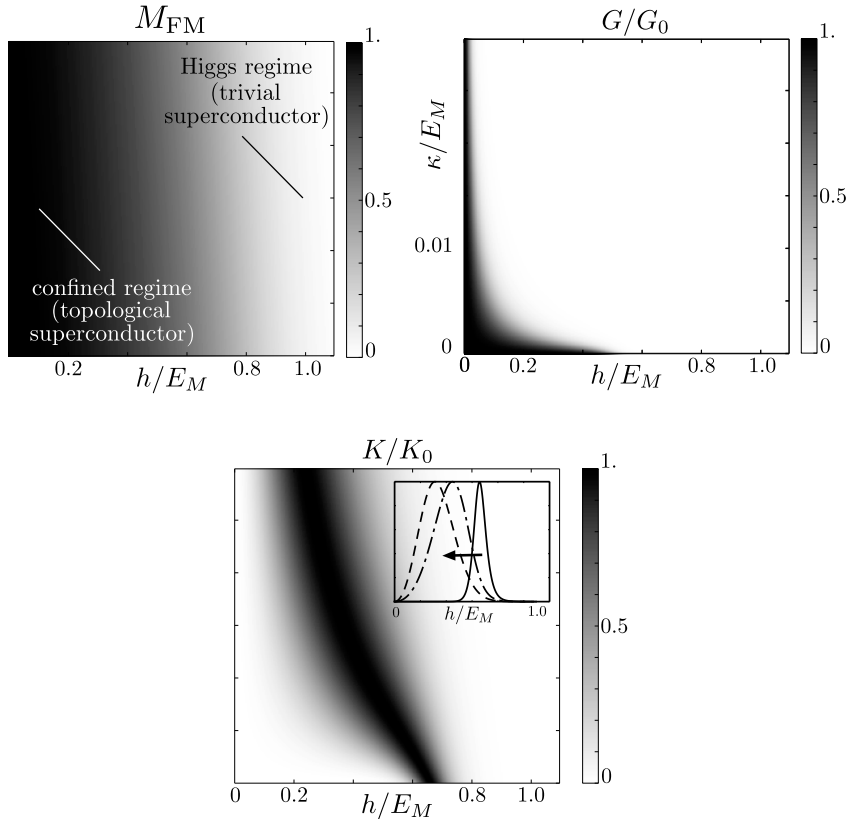


Figure 11.2: Numerical results: Andreev conductance (top left, in units of $G_0 = 2e^2/h$), Fredenhagen-Marcu order parameter M_{FM} (top right), and thermal conductance (bottom, in units of $K_0 = \pi^2 k_B^2 T / 6h$) plotted as a function of h and κ . The results are obtained for a chain of $N = 11$ islands with coupling constant $\Gamma = 0.01E_M$ to the leads, in the limit of vanishing temperature T and small applied voltage V . The Andreev conductance G is averaged over a small voltage interval $10^{-4}E_M$ to account for the finite-size energy splitting of the Majorana modes as for a finite size wire we trivially have $G = 0$ [88, 303]. The Andreev conductance only shows a signal along the axis. On the other hand, the string-order parameter allows to distinguish a confined regime - corresponding to the topological regime with Majorana end modes - from the trivial Higgs-regime. The separation between these two regimes can be clearly identified by the peak in the thermal conductance. The inset in the right panel shows line cuts of the thermal conductance at $\kappa/E_M = 0, 0.01, 0.02$, going from right to left as shown by the arrow. Due to finite size effects, the transition at $\kappa = 0$ is shifted from $h/E_M = 1$ to $h/E_M \simeq (\Gamma/E_M)^{1/11} \simeq 0.7$, as expected. Increasing κ , the topological regime shrinks and only the Higgs-regime survives.

the Fredenhagen-Marcu string-order parameter [314],

$$M_{\text{FM}} = -i \langle b_N \prod_{m=1}^{N-1} \tau_m^z a_1 \rangle, \quad (11.9)$$

which measures the presence of the topological phase in the model with fluctuation gauge degrees of freedom. In the following we probe this relation numerically.

To calculate the Green's function $G_{mn}(\omega)$, we follow the approach [328] of decoupling the gauged Majorana chain from the leads to first order in the lead coupling Γ and neglecting higher-order (co-)tunneling processes. The bare Green's functions without the leads are calculated by exact diagonalization of the Hamiltonian (11.2), using a Lehmann spectral representation in terms of the exact eigenstates. The presence of the symmetries (11.3) greatly simplifies the task of computing G_{mn} . In fact, we only need to know the energy and the wave function of the ground state $|0\rangle$ and of all the states $|\psi\rangle$ such that $C_1|\psi\rangle = -|\psi\rangle$ while $C_{m \neq 1}|\psi\rangle = |\psi\rangle$. Indeed, since C_1 is the only symmetry of H which does not commute with the tunneling Hamiltonian $H_{\text{L,R}}$, but anti-commutes instead, these are the only excited states to which transitions from the ground states are possible upon tunneling of an electron from the leads. For a chain of N islands, there are 2^{N-1} of these states—against a dimension of 2^{2N-1} of the total Hilbert space².

The numerical results for a chain of $N = 11$ islands are shown in Fig. 11.2. At $\kappa = 0$, coherently with known results, we observe an Andreev reflection plateau at G_0 in the non-trivial regime and a thermal conductance peak at the transition, which appears shifted to $h \simeq E_M(\Gamma/E_M)^{1/N}$ due to finite chain size and coupling to the leads. At finite κ , the Andreev plateau is quickly suppressed, except close to $h = 0$, a limit where two isolated Majorana modes are always present. However, the quantized peak in thermal conductance persists in the interacting part of the parameter space, indicating the presence of a gapless transmitting mode and hence a strong signature of the existence of a topological regime. In fact, the position of the thermal conductance peak qualitatively follows the line of maximum change in the order parameter. We have checked that the agreement persists when varying the system size N .

11.4 Conclusions

To conclude, we have shown that QPS in a Majorana chain implement the \mathbb{Z}_2 Higgs model where the fluctuations of the gauge field are determined by the rate κ/\hbar for QPS. QPS *locally* destroy the topological phase of the Kitaev model at fixed fermion parity via a \mathbb{Z}_2 version of the Higgs mechanism. However, for finite system size and small κ , signatures of the topological phase remain visible in the thermal conductance through the system. The reason is that it is linked to the Fredenhagen-Marcu order parameter for the \mathbb{Z}_2 Higgs theory, which indicates the topological regime with

²Note that when the total Hamiltonian is projected onto a single gauge sector, it takes the form of a transverse-field Ising model in a longitudinal field κ . This projected Hamiltonian is the one we numerically diagonalize. Within this simpler model in a fixed gauge sector, it is well known that any finite $\kappa > 0$ introduces a relevant perturbation [326].

gauge fluctuations present. The thermal conductance provides a clear transport signature of the transition from the topological to the trivial regimes in the presence of the interactions with the gauge field, whereas no signature of the transition is present in the Andreev conductance at a finite rate of QPS. Our results suggest that in topological quantum matter, bulk transport measurements offer access to non-local order parameters, just like susceptibility measurements do for local order parameters in broken-symmetry phases. It remains an interesting question for further studies how this scenario can be generalized to higher dimensions and non-Abelian gauge fields.

Chapter 12

Outlook

This thesis contains the theoretical design of a topological quantum computer based on Majorana modes in superconducting circuits. Will the theoretical ideas contained in this thesis be realized in practice? What is the status of the field, and what are its prospects? To guide the discussion of these crucial questions, I have assembled the schematic table in Fig. 12.1, which identifies some intermediate stages of development, and which might be useful to make a rough measurement of future experimental progress.

Where are we now? Chapter 7 of this thesis reaches the first milestone along this road, the successful realization of microwave quantum circuits with semiconducting nanowire Josephson elements embedded in a cQED chip [329]¹. These circuits contained no Majorana modes, so current efforts are focusing on achieving the second stage in the figure. Mainly three different platforms are under scrutiny in this race: semiconducting nanowires [38, 74, 77], quantum spin Hall systems [116, 154, 330], and chains of magnetic adatoms [117], all covered by a large body of theoretical work.

While realizing Majorana modes is obviously a prerequisite for all stages in the figure beyond the second, there will certainly be many other practical challenges. A commonly mentioned one is the ubiquitous presence of non-equilibrium quasiparticles in superconducting circuits, which breaks the topological protection of Majorana qubits. Recently, there has been a lot of progress in the suppression of quasiparticle poisoning [32–34], even though the origins and dynamics of these stray quasiparticles remain largely unknown. Quasiparticle poisoning can prevent a clear observation of the 4π -periodic Josephson effect, which represents the third step - see for instance the discussion in Chapter 2. It certainly poses an upper bound on the coherence time of a Majorana qubit, which must always be operated in a parity-protected fashion.

Chapters 3 to 6 describe in great detail stages four to seven in Fig. 12.1, from the characterization of a Majorana qubit to the full execution of a quantum algorithm

¹Similar results were also achieved by the group of C. Marcus at the University of Copenhagen [177].

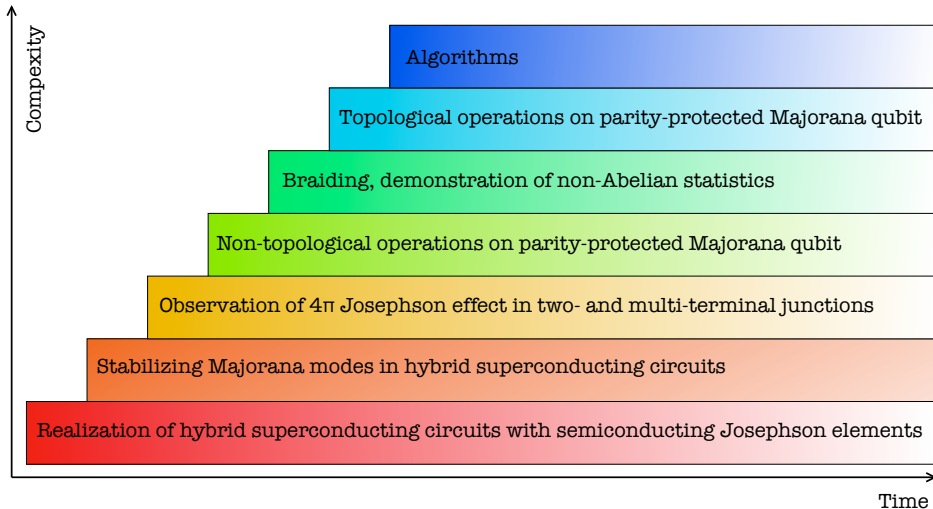


Figure 12.1: Development stages for the realization of a topological quantum computer with Majorana modes, following the ideas presented in this thesis. The drawing is inspired by a similar one by Devoret and Schoelkopf appearing in Ref. [31], outlining the realization of a universal quantum computer with conventional qubits. It should in fact be interpreted by quoting their words: “Each advancement requires mastery of the preceding stages, but each also represents a continuing task that must be perfected in parallel with the others” [31].

in a topological fashion. The major milestone is certainly the demonstration of non-Abelian statistics, which stands out in this research program as a fundamental discovery. Whether or not a topological quantum computer is eventually realized, non-Abelian statistics are a fascinating feature of quantum mechanics. Their observation would once again demonstrate the seemingly inextinguishable ability of quantum mechanics to predict new phenomena, and to surprise us.

As usual, the next generations of experiments will yield unexpected results, and most probably offer opportunities to deviate from the path outlined here and explore territories which are at the moment unforeseen. Perhaps, these unknown unknowns will be what will keep us busy and curious in the years to come.

References

- [1] M. A. Nielsen and I. L. Chuang, *Quantum computation and quantum information* (Cambridge university press, 2010).
- [2] S. Aaronson, *Quantum computing since Democritus* (Cambridge University Press, 2013).
- [3] D. Gottesman, arXiv:quant-ph/9705052 (1997).
- [4] J. Preskill, Proc. R. Soc. London, Ser. A **454**, 385 (1998).
- [5] A. Y. Kitaev, Ann. Phys. **303**, 2 (2003).
- [6] C. Nayak, S. H. Simon, A. Stern, M. Freedman, and S. Das Sarma, Rev. Mod. Phys. **80**, 1083 (2008).
- [7] G. Moore and N. Seiberg, Phys. Lett. B **212**, 451 (1988).
- [8] G. Moore and N. Seiberg, Comm. Math. Phys **123**, 177 (1989).
- [9] E. Witten, Comm. Math. Phys **121**, 351 (1989).
- [10] J. Fröhlich and F. Gabbiani, Rev. Math. Phys. **2**, 251 (1990).
- [11] G. Moore and N. Read, Nucl. Phys. B **360**, 362 (1991).
- [12] C. Nayak and F. Wilczek, Nucl. Phys. B **479**, 529 (1996).
- [13] A. Stern, Ann. Phys. **323**, 204 (2008).
- [14] N. Read and D. Green, Phys. Rev. B **61**, 10267 (2000).
- [15] L. E. Ballentine, *Quantum mechanics*, vol. 280 (Prentice Hall Englewood Cliffs, 1990).
- [16] J. Preskill, *Lecture Notes for Physics 219: Quantum Computation.*, chap. Topological Quantum Computation (2004).
- [17] J. M. Leinaas and J. Myrheim, Nuovo Cimento B Series 11 **37**, 1 (1977).

- [18] M. V. Berry, Proc. R. Soc. London, Ser. A **392**, 45 (1984).
- [19] B. Simon, Phys. Rev. Lett. **51**, 2167 (1983).
- [20] F. Wilczek and A. Zee, Phys. Rev. Lett. **52**, 2111 (1984).
- [21] J. Alicea, Y. Oreg, G. Refael, F. von Oppen, and M. P. A. Fisher, Nat. Phys. **7**, 412 (2011).
- [22] J. Alicea, Rep. Progr. Phys. **75**, 076501 (2012).
- [23] C. Beenakker, Annu. Rev. Condens. Matter Phys. **4**, 113 (2013).
- [24] M. Leijnse and K. Flensberg, Semi. Sci. Tech. **27**, 124003 (2012).
- [25] G. Volovik, JETP Lett. **70**, 609 (1999).
- [26] A. Y. Kitaev, Phys.-Usp. **44**, 131 (2001).
- [27] D. A. Ivanov, Phys. Rev. Lett. **86**, 268 (2001).
- [28] M. H. Devoret, A. Wallraff, and J. M. Martinis, arXiv:cond-mat/0411174 (2004).
- [29] R. Schoelkopf and S. Girvin, Nature **451**, 664 (2008).
- [30] J. Clarke and F. K. Wilhelm, Nature **453**, 1031 (2008).
- [31] M. H. Devoret and R. J. Schoelkopf, Science **339**, 1169 (2013).
- [32] I. M. Pop, K. Geerlings, G. Catelani, R. J. Schoelkopf, L. I. Glazman, and M. H. Devoret, Nature **508**, 369 (2014).
- [33] U. Vool, I. M. Pop, K. Sliwa, B. Abdo, C. Wang, T. Brecht, Y. Y. Gao, S. Shankar, M. Hatridge, G. Catelani, *et al.*, Physical review letters **113**, 247001 (2014).
- [34] D. J. van Woerkom, A. Geresdi, and L. P. Kouwenhoven, arXiv preprint arXiv:1501.03855 (2015).
- [35] F. Hassler, A. R. Akhmerov, C.-Y. Hou, and C. W. J. Beenakker, New. J. Phys. **12**, 125002 (2010).
- [36] L. Fu, Phys. Rev. Lett. **104**, 056402 (2010).
- [37] J. Koch, T. M. Yu, J. M. Gambetta, A. A. Houck, D. I. Schuster, J. Majer, A. Blais, M. H. Devoret, S. M. Girvin, and R. J. Schoelkopf, Phys. Rev. A **76**, 042319 (2007).
- [38] S. R. Plissard, I. van Weperen, D. Car, M. A. Verheijen, G. W. G. Immink, J. Kammhuber, L. J. Cornelissen, D. B. Szombati, A. Geresdi, S. M. Frolov, L. P. Kouwenhoven, and E. P. A. M. Bakkers, Nature Nano. **8**, 859 (2013).

- [39] B. D. Josephson, Phys. Lett. **1**, 251 (1962).
- [40] M. Tinkham, *Introduction to superconductivity* (Courier Dover Publications, 2012).
- [41] H.-J. Kwon, K. Sengupta, and V. M. Yakovenko, Eur. Phys. J. B **37**, 349 (2003).
- [42] L. Fu and C. L. Kane, Phys. Rev. B **79**, 161408 (2009).
- [43] M. Z. Hasan and C. L. Kane, Rev. Mod. Phys. **82**, 3045 (2010).
- [44] X.-L. Qi and S.-C. Zhang, Rev. Mod. Phys. **83**, 1057 (2011).
- [45] R. M. Lutchyn, J. D. Sau, and S. Das Sarma, Phys. Rev. Lett. **105**, 077001 (2010).
- [46] Y. Oreg, G. Refael, and F. von Oppen, Phys. Rev. Lett. **105**, 177002 (2010).
- [47] P. A. Ioselevich and M. V. Feigel'man, Phys. Rev. Lett. **106**, 077003 (2011).
- [48] F. S. Nogueira and I. Eremin, J. Phys. Cond. Mat. **24**, 325701 (2012).
- [49] K. T. Law and P. A. Lee, Phys. Rev. B **84**, 081304 (2011).
- [50] L. Jiang, D. Pekker, J. Alicea, G. Refael, Y. Oreg, and F. von Oppen, Phys. Rev. Lett. **107**, 236401 (2011).
- [51] R. F. Service, Science **332**, 193 (2011).
- [52] C. Xu and L. Fu, Phys. Rev. B **81**, 134435 (2010).
- [53] J. R. Friedman and D. V. Averin, Phys. Rev. Lett. **88**, 050403 (2002).
- [54] R. P. Tiwari and D. Stroud, Phys. Rev. B **76**, 220505 (2007).
- [55] E. Grosfeld and A. Stern, Proc. Nat. Acad. Sci. **108**, 11810 (2011).
- [56] E. Grosfeld, B. Seradjeh, and S. Vishveshwara, Phys. Rev. B **83**, 104513 (2011).
- [57] P. J. de Visser, J. J. A. Baselmans, P. Diener, S. J. C. Yates, A. Endo, and T. M. Klapwijk, Phys. Rev. Lett. **106**, 167004 (2011).
- [58] S. Ryu, J. E. Moore, and A. W. W. Ludwig, Phys. Rev. B **85**, 045104 (2012).
- [59] D. V. Averin and Y. V. Nazarov, Phys. Rev. Lett. **69**, 1993 (1992).
- [60] J. A. Schreier, A. A. Houck, J. Koch, D. I. Schuster, B. R. Johnson, J. M. Chow, J. M. Gambetta, J. Majer, L. Frunzio, M. H. Devoret, S. M. Girvin, and R. J. Schoelkopf, Phys. Rev. B **77**, 180502 (2008).
- [61] F. Hassler, A. R. Akhmerov, and C. W. J. Beenakker, New. J. Phys. **13**, 095004 (2011).

- [62] S. Bravyi and A. Y. Kitaev, Phys. Rev. A **71**, 022316 (2005).
- [63] J. D. Sau, S. Tewari, and S. Das Sarma, Phys. Rev. A **82**, 052322 (2010).
- [64] K. Flensberg, Phys. Rev. Lett. **106**, 090503 (2011).
- [65] L. Jiang, C. L. Kane, and J. Preskill, Phys. Rev. Lett. **106**, 130504 (2011).
- [66] P. Bonderson and R. M. Lutchyn, Phys. Rev. Lett. **106**, 130505 (2011).
- [67] J. D. Sau, D. J. Clarke, and S. Tewari, Phys. Rev. B **84**, 094505 (2011).
- [68] A. Romito, J. Alicea, G. Refael, and F. von Oppen, Phys. Rev. B **85**, 020502 (2012).
- [69] B. van Heck, F. Hassler, A. R. Akhmerov, and C. W. J. Beenakker, Phys. Rev. B **84**, 180502 (2011).
- [70] Y. Makhlin, G. Schön, and A. Shnirman, Rev. Mod. Phys. **73**, 357 (2001).
- [71] P. Bonderson, M. Freedman, and C. Nayak, Phys. Rev. Lett. **101**, 010501 (2008).
- [72] M. Cheng, V. Galitski, and S. Das Sarma, Phys. Rev. B **84**, 104529 (2011).
- [73] Y. V. Nazarov and Y. M. Blanter, *Quantum transport: introduction to nanoscience* (Cambridge University Press, 2009).
- [74] V. Mourik, K. Zuo, S. M. Frolov, S. R. Plissard, E. P. A. M. Bakkers, and L. P. Kouwenhoven, Science **336**, 1003 (2012).
- [75] M. T. Deng, C. L. Yu, G. Y. Huang, M. Larsson, P. Caroff, and H. Q. Xu, Nano Lett. **12**, 6414 (2012).
- [76] L. P. Rokhinson, X. Liu, and J. K. Furdyna, Nat. Phys. **8**, 795 (2012).
- [77] A. Das, Y. Ronen, Y. Most, Y. Oreg, M. Heiblum, and H. Shtrikman, Nat. Phys. **8**, 887 (2012).
- [78] A. Y. Kitaev, Ann. Phys. **321**, 2 (2006).
- [79] S. Das Sarma, M. Freedman, and C. Nayak, Phys. Rev. Lett. **94**, 166802 (2005).
- [80] A. Stern and B. I. Halperin, Phys. Rev. Lett. **96**, 016802 (2006).
- [81] P. Bonderson, A. Kitaev, and K. Shtengel, Phys. Rev. Lett. **96**, 016803 (2006).
- [82] L. DiCarlo, J. M. Chow, J. M. Gambetta, L. S. Bishop, B. R. Johnson, D. I. Schuster, J. Majer, A. Blais, L. Frunzio, S. M. Girvin, and R. J. Schoelkopf, Nature **460**, 240 (2009).
- [83] A. A. Houck, J. Koch, M. H. Devoret, S. M. Girvin, and R. J. Schoelkopf, Quantum Information Processing **8**, 105 (2009).

- [84] B. van Heck, A. R. Akhmerov, F. Hassler, M. Burrello, and C. W. J. Beenakker, *New. J. Phys.* **14**, 035019 (2012).
- [85] M. Leijnse and K. Flensberg, *Phys. Rev. Lett.* **107**, 210502 (2011).
- [86] B. I. Halperin, Y. Oreg, A. Stern, G. Refael, J. Alicea, and F. von Oppen, *Phys. Rev. B* **85**, 144501 (2012).
- [87] T. L. Schmidt, A. Nunnenkamp, and C. Bruder, *Phys. Rev. Lett.* **110**, 107006 (2013).
- [88] F. Hassler and D. Schuricht, *New. J. Phys.* **14**, 125018 (2012).
- [89] F. Helmer, M. Mariantoni, A. G. Fowler, J. von Delft, E. Solano, and F. Marquardt, *Europhys. Lett.* **85**, 50007 (2009).
- [90] D. P. DiVincenzo, *Phys. Scripta* **T137**, 014020 (2009).
- [91] M. Mariantoni, H. Wang, T. Yamamoto, M. Neeley, R. C. Bialczak, Y. Chen, M. Lenander, E. Lucero, A. D. O'Connell, D. Sank, M. Weides, J. Wenner, Y. Yin, J. Zhao, A. N. Korotkov, A. N. Cleland, and J. M. Martinis, *Science* **334**, 61 (2011).
- [92] S. Bravyi and A. Y. Kitaev, *Ann. Phys.* **298**, 210 (2002).
- [93] S. Bravyi, *Phys. Rev. A* **73**, 042313 (2006).
- [94] M. Hein, W. Dür, J. Eisert, R. Raussendorf, M. van den Nest, and H.-J. Briegel, *arXiv:quant-ph/0602096* (2006).
- [95] H. J. Briegel, D. E. Browne, W. Dür, R. Raussendorf, and M. van den Nest, *Nat. Phys.* **5**, 19 (2009).
- [96] H. J. Briegel and R. Raussendorf, *Phys. Rev. Lett.* **86**, 910 (2001).
- [97] R. Raussendorf and H. J. Briegel, *Phys. Rev. Lett.* **86**, 5188 (2001).
- [98] A. M. Steane, *Phys. Rev. Lett.* **77**, 793 (1996).
- [99] S. Bravyi and A. Y. Kitaev, *arXiv:quant-ph/9811052* (1998).
- [100] A. G. Fowler, M. Mariantoni, J. M. Martinis, and A. N. Cleland, *Phys. Rev. A* **86**, 032324 (2012).
- [101] D. J. Clarke, J. D. Sau, and S. Tewari, *Phys. Rev. B* **84**, 035120 (2011).
- [102] A. M. Meier, B. Eastin, and E. Knill, *arXiv:1204.4221* (2012).
- [103] T. Jochym-O'Connor, Y. Yu, B. Helou, and R. Laflamme, *arXiv:1205.6715* (2012).

- [104] L. Sun, L. DiCarlo, M. D. Reed, G. Catelani, L. S. Bishop, D. I. Schuster, B. R. Johnson, G. A. Yang, L. Frunzio, L. Glazman, M. H. Devoret, and R. J. Schoelkopf, *Phys. Rev. Lett.* **108**, 230509 (2012).
- [105] D. Ristè, C. C. Bultink, M. J. Tiggelman, R. N. Schouten, K. W. Lehnert, and L. DiCarlo, *Nat. Comm.* **4**, 1913 (2013).
- [106] A. Stern, F. von Oppen, and E. Mariani, *Phys. Rev. B* **70**, 205338 (2004).
- [107] T. Hyart, B. van Heck, I. C. Fulga, M. Burrello, A. R. Akhmerov, and C. W. J. Beenakker, *Phys. Rev. B* **88**, 035121 (2013).
- [108] S. Mi, D. I. Pikulin, M. Wimmer, and C. W. J. Beenakker, *Phys. Rev. B* **87**, 241405 (2013).
- [109] T.-P. Choy, J. M. Edge, A. R. Akhmerov, and C. W. J. Beenakker, *Phys. Rev. B* **84**, 195442 (2011).
- [110] I. Martin and A. F. Morpurgo, *Phys. Rev. B* **85**, 144505 (2012).
- [111] S. Nadj-Perge, I. K. Drozdov, B. A. Bernevig, and A. Yazdani, *Phys. Rev. B* **88**, 020407 (2013).
- [112] J. Klinovaja, P. Stano, A. Yazdani, and D. Loss, *Phys. Rev. Lett.* **111**, 186805 (2013).
- [113] M. M. Vazifeh and M. Franz, *Phys. Rev. Lett.* **111**, 206802 (2013).
- [114] B. Braunecker and P. Simon, *Phys. Rev. Lett.* **111**, 147202 (2013).
- [115] I. Knez, R.-R. Du, and G. Sullivan, *Phys. Rev. Lett.* **109**, 186603 (2012).
- [116] L. Du, I. Knez, G. Sullivan, and R.-R. Du, *arXiv:1306.1925* (2013).
- [117] S. Nadj-Perge, I. K. Drozdov, J. Li, H. Chen, S. Jeon, J. Seo, A. H. MacDonald, B. A. Bernevig, and A. Yazdani, *Science* 1259327 (2014).
- [118] A. R. Akhmerov, *Phys. Rev. B* **82**, 020509 (2010).
- [119] M. S. Scheurer and A. Shnirman, *Phys. Rev. B* **88**, 064515 (2013).
- [120] T. Karzig, G. Refael, and F. von Oppen, *Phys. Rev. X* **3**, 041017 (2013).
- [121] G. Goldstein and C. Chamon, *Phys. Rev. B* **84**, 205109 (2011).
- [122] M. Cheng, R. M. Lutchyn, and S. Das Sarma, *Phys. Rev. B* **85**, 165124 (2012).
- [123] J. C. Budich, S. Walter, and B. Trauzettel, *Phys. Rev. B* **85**, 121405 (2012).
- [124] D. Rainis and D. Loss, *Phys. Rev. B* **85**, 174533 (2012).

- [125] M. J. Schmidt, D. Rainis, and D. Loss, Phys. Rev. B **86**, 085414 (2012).
- [126] L. Mazza, M. Rizzi, M. D. Lukin, and J. I. Cirac, Phys. Rev. B **88**, 205142 (2013).
- [127] F. Konschelle and F. Hassler, Phys. Rev. B **88**, 075431 (2013).
- [128] P. W. Anderson, J. Phys. Chem. Sol. **11**, 26 (1959).
- [129] O. Motrunich, K. Damle, and D. A. Huse, Phys. Rev. B **63**, 224204 (2001).
- [130] P. W. Brouwer, A. Furusaki, I. A. Gruzberg, and C. Mudry, Phys. Rev. Lett. **85**, 1064 (2000).
- [131] I. A. Gruzberg, N. Read, and S. Vishveshwara, Phys. Rev. B **71**, 245124 (2005).
- [132] A. C. Potter and P. A. Lee, Phys. Rev. B **83**, 094525 (2011).
- [133] P. W. Brouwer, M. Duckheim, A. Romito, and F. von Oppen, Phys. Rev. B **84**, 144526 (2011).
- [134] P. W. Brouwer, M. Duckheim, A. Romito, and F. von Oppen, Phys. Rev. Lett. **107**, 196804 (2011).
- [135] T. D. Stanescu, R. M. Lutchyn, and S. Das Sarma, Phys. Rev. B **84**, 144522 (2011).
- [136] J. Liu, A. C. Potter, K. T. Law, and P. A. Lee, Phys. Rev. Lett. **109**, 267002 (2012).
- [137] D. Bagrets and A. Altland, Phys. Rev. Lett. **109**, 227005 (2012).
- [138] D. I. Pikulin, J. P. Dahlhaus, M. Wimmer, H. Schomerus, and C. W. J. Beenakker, New J. Phys. **14**, 125011 (2012).
- [139] R. M. Lutchyn, T. D. Stanescu, and S. Das Sarma, Phys. Rev. B **85**, 140513 (2012).
- [140] J. D. Sau and E. Demler, Phys. Rev. B **88**, 205402 (2013).
- [141] A. M. Lobos, R. M. Lutchyn, and S. Das Sarma, Phys. Rev. Lett. **109**, 146403 (2012).
- [142] S. Takei, B. M. Fregoso, H.-Y. Hui, A. M. Lobos, and S. Das Sarma, Phys. Rev. Lett. **110**, 186803 (2013).
- [143] M.-T. Rieder, P. W. Brouwer, and İ. Adagideli, Phys. Rev. B **88**, 060509 (2013).
- [144] İ. Adagideli, M. Wimmer, and A. Teker, Phys. Rev. B **89**, 144506 (2014).
- [145] J. D. Sau and S. Das Sarma, Phys. Rev. B **88**, 064506 (2013).

- [146] B. M. Fregoso, A. M. Lobos, and S. Das Sarma, Phys. Rev. B **88**, 180507 (2013).
- [147] M. Burrello, B. van Heck, and A. R. Akhmerov, Phys. Rev. A **87**, 022343 (2013).
- [148] P. Bonderson, Phys. Rev. B **87**, 035113 (2013).
- [149] T. L. Schmidt, A. Nunnenkamp, and C. Bruder, Phys. Rev. Lett. **110**, 107006 (2013).
- [150] C. Müller, J. Bourassa, and A. Blais, Phys. Rev. B **88**, 235401 (2013).
- [151] E. Ginossar and E. Grosfeld, Nat. Comm. **5** (2014).
- [152] A. Cottet, T. Kontos, and B. Douçot, Phys. Rev. B **88**, 195415 (2013).
- [153] L. Fu and C. L. Kane, Phys. Rev. Lett. **100**, 096407 (2008).
- [154] S. Hart, H. Ren, T. Wagner, P. Leubner, M. Mühlbauer, C. Brüne, H. Buhmann, L. W. Molenkamp, and A. Yacoby, Nat. Phys. **10**, 638 (2014).
- [155] D. Pekker, C.-Y. Hou, V. E. Manucharyan, and E. Demler, Phys. Rev. Lett. **111**, 107007 (2013).
- [156] Z.-Y. Xue, L. B. Shao, Y. Hu, S.-L. Zhu, and Z. D. Wang, Phys. Rev. A **88**, 024303 (2013).
- [157] C. Wei, X. Zheng-Yuan, W. Z. D, and S. Rui, Chinese Physics B **23**, 030309 (2014).
- [158] J. Li, T. Neupert, B. A. Bernevig, and A. Yazdani, arXiv:1404.4058 arXiv: 1404.4058 (2014).
- [159] Z. Wang, Q.-F. Liang, D.-X. Yao, and X. Hu, arXiv:1406.1429 arXiv: 1406.1429 (2014).
- [160] A. A. Kovalev, A. De, and K. Shtengel, Phys. Rev. Lett. **112**, 106402 (2014).
- [161] Z.-T. Zhang and Y. Yu, Phys. Rev. A **87**, 032327 (2013).
- [162] F.-Y. Hong, J.-L. Fu, and Z.-Y. Zhu, arXiv:1301.4537 arXiv: 1301.4537 (2013).
- [163] I. C. Fulga, B. van Heck, M. Burrello, and T. Hyart, Phys. Rev. B **88**, 155435 (2013).
- [164] O.-P. Saira, A. Kemppinen, V. F. Maisi, and J. P. Pekola, Phys. Rev. B **85**, 012504 (2012).
- [165] A. Blais, R.-S. Huang, A. Wallraff, S. M. Girvin, and R. J. Schoelkopf, Phys. Rev. A **69**, 062320 (2004).

- [166] A. Wallraff, D. I. Schuster, A. Blais, L. Frunzio, R.-S. Huang, J. Majer, S. Kumar, S. M. Girvin, and R. J. Schoelkopf, *Nature* **431**, 162 (2004).
- [167] Y.-J. Doh, J. A. v. Dam, A. L. Roest, E. P. A. M. Bakkers, L. P. Kouwenhoven, and S. D. Franceschi, *Science* **309**, 272 (2005).
- [168] T. S. Jespersen, M. Polianski, C. Sørensen, K. Flensberg, and J. Nygård, *New Journal of Physics* **11**, 113025 (2009).
- [169] N. L. B. Ziino, P. Krogstrup, M. H. Madsen, E. Johnson, J. B. Wagner, C. M. Marcus, J. Nygård, and T. S. Jespersen, *Epitaxial aluminum contacts to InAs nanowires* (2014).
- [170] S. Abay, D. Persson, H. Nilsson, F. Wu, H. Q. Xu, M. Fogelström, V. Shumeiko, and P. Delsing, *Phys. Rev. B* **89**, 214508 (2014).
- [171] I. Sochnikov, L. Maier, C. A. Watson, J. R. Kirtley, C. Gould, G. Tkachov, E. M. Hankiewicz, C. Brüne, H. Buhmann, L. W. Molenkamp, *et al.*, *arXiv:1410.1111* (2014).
- [172] M. D. Reed, L. DiCarlo, B. R. Johnson, L. Sun, D. I. Schuster, L. Frunzio, and R. J. Schoelkopf, *Phys. Rev. Lett.* **105**, 173601 (2010).
- [173] L. S. Bishop, E. Ginossar, and S. Girvin, *Physical review letters* **105**, 100505 (2010).
- [174] C. W. J. Beenakker, *Phys. Rev. Lett.* **67**, 3836 (1991).
- [175] D. Vion, A. Aassime, A. Cottet, P. Joyez, H. Pothier, C. Urbina, D. Esteve, and M. H. Devoret, *Science* **296**, 886 (2002).
- [176] W. Chang, S. Albrecht, T. Jespersen, F. Kuemmeth, P. Krogstrup, J. Nygård, and C. Marcus, *arXiv preprint arXiv:1411.6255* (2014).
- [177] T. W. Larsen, K. D. Petersson, F. Kuemmeth, T. S. Jesperesen, P. Krogstrup, J. Nygård, and C. M. Marcus, *arXiv:1503.08339* (2015).
- [178] A. A. Golubov, M. Y. Kupriyanov, and E. Il'ichev, *Reviews of Modern Physics* **76**, 411 (2004).
- [179] I. O. Kulik and A. N. Omel'yanchuk, *JETP Lett. (USSR)* (Engl. Transl.), v. 21, no. 4, pp. 96-97 (1975).
- [180] J. E. Mooij, T. P. Orlando, L. Levitov, L. Tian, C. H. van der Wal, and S. Lloyd, *Science* **285**, 1036 (1999).
- [181] A. J. Leggett, *Prog. Theor. Phys. Suppl.* **69**, 80 (1980).
- [182] A. Imamoglu, *Phys. Rev. Lett.* **102**, 083602 (2009).

- [183] V. Ranjan, G. de Lange, R. Schutjens, T. Debelhoir, J. P. Groen, D. Szombati, D. J. Thoen, T. M. Klapwijk, R. Hanson, and L. DiCarlo, *Phys. Rev. Lett.* **110**, 067004 (2013).
- [184] M. Scheffler, S. Nadj-Perge, L. P. Kouwenhoven, M. T. Borgström, and E. P. Bakkers, *Physica E: Low-dimensional Systems and Nanostructures* **40**, 1202 (2008).
- [185] V. E. Manucharyan, J. Koch, L. I. Glazman, and M. H. Devoret, *Science* **326**, 113 (2009).
- [186] L. Bretheau, Ç. Girit, H. Pothier, D. Esteve, and C. Urbina, *Nature* **499**, 312 (2013).
- [187] S.-S. Lee, S. Ryu, C. Nayak, and M. P. A. Fisher, *Phys. Rev. Lett.* **99**, 236807 (2007).
- [188] M. Levin, B. I. Halperin, and B. Rosenow, *Phys. Rev. Lett.* **99**, 236806 (2007).
- [189] P. Bonderson, V. Gurarie, and C. Nayak, *Phys. Rev. B* **83**, 075303 (2011).
- [190] E. Fradkin, C. Nayak, A. Tsvelik, and F. Wilczek, *Nucl. Phys. B* **516**, 704 (1998).
- [191] W. Bishara, P. Bonderson, C. Nayak, K. Shtengel, and J. K. Slingerland, *Phys. Rev. B* **80**, 155303 (2009).
- [192] R. L. Willett, L. N. Pfeiffer, and K. W. West, *Proc. Nat. Acad. Sci.* **106**, 8853 (2009).
- [193] R. L. Willett, L. N. Pfeiffer, and K. W. West, *Phys. Rev. B* **82**, 205301 (2010).
- [194] S. An, P. Jiang, H. Choi, W. Kang, S. H. Simon, L. N. Pfeiffer, K. W. West, and K. W. Baldwin, arXiv:1112.3400 arXiv: 1112.3400 (2011).
- [195] R. L. Willett, L. N. Pfeiffer, and K. W. West, arXiv:1204.1993 (2012).
- [196] P. Fendley, M. P. A. Fisher, and C. Nayak, *Phys. Rev. B* **75**, 045317 (2007).
- [197] Y. Gross, M. Dolev, M. Heiblum, V. Umansky, and D. Mahalu, *Phys. Rev. Lett.* **108**, 226801 (2012).
- [198] V. Venkatachalam, S. Hart, L. Pfeiffer, K. West, and A. Yacoby, *Nat. Phys.* **8**, 676 (2012).
- [199] B. J. Overbosch and X.-G. Wen, arXiv:0706.4339 (2007).
- [200] W. Bishara and C. Nayak, *Phys. Rev. B* **80**, 155304 (2009).
- [201] B. Rosenow, B. I. Halperin, S. H. Simon, and A. Stern, *Phys. Rev. Lett.* **100**, 226803 (2008).

- [202] B. Rosenow and S. H. Simon, Phys. Rev. B **85**, 201302 (2012).
- [203] K. T. Law, D. E. Feldman, and Y. Gefen, Phys. Rev. B **74**, 045319 (2006).
- [204] D. E. Feldman and A. Kitaev, Phys. Rev. Lett. **97**, 186803 (2006).
- [205] K. Yang and B. I. Halperin, Phys. Rev. B **79**, 115317 (2009).
- [206] C. Wang and D. E. Feldman, Phys. Rev. B **81**, 035318 (2010).
- [207] K. Ono, D. G. Austing, Y. Tokura, and S. Tarucha, Science **297**, 1313 (2002).
- [208] A. C. Johnson, J. R. Petta, J. M. Taylor, A. Yacoby, M. D. Lukin, C. M. Marcus, M. P. Hanson, and A. C. Gossard, Nature **435**, 925 (2005).
- [209] F. H. L. Koppens, J. A. Folk, J. M. Elzerman, R. Hanson, L. H. W. v. Beveren, I. T. Vink, H. P. Tranitz, W. Wegscheider, L. P. Kouwenhoven, and L. M. K. Vandersypen, Science **309**, 1346 (2005).
- [210] J. R. Petta, A. C. Johnson, J. M. Taylor, E. A. Laird, A. Yacoby, M. D. Lukin, C. M. Marcus, M. P. Hanson, and A. C. Gossard, Science **309**, 2180 (2005).
- [211] J. M. Taylor, J. R. Petta, A. C. Johnson, A. Yacoby, C. M. Marcus, and M. D. Lukin, Phys. Rev. B **76**, 035315 (2007).
- [212] S. Foletti, H. Bluhm, D. Mahalu, V. Umansky, and A. Yacoby, Nat. Phys. **5**, 903 (2009).
- [213] C. Barthel, D. J. Reilly, C. M. Marcus, M. P. Hanson, and A. C. Gossard, Phys. Rev. Lett. **103**, 160503 (2009).
- [214] H. Bluhm, S. Foletti, D. Mahalu, V. Umansky, and A. Yacoby, Phys. Rev. Lett. **105**, 216803 (2010).
- [215] A. A. Koulakov and B. I. Shklovskii, Phys. Rev. B **57**, 2352 (1998).
- [216] M. Field, C. G. Smith, M. Pepper, D. A. Ritchie, J. E. F. Frost, G. A. C. Jones, and D. G. Hasko, Phys. Rev. Lett. **70**, 1311 (1993).
- [217] M. J. Yoo, T. A. Fulton, H. F. Hess, R. L. Willett, L. N. Dunkleberger, R. J. Chichester, L. N. Pfeiffer, and K. W. West, Science **276**, 579 (1997).
- [218] V. Venkatachalam, A. Yacoby, L. Pfeiffer, and K. West, Nature **469**, 185 (2011).
- [219] M. Baraban, G. Zikos, N. Bonesteel, and S. H. Simon, Phys. Rev. Lett. **103**, 076801 (2009).
- [220] X. Wan, Z.-X. Hu, E. H. Rezayi, and K. Yang, Phys. Rev. B **77**, 165316 (2008).
- [221] M. Storni and R. H. Morf, Phys. Rev. B **83**, 195306 (2011).

- [222] P. Bonderson, A. E. Feiguin, and C. Nayak, Phys. Rev. Lett. **106**, 186802 (2011).
- [223] B. I. Halperin, Helv. Phys. Acta **56**, 75 (1983).
- [224] M. Freedman, C. Nayak, and K. Walker, Phys. Rev. B **73**, 245307 (2006).
- [225] M. D. Shulman, O. E. Dial, S. P. Harvey, H. Bluhm, V. Umansky, and A. Yacoby, Science **336**, 202 (2012).
- [226] P. Bonderson, M. Freedman, and C. Nayak, Ann. Phys. **324**, 787 (2009).
- [227] P. Bonderson, K. Shtengel, and J. K. Slingerland, Ann. Phys. **323**, 2709 (2008).
- [228] P. Bonderson, *Non-Abelian anyons and interferometry*, Ph.d. thesis, California Institute of Technology (2007).
- [229] P. Bonderson, Phys. Rev. Lett. **103**, 110403 (2009).
- [230] A. Feiguin, S. Trebst, A. W. W. Ludwig, M. Troyer, A. Kitaev, Z. Wang, and M. H. Freedman, Phys. Rev. Lett. **98**, 160409 (2007).
- [231] S. Trebst, E. Ardonne, A. Feiguin, D. A. Huse, A. W. W. Ludwig, and M. Troyer, Phys. Rev. Lett. **101**, 050401 (2008).
- [232] C. Gils, E. Ardonne, S. Trebst, A. W. W. Ludwig, M. Troyer, and Z. Wang, Phys. Rev. Lett. **103**, 070401 (2009).
- [233] E. Ardonne, J. Gukelberger, A. W. W. Ludwig, S. Trebst, and M. Troyer, New J. Phys. **13**, 045006 (2011).
- [234] D. Poilblanc, A. W. W. Ludwig, S. Trebst, and M. Troyer, Phys. Rev. B **83**, 134439 (2011).
- [235] P. Fendley, Journal of Statistical Mechanics: Theory and Experiment **2012**, P11020 (2012).
- [236] L. Fidkowski, G. Refael, N. E. Bonesteel, and J. E. Moore, Phys. Rev. B **78**, 224204 (2008).
- [237] C. R. Laumann, A. W. Ludwig, D. A. Huse, and S. Trebst, Phys. Rev. B **85**, 161301 (2012).
- [238] D. J. Clarke, J. Alicea, and K. Shtengel, Nat. Comm. **4**, 1348 (2013).
- [239] N. H. Lindner, E. Berg, G. Refael, and A. Stern, Phys. Rev. X **2**, 041002 (2012).
- [240] M. Cheng, Phys. Rev. B **86**, 195126 (2012).
- [241] A. Vaezi, Phys. Rev. B **87**, 035132 (2013).
- [242] Y.-Z. You, C.-M. Jian, and X.-G. Wen, Phys. Rev. B **87**, 045106 (2013).

- [243] B. van Heck, M. Burrello, A. Yacoby, and A. Akhmerov, Phys. Rev. Lett. **110**, 086803 (2013).
- [244] M. Barkeshli, C.-M. Jian, and X.-L. Qi, Phys. Rev. B **87**, 045130 (2013).
- [245] L.-M. Duan, E. Demler, and M. Lukin, Phys. Rev. Lett. **91**, 090402 (2003).
- [246] A. Micheli, G. Brennen, and P. Zoller, Nat. Phys. **2**, 341 (2006).
- [247] G. Jackeli and G. Khaliullin, Phys. Rev. Lett. **102**, 017205 (2009).
- [248] N. R. Cooper, Advances in Physics **57**, 539 (2008).
- [249] M. Lewenstein, A. Sanpera, and V. Ahufinger, *Ultracold Atoms in Optical Lattices: Simulating quantum many-body systems* (Oxford University Press, 2012).
- [250] X.-G. Wen, *Quantum Field Theory of Many-body Systems from the Origin of Sound to an Origin of Light and Electrons* (Oxford University Press, 2004).
- [251] X.-G. Wen, Phys. Rev. B **41**, 12838 (1990).
- [252] D.-H. Lee and X.-G. Wen, Phys. Rev. Lett. **66**, 1765 (1991).
- [253] M. Levin and A. Stern, Phys. Rev. Lett. **103**, 196803 (2009).
- [254] B. A. Bernevig and S.-C. Zhang, Phys. Rev. Lett. **96**, 106802 (2006).
- [255] M. Levin, F. Burnell, M. Koch-Janusz, and A. Stern, Phys. Rev. B **84**, 235145 (2011).
- [256] T. Neupert, L. Santos, S. Ryu, C. Chamon, and C. Mudry, Phys. Rev. B **84**, 165107 (2011).
- [257] L. Santos, T. Neupert, S. Ryu, C. Chamon, and C. Mudry, Phys. Rev. B **84**, 165138 (2011).
- [258] M. Levin and A. Stern, Phys. Rev. B **86**, 115131 (2012).
- [259] Y. Oreg, E. Sela, and A. Stern, Phys. Rev. B **89**, 115402 (2014).
- [260] Y.-Z. You and X.-G. Wen, Phys. Rev. B **86**, 161107 (2012).
- [261] M. B. Hastings, C. Nayak, and Z. Wang, Phys. Rev. B **87**, 165421 (2013).
- [262] G. Mussardo, *Statistical field theory* (Oxford Univ. Press, 2010).
- [263] E. Fradkin and L. P. Kadanoff, Nucl. Phys. B **170**, 1 (1980).
- [264] M. Rajabpour and J. Cardy, J. Phys. A **40**, 14703 (2007).
- [265] G. Ortiz, E. Cobanera, and Z. Nussinov, Nucl. Phys. B **854**, 780 (2012).

- [266] E. Cobanera, G. Ortiz, and Z. Nussinov, *Advances in Physics* **60**, 679 (2011).
- [267] A. Zamolodchikov and V. Fateev, *Sov. Phys. JETP* **62**, 215 (1985).
- [268] G. Delfino, *Ann. Phys.* **333**, 1 (2013).
- [269] B. M. Terhal, F. Hassler, and D. P. DiVincenzo, *Phys. Rev. Lett.* **108**, 260504 (2012).
- [270] Z. Nussinov, G. Ortiz, and E. Cobanera, *Ann. Phys.* **327**, 2491 (2012).
- [271] S. Bravyi, B. M. Terhal, and B. Leemhuis, *New J. Phys.* **12**, 083039 (2010).
- [272] S. S. Bullock and G. K. Brennen, *J. Phys. A* **40**, 3481 (2007).
- [273] C. d. C. Chamon and X. Wen, *Phys. Rev. Lett.* **70**, 2605 (1993).
- [274] Y. Aharonov and A. Casher, *Phys. Rev. Lett.* **53**, 319 (1984).
- [275] T. Smith, *Pacific Journal of Mathematics* **149**, 157 (1991).
- [276] T. Smith, *Pacific Journal of Mathematics* **149**, 185 (1991).
- [277] R. Jagannathan, in *The legacy of Alladi Ramakrishnan in the mathematical sciences*, 465–489 (Springer, 2010).
- [278] R. Guyon, P. Devillard, T. Martin, and I. Safi, *Phys. Rev. B* **65**, 153304 (2002).
- [279] E.-A. Kim, M. J. Lawler, S. Vishveshwara, and E. Fradkin, *Phys. Rev. B* **74**, 155324 (2006).
- [280] D. Horn, M. Weinstein, and S. Yankielowicz, *Phys. Rev. D* **19**, 3715 (1979).
- [281] M. D. Schulz, S. Dusuel, R. Orús, J. Vidal, and K. P. Schmidt, *New J. Phys.* **14**, 025005 (2012).
- [282] L. Ioffe and M. Feigel'man, *Phys. Rev. B* **66**, 224503 (2002).
- [283] L. Ioffe, M. Feigel'man, A. Ioselevich, D. Ivanov, M. Troyer, and G. Blatter, *Nature* **415**, 503 (2002).
- [284] B. Doucot and J. Vidal, *Phys. Rev. Lett.* **88**, 227005 (2002).
- [285] B. Doucot, L. B. Ioffe, and J. Vidal, *Phys. Rev. B* **69**, 214501 (2004).
- [286] S. Gladchenko, D. Olaya, E. Dupont-Ferrier, B. Douçot, L. B. Ioffe, and M. E. Gershenson, *Nat. Phys.* **5**, 48 (2008).
- [287] S. Bravyi, D. P. DiVincenzo, and D. Loss, *Ann. Phys.* **326**, 2793 (2011).
- [288] F. Burnell, S. H. Simon, and J. Slingerland, *Phys. Rev. B* **84**, 125434 (2011).

- [289] F. Burnell, S. H. Simon, and J. Slingerland, *New J. Phys.* **14**, 015004 (2012).
- [290] M. A. Levin and X.-G. Wen, *Phys. Rev. B* **71**, 045110 (2005).
- [291] P. Fendley, *J. Phys. A* **39**, 15445 (2006).
- [292] S. Elitzur, *Phys. Rev. D* **12**, 3978 (1975).
- [293] E. Cobanera, G. Ortiz, and Z. Nussinov, *Phys. Rev. B* **87**, 041105 (2013).
- [294] E. Cobanera, G. Ortiz, and Z. Nussinov, *Phys. Rev. Lett.* **104**, 020402 (2010).
- [295] E. Dennis, A. Kitaev, A. Landahl, and J. Preskill, *J. Math. Phys.* **43**, 4452 (2002).
- [296] Z. Nussinov and G. Ortiz, *Phys. Rev. B* **77**, 064302 (2008).
- [297] J. R. Wootton and J. K. Pachos, *Phys. Rev. Lett.* **107**, 030503 (2011).
- [298] C. Stark, L. Pollet, A. Imamoğlu, and R. Renner, *Phys. Rev. Lett.* **107**, 030504 (2011).
- [299] A. Kitaev, arXiv:0901.2686 (2009).
- [300] S. Ryu, A. P. Schnyder, A. Furusaki, and A. W. Ludwig, *New J. Phys.* **12**, 065010 (2010).
- [301] X.-G. Wen, *Phys. Rev. B* **85**, 085103 (2012).
- [302] K. T. Law, P. A. Lee, and T. K. Ng, *Phys. Rev. Lett.* **103**, 237001 (2009).
- [303] K. Flensberg, *Phys. Rev. B* **82**, 180516 (2010).
- [304] M. Wimmer, A. Akhmerov, J. Dahlhaus, and C. Beenakker, *New J. Phys.* **13**, 053016 (2011).
- [305] L. Fidkowski, J. Alicea, N. H. Lindner, R. M. Lutchyn, and M. P. A. Fisher, *Phys. Rev. B* **85**, 245121 (2012).
- [306] A. R. Akhmerov, J. P. Dahlhaus, F. Hassler, M. Wimmer, and C. W. J. Beenakker, *Phys. Rev. Lett.* **106**, 057001 (2011).
- [307] L. Fidkowski and A. Kitaev, *Phys. Rev. B* **81**, 134509 (2010).
- [308] X.-G. Wen, *Phys. Rev. B* **89**, 035147 (2014).
- [309] L.-Y. Hung and X.-G. Wen, *Phys. Rev. B* **89**, 075121 (2014).
- [310] F. J. Wegner, *J. Math. Phys.* **12**, 2259 (1971).
- [311] Z. Nussinov and G. Ortiz, *Ann. Phys.* **324**, 977 (2009).
- [312] Y. Bahri and A. Vishwanath, *Phys. Rev. B* **89**, arXiv: 1303.2600 (2014).

- [313] E. Fradkin and S. H. Shenker, *Phys. Rev. D* **19**, 3682 (1979).
- [314] K. Fredenhagen and M. Marcu, *Comm. Math. Phys.* **92**, 81 (1983).
- [315] K. Fredenhagen and M. Marcu, *Phys. Rev. Lett.* **56**, 223 (1986).
- [316] K. Gregor, D. A. Huse, R. Moessner, and S. Sondhi, *New J. Phys.* **13**, 025009 (2011).
- [317] A. D. Zaikin, D. S. Golubev, A. van Otterlo, and G. T. Zimányi, *Phys. Rev. Lett.* **78**, 1552 (1997).
- [318] C. N. Lau, N. Markovic, M. Bockrath, A. Bezryadin, and M. Tinkham, *Phys. Rev. Lett.* **87**, 217003 (2001).
- [319] D. S. Golubev and A. D. Zaikin, *Phys. Rev. B* **64**, 014504 (2001).
- [320] J. D. Sau, B. I. Halperin, K. Flensberg, and S. Das Sarma, *Phys. Rev. B* **84**, 144509 (2011).
- [321] K. A. Matveev, A. I. Larkin, and L. I. Glazman, *Phys. Rev. Lett.* **89**, 096802 (2002).
- [322] D. Pekker, C.-Y. Hou, D. L. Bergman, S. Goldberg, İ. Adagideli, and F. Hassler, *Phys. Rev. B* **87**, 064506 (2013).
- [323] V. Shivamoggi, G. Refael, and J. E. Moore, *Phys. Rev. B* **82**, 041405 (2010).
- [324] K. G. Wilson, *Phys. Rev. D* **10**, 2445 (1974).
- [325] J. Kogut and L. Susskind, *Phys. Rev. D* **11**, 395 (1975).
- [326] K. Uzelac, R. Jullien, and P. Pfeuty, *Phys. Rev. B* **22**, 436 (1980).
- [327] R. Hützen, A. Zazunov, B. Braunecker, A. L. Yeyati, and R. Egger, *Phys. Rev. Lett.* **109**, 166403 (2012).
- [328] C. Lacroix, *J. Phys. F: Met. Phys.* **11**, 2389 (1981).
- [329] G. de Lange, B. van Heck, A. Bruno, D. van Woerkom, A. Geresdi, S. R. Plissard, E. P. A. M. Bakkers, A. R. Akhmerov, and L. DiCarlo, arXiv:1503.08483 (2015).
- [330] V. S. Pribiag, A. J. Beukman, F. Qu, M. C. Cassidy, C. Charpentier, W. Wegscheider, and L. P. Kouwenhoven, arXiv:1408.1701 (2014).

Samenvatting

Majorana toestanden zijn een speciaal soort deeltjes die kunnen verschijnen aan de eindpunten van supergeleidende draden of in magnetische vortices in supergeleidende films. Zij zijn interessant vanwege de voorspelling dat ze een nieuw soort “niet-Abelse” statistiek bezitten. Dat houdt in dat de aanwezigheid van meerdere Majorana toestanden in een supergeleider een ontaarding in de grondtoestand veroorzaakt, en dat het uitwisselen van de positie van twee toestanden tot een rotatie van de golffunctie in deze ontaarde ruimte leidt. Omdat opeenvolgende rotaties niet commuteren, kun je met een serie rotaties een gecompliceerde bewerking uitvoeren op de golffunctie. Deze bewerking kan een bouwsteen zijn voor een kwantumcomputer. Supergeleiders met Majorana toestanden hebben een ingebouwde bescherming voor fouten die bij de berekening kunnen optreden, vanwege het topologische karakter van de niet-Abelse statistiek.

Hoe je in de praktijk de Majorana toestanden kunt uitwisselen is makkelijker gezegd dan gedaan. De eerste zes hoofdstukken van het proefschrift bevatten een concreet voorstel om Majorana toestanden te manipuleren, uitgaande van bestaande technieken uit de supergeleidende elektronica. Het kernidee achter dit voorstel is dat de grondtoestand weliswaar ontaard is als de supergeleider geraard is, maar dat de ontaarding kan worden opgeheven als de supergeleider elektrisch geïsoleerd is. Dit is mogelijk omdat de ontaarde toestanden corresponderen met een verschillend aantal elektronen. Het verschil in elektrostatische energie kan in een elektrisch geïsoleerde supergeleider gemeten worden, en zo kun je de ontaarding opheffen.

De elektrostatische energie van een supergeleidend gebiedje kan heel nauwkeurig gecontroleerd worden door het magnetische veld te variëren in een zogenaamde Josephson-junctie, die de supergeleider met aarde verbindt. Dit is een bekende techniek uit de supergeleidende elektronica. Zo hebben we een praktische en nauwkeurige manier om de wisselwerking van de Majorana toestanden te beheersen. Het effect van een magnetisch veld op de Majorana toestanden wordt in hoofdstuk 2 bestudeerd in een zogenaamde DC SQUID geometrie, en in hoofdstukken 3 en 4 in grotere schakelingen, die meer mogelijkheden bieden: het uitwisselen van Majorana toestanden, het uitlezen van de rotatie van de golffunctie, en de toepassing op complexe bewerkingen. De uitwisselingsoperatie wordt uitgevoerd zonder de Majorana toestanden fysiek door de ruimte te bewegen, hetgeen grote praktische voordelen biedt.

Hoofdstuk 7 bevat de resultaten van een samenwerking met de experimentele groep van Dr. Leo DiCarlo in Delft. We analyseren het gedrag van eenvoudige schakelingen gemaakt van niobium-titaan-nitride, een bijzondere supergeleider die bestand is tegen hoge magnetische velden. Omdat de dichtheid van elektronen door een elektrisch veld kan worden gevareerd, hebben deze schakelingen een resonantiefrequentie die variabel is. Mijn theoretische analyse van het microgolfspectrum toont aan dat de schakeling heel gevoelig is voor afwijkingen van de sinus-vorm in de stroom-fase relatie van de Josephson-junctie. Deze supergeleidende schakelingen vormen een eerste stap op weg naar de experimentele realisatie van de door ons ontworpen Majorana-schakelingen.

In de volgende hoofdstukken passen we de theoretische ideën uit de eerdere hoofdstukken toe op gerelateerde problemen. In hoofdstuk 8 tonen we aan dat de elektrostatische wisselwerking niet alleen nuttig is om Majorana toestanden in supergeleiders te manipuleren, maar ook van dienst kan zijn in het zogenaamde fractionele kwantum-Hall effect, waar ook het optreden van Majorana toestanden is voorspeld (bij vulfractie $\nu = 5/2$). Hoofdstuk 9 laat zien dat het idee om Majorana toestanden te verwisselen zonder ze fysiek door de ruimte te bewegen uitgebreid kan worden naar andere deeltjes met niet-Abelse statistiek, zogenaamde “niet-Abelse anyonen”. We hoeven slechts enkele eenvoudige veronderstellingen te maken over hun wisselwerking. In hoofdstuk 10 onderzoeken we de eigenschappen van zogenaamde parafermion-toestanden, die beschouwd kunnen worden als het analogon van de Majorana toestanden in het fractionele kwantum-Hall effect bij vulfractie $1/3$. Tenslotte, in hoofdstuk 11 behandelen we de transpordeigenschappen van een reeks supergeleidende gebiedjes op de rand van een zogenaamde kwantum spin-Hall isolator. Dit is een veelbelovende methode om Majorana toestanden te realiseren. We laten zien dat elektrische wisselwerking een storend effect heeft op de elektrische geleiding (de kwantisatie verdwijnt), maar niet op de thermische geleiding (die blijft gekwantiseerd).

Summary

Majorana modes are special zero-energy quasiparticles that can appear at the ends of superconducting wires or bound to vortices in superconducting films. They are interesting because they are predicted to have non-Abelian quantum statistics. This means that the presence of several Majorana modes in a superconductor leads to a degenerate quantum ground state, and that exchanging the position of two modes may result in a rotation of the ground state wave function within this degenerate manifold. Different rotations may not commute with each other, hence a sequence of these exchanges can be seen as a quantum algorithm executed on the initial wave function. Superconductors with Majorana modes are prominent candidates to realize a quantum computer naturally endowed with resilience to errors and decoherence, so that, ideally, its operation would not require quantum error correction.

It is a challenge to manipulate and measure the quantum state of a collection of Majorana modes. The first six chapters of this thesis contain a concrete design proposal to realize both tasks using the powerful techniques of superconducting circuits. The main idea behind the proposal is that different ground states of a collection of Majorana modes are degenerate if the superconductor is grounded, but can be split in energy if the superconductor is floating. The reason behind this behavior is that the quantum states differ by fermion parity, which is equal to the electric charge contained in the superconductor modulo $2e$. In the presence of a small but finite electrostatic energy, this difference in fermion parity becomes measurable.

The electrostatic energy of a superconducting island can be controlled with exponential sensitivity by varying the magnetic flux through a split Josephson junction connecting the island to the ground, as is routinely done in experiments with superconducting circuits. This gives us a realistic and flexible tool to control the interaction between Majorana modes. The response of Majorana modes to a magnetic flux is studied in chapter 2 in a simple DC SQUID geometry, and in chapters 3 and 4 in larger circuits which allow for braiding of two Majorana modes, the readout of the result, and even the execution of more complex algorithms. The braiding operation, in particular, is implemented not by adiabatic motion of the Majorana modes, but by performing an adiabatic trajectory in the parameter space of their pairwise Coulomb couplings.

Chapter 7 contains the results of a collaboration with the experimental group of

Dr. Leo DiCarlo in Delft. We analyze the behavior of simple NbTiN superconducting circuits with Josephson junction formed by InSb nanowires, rather than the more conventional oxide tunnel junctions. Because the density of carriers can be modulated by a side gate, these devices have a gate-tunable plasma frequency. Moreover, the theoretical analysis of the microwave spectroscopy of current oscillations across a split junction reveals that the spectrum is very sensitive to the non-sinusoidal current-phase relation of the nanowire junction. These hybrid superconducting circuits constitute a first step towards the realization of the Majorana circuits described in the previous chapters.

In chapters 8 we apply the ideas of the first six chapters in different contexts. For instance, in chapter 8 we demonstrate that charging interactions are useful not only for manipulating Majorana modes appearing in superconductors, but also for their ancestors appearing in the fractional quantum Hall effect at filling $\nu = 5/2$. Chapter 9 shows instead that the idea to braid Majorana modes by controlling their mutual coupling - rather than directly moving them in space - can be generalized to all types of non-Abelian anyons, provided some simple assumptions on their mutual interactions hold. Chapter 10 explores the properties of parafermionic zero modes, which are the “fractional” analogue of Majorana modes occurring in systems where superconductivity is induced on the edge of a fractional quantum Hall edge at filling $1/3$. Finally, chapter 11 focuses on the transport properties of a linear array of superconducting islands situated on the quantum spin Hall edge, a system which effectively realizes a chain of coupled Majorana modes. We show that weak Coulomb interactions, appearing as quantum phase slips between different islands, remove the quantization of Andreev conductance in the topological phase, while thermal conductance at the Majorana phase transition remains quantized.

Curriculum Vitæ

I was born on 4th June 1986 in Rome, where I attended primary and middle school. I received my secondary education during the years 2000 – 2005 at the Liceo Virgilio in Rome, specializing in classical studies.

After finishing high school I enrolled in the Physics Department at the University of Rome “La Sapienza”. There, I received my Bachelor degree under the supervision of Prof. Massimo Testa in December 2008, and my Master degree under the supervision of Prof. Antonio Polosa in April 2011, with a thesis entitled “The problem of confinement for two-dimensional massless Dirac fermions”. During the final year of my studies, my research interests shifted from high energy to condensed matter physics.

After my graduation I moved to Leiden University, where I began my Ph.D. under the supervision of Prof. Carlo Beenakker. Since September 2013, I am also a guest student at the Kavli Institute for Nanoscience at the Technical University of Delft, where I work with my co-supervisor Dr. Anton Akhmerov. This thesis contains part of the research performed in these four years, during which I greatly benefited from a lively and diverse research environment.

During my Ph.D. studies I taught exercise classes in quantum mechanics. I participated in several schools, workshop and conferences, and I presented my work in Italy, Austria, Germany and the United States of America.

After completing my Ph.D. studies, I will join the Physics Department of Yale University as a Postdoctoral Associate.

List of Publications

1. *Realization of microwave quantum circuits using hybrid superconducting semiconducting nanowire Josephson elements*, G. de Lange, B. van Heck, A. Bruno, D.J. van Woerkom, A. Geresdi, S.R. Plissard, E.P.A.M. Bakkers, A.R. Akhmerov, and L. DiCarlo, arXiv:1503.08483 (2015) [Chapter 7].
2. *Single fermion manipulation via superconducting phase differences in multiterminal Josephson junctions*, B. van Heck, S. Mi, and A.R. Akhmerov, Phys. Rev. B **90**, 155450 (2014), Editors' Suggestion.
3. *Minimal circuit for a flux-controlled Majorana qubit in a quantum spin-Hall insulator*, B. van Heck, T. Hyart, and C.W.J. Beenakker, arXiv:1407.2851, submitted to *Physica Scripta* as contribution for the proceedings of the Nobel Symposium on topological insulators [Chapter 6].
4. *Thermal conductance as a probe of the non-local order parameter for a topological superconductor with gauge fluctuations*, B. van Heck, E. Cobanera, J. Ulrich, and F. Hassler, Phys. Rev. B **89**, 165416 (2014) [Chapter 11].
5. *Statistical Topological Insulators*, I.C. Fulga, B. van Heck, J.M. Edge, and A.R. Akhmerov, Phys. Rev. B **89**, 155424 (2014), Editors' Suggestion.
6. *Effects of disorder on Coulomb-assisted braiding of Majorana zero modes*, I.C. Fulga, B. van Heck, M. Burrello, and T. Hyart, Phys. Rev. B **88**, 155435 (2013) [Chapter 5].
7. *Flux-controlled quantum computation with Majorana fermions*, T. Hyart, B. van Heck, I.C. Fulga, M. Burrello, A.R. Akhmerov, and C.W.J. Beenakker, Phys. Rev. B **88**, 035121 (2013) [Chapter 4].
8. *Topological phases in two-dimensional arrays of parafermionic zero modes*, M. Burrello, B. van Heck, and E. Cobanera, Phys. Rev. B **87**, 195422 (2013) [Chapter 10].
9. *Braiding of non-Abelian anyons using pairwise interactions*, M. Burrello, B. van Heck, and A.R. Akhmerov, Phys. Rev. A **87**, 022343 (2013); **87**, 049905(E) (2013) [Chapter 9].

10. *Topological blockade and measurement of topological charge*, B. van Heck, M. Burrello, A. Yacoby, and A.R. Akhmerov, Phys. Rev. Lett. **110**, 086803 (2013) [Chapter 8].
11. *Coulomb-assisted braiding of Majorana fermions in a Josephson junction array*, B. van Heck, A.R. Akhmerov, F. Hassler, M. Burrello, and C.W.J. Beenakker, New J. Phys. **14**, 035019 (2012) [Chapter 3].
12. *Coulomb stability of the 4π -periodic Josephson effect of Majorana fermions*, B. van Heck, F. Hassler, A.R. Akhmerov, and C.W.J. Beenakker, Phys. Rev. B **84**, 180502 (2011), Rapid Communication [Chapter 2].